ATOMS AND CLUSTERS IN STRONG LASER FIELDS

TATIANA MARCHENKO

DOCTORAL THESIS

2008

ATOMS AND CLUSTERS IN STRONG LASER FIELDS

Cover: Wassily Kandinsky “Trente”, 1937 (Centre Pompidou, Paris)

Printed in Paris, 2008

ATOMS AND CLUSTERS IN STRONG LASER FIELDS

EEN WETENSCHAPPELIJKE PROEVE OP HET GEBIED VAN DE NATUURWETENSCHAPPEN, WISKUNDE EN INFORMATICA

PROEFSCHRIFT

ter verkrijging van de graad van doctor
aan de Radboud Universiteit Nijmegen
op gezag van de rector magnificus prof. mr. S.C.J.J. Kortmann,
volgens besluit van het College van Decanen
in het openbaar te verdedigen op woensdag 29 oktober 2008
om 10.30 uur precies

door

Tatiana Marchenko

geboren op 30 november 1978
te Moskou, Rusland

Promotores:

Prof. dr. M.J.J. Vrakking
Prof. dr. W.J. van der Zande

Manuscriptcommissie:

Prof. dr. D. H. Parker
Prof. dr. H. J. Bakker (FOM-AMOLF)
Dr. Th. Schlathölter (Rijksuniversiteit Groningen)

The work described in this thesis has been performed at FOM Institute for Atomic and Molecular Physics, Kruislaan 407, 1098 SJ Amsterdam, The Netherlands (www.amolf.nl)

This work is part of the research program of the “Stichting voor Fundamenteel Onderzoek der Materie (FOM)”, which is financially supported by the “Nederlandse organisatie voor Wetenschappelijk Onderzoek (NWO)”.

ATOMS AND CLUSTERS IN STRONG LASER FIELDS

AN ACADEMIC ESSAY IN SCIENCE

DOCTORAL THESIS

to obtain the degree of doctor
from Radboud University Nijmegen
on the authority of the rector magnificus prof. dr. S.C.J.J. Kortmann,
according to the decision of the Council of Deans
to be defended in public on Wednesday, 29 October 2008
at 10.30 hours

by

Tatiana Marchenko

born in Moscow, Russia
on 30 November 1978

Supervisors:

Prof. dr. M.J.J. Vrakking
Prof. dr. W.J. van der Zande

Doctoral Thesis Committee:

Prof. dr. D. H. Parker
Prof. dr. H. J. Bakker (FOM-AMOLF)
Dr. Th. Schlathölter (Rijksuniversiteit Groningen)

The work described in this thesis has been performed at FOM Institute for Atomic and Molecular Physics, Kruislaan 407, 1098 SJ Amsterdam, The Netherlands (www.amolf.nl)

This work is part of the research program of the “Stichting voor Fundamenteel Onderzoek der Materie (FOM)”, which is financially supported by the “Nederlandse organisatie voor Wetenschappelijk Onderzoek (NWO)”.

ACKNOWLEDGEMENTS

Now I wish to thank those who contributed positively to the completion of my thesis and those who made this long journey more cheerful.

Being a student of Marc Vrakking is both demanding and rewarding. His personal dedication to science, his enthusiasm and efficiency set an example for his team. Marc's attitude to work was always very encouraging: my small intermediate successes were regularly met with his optimistic "sounds promising" and I learnt that any problems that came up were only there to build my character. I thank you, Marc, for your choice of interesting projects, which formed the core of my thesis, and for the opportunity to take part in several collaborations both in the Netherlands and abroad, which has provided me with invaluable experience. I very much appreciate your support, which reaches far beyond my work at AMOLF.

Doing PhD at AMOLF would not be possible without my university foundation. I would like to thank Prof. Dr. V.A. Makarov and Dr. T.M. Il'inova, who helped me make my first steps in fundamental research at M.V. Lomonosov Moscow State University.

A substantial part of my thesis relies on numerical simulations based on the codes by Harm-Geert Muller and Ken Schafer (Louisiana State University, USA). I gratefully acknowledge them for the opportunity they provided to discuss my results at the analysis stage and also for their critical reading of the selected chapters of my thesis.

Thanks to the first-class technical support, researchers at AMOLF are provided with a luxury of working on nearly plug-and-play experimental setups. I am grateful to those who took care of my lasers, pumps, electronics, computers and those who designed and built the various upgrades for my setups – Rob, Ad, Hinco, Han-Kwang, Iliya, Dirk-Jan, Richard, Rutger, Jan, Idsart, Duncan and everybody from the mechanical workshop. My special thanks are to Rob who was my fairy godfather in the lab.

I thank everybody from the secretariat, financial and personnel departments, library, reception desk and domestic services, who created comfortable conditions for work at AMOLF. Particularly I would like to thank Wouter for helping me with all the “alien” administration and Roudy for providing me with a nice home next to Vondelpark, where I spent all my 5 years in Amsterdam.

Having left Moscow nearly 6 years ago I have realised how strongly I am attached to my life there. My neighbourhood, my school, my university, our student slang, people in the metro, the Moscow crows…I am grateful to those who kept me attached. Vasya, Andrey, Katia, Serega, Pasha, you are my precious links to our happy university years. Thank you for that! Mama, Papa, Katia, thank you for being always on my side no matter what I make up my mind for. Doug, thank you for putting up with my pessimistic Russian nature with all the hilarious consequences and especially thanks for our little orange monster. Grishka, little monster, thank you too!

While working at AMOLF I met people whose company I greatly enjoyed. I thank Sébastien for being my spiritual guru during the first years, Christian for our unforgettable profound discussions on abstract topics, Franck for your “so-out-of-place” simple elegance, Yongfeng for staying yourself at any time and for dumplings we had at your place, Chantal for your enthusiasm for life in general, Anna for sharing the joy from watching “Dirty Dancing”, Omair for your paradoxal humour and cute Scottish accent, Per for your imperturbability and diplomacy witnessed in the most challenging situations, and the new generation of the XUV group – Arjan, Freek, Wing Kiu and Ymkje – for your drive and energy both at work and outside.

Finally I want to thank my new colleagues at Laboratoire d’Optique Appliquée, who welcomed me after my departure from AMOLF. I am particularly grateful to Philippe Zeitoun, who kept a position open for me during 2 years before I could come to Paris and created all the conditions so that I could finish writing my thesis in parallel with my work at LOA. My special thanks are also to Guillaume for reminding me daily about the date of my defence and to Evangelos for his magic VMIS, which I hope will bring me luck.

Paris, September 2008

Why is it so that you've become
The one that you've become
"No redemption", Spaint

to people I love

PUBLICATIONS

Control of the Production of Highly Charged Ions in Femtosecond-Laser Cluster Fragmentation
S. Zamith, T. Martchenko, Y. Ni, S.A. Aseyev, H.G. Muller, and M.J.J. Vrakking
Phys. Rev. A **70**, 011201(R), 2004 (***Chapter 5***)

Optimal Control of Femtosecond Laser-Cluster Interactions
T. Martchenko, Ch. Siedschlag, S. Zamith, H.G. Muller, and M.J.J. Vrakking
Phys. Rev. A, **72**, 053202, 2005 (***Chapter 6***)

Short XUV Pulses to Characterize Field-free Molecular Alignment
F. Lépine, M. Kling, Y. Ni, J. Khan, O. Ghafur, T. Martchenko, E. Gustafsson,
P. Johnsson, K. Varjú, T. Remetter, A. L'Huillier, and M.J.J. Vrakking
J. Mod. Optics, **54**, 953-956, 2007

Above-Threshold Ionisation in a Strong DC Electric Field
Y. Ni, S. Zamith, F. Lépine, T. Martchenko, M. Kling, O. Ghafur, H.G. Muller,
G. Berden, F. Robicheaux and M.J.J. Vrakking
Phys. Rev. A **78**, 013413, 2008

Wavelength-dependent Above-Threshold Ionisation in Argon and Xenon
T. Marchenko, H.K. Nienhuys, H.G. Muller, K. Schafer, and M.J.J. Vrakking
In preparation, 2008 (***Chapter 3***)

CONTENTS

PART I. INTRODUCTION

Chapter 1. Towards sub-atomic control of matter.

Curiosity and imagination backed up with creativity and persistence drive those who consciously enter the club of natural scientists. The tease of the unknown makes them spending long days and nights in the lab trying to unveil the mysteries of nature. Harvesting knowledge cuts through the struggle and frustration of failed attempts, which are entirely compensated with a rewarding feeling of satisfaction when (if) finally the experiment (real or numerical) works and a conclusive explanation of the results can be found.

From a historical perspective most of the research findings form a database for a certain scientific field. Upon reaching critical mass the collected knowledge leads to the formulation of a qualitatively new vision, which can explain and generalise the previous results and open prospectives for future research.

Chapter 1 describes the current status of strong-field light-matter interactions in its historical context and emphasizes the scientific endeavour towards the fundamental control of matter in space and time.

1.1. A history of light.

An enormous scientific heritage bridges the state-of-the-art understanding of the nature of light and the ancient perceptions of human vision, which was thought to occur through special thin sensors stretching out from the eyes to the surrounding objects. Since the XVII century the nature of light, its propagation and interaction with matter became a subject of hot debate which still maintains its topicality nowadays. The parallel coexistence of Newton's "corpuscular" theory of light and the early wave theory of Huygens lasted till the beginning of the XIX century, when the now famous experiments by Thomas Young brought the discovery of interference and diffraction of light. The explanation of these phenomena was found to lie in the framework of the wave theory, which was further conceptualised by Augustin Fresnel, who was also the first to prove the transverse character of light waves. The dominance of wave theory of light was further strengthened by the development of Maxwell's electromagnetic field theory in the second half of the XIX century. Experimental discovery of electromagnetic waves by Hertz in 1886 perfectly confirmed Maxwell's predictions and established the modern view of propagating light as an electromagnetic wave.

The beginning of the XX century coincided with the greatest revolution in physics. To the great surprise of all the scientific community the all-round tested and verified Maxwell's laws failed to explain the radiation spectrum of a heated body. The solution was offered by Max Planck, who introduced a hypothesis of quantum properties of electromagnetic radiation. Therefore the previously rejected corpuscular theory of light turned out to be relevant when considering interaction of light with matter. The experimental observation of electron ejection from a metal plate irradiated by light – the phenomenon presently known as the photoeffect – became the first proof of the quantum nature of light. The theory of the photoeffect, developed in 1905 by Einstein from the quantum hypothesis of Planck, requires that a photon energy exceeds the binding energy of the electron involved. This requirement sets the lower boundary for the frequency of light (photon energy) capable of inducing a photoeffect for a given system under a condition of a *weak* electric field. The development of lasers providing *strong* electromagnetic radiation allowed for observation of non-linear light-matter interactions with the involvement of multiple photons. Multi-photon ionisation (MPI) – ionisation of atoms via absorption of multiple photons – generalises the Einstein requirement for the atomic photoeffect: electron ejection occurs if the total energy of the absorbed photons exceeds the ionisation potential of an atom. In the following section we will consider the main ionisation mechanisms in strong laser fields.

1.2. Ionisation mechanisms in strong laser fields.

Atomic ionisation mechanisms are usually classified according to the relative strength of the laser field invoked. In general ionisation of an atom can be characterised with three energies: the binding energy of an electron in the absence of a laser field (or in other terms the ionisation potential of an atom IP), the photon energy ħω and the ponderomotive energy of a free electron in the laser field U_p. The ponderomotive enegy is related to the laser intensity I_{laser} and frequency ω as

$$U_p=I_{laser}/4\omega^2 \qquad (1)$$

in the system of atomic units ($e=m_e=\hbar=1$). If a photon energy exceeds the atomic ionisation potential ($\hbar\omega>IP$) single-photon ionisation occurs. This mechanism is operative for example in ionisation of a noble-gas atom by high-frequency XUV radiation. In the opposite case of low-energy photons ($\hbar\omega<IP$) strong-field MPI takes place. If the laser field is relatively weak so that $U_p<<\hbar\omega$ one can assume that the bound atomic states are not affected by the laser field and then ionisation can be described in terms of perturbation theory.

At stronger laser fields the ponderomotive energy of a free electron may become comparable to the photon energy ($U_p\geq\hbar\omega$). Under these conditions the ionisation threshold as well as the bound states of an atom experience an ac-Stark shift in the oscillating laser field and the interaction becomes non-perturbative. At a certain value of the ac-Stark shift a high-lying Rydberg state may resonantly couple with an integer number of laser photons. Ionisation via intermediate resonant states is called Resonance-Enhanced Multi-Photon Ionisation (REMPI), since the ionisation rate in this case is always significantly larger than in the case of direct MPI. Properties of electrons resulting from REMPI and direct MPI processes will be discussed in PART II of this thesis.

At sufficiently high laser intensities and/or low frequencies when U_p approaches the value of the atomic ionisation potential IP, distortion of the ionisation threshold in the direction of the laser polarisation creates a potential barrier which an electron can tunnel through. Further increase of the laser intensity lowers the potential barrier below the ground state, which leads to over-the-barrier ionisation.

It is a common practice to distinguish between conventional photoionisation (single-photon ionisation or MPI) and quasi-static ionisation (tunnelling or over-the-barrier ionisation). The distinction between these types of ionisation is usually linked to the value of the Keldysh parameter $\gamma=(IP/2U_p)^{1/2}$ [1], the dominant ionisation mechanism being quasi-static when $\gamma\leq1$ and single- or multi-photon when $\gamma\geq1$. Coexistence of multi-photon and tunnelling ionisation mechanisms in the parameter region where $\gamma\sim1$ has been discussed by Ivanov et al [2]. In a classical description of an MPI process an electron moves "vertically" along the atomic potential well in the classically allowed region, while being heated by the shaking walls of the potential well. In a quasi-static tunnelling regime an electron moves "horizontally" under a potential barrier without changing its energy. At $\gamma\sim1$ a quasi-static picture is not applicable since the potential barrier moves non-adiabatically changing the electron energy during tunnelling. Therefore at $\gamma\sim1$ horizontal tunnelling of an electron is combined with vertical multi-photon energy absorption in the classically forbidden region (see Figure 1-1).

An important qualitative difference between MPI and tunnelling ionisation lies in the frequency dependence of ionisation rates. In the case of MPI the strong dependence on the radiation frequency is determined by the number of photons required for ionisation and by the frequency-dependent ionisation cross-section. The tunnelling ionisation rate shows an exponential dependence on the laser field as given by the Ammosov-Delone-Krainov (ADK) theory [3], but is independent of the laser frequency.

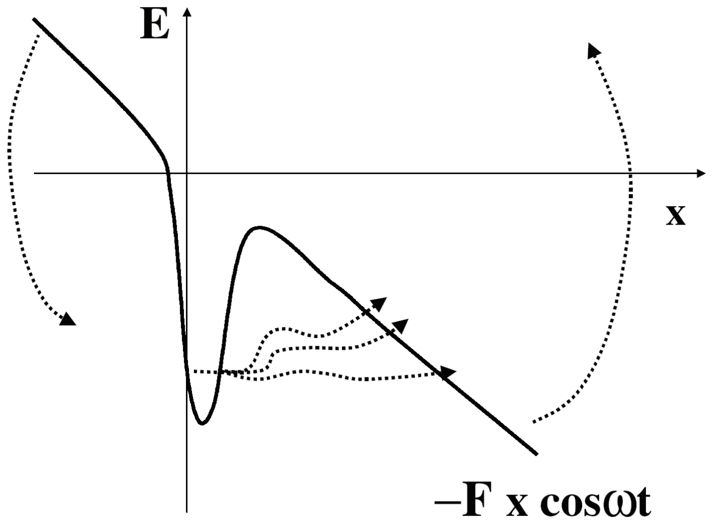

Figure 1-1. Tunneling ionisation channel, with the possibility of changing the electron energy during tunneling due to the oscillation of the barrier (non-adiabatic tunnelling). The figure is taken from M Yu Ivanov, O Smirnova and M Spanner 2005 J. Mod. Opt. 52 165-84 [2].

Most of experiments on strong-field ionisation of atoms using intense 800 nm radiation of a Ti: Sapphire laser were performed in the MPI regime. Only a few experiments on Helium [4, 5, 6] were carried out at the transition to the tunnelling regime. The recent development of intense mid-infrared lasers [7] allows a significant extension of the parameter range into the tunnelling regime. In practice it is a non-trivial task to determine which of the mechanisms is dominant in the experiment. Evaluation of the Keldysh parameter requires knowledge of the laser intensity, which usually can only be roughly estimated. The situation is further complicated by the distribution of laser intensities over the focal volume and the temporal profile of the laser pulse. However careful study of electron properties resulting from strong-field ionisation of atoms sometimes allows extraction of experimental observables, which may be associated with one or the other ionisation mechanism. For example, Ni et al [8] observed that the electron energy spectra resulting from ionisation of high-lying Rydberg states of Xenon atoms by far-infrared radiation (108 μm) of a free-electron laser in the presence of a DC electric field contained a unique feature, which could only be explained in terms of an MPI mechanism. The characteristic properties of electron spectra at the transition from multi-photon to tunnelling regime for visible and near-infrared radiation will be discussed in PART II of this thesis.

Ionisation is the first step for the majority of strong-field processes in atomic physics. In larger systems such as molecules and clusters ionisation can induce interesting dynamics of electrons and nuclei. The following section gives an overview of the main strong-field phenomena observed in atoms, molecules and clusters.

1.3. Strong-field phenomena in atoms, molecules and clusters.

1.3.1. Atoms.

Among all the quantum systems interacting with strong laser fields the atom is a fundamental object of research. Extensive studies in this field led to the conclusion that there exist a number of phenomena resulting from strong-field laser-atom interactions that can be described in the framework of a universal three-step model [9, 10, 11, 12]. The essential physics can be understood using a semi-classical picture (see Figure 1-2). In the first step of this model an electron tunnels and emerges outside the potential barrier formed by the combined laser field and the atomic potential with zero initial velocity. In the second step the electron is driven by the laser field as a free particle, the ionic potential is neglected. After about half a cycle of free propagation some of the electrons may return to the core. Electron re-scattering on the parent ion forms the third principal step of the model. This last scattering event determines the energetics of the main strong-field atomic phenomena. Elastic electron scattering with the absorption of extra photons from the laser field leads to the production of high-energy electrons in above-threshold ionisation (ATI), the phenomenon described in detail in PART II of this thesis. If the instantaneous energy of the returning electron exceeds the binding energy of a bound electron, inelastic scattering can lead to two-electron ionisation, known as non-sequential double ionisation [13, 5]. Finally, recombination of the returning electron to the ground state leads to the emission of a high-energy photon, the phenomenon known as high-order harmonic generation (HHG) [14].

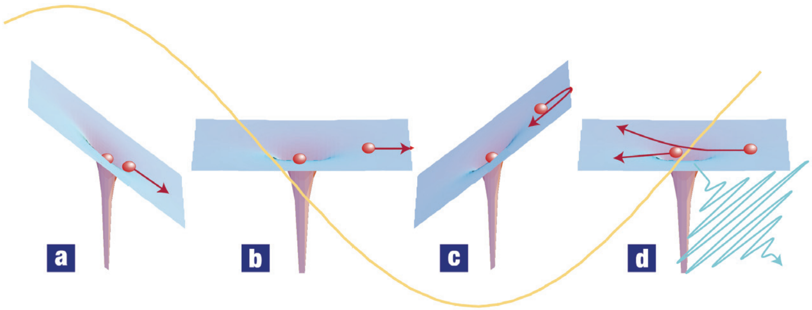

Figure 1-2. Illustration of the tree-step model. Initially, the electron is pulled away from the atom (**a**, **b**), but after the field reverses, the electron is driven back (**c**) where it can ‘recollide’ during a small fraction of the laser oscillation cycle (**d**). The figure is taken from P B Corkum and F Krausz 2007 Nature Phys. 3 381 [20].

From a quantum-mechanical point of view the re-scattering model can be described as follows. The electron wave-function splits upon ionisation into a free and a bound component. The free component propagates as a wave-packet along the classical trajectories in the laser field. Upon the return of the electron wave-packet the two components of the wave-function interfere leading to the process of ATI or HHG [15].

In the time domain the process of HHG from multi-cycle laser pulses occurs in a series of attosecond XUV pulses, produced every half an optical cycle of the fundamental frequency. Generation of an isolated attosecond pulse becomes possible when the HHG process is confined to a single recombination event per laser pulse. This has been achieved by using few-cycle driving pulses [16, 17] or applying polarisation-gating technique [18, 19]. Application of attosecond pulse trains and isolated attosecond pulses synchronised with the dressing infrared field has been demonstrated in a number of experiments on strong-field atomic interactions (see [20] and references therein).

1.3.2. Molecules.

The interaction of strong laser fields with molecules is largely determined by the additional degrees of freedom present in molecules as compared to atoms. Excitation and probing of vibrational and rotational molecular motion under the influence of a strong laser field has been an active research topic in the last decade [21]. Recently, the influence of molecular alignment on HHG and ATI has been theoretically demonstrated [22]. While molecular rotation and vibration typically occur on a picosecond time scale, ionisation of molecules induces nuclear and electronic dynamics on femtosecond and attosecond time scales, respectively. Depending on the experimental conditions a femtosecond process of molecular dissociation can involve different physical mechanisms, which can be experimentally determined from the momentum or energy spectra of the molecular fragments and femtosecond pump-probe measurements [e.g. 23, 24].

Monitoring electron dynamics in molecules has become possible with the development of attosecond technology. The emerging ability to control electron motion within a molecule [25] opens important perspectives for biochemical control. On the other hand electron motion induced by a laser field can be used for measuring the structure of the molecule itself. A number of molecular imaging techniques exploiting the unique properties of recollision electrons have been proposed and demonstrated, such as laser-induced electron diffraction [26, 27], electron holography [28] and tomographic reconstruction [29, 30, 31]. Simultaneous measurement of structure and dynamics of small molecules with sub-atomic spatial and temporal resolution is the state-of-the-art in strong-field molecular science [32].

1.3.3. Clusters.

Extension of the fundamental aspects of strong-field interaction with matter towards potential applications requires a transition from atoms and small molecules to larger systems, such as large organic molecules, solids or surfaces. In contrast to atoms where most of the observed phenomena can be described in the single active electron approximation (SAE) [33] the physics of large quantum systems is essentially determined by their multi-electron response to strong fields. While experimental and theoretical tools correctly addressing multi-electron effects in complex quantum systems are still to be developed, important knowledge can be obtained from the physics of clusters. The high local density and nanometer size determine the unique properties of clusters and make them a bridge system between solids and the gas phase.

Strong field ionisation of clusters followed by fragmentation into positive ions and electrons has been extensively studied both experimentally and numerically [34]. Very efficient laser energy absorption in clusters leads to a number of remarkable phenomena such as the production of highly charged and energetic ions [35], keV electrons [36, 37, 38], X-ray emission [39] and even nuclear fusion [40]. The efficiency of laser-cluster energy coupling can be significantly enhanced under selected experimental conditions determined by an optimal combination of an average cluster size, laser intensity, pulse duration and pulse shape. In Chapter 5 we present an optimal-control experiment aimed at the enhancement of highly charged ion yields resulting from ionisation of large Xenon clusters with shaped laser pulses.

The cluster size is the major aspect of laser-cluster interaction since it determines the relative position of the system between atoms and solids and therefore qualitatively determines the mechanism of laser energy transfer to clusters. Numerical simulations for size-selected clusters presented in Chapter 6 demonstrate a transition from molecular to plasma behaviour for increasing cluster sizes. For medium-sized clusters of several hundreds atoms we have identified a regime of coexistence of the both mechanisms in a single cluster expansion. We propose an experiment where numerical predictions can be verified on size-selected clusters.

In analogy with molecules femtosecond dynamics of cluster fragmentation is accompanied by attosecond dynamics of electrons within an ionised cluster [41, 42]. However in contrast to small molecules, where electron behaviour can still be predicted by solving the Schrödinger equation, such complex systems as clusters only allow making model assumptions about their transient evolution. The challenge to experimentally determine the character of electron dynamics makes clusters a relevant and interesting system for attosecond probing [43].

The development of X-ray free-electron lasers (XFEL) in Germany, the USA and Japan opens a new parameter range for laser-cluster interactions. Moreover, potential application of XFEL for X-ray diffraction imaging on single bio-molecules stimulates further interest to the physics of clusters in this new regime since clusters can be considered as a reasonable and practical gas-phase prototype system of large biological samples. The dynamics of cluster fragmentation in response to XFEL radiation can give an idea of the damage threshold for a bio-molecule, which sets the limit for obtaining structural information of an unperturbed sample [44, 45].

Attosecond probing of cluster ionisation and fragmentation and X-ray diffraction imaging of size-selected clusters with high temporal resolution provide the motivation for the future research on clusters.

1.4. Look forward.

The primary goal of scientists in physics, chemistry and biology is the measurement and control of matter on the most fundamental level both in space and time. For this to become possible development of new technologies goes hand in hand with the most fundamental of research. Understanding behaviour of electrons strongly driven in an atom by a laser field brought us to the development of attosecond technology, which in turn opens new exciting possibilities in fundamental science [20, 46].

Development of new light sources covering previously inaccessible spectral ranges on both sides of the visible light allows access to the hardly explored regimes of light-matter interactions [7, 47], where new phenomena may be observed and new information about the dynamics and structure of matter can be extracted.

Among the other promising and rapidly developing techniques attosecond pump/attosecond probe spectroscopy and single-pulse ultra-short X-ray imaging of macromolecules should become possible in the nearest future, which will allow capturing the motion of electrons and atoms with subatomic spatio-temporal resolution undoubtedly boosting further progress in science and technology.

PART II. ATOMS IN STRONG LASER FIELDS

Chapter 2. Cornerstones of ATI.

The most fundamental phenomena in nature are also the most desirable to be thoroughly understood since they are the basis for advanced scientific theories and concepts serving as indications for the future research directions. Continuous development of new experimental tools and techniques requires continuous reconsideration of the well-known phenomena, bringing them to the next level of understanding.

More than a hundred years have passed since Einstein published his explanation of the photoeffect and established the concept of an ionisation threshold. At that time single-photon ionisation was the only experimentally achievable process. Sixty years later advancement of laser technology provided the possibility of atomic ionisation via the absorption of multiple photons. The possibility of multi-photon ionisation (MPI) led to a generalisation of Einstein's concept of a threshold photon energy required for the photoeffect. A second departure from the initial theory of the photoeffect came with the observation of above-threshold ionisation (ATI) [48] in 1979: at sufficiently high laser intensity an atom was shown to absorb photons above the ionisation threshold. The discovery of ATI became the first experimental manifestation of a strong-field light-matter interactions and has remained an active subject of research ever since.

Chapter 2 gives an overview of the major aspects of atomic ATI, crucial for shaping of the modern understanding of this phenomenon, and highlights the open questions in the field, which are addressed in Chapter 3 of this thesis.

2.1. ATI in the multi-photon regime.

Following the natural development of laser technology the vast majority of experimental work in atomic physics lies in the multi-photon regime, which requires only moderate intensities at optical frequencies. Note that for hydrogen atoms (IP=0.5 a.u.) that are irradiated by an 800 nm Ti:Sapphire laser (ω=0.057 a.u.), the Keldysh parameter (which has been introduced above in section 1.2) becomes equal to 1 when $I_{laser} = 3.25\times10^{-3}$ a.u. = 1.14×10^{14} W/cm^2. A strong support of the multi-photon theory of ionisation was provided by Agostini et al [48] who demonstrated in their experiment that a photoelectron energy spectrum resulting from ATI exhibits peaks separated by the photon energy (see Figure 2-1).

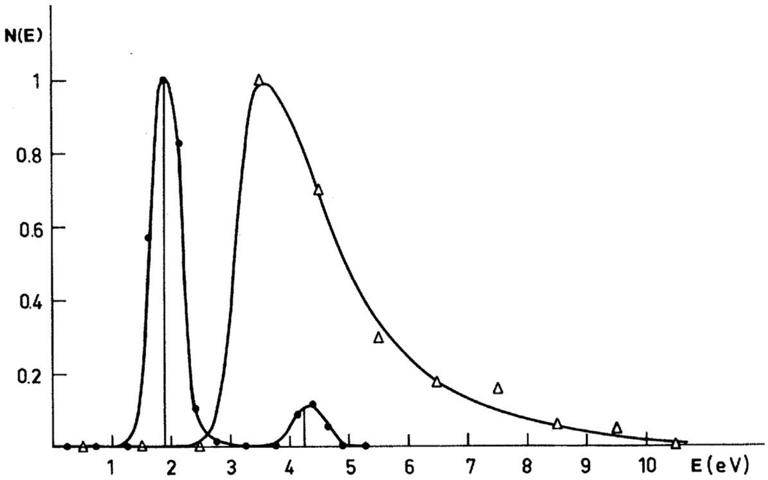

Figure 2-1. Energy spectra of the emitted electrons for two photon energies: circles, $\hbar\omega=2.34$ eV, $I=8\times10^{12}$ W/cm^2; triangles, $\hbar\omega=1.17$ eV, $I=4\times10^{13}$ W/cm^2. The solid curves have been hand drawn through the experimental points. The figure is taken from P Agostini et al 1979 Phys. Rev. Lett. **42** 1127 [48]

2.1.1. Role of the ponderomotive potential.

The absolute position of ATI peaks in the photoelectron energy spectra strongly depends on the ionisation regime. In the long-pulse regime, when the duration of the ionising laser pulse is longer than the time it takes a photoelectron to leave the interaction volume, the positions of ATI peaks in the energy spectrum are given by

$$E_{\text{long pulse}}=(n+s)\hbar\omega-IP \qquad (2)$$

where n is the minimum number of photons with energy ħω necessary to overcome the ionisation potential IP, and s=0,1,2… is the number of photons absorbed by the atom above the ionisation threshold and consequently the number of the ATI order. In the short-pulse regime (i.e. when the duration of the ionising laser pulse is shorter than the time it takes a photoelectron to leave the interaction volume, typically below 1ps) the ATI peaks in the photoelectron spectrum shift to lower energies by the value of the ponderomotive potential U_p:

$$E_{\text{short pulse}}=(n+s)\hbar\omega-(IP+U_p) \qquad (3)$$

This effect takes place since the ionisation potential of an atom increases in the presence of an intense field by U_p [49] and consequently the kinetic energy of the photoelectrons is reduced by the same amount. If the laser pulse is long, the ionised electron leaves the laser field when the field is still on and the electron compensates for the reduction of its initial kinetic energy by converting the ponderomotive energy in the laser field into kinetic energy. Conversely, in the short-pulse regime electrons do not gain any energy from the laser field after ionisation has occurred, and therefore the energy spectrum maps the actual kinetic energy of the electron at the moment of ionisation.

2.1.2. Freeman resonances.

A next milestone in the physics of ATI was the work by Freeman et al [50], who demonstrated that in the short-pulse regime each of the low-energy ATI peaks breaks up into a series of narrow peaks (see Figure 2-2).

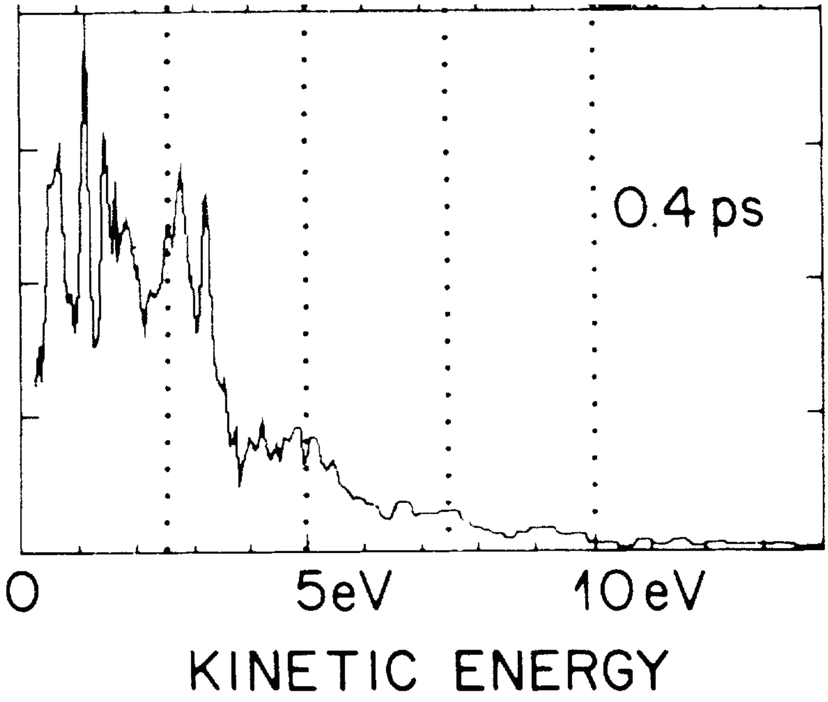

Figure 2-2. Kinetic energy of photoelectrons emitted from Xenon. At the pulse duration of 0.4 ps the individual ATI peaks break up into a narrow fine structre. The figure is taken from R R Freeman et al 1987 Phys. Rev. Lett. **59** 1092 [50]

These sub-structures within each ATI peak, presently known as *Freeman resonances*, are related to the Rydberg states of an atom. Similar to the ionisation potential, the energies of Rydberg states are ponderomotively increased in a strong laser field (ac Stark shift). When a Stark-shifted Rydberg level comes into resonance with an integer number of laser photons, resonant enhancement of ionisation takes place. The position of the corresponding peak in the photoelectron energy spectrum is independent of the temporal and spatial profile of the laser pulse (incl. the peak laser intensity). Rather, Freeman resonances give rise to peaks in the photoelectron spectrum that are given by

$$E_{\text{short pulse, resonant}}=n\hbar\omega-E_b \qquad (4)$$

where E_b is the binding energy of the respective Rydberg level and n will generally be a low number. Importantly, the intensity of the laser, which entered Eqn. (3) through U_p, does not appear in Eqn. (4). Thus it turns out to be impossible to obtain the intensity dependence of the ponderomotive Stark shifts at a single wavelength. However, monitoring the energy of a given Freeman resonance while scanning the wavelength provides the intensity and wavelength dependence of the corresponding Stark shift. Changing the wavelength between 575 and 675 nm and measuring photoelectron spectra of xenon ionised by150 fs laser pulses with intensity up to 3×10^{13} W/cm^2 Agostini et al [51] concluded that Stark shifts of the most excited Rydberg states are close to the ponderomotive value U_p.

The original explanation of experimentally observed Freeman resonances suggested that enhancement of the ionisation rate occurs at one specific intensity which also provides the ac Stark shift of the excited Rydberg state into resonance. Thus it assumes that ionisation from the excited state occurs before the resonant intensity changed significantly, which requires that ionisation takes place mainly at the peak pulse intensity, where the intensity changes slowly. An alternative model [52] suggested that the narrow peaks in the photoelectron ATI spectra come from a two-step process that involves actual population transfer from the ground state to the ac-Stark shifted Rydberg levels, which are consequently ionised by one or more photons. Essentially this model suggests that the populated intermediate Rydberg state can survive during the laser pulse so that ionisation does not necessarily occur at the resonant intensity, but may take place at any other intensity at later times within the laser pulse. The energy of electrons ionised from the same state is independent of the ionising intensity since both the ionisation threshold and the corresponding Rydberg state shift by U_p. Thus both models predict identical photoelectron spectra with ATI peak positions in the energy spectrum that are independent of the peak laser intensity. On the other hand, for *non*-ponderomotively shifted states, the predictions of the two models diverge. Gibson et al [53] demonstrated experimental results in favour of the first model by presenting photoelectron spectra of argon, ionised by a 120 fs laser pulse at 308 nm. The use of ultra-violet radiation allowed them to observe ionisation via low-lying states with an ac Stark shift different from the ponderomotive energy U_p. The two-step model involving population transfer predicts an intensity dependence of the spectra in this case, since the ponderomotive shift changes from the moment of the resonant Rydberg level population to the moment of the electron ionisation. However, the spectra measured over a range of intensities did not show any intensity dependent broadening of the resonant peaks, which allowed the authors to conclude that the electron peaks resulted from the resonance enhanced ionisation rate.

Later experiments provided strong arguments in support of the two-step model, by demonstrating the phenomenon called channel switching (e.g. ref [54]). In their experiment Schyja et al [54] observed a qualitative change of the photoelectron momentum spectra of xenon, ionised by a 100 fs laser pulse at 800 nm, with the intensity increasing from 1.2×10^{13} W/cm^2 to 4×10^{13} W/cm^2. The photoelectron kinetic energy and angular distributions could be interpreted in terms of the model of ac Stark shifted resonances. At intensities up to around 3×10^{13} W/cm^2 ionisation was shown to occur via 8-photon resonantly excited Rydberg states of the f-series. Upon further increase of the intensity channel switching occurred leading to ionisation via 9-photon resonantly excited g-series. This phenomenon proves that the intensity, at which a Rydberg level is tuned into resonance with an integer number of photons may differ significantly from the intensity, at which the actual ionisation occurs.

2.1.3. High-energy plateau.

In the following years attention of the strong-field research community concentrated on the high-energy region of ATI electron spectra, the landmark being the discovery of the plateau in the ATI photoelectron spectra [55] similar to the one observed in high-harmonic generation (HHG) (see Figure 2-3). So far the low-energy part of the photoelectron energy spectra could be described by the semi-classical theory of ionisation, which considers classical motion of the ionised electron in the oscillating laser field after it has tunnelled into the continuum with zero momentum [9, 56, 57]. According to this theory a cut-off must be observed at a kinetic energy equal to $2U_p$, where U_p is the ponderomotive energy. The appearance of the cut-off is related to the maximum kinetic energy an electron can acquire due to classical motion in the laser field after it has been ionised. However, the appearance of electrons with energies higher than $2U_p$ could not be explained by the semi-classical theory and the interaction of the free electron with the parent ion core upon ionisation had to be taken into account, which allowed to explain the production of electrons with energies up to $10U_p$ [11, 58].

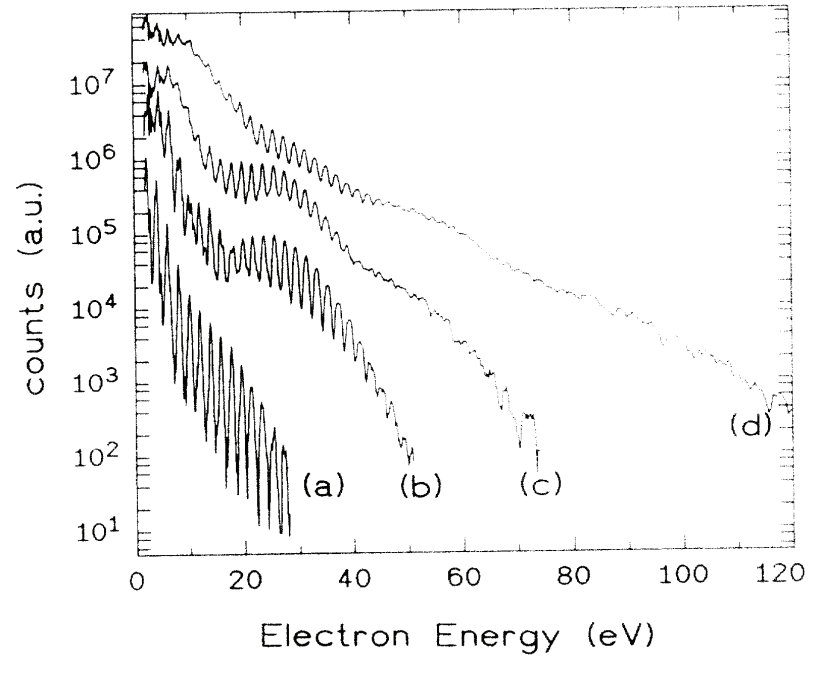

Figure 2-3. ATI spectra from Argon with 40 fs, 630 nm pulses at intensities of 6×10^{13} W/cm^2 (a), 1.2×10^{14} W/cm^2 (b), 2.4×10^{14} W/cm^2 (c), and 4.4×10^{14} W/cm^2 (d) The figure is taken from G G Paulus et al 1994 Phys. Rev. Lett. **72** 2851 [55].

High-resolution experiments in the plateau region of xenon [59] and argon [60] ATI electron spectra revealed the presence of narrow individual peaks within single ATI orders. The independence of the position of these narrow peaks on the intensity pointed at their resonant character. However the appearance of this sub-structure could not be explained in terms of resonant enhancement of ionisation via intermediate Rydberg states which account for the appearance of Freeman resonances in the low orders of ATI spectra. Numerical solution of the time-dependent Schrödinger equation (TDSE) for a model argon atom in the SAE approximation [61, 62] revealed that the envelope of the ATI spectrum was related to bunching of the tunnelling wave packet on the first re-encounter with its parent ion, followed by backscattering of such bunches on subsequent encounters. Interference between bunches produced in different optical cycles accounted for the appearance of the resonant sub-structure in the plateau region. A detailed comparison between high-resolution experimental photoelectron spectra and high-precision TDSE calculations in the SAE approximation for argon demonstrated a very good quantitative agreement over a wide range of electron kinetic energies and laser intensities [63].

The recent measurements of photoelectron energy spectra with few-cycle pulses [64] showed that the ATI plateau behaves similarly for long and few-cycle pulses. Namely, the ATI plateau is present at linear laser polarisation and disappears when the polarisation becomes circular. This observation confirms the hypothesis that the ATI plateau is due to rescattering of electrons from the parent ion within one optical cycle after ionisation. Furthermore the authors observed the absence of any structure in the photoelectron spectra measured with few-cycle pulses, which allowed them to conclude that atomic resonances do not play a role at the few-cycle limit.

2.1.4. Angular distributions of photoelectrons.

The discovery of a plateau in the ATI photoelectron spectrum was accompanied by the observation of a dramatic qualitative change in the angular distributions at the onset of the plateau [65]. In the long pulse regime (pulse duration 50 ps) the angular distributions of high-energy photoelectrons from xenon and krypton displayed unexpected structures at an angle of 45 degrees with respect to the laser polarisation axis. Examination of the evolution of the time-dependent wave function calculated in the SAE approximation revealed a strong interaction of the ionised electrons with the ion core before they leave the vicinity of the atom. While the experimental parameters implied an intermediate regime between multi-photon and tunnelling, the authors observed in the calculations that the off-axis structures in the angular distributions are caused by backscattering of the tunnelling component of the wave function. Later classical calculations of Paulus et al [58] showed that for a given photoelectron energy and number of return times there is a minimum angle at which the photoelectron could have scattered off the ion core, thus relating the off-axis structures in the angular distributions in [65] to the scattering angles.

Similar off-axis structures in the electron angular distributions were observed in the short-pulse regime of ATI. Using 110 fs laser pulses, Nandor et al [66] performed extensive measurements of angle-resolved photoelectron spectra of xenon at 800 nm, for various intensities in the range 10^{13} -10^{14} W/cm^2. They showed that at each intensity studied, the angular distributions of high-order ATI peaks display abrupt variations at the onset of the plateau region. Furthermore, angular distributions of the low-order ATI peaks exhibited rich structure, which partly was related to the angular momenta of the corresponding Rydberg-resonant photoelectrons (so-called “jets”) and partly remained unidentified (“wings” in the authors’ terminology). Note that such structures in the angular distributions were not observed in argon either experimentally or in calculations [63], which demonstrates a major difference between the responses of the two atoms to the strong laser field and implies the need for precise calculations for xenon.

The development of photoelectron imaging techniques provided further insight into multi-photon ionisation processes. Specifically, the simultaneous observation of electron energy and angular distributions facilitated the identification and classification of ionisation mechanisms. The dependence of electron angular distributions within each ATI peak on the intermediate resonant state that the electron goes through before ionisation was naturally expected since the discovery of Freeman resonances [50]. Indeed, examination of the energy and angular distributions of xenon atoms ionised by a ps laser at 620 and 640 nm for intensities between 10^{13} W/cm^2 and 10^{14} W/cm^2 allowed Helm et al [67] to identify the intermediate state resonances that dominate ionisation in the low intensity range. At higher intensities the appearance of continuously distributed low-energy electrons suggested that an additional ionisation mechanism became operative.

A number of experiments followed, where electron momentum distributions were measured. Making use of an imaging spectrometer Helm et al [68] observed the simultaneous appearance of resonant and non-resonant ionisation in helium and a change of the dominant ionisation path upon increase of the laser intensity from 6-photon resonant to 7-photon non-resonant to 7-photon resonant ionisation. These experiments were performed at wavelengths between 310 and 330 nm and intensities between 8×10^{13} W/cm^2 and 5×10^{14} W/cm^2. Distinct differences in the angular distributions could be observed for the different ionisation channels studied. Channel switching from 8- to 9-photon resonant ionisation of xenon at 800 nm was observed by Hansch et al [69] in the range of intensities between 1×10^{13} W/cm^2 and 5×10^{13} W/cm^2. In the same way Schyja et al observed switching of ionisation channels in ATI of xenon [54] and argon [70] ionised by 800 nm laser light.

A careful quantitative comparison of experimental electron-momentum distributions with theoretical volume integrated spectra was carried out by Wiehle et al [71] for argon ionised at 800 nm, allowing the authors to identify such processes as channel switching, multi-photon resonant and non-resonant ionisation, and ac Stark splitting.

2.1.5. Wavelength-dependence of photoelectron spectra.

Measurement of photoelectron spectra at a number of laser intensities and at a fixed frequency (usually 800 nm) is the conventional method of ATI studies. As one can see this approach allowed describing many of the main phenomena in the physics of ATI, such as channel switching. However, the limited range of experimentally available intensities and the inability of having smooth intensity variations restrict the observed phenomena to a relatively narrow set of parameters.

An attempt to broaden the range of parameters was performed by Maharjan et al [72] by measuring 2D ATI photoelectron spectra of argon at a number of frequencies and intensities. Although being of significant interest, their results cannot be used to follow any trends in the physical processes, but rather should be considered as results of independent experiments, each performed at a given set of laser parameters.

The adequate measurements of wavelength-dependent ATI photoelectron spectra performed in a limited range of parameters proved to be useful for monitoring the invoked ionisation channels. Varying a laser wavelength between 592 and 616 nm and measuring photoelectron energy and angular distributions Rottke et al [73] observed channel switching from 6- to 7-photon resonant ionisation in Xenon.

Continuous variation of laser frequency in Xenon ATI photoelectron energy measurements was performed by Kaminski et al [74] in the range of wavelengths between 500 and 650 nm and intensities between 10^{12} and 10^{13} W/cm^2. Measuring photoelectron energy and angular distributions as a function of the ionising wavelength allowed the authors to observe the transition between resonant and non-resonant ionisation channels and to identify the excited states involved in the ionisation process.

In our experiments described in Chapter 3 we aimed to collect data that could provide continuous trends in photoelectron spectra measured over a wide range of laser wavelengths from 600 to 800 nm and from 1200 to 1600 nm, and both in argon and xenon. Choosing an adequate wavelength step we track the smooth evolution of the properties of the ATI photoelectron spectra as a function of the laser wavelength, which provides a deep insight into the nature of the underlying ionisation processes. We obtain excellent quantitative agreement between our experimental results and the results of TDSE calculations, integrated over the laser focus volume.

2.2. ATI in the tunnelling regime.

As mentioned above the majority of previous experimental work on ATI has been conducted in the multi-photon regime. However the present accessibility of high laser intensities encourages the exploration of ATI properties in the tunnelling regime, where the Keldysh parameter $\gamma<1$. In early experiments Mevel et al [75] presented an interesting demonstration of the qualitative evolution of ATI spectra at the transition from the multi-photon to the tunnelling regime by studying rare-gas atoms with increasing ionisation potential. They have observed the gradual disappearance of ATI structure from xenon to helium in accordance with the transition of Keldysh parameter through unity.

The disappearance of the ATI peak structure is related to the spatiotemporal intensity distribution in the laser focus. As pointed out in section 2.1.1 in the short-pulse regime the ATI photoelectron spectra are shifted to lower energies by the value of the ponderomotive potential U_p. At high laser intensities the value of U_p may significantly exceed the photon energy and thus the separation between the ATI peaks. For example, at 800 nm the photon energy $\hbar\omega=1.55$ eV and one obtains U_p = 6 eV at the peak laser intensity of 10^{14} W/cm^2. Correspondingly, low intensities present in the focal volume lead to smaller ponderomotive shifts. In spite of the generally high non-linearity of the ionisation process, the resulting photoelectron spectra contain significant contributions from both high and low intensities, since the high ionisation rate at the peak laser intensity is compensated by a larger presence of lower intensities in the focal volume. Therefore in the tunnelling regime, where the peak laser intensity is high, one can expect the ATI peak structure to be completely washed out due to the fact that all laser intensities below the peak laser intensity are present in the focal volume.

Note that in the few-cycle regime the disappearance of ATI peak structure can be due to a different reason. From the time-domain point of view ATI is a periodic process, and a typical ATI spectrum arises from the repetition of the process every laser cycle. As shown by Wickenhauser et al in their simulations the number of peaks in the ATI spectra increases with the number of laser cycles relevant for the ionisation process [76]. The loss of conventional ATI structure and the onset of an interference pattern resulting from different spectral components of a few-cycle laser pulse has been recently theoretically predicted by Martiny et al [77].

Thus, the loss of ATI structure is generally expected in the few-cycle limit and/or at the transition to the tunnelling regime. However, recent high-resolution experiments [78, 79] have demonstrated the persistence of the structures into the tunnelling regime. The structure observed by Alnaser et al [78] in ion momentum distributions measured along the polarisation direction as a function of intensity in neon and argon at 400 nm (multi-photon regime) and 800 nm (tunnelling regime) suggests the importance of a resonant ionisation mechanism in both cases. However, the authors could not assign the Rydberg states that could be responsible for the observed structure.

Rudenko et al [79] reported measurements of ion momentum distributions for helium, neon and argon at 800 nm and intensities 0.15-2.0×10^{15} W/cm^2, which spans a broad range of Keldysh parameter γ from 1.1 to 0.29. They observed a remarkably rich ATI-like structure in the low-energy region of the ion momentum spectra, which was preserved deep into the tunnelling regime, contrary to the expected featureless energy distribution (Figure 2-4). The independence of the position of the observed ATI-like peaks on the laser peak intensity and the disappearance of the peaks upon shortening the pulse from 25 to 6 fs allowed the authors to suggest that the observed structures originate from resonant ionisation which remains operational even in the tunnelling regime. This hypothesis was confirmed by their high-resolution measurements of electron momentum spectra for neon at 25 fs demonstrating an intensity independent fine structure within separate ATI orders.

Furthermore, two-dimensional photoelectron momentum spectra measured by Rudenko et al. in [79] in the tunnelling regime demonstrated unexpectedly complex structures within the first few ATI orders, characterised by highly oscillatory angular distributions. The features were significantly washed out when the laser pulse duration was reduced from 25 to 6-7 fs. Similar structures were observed by Maharjan et al [72] for argon in a wavelength range from 400 to 800 nm and peak intensities corresponding to $\gamma<1$. While some of the observed features could be identified as Freeman resonances, part of the structure remained of unclear origin.

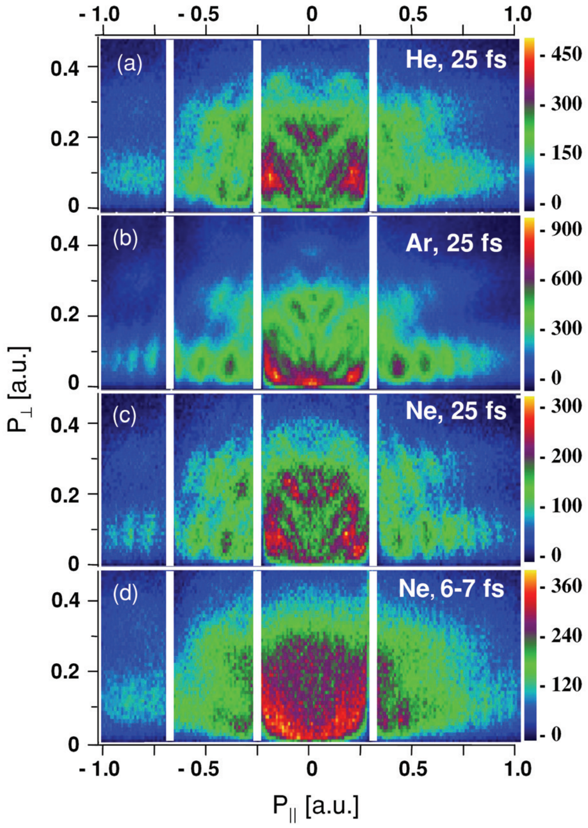

Figure 2-4. Electron momentum distribution parallel and perpendicular to the laser polarisation direction. (a) He, 25 fs, 0.6 PW cm^{-2}. (b) Ar, 25 fs, 0.5 PW cm^{-2}. (c)Ne, 25 fs, 0.6 PW cm^{-2}. (d) Ne, 6–7 fs, 0.5 PW cm^{-2}. Vertical cuts show regions where the spectrometer has no resolution in the transverse direction. The figure is taken from A Rudenko et al 2004 J. Phys. B **37** L407 [79].

A few theoretical attempts to explain the observed structures have been reported. TDSE calculations supported by classical-trajectory Monte-Carlo calculations with tunnelling (CTMC-T) performed by Arbo et al [80] for a hydrogen atom at ω=0.05 a.u. (λ=910 nm) for a number of intensities in the transition regime ($\gamma\sim1$) demonstrated a good qualitative agreement with the experimental results of

Rudenko [79] and suggested that the observed features could be attributed to the interference between different trajectories of the continuum electrons in the combined laser and Coulomb field of the parent ion. Such an interpretation is also consistent with the ability of the angular distribution to stay constant over a wide energy range as observed by Maharjan [72]. However, Arbo et al highlight the independence of the interference pattern of the ion core potential, since in this theoretical frame the continuum electron propagates at large distances from the ion upon tunnelling, where the core potential does not play any important role, while Rudenko [79] and Alnaser [78] argued for the atomic core dependency of the structures observed in their experiments.

Wickenhauser et al [81] presented simulations of electron–momentum distributions for argon ionised by a 10 fs (few-cycle) laser pulse at 400 and 800 nm for peak intensities in the range $1.7\text{-}3.9\times10^{14}$ W/cm^2, which corresponds to the transition regime from multi-photon to tunnelling ionisation with γ ranging from 1.75 to 0.85. Comparing electron–momentum spectra resulting from numerical solutions of TDSE and, from a model based on Strong Field Approximation (SFA), the authors observed qualitative agreement between the two approaches in the high-energy regions of the spectrum. However, the spectra exhibited considerable differences within the first ATI order. The radial fan-like structures obtained in TDSE calculations, which were observed in the experiments of Rudenko and Maharjan, become significantly distorted in SFA calculations.

These observations were further confirmed by Chen et al [82] who carried out calculations of ATI electron-momentum spectra for different atoms ionised by 10 fs laser pulses of various intensities at wavelengths ranging from 400 to 800 nm. By turning on and off the Coulomb potential tail in TDSE simulations as well as comparing to the results of SFA the authors concluded that in agreement with Arbo [80] and Wickenhauser [81] the radial fan-like structures in the electron momentum spectra within the first ATI order observed by Rudenko and Maharjan are due to the long range Coulomb potential. Chen et al [82] have derived an empirical rule to predict the dominant orbital angular momentum of the initial state responsible for these low-energy electron momentum distributions at a given laser peak intensity and associated this momentum with the minimum number of photons needed to ionise the atom. Morishita et al [83] developed a further comparison of TDSE calculations to the experiments of Maharjan and Rudenko. They performed laser focus volume integration in their simulations and showed that a quantitative comparison of theoretical calculations at a given peak laser intensity with experimental results of Rudenko and Maharjan was inadequate since at high laser peak intensities an atom can be completely singly ionised before the peak intensity is reached. Qualitatively the main spectral features of Rudenko and Maharjan have been reproduced with resonant-like structures being attributed to Freeman resonances and radial fan-like structures within the first ATI order characterized by a dominant angular momentum that only slowly varies with intensity and hence can survive volume integration and show up in the experiment. However no physical interpretation of the dominant angular momentum has been provided.

In spite of the variety of experimental observations and theoretical descriptions of the ATI electron momentum spectra, a consistent understanding of all the observed features is missing at the moment. In Chapter 3 we present the results of TDSE calculations over a wide range of parameters, which allow us to assert a comprehensive overview of the electron momentum spectra evolution with the laser wavelength and intensity both in the multi-photon and in the tunnelling regimes, in the infrared and in the visible wavelength ranges.

Chapter 3. Wavelength-dependent ATI in Xenon and Argon.

Chapter 3 presents the experimental results on ATI in Xenon and Argon carried out over a wide range of laser wavelengths from 600 to 800 nm and from 1200 to 1600 nm. Photoelectron momentum spectra recorded with an imaging spectrometer are carefully reproduced in TDSE calculations. Generally the electron momentum spectra contain a superposition of contributions with a different origin. Our goal is to disentangle the observed patterns into separate contributions and to link them to the various processes taking place in the ionisation of the atom.

Continuous variation of the laser wavelength allows measuring a smooth evolution of the properties of the ATI photoelectron spectra as a function of the laser wavelength, where a number of consecutive channel-switching effects can be identified. Inspection of the electron kinetic energy spectra and the angular distributions of the resonantly ionised electrons allow us to reliably assign the intermediate Rydberg states involved in the ionisation process.

Furthermore we identify and describe two characteristic patterns contributing to the photoelectron momentum spectra: a radial pattern appearing in the momentum maps within the first ATI ring (further referred to as the low-energy region) and an off-axis pattern observed within the whole detectable energy range above the first ATI order (further referred to as the high-energy region). Preliminary analysis of these patterns has been carried out and general trends on their evolution with the laser wavelength and laser intensity observed in our experimental data as well as in the TDSE calculations over a broad range of parameters are investigated and described in detail.

The chapter is organised as follows. Sections 3.1 and 3.2 describe the methods and approaches used in the experiment and in the TDSE calculations. Experimental results for Xenon and Argon obtained between 600 and 800 nm and the analysis of resonant ionisation, dominating the spectra in the visible wavelength range, are presented in sections 3.3 and 3.5, respectively. Sections 3.4 and 3.6 present experimental results in Xenon and Argon in the infrared wavelength range between 1200 and 1600 nm. The final sections 3.7 and 3.8 are devoted to the discussion of the radial pattern in the low-energy region and the off-axis pattern observed in the high-energy region of the momentum spectra. The chapter is summarised in section 3.9.

3.1. Experimental methods.

We use a commercial laser system consisting of an optical parametric amplifier (OPA, *Coherent Opera*) pumped by 1 mJ of a *Coherent* kilohertz Ti:Sapphire amplifier system (800 nm, 50 fs). The signal output wavelength of the OPA system varies between 1200 and 1600 nm with a FWHM of 10-15 nm. The central wavelength is determined with a monochromator with an accuracy of 2 nm. For the experiments in the visible wavelength range, where the wavelength varies from 600 to 800 nm, the OPA output passes through a BBO doubling crystal. A schematic of the experimental setup is shown in Figure 3-1.

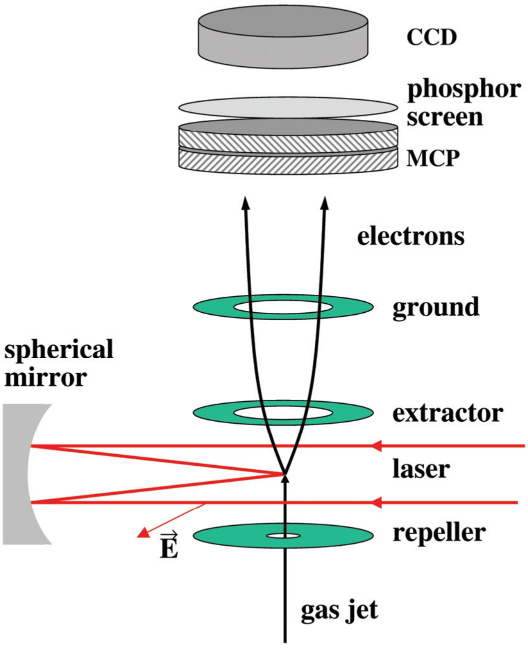

Figure 3-1. Schematic of the experimental setup. The laser beam is focused with a spherical mirror onto a jet of Argon or Xenon. The laser polarisation is perpendicular to the detection axis of the velocity map imaging electron spectrometer. Electrons created in the interaction region are extracted with a dc electric field and are accelerated towards a 2D position sensitive detector, consisting of a dual MCP and a phosphor screen. The impact of the electrons causes fluorescence of the phosphor screen, which is recorded with a computer controlled CCD camera.

The linearly polarised laser beam propagates into the vacuum chamber and is focused onto a gas jet pulsed at 25 Hz and synchronised with the laser using a spherical normal-incidence silver mirror (f=75 mm). The synchronisation of the pulsed gas input with the laser allows having a sufficiently high number of ionisation events per laser shot while keeping a relatively low pressure in the interaction vacuum chamber. Typically the pressure in the interaction chamber is kept around 10^{-7} - 10^{-6} mbar during experiments. Without the gas jet, the background pressure is approximately 10^{-8} mbar. The backing gas pressure was kept sufficiently low to avoid clustering. Space charge effects are avoided by adjustment of the gas concentration in the interaction region, which in turn can be influenced by the delay of the gas input with respect to the laser. The ejected electrons propagate in the Velocity Map Imaging (VMI) spectrometer towards a 2D position sensitive detector, consisting of a dual MCP and a phosphor screen. The impact of the electrons causes fluorescence of the phosphor screen, which is recorded with a computer controlled CCD camera. The experimental images presented in this chapter contain electron signals accumulated during one to five minutes of acquisition time. The polarisation of the laser beam is parallel to the MCP detector and perpendicular to the static electric field. Using the VMI spectrometer in the ion time of flight mode we determined the maximum laser pulse energy at every wavelength that provided a constant ratio between singly and doubly charged ions. In the imaging wavelength scans the laser intensity was reduced where necessary so that the contribution from the doubly charged ions did not exceed 2% of the singly charged ion signal.

Images recorded in the experiment represent 2D projections of the original 3D distribution of the photoelectron velocity vectors. Applying an iterative Abel inversion procedure [84] to the recorded 2D projections one can reconstruct the 3D velocity and angular distribution $P(v,\theta)$ of the photoelectrons and therefore obtain photoelectron momentum maps.

In order to obtain photoelectron kinetic energy distributions from the 3D velocity and angular distribution an integration over the polar angle θ has to be carried out:

$$P(v)=2\pi\int P(v,\theta)v^2\sin\theta d\theta \qquad (5)$$

and a conversion from the velocity to the energy distribution performed

$$P(E) = P(v)/mv \qquad (6)$$

The angular distributions can be acquired by integration of the 3D velocity and angular distribution, obtained from the inversion of the experimental images, over a certain velocity range around the position of a particular feature in the photoelectron spectrum.

3.2. Theoretical treatment.

The experimental results presented in this chapter are directly compared to the results obtained from the numerical solutions of a 3D TDSE within the SAE approximation [33]. This approximation considers only the response of the outermost valence electron to the laser field.

In order to solve the TDSE for Xenon we use the code based on the method outlined in ref [85] with a pseudo-potential described in ref [86]. Solution of TDSE for Argon relies on the original numerical algorithm [87], which allows to significantly reduce calculation time. Application of this algorithm for calculations of ATI electron spectra in a model Argon atom was demonstrated in [61]. Both codes provide the energy-resolved electron angular distributions (in the form of an expansion over a series of Legendre polynomials in the case of Xenon), which can be subsequently converted into a 2D momemtum map for comparison to the experimentally recorded images. We note that due to the SAE approximation and due to the nonrelativistic approximation the models used in the numerical simulations do not take into account angular coupling with the ionic core as well as spin-orbit splitting. For this reason all levels belonging to the same configuration degenerate (i.e. there exists a single energy level for a given set of quantum numbers n, l and m), which has to be taken into account when comparing to the experimental level energies provided in the NIST atomic database (http://physics.nist.gov/cgi-bin/ASD).

For an adequate comparison to the experiment the results of the TDSE calculations must be integrated over the laser focal volume. The necessity of this procedure was previously highlighted in [71] and [83]. In the calcualtions presented in this chapter the volume integration was performed using the prescription described in [88] and assumes a Gaussian focus in an infinitely extended medium. The temporal profile of the laser pulse is modelled with a sine-squared envelope typically containing 60 optical cycles. The laser polarisation is linear.

3.3. Xenon in the visible frequency range.

The experimental images presented in this section were obtained by summing the electron yield during one minute of acquisition time. The left panel in Figure 3-2 shows an example of a raw experimental image obtained for ionisation of Xenon with 700 nm laser light. The right panel in Figure 3-2 shows a 2D slice through the 3D velocity and angular distribution reconstructed from the experimental image in the left panel. The laser polarisation is vertical in all the figures in this chapter.

Several contributions can be distinguished in the 2D photoelectron momentum spectrum. The most prominent one peaks along the laser polarisation axis and consists of a series of relatively broad features. When the 2D momentum distributions are converted to energy distributions, these features are spaced by the energy of one photon. In the 2D momentum maps this translates into a series of concentric rings spaced with radii that increase with the square root of the photoelectron kinetic energy. We use these spectral structures for the electron energy calibration of the experimental images. Within the broad ATI features narrow sub-structures can be observed, which continue into the area away from the polarisation axis and form the second major contribution to the photoelectron momentum spectrum. Highly oscillatory angular distributions are characteristic for these narrow features. In the low-energy region the spectrum contains cross-like structures fanning out from the centre of the image, which were observed in earlier experimental and theoretical studies of ATI [66, 54, 72, 79-83]. Furthermore, an additional weak off-axis pattern can be observed in the high-energy region.

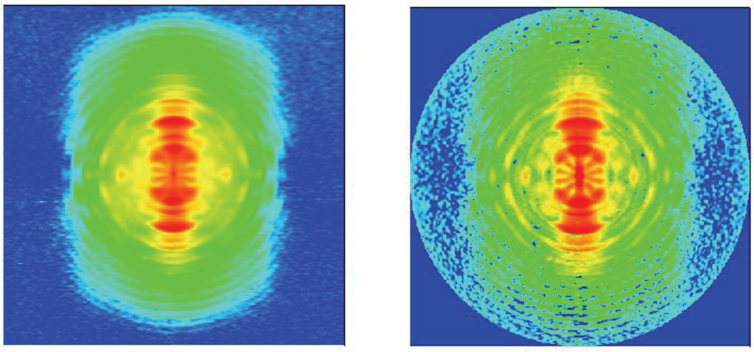

Figure 3-2. Left: raw experimental image resulting from ATI of Xenon atom at 700 nm. Right: 2D slice through the 3D velocity and angular distribution obtained from the raw image by applying an iterative Abel inversion procedure.

The superposition of many patterns on a single momentum map corresponds to the photoelectrons involved in different ionisation mechanisms. In this experiment we aim to explore how the momentum spectra evolve as a function of the laser intensity and the laser wavelength[1] and try to identify the processes responsible for the creation of the observed patterns.

3.3.1. Intensity dependence of the electron momentum spectra.

---

[1] In the following sections of this chapter only the wavelength dependence of the experimental photoelectron spectra will be discussed, since the relatively low ionisation rate in Argon and in Xenon in the infrared frequency range did not allow us to study the intensity dependence of the momentum spectra.

In order to explore the evolution of the momentum spectra with the laser intensity photoelectron momentum maps were recorded at 700 nm for various intensities. The laser pulse energy measured in the experiment was varied from 25 to 60 μJ by inserting a neutral density filter in the path of the laser beam. Calibration of the intensity in the experiment was performed in two ways: by a direct comparison of the recorded momentum maps to the results of the TDSE calculations and by monitoring the emergence of the classical cut-off in the angle-integrated spectra.

Figure 3-3 shows a series of photoelectron momentum maps acquired at 700 nm at various laser intensities, where the experimental images presented in the left column are compared to the results of calculations in the right column. The vertical and horizontal axes in Figure 3-3 show the electron momenta in the range between –1 and 1 a.u. parallel and perpendicular to the laser polarisation, respectively. This momentum scale corresponds to the electron kinetic energies up to 13.6 eV. The low-energy part of the momentum spectra is presented in Figure 3-4, where the electron momenta up to 0.4 a.u are shown, corresponding to the kinetic energy up to around 2.2 eV. The colour scale Figure 3-4 is adapted to emphasize the off-axis structures of the momentum spectrum. The calculations are simulations of the experiment including full 3D volume averaging, assuming a laser focus up to an intensity specified by a value of the vector potential $A_{max} = (I_{laser}/\omega^2)^{1/2} = F_{laser}/\omega$, where F_{laser} is the amplitude of the laser field. The peak laser intensity used in the calculations was chosen to provide the best fit to the experimental data. Careful comparison of the experimental and calculated momentum maps provides a very accurate way to determine the laser intensity, since the rich intensity-dependent structure observed in the experimental momentum maps allows to fine-tune the value of the vector potential in the calculations in order to find the best match. Assignment of the matching pairs shows that the experiment covers the range of intensities from 3.4×10^{13} W/cm^2 to 9.5×10^{13} W/cm^2 with an estimated error of less than 5%. In the analysis of the following results we will use the intensity calibration derived from the comparison of the experimental and theoretical momentum maps.

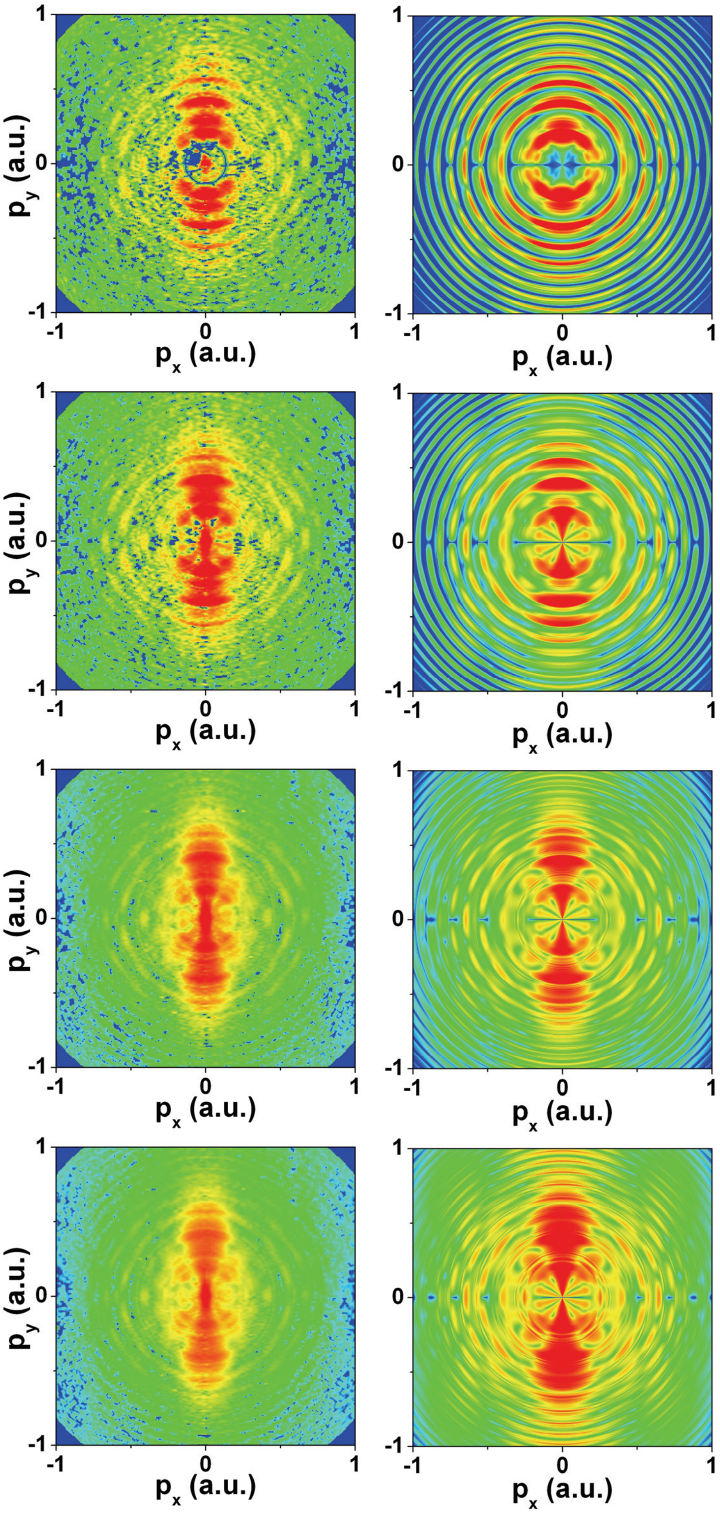
1
0
-1
p_y (a.u.)
-1
0
1
p_x (a.u.)

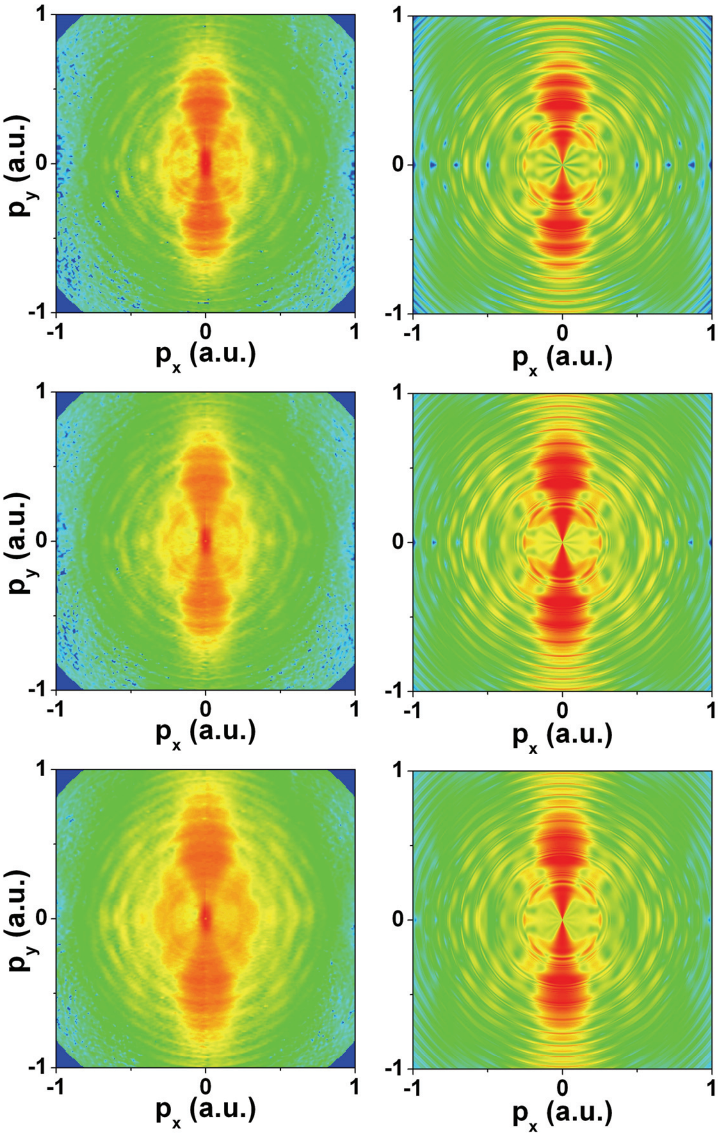

Figure 3-3. Experimental (left column) and calculated (right column) momentum maps of photoelectrons ionised from xenon at 700 nm and at various intensities increasing from top to bottom: 25 µJ, A_{max}=0.48 a.u. (3.4×10^{13} W/cm^2); 30 µJ, A_{max}=0.55 a.u. (4.5×10^{13} W/cm^2); 35 µJ, A_{max}=0.63 a.u. (5.9×10^{13} W/cm^2); 40 µJ, A_{max}=0.66 a.u. (6.4×10^{13} W/cm^2); 45 µJ, A_{max}=0.71 a.u. (7.5×10^{13} W/cm^2); 50 µJ, A_{max}=0.75 a.u. (8.3×10^{13} W/cm^2); 60 µJ, A_{max}=0.8 a.u. (9.5×10^{13} W/cm^2). The logarithmic false-colour scale covers 5 orders of magnitude.

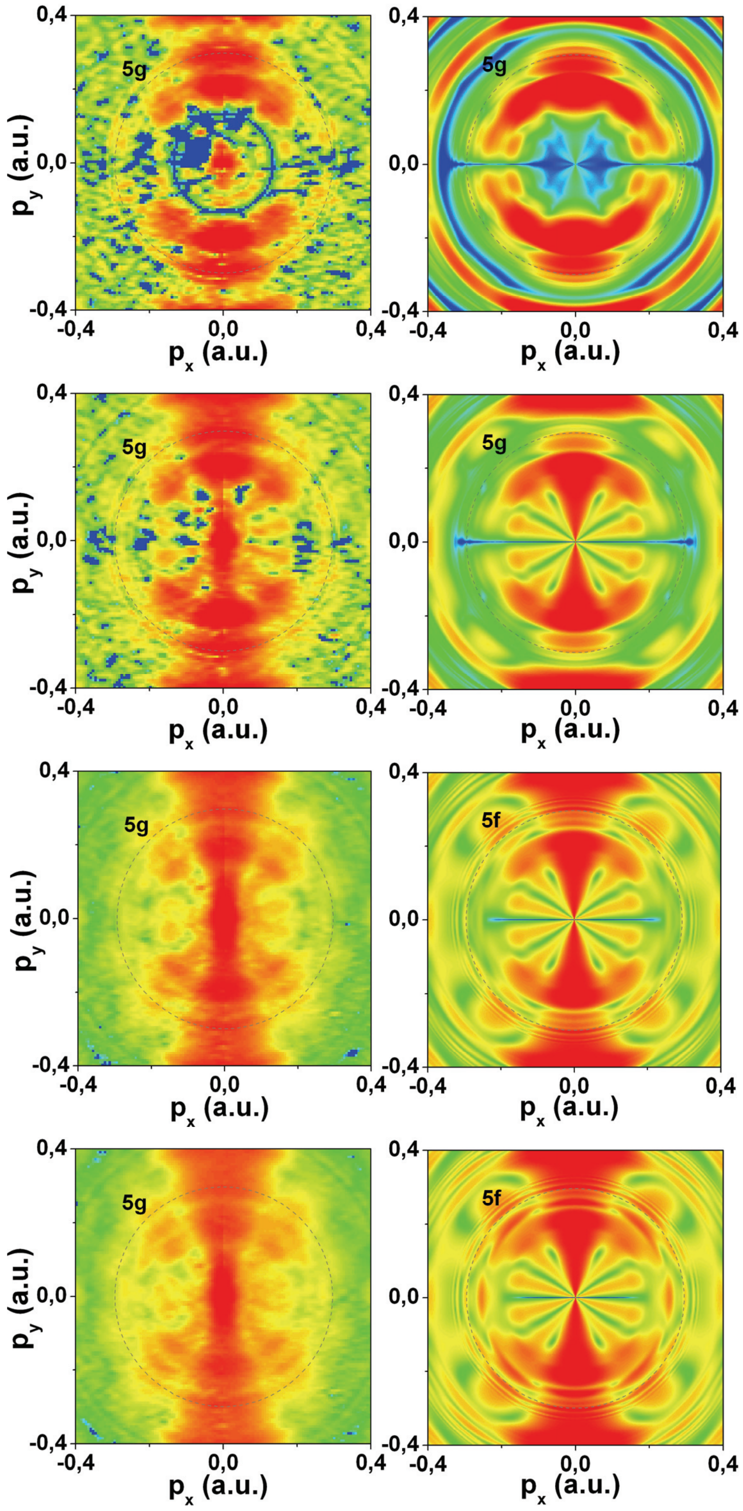
0,4
0,0
-0,4
p_y (a.u.)
-0,4
0,0
0,4
p_x (a.u.)
5g
5g
5g
5g
5g
5g
5f
5g
5f

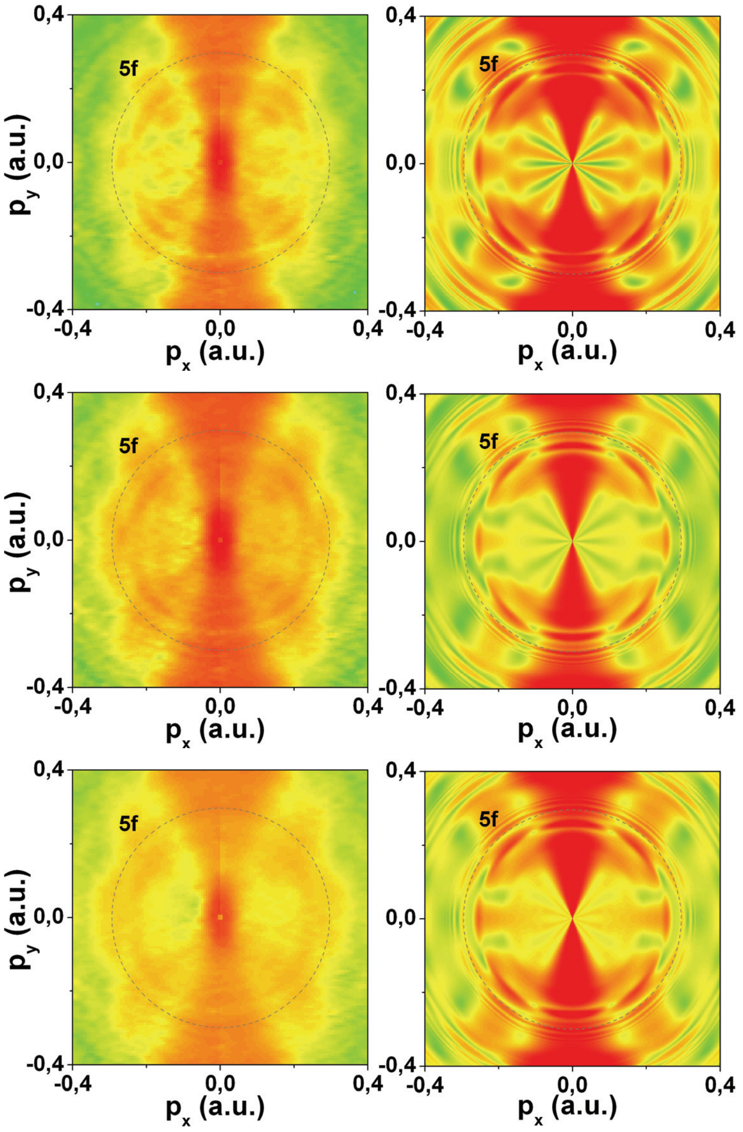

Figure 3-4. The same as in the previous figure zoomed in on the low-energy part. The logarithmic false-colour scale covers 5 orders of magnitude. The black circles show the contribution from electrons, corresponding to one-photon ionisation via 5g/5f Rydberg state.

Figure 3-5 shows experimental photoelectron kinetic energy spectra corresponding to the data shown in the previous two figures. The photoelectron spectra were integrated within ±10 degrees with respect to the polarisation axis and normalised to the integral over the total energy range. The arrows indicate the predicted positions of the classical 2U_p cut-offs, where U_p is the ponderomotive energy related to the laser frequency ω and intensity I_{laser} as in Eqn. (1). The curves are plotted with an arbitrary vertical offset for convenience of presentation.

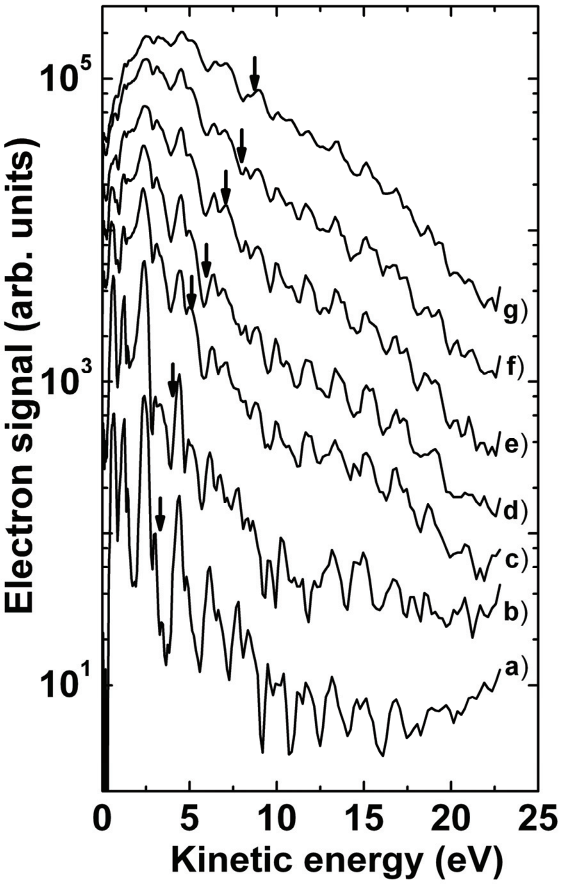

Figure 3-5. Normalised photoelectron spectra integrated within ±10 degrees along the polarisation axis at 700 nm and at various intensities. The 2U_p cut-offs predicted on the basis of the comparison of the momentum maps are indicated with arrows. (a) 2U_p=3 eV (3.4×10^{13} W/cm^2); (b) 2U_p=4 eV (4.5×10^{13} W/cm^2); (c) 2U_p=5.5 eV (5.9×10^{13} W/cm^2); (d) 2U_p=6 eV (6.4×10^{13} W/cm^2); (e) 2U_p=7 eV (7.5×10^{13} W/cm^2); (f) 2U_p=8 eV (8.3×10^{13} W/cm^2); (g) 2U_p=8.7 eV (9.5×10^{13} W/cm^2). The curves are plotted with an arbitrary vertical offset for convenience of presentation.

In the evolution of the momentum maps with intensity in Figure 3-4 we can distinguish the development of two qualitatively different contributions. One contribution corresponds to electrons with an absolute value of the momentum below 0.2 a. u., i.e. a kinetic energy below 0.5 eV. Highly oscillatory angular distributions and a continuous energy distribution extending down to zero characterise this low-energy part of the photoelectron spectrum. The features observed in the low-energy region will be discussed in section 3.7. At values of the electron momentum higher than 0.2 a. u. the momentum maps are dominated by sharp oscillatory features, which can be attributed to one-photon resonantly enhanced ionisation, as we will show below.

Assuming a ponderomotive Stark shift of high-lying Rydberg levels we expect that ionisation via a selected resonant state will always result in a photoelectron with the same kinetic energy independent of the laser intensity. The energy level of a Rydberg state experiences the same shift as the ionisation threshold, and therefore, as given by Eqn. (4), the final kinetic energy of a photoelectron depends only on the energy of the photon involved in the ionisation and not on the laser intensity. The influence of the rising intensity will mainly be reflected in the increasing ponderomotive energy (being a measure of the Stark shift effect) and hence in the number of photons necessary in order to couple resonantly to a given Stark-shifted Rydberg state. A change in the number of photons required for resonant population of a Rydberg series is known as channel switching. We note that variation of the laser intensity at a constant laser frequency is the conventional but not the only way to observe the phenomenon of channel switching, since variation of the laser frequency leads to the equivalent effect, as we will demonstrate below. Due to parity-selection rules (in the dipole approximation) channel switching is accompanied by alternation between odd- and even-parity Rydberg states involved in the ionisation. Namely, since the ground state of the Xenon atom (5p) has odd parity (l=1), population of Rydberg states with odd-l is only allowed with an even number of photons, whereas population of even-l resonant states requires an odd number of photons.

Figure 3-6 shows the experimental and the corresponding theoretical full-angle integrated photoelectron spectra at various intensities. Taking into account the above-mentioned considerations we choose to monitor the development of the resonant feature at the kinetic energy 1.2 eV (selected with a circle in Figure 3-4) as a function of intensity.

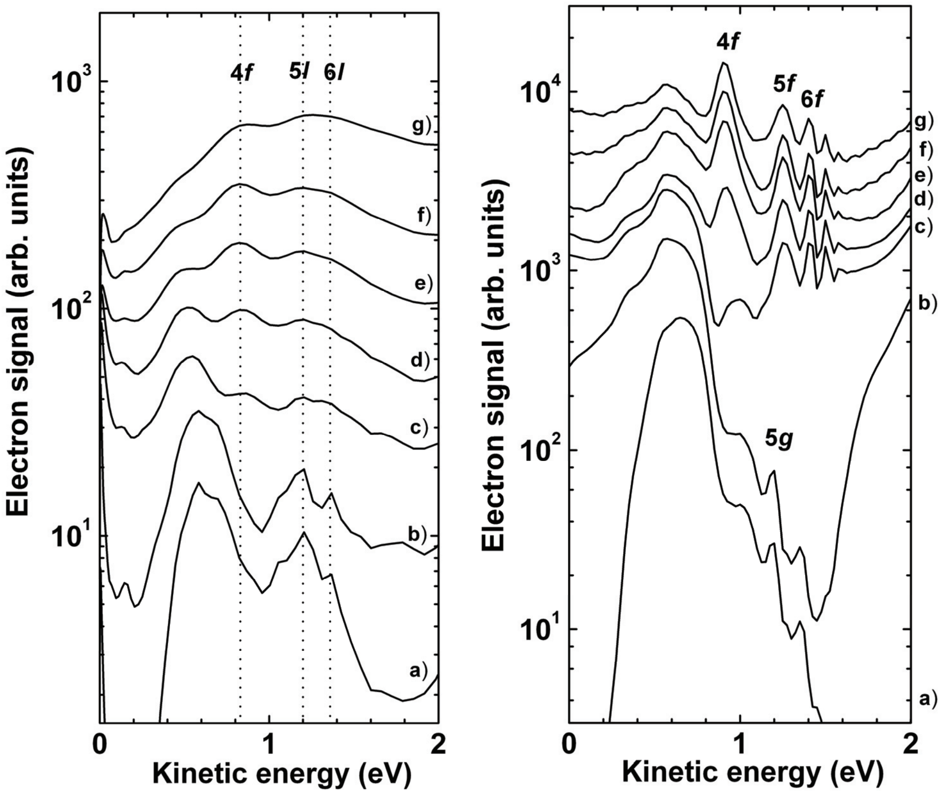

Figure 3-6. Angle-integrated and normalised experimental photoelectron spectra at a central wavelength of 700 nm (left) and angle-integrated theoretical spectra (right) at the intensities given in Figure 3-5: (a) 3.4×10^{13} W/cm^2; (b) 4.5×10^{13} W/cm^2; (c) 5.9×10^{13} W/cm^2; (d) 6.4×10^{13} W/cm^2; (e) 7.5×10^{13} W/cm^2; (f) 8.3×10^{13} W/cm^2; (g) 9.5×10^{13} W/cm^2.

The evolution of its angular distribution is expected to follow a switching of the ionisation channel as the intensity rises. Figure 3-7 shows angular distributions acquired by integration of the 3D velocity and angular distribution, obtained from the inversion of the experimental images, over a small velocity range corresponding to the energy range of 0.1 eV around the position of the resonant peak centred at 1.2 eV in the photoelectron spectra. At the lowest intensity in our experiment, 3.4×10^{13} W/cm^2, the angular distribution of the resonant feature at 1.2 eV contains five minima between 0 and 180 degrees, demonstrating that l=5 is the dominant angular momentum of the photoelectrons. According to the selection rule for the orbital quantum number absorption of one photon changes the orbital angular momentum by one. Since we consider one-photon ionisation from an intermediate Rydberg state, the orbital angular momentum of this state is l=4 or l=6. Subtracting the energy of one photon (1.77 eV at 700 nm) from the photoelectron kinetic energy we obtain the negative of the binding energy for the corresponding intermediate state E_b=0.57 eV. This allows identifying the resonant state involved in the ionisation as 5g, which shifts into resonance with seven photons at an intensity of 1.8×10^{13} W/cm^2, which is available in the laser focus volume. We note that excitation of the 5g state (having even parity (l=4)) by means of a 7-photon transition is consistent with the parity selection rule. We note that one-photon ionisation has a propensity to, but does not always lead to the change of the orbital angular momentum by one. Since the ionisation process may involve the absorption of two and emission of one photon, the orbital angular momentum may change by three. An example of a photoelectron spectrum suggesting the involvement of such an ionisation scheme will be shown below.

At 4.5×10^{13} W/cm^2 the ionisation still proceeds via the 5g state leading to 5 minima in the photoelectron angular distribution, as shown in Figure 3-7. However, a qualitative change can be observed in the momentum maps as the intensity reaches 5.9×10^{13} W/cm^2, when the Stark shift at the peak intensity of the laser is such that resonant population of the Rydberg states cannot be obtained with 7 photons anymore. A switch to the (8+1)-photon channel then occurs. This channel switching allows ionisation via Rydberg states with odd parity. Indeed, the angular distribution of the selected resonant feature shows the appearance of a maximum at 90 degrees in the calculations at 5.9×10^{13} W/cm^2, which confirms that the main ionisation contribution comes from the 5f state.

With the onset of the f-series a new peak at a lower kinetic energy (0.85 eV) appears in the experimental and theoretical photoelectron spectra (see Figure 3-6). The binding energy (around 0.9 eV) and the angular distribution, with 4 minima between 0 and 180 degrees identify this contribution as one-photon ionisation via the 4f state. The appearance of the 4f resonance in the photoelectron spectrum occurs at 6.4×10^{13} W/cm^{2}, when the laser peak intensity exceeds the appearance threshold for the 4f resonance via 8-photon resonant excitation (6.15×10^{13} W/cm^{2}). A further increase in the intensity leads to the dominance of the 4f resonance in the photoelectron spectra as can be seen from Figure 3-4 and Figure 3-6.

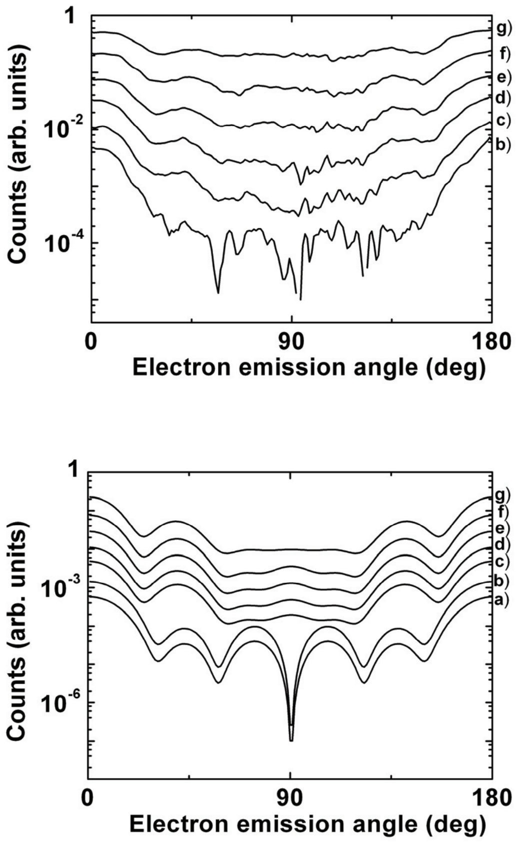

Figure 3-7. Experimental (left) and theoretical (right) angular distributions calculated for ionisation at a central wavelength of 700 nm and at photoelectron kinetic energies corresponding to one-photon ionisation via 5g/5f (E=1.2 eV) Rydberg states at the same intensities as given in Figure 3-5: (a) 3.4×10^{13} W/cm^{2}; (b) 4.5×10^{13} W/cm^{2}; (c) 5.9×10^{13} W/cm^{2}; (d) 6.4×10^{13} W/cm^{2}; (e) 7.5×10^{13} W/cm^{2}; (f) 8.3×10^{13} W/cm^{2}; (g) 9.5×10^{13} W/cm^{2}.

To summarise, monitoring the evolution of the ionisation via intermediate Rydberg states as a function of the intensity at 700 nm we have observed channel switching from (7+1)-photon ionisation via the g-series to (8+1)-photon ionisation via the f-series at an intensity around 6×10^{13} W/cm^2. A similar switching from (8+1)-photon ionisation via the f-series to (9+1)-photon ionisation via the g-series was observed in xenon at 800 nm in [66,54]. In our experiment the 800 nm wavelength was on the edge of the efficiency curve of the OPA system, therefore we chose to study the intensity dependence of the photoelectron momentum spectrum at 700 nm, close to the maximum of the efficiency curve, which provides a larger range of available intensities.

3.3.2. Wavelength dependence of the electron momentum spectra.

In this section we aim to explore the evolution of the main properties of the energy- and angular-resolved photoelectron spectra as a function of the laser wavelength. Electron spectra were measured at 21 wavelengths in the range from 600 to 800 nm with a step of 10 nm. In Figure 3-8 experimental momentum maps at several wavelengths are compared to the results of the corresponding volume-integrated TDSE calculations. The values of the maximum vector potential in the calculations are chosen for the best matching to the experimental results. The data of Figure 3-8 zoomed in on the low-energy part (electron kinetic energies up to around 2 eV) is shown in Figure 3-9, where the colour scale is adapted to emphasize the off-axis structures of the momentum spectrum. The comparison shows a good agreement between the experimental and theoretical results.

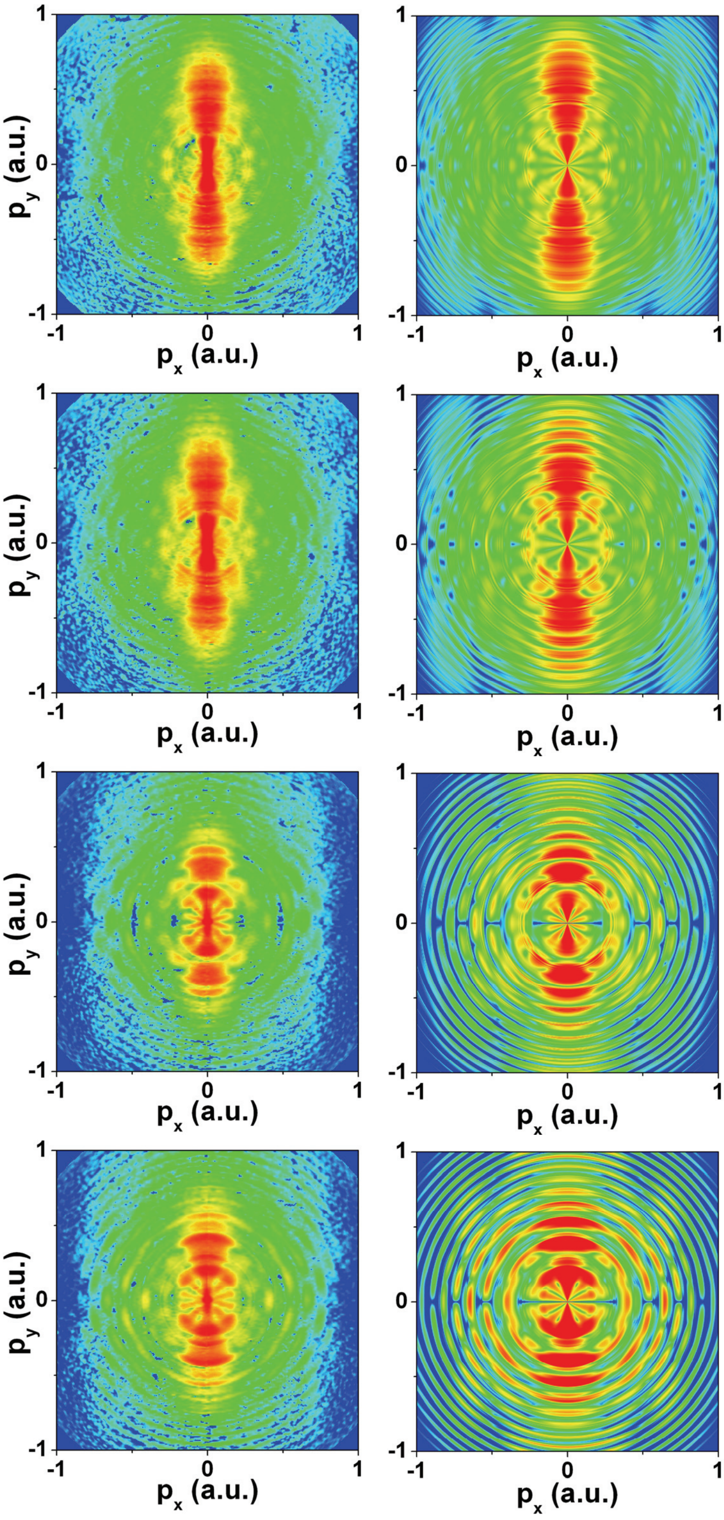
1
0
-1
p_y (a.u.)
-1
0
1
p_x (a.u.)

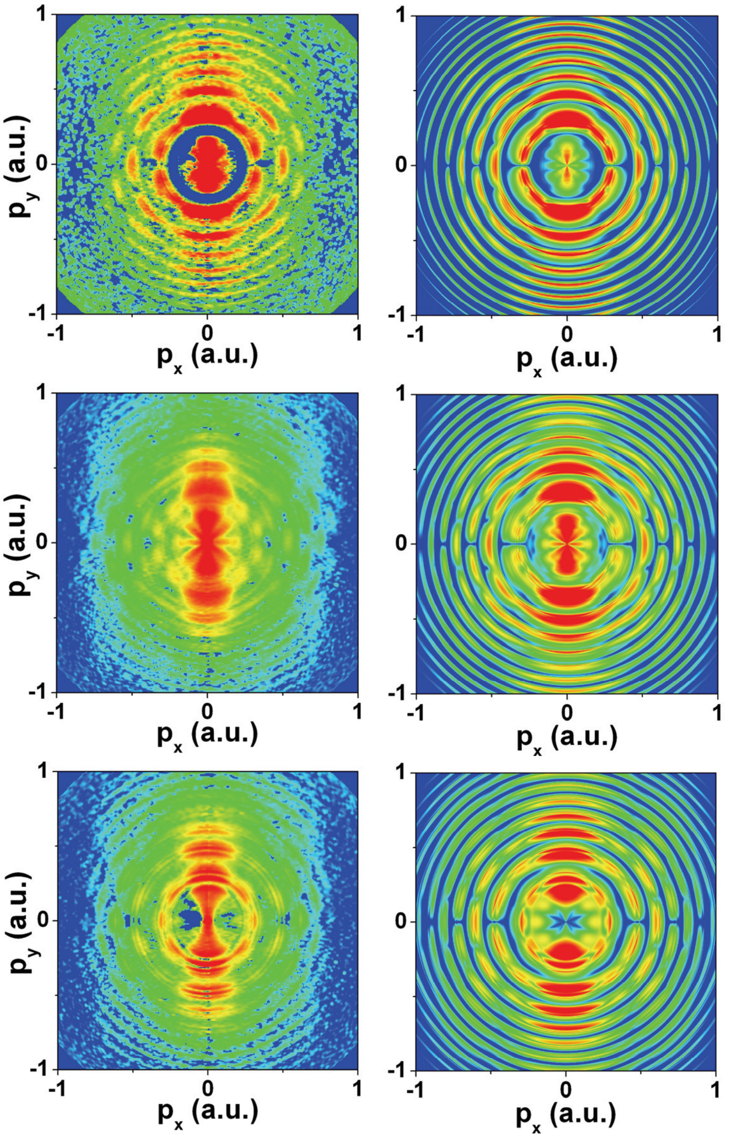

Figure 3-8. Comparison of the experimental (left column) and the calculated (right column) momentum maps of photoelectrons ionised from xenon at (from top to bottom) 800 nm, A_{max}=0.77 a. u., 6.7×10^{13} W/cm^2; 770 nm, A_{max}=0.7 a. u., 6×10^{13} W/cm^2; 730 nm, A_{max}=0.54 a. u., 3.9×10^{13} W/cm^2, 700 nm, A_{max}=0.55 a. u., 4.5×10^{13} W/cm^2; 680 nm, A_{max}=0.45 a. u., 3.2×10^{13} W/cm^2; 650 nm, A_{max}=0.52 a. u., 4.6×10^{13} W/cm^2; 600 nm, A_{max}=0.53 a. u. , 5.7×10^{13} W/cm^2. The logarithmic false-colour scale covers 4 orders of magnitude.

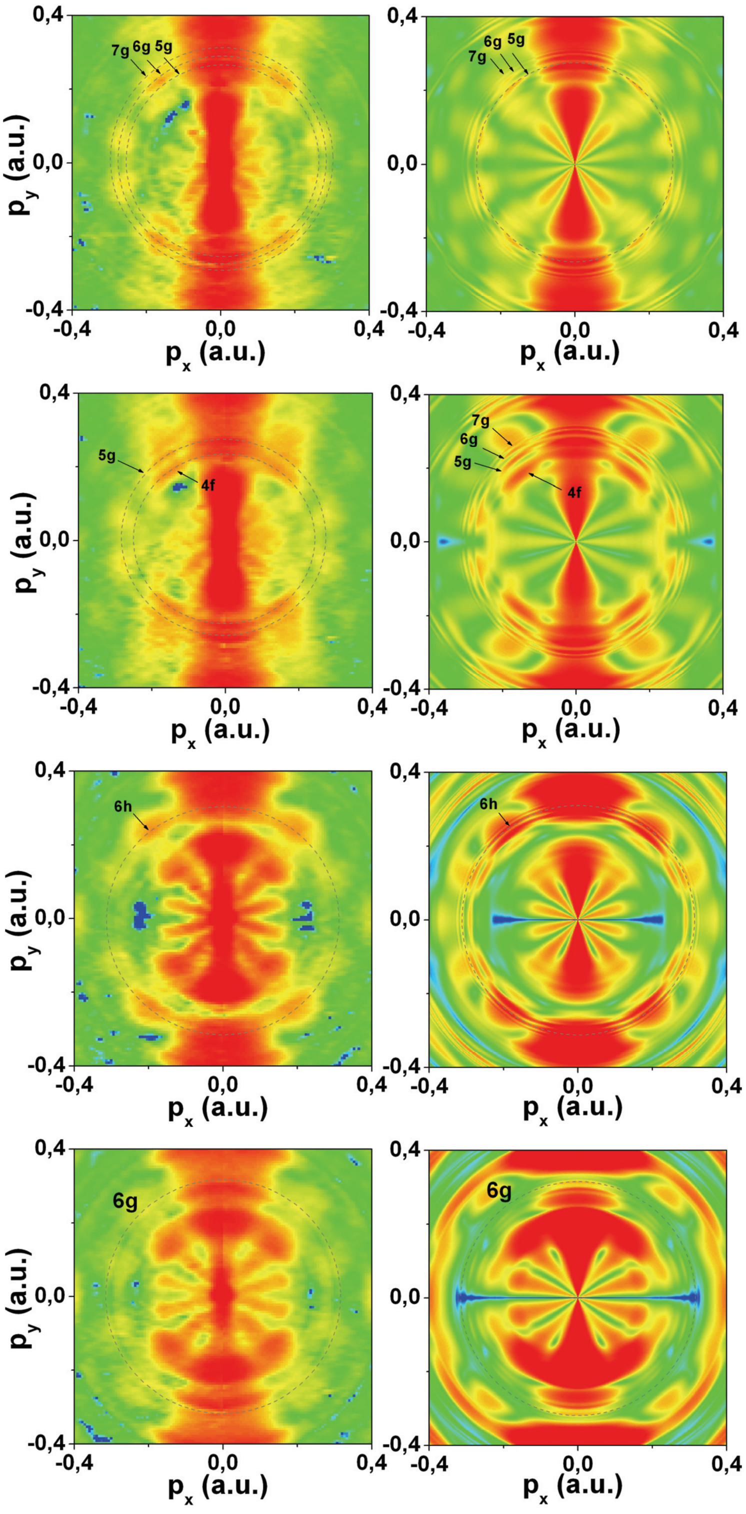
0,4
0,0
-0,4
-0,4
0,0
0,4
p_y (a.u.)
p_x (a.u.)
7g
6g
5g
7g
6g
5g
5g
4f
7g
6g
5g
4f
6h
6h
6g
6g

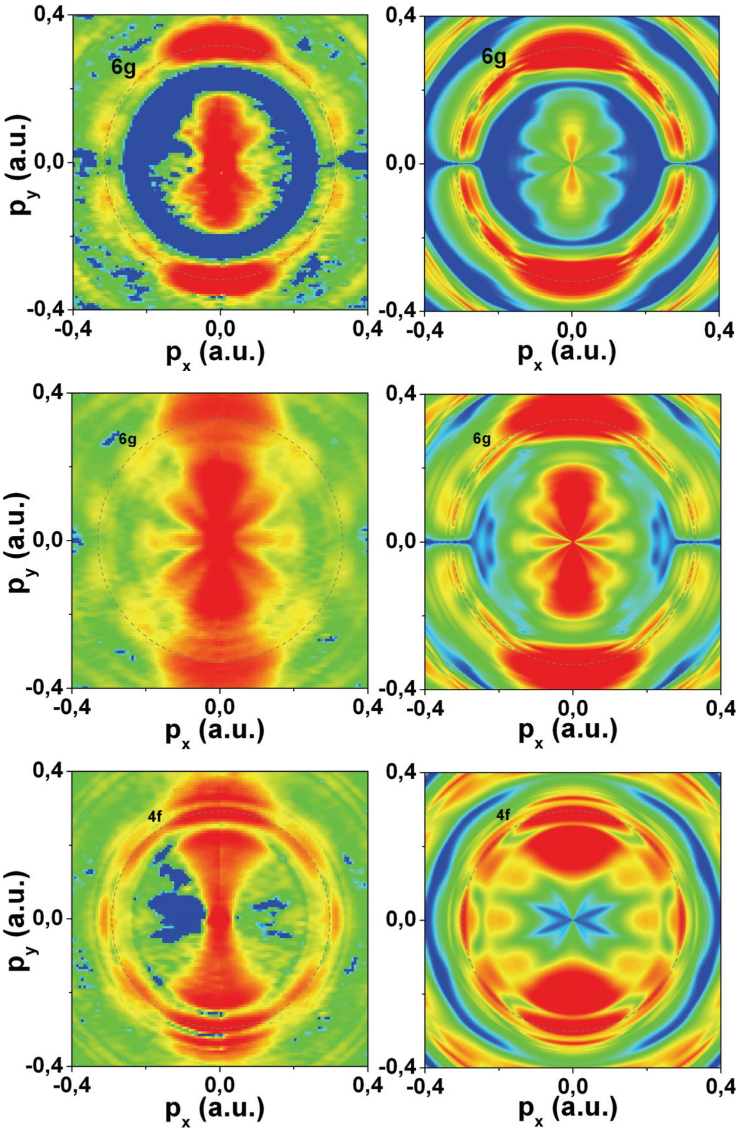

Figure 3-9. The same as in Figure 3-8 zoomed in on the low-energy part (from top to bottom): 800 nm, A_{max}=0.77 a. u., 6.7×10^{13} W/cm^2; 770 nm, A_{max}=0.7 a. u., 6×10^{13} W/cm^2; 730 nm, A_{max}=0.54 a. u., 3.9×10^{13} W/cm^2, 700 nm, A_{max}=0.55 a. u., 4.5×10^{13} W/cm^2; 680 nm, A_{max}=0.45 a. u., 3.2×10^{13} W/cm^2; 650 nm, A_{max}=0.52 a. u., 4.6×10^{13} W/cm^2; 600 nm, A_{max}=0.53 a. u. , 5.7×10^{13} W/cm^2. The logarithmic false-colour scale covers 4 orders of magnitude. The black circles show the contribution from electrons, corresponding to one-photon ionisation via intermediate Rydberg states.

Resonant ionisation. Interpretation of the experimental results.

An example of an experimental photoelectron kinetic energy spectrum recorded at 700 nm is shown in Figure 3-10. The conversion procedure from the 3D velocity and angular distribution, obtained in the experiment, to the electron kinetic energy distribution is described in section 3.1. Choosing an appropriate angular integration range we can make the distinction between the on- and off-axis contributions to the photoelectron spectra. By doing so we hope to distinguish between resonant and non-resonant ionisation contributions, which have qualitatively different angular distributions reflecting the nature of the ionisation process.

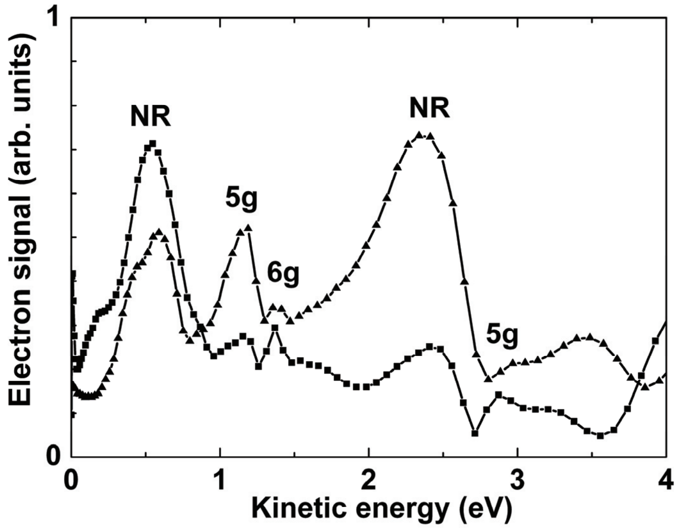

Figure 3-10. Experimental PES integrated beyond ±30 degrees from the polarisation axis (squares) and within ±10 degrees along the polarisation axis (triangles) at the laser wavelength 700 nm (frequency 0.065 a.u.).

In the case of non-resonant ionisation, the electron is ionised from the ground state of the atom by the absorption of many laser photons. Therefore the angular distribution of the photoionised electron is strongly aligned along the polarisation axis. On the other hand, electrons that are first excited to an intermediate Rydberg level and that are subsequently ionised in a low-order process, are expected to have an angular distribution that reflects the orbital angular momentum of the Rydberg state, generally implying a significant off-axis component.

The two curves shown in Figure 3-10 correspond to the angular integration range within ±10 degrees along the polarisation axis and beyond ±30 degrees from the polarisation axis, respectively. The curves are plotted with an arbitrary vertical offset and are shown only for the first two ATI orders for clarity. One can observe a significant difference between the spectra: the PES integrated away from the laser polarisation axis contains narrow sub-structures recurring every ATI order (labelled as 5g and 6g), whereas in the PES integrated along the polarisation axis the spectrum is dominated by broad features (labelled as NR), separated by the energy of one photon. This is in line with our expectations: broad non-resonant features are characterised by narrow angular distributions and hence are mostly observable along the polarisation axis. In contrast, narrow resonant features are characterised by broad angular distributions and dominate the PES away from the polarisation axis.

Monitoring the kinetic energy of a particular resonant or non-resonant feature in the photoelectron spectra as a function of the laser frequency one can obtain a linear dependence according to Eqns. (3) and (4), respectively, with a slope corresponding to the number of photons involved in the ionisation process. In the case of non-resonant ionisation the linear frequency dependence is only possible under the condition of constant value of the ponderomotive energy (Eqn. (3)). However, in the present experimental dataset the laser intensity could not be strictly controlled throughout the wavelength scan. As mentioned above the laser intensity was adapted in order to assure the dominance of the singly charged ion contribution in the photoelectron spectra. Moreover we have observed sensitivity of the appearance of the resonant features to variations of the ponderomotive energy, which points towards a simultaneous action of resonant and non-resonant ionisation. As we show below an overlap of both contributions in a photoelectron energy spectrum may lead to their constructive interference and modulate the relative amplitude of the resonant sub-structure. An example of a continuous linear frequency dependence of the resonant features in the experimental photoelectron kinetic energy spectra will be shown below in section 3.5.

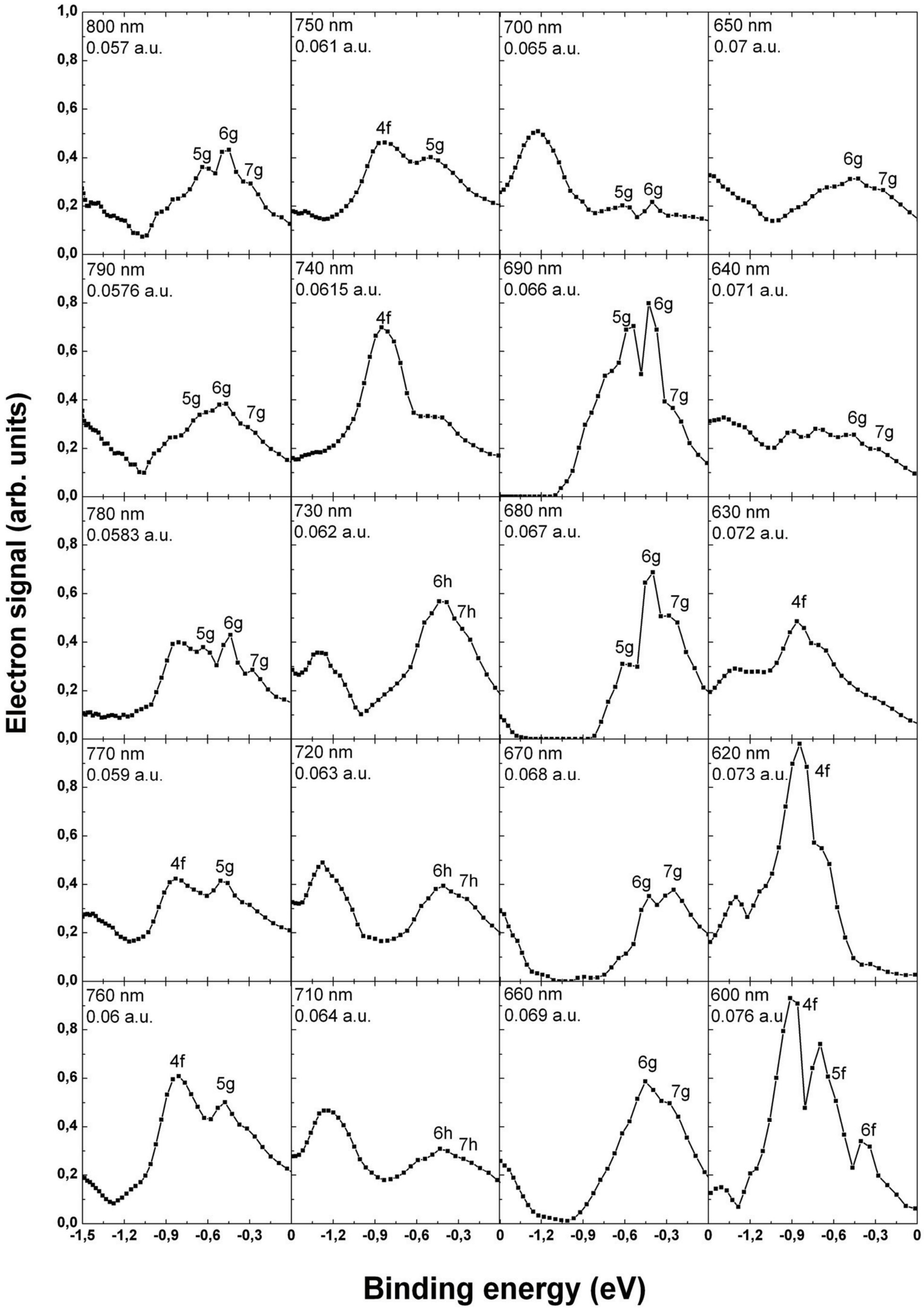

Figure 3-11. Experimental PES integrated over polar angles beyond ±30 degrees from the polarisation axis and downshifted by the energy of one photon.

In order to identify the intermediate resonant states involved in the low-order photoionisation processes we plot the experimental photoelectron spectrum downshifted by the energy of one photon at a number of laser wavelengths (Figure 3-11). As a result of this procedure suggested by Maharjan et al [72], the position of a peak corresponding to a particular resonance becomes independent of the wavelength and corresponds to the negative of the binding energy of this resonance. To minimize interference with non-resonant ionisation as much as possible, which may hinder the identification of the resonant sub-structures, photoelectron spectra integrated beyond ±30 degrees from the polarisation axis will be considered. The spectra are normalised so that $\int P(E)dE=1$ and are plotted on a common scale.

Assignment of the resonant states was performed in the following way: the binding energy corresponding to a peak observed in the spectrum is compared to the NIST atomic database (http://physics.nist.gov/cgi-bin/ASD), which allows to determine the principal quantum number of the contributing Rydberg state. However, for states with a high orbital angular momentum the quantum defect is negligible, so that a peak observed in the spectrum with a given binding energy can be attributed to different angular momentum states with the same principal quantum number. A unique assignment of the peaks observed in the photoelectron spectra requires inspection of the angular distributions. Figure 3-12 shows experimental angular distributions of the photoelectrons appearing in the photoelectron spectra within the first ATI order at the position of the peaks attributed to ionisation via $4l$, $5l$, $6l$, and $7l$ Rydberg states.

At 800 nm peaks in the spectrum are observable at binding energies of 0.6, 0.4 and 0.3 eV. The corresponding binding energies for $5l$, $6l$ and $7l$ resonances with high orbital angular momentum l according to NIST are 0.55, 0.38 and 0.28 eV, which is in reasonable agreement within the accuracy of the experiment. In order to determine the ionisation channel responsible for the appearance of these resonances we need to know the laser intensity used in the experiment. At 800 nm the estimated value is 6.7×10^{13} W/cm^2, which means that 11-photon ionisation is possible (closing of 10- and 11-photon channels is expected at 5.6×10^{13} W/cm^2 and 8.2×10^{13} W/cm^2, respectively). Ionisation from the f-series via (10+1)-photon ionisation is allowed by the parity selection rules. However, resonant population of the 4f state with 10 photons at 800 nm requires an intensity equal to 7.1×10^{13} W/cm^2, which exceeds the peak laser intensity in the experiment. Therefore the 4f state is not present in the spectra under these conditions.

Figure 3-12 a-c show the angular distributions evaluated for photoelectrons resulting from one-photon ionisation via resonant states 7*l*, 6*l* and 5*l*. At 800 nm the angular distributions contain 5 minima between 0 and 180 degrees, consistent with g-character of the corresponding resonant states. The nearest parity-allowed multi-photon resonance for the g-series observed in the PES involves 9 photons. The intensity required in order to shift the 5g Rydberg state into resonance with 9 photons of 800 nm light equals 4.1×10^{13} W/cm^2 and is available in the laser focus volume. When the wavelength of the laser is decreased the appearance of the 4f resonance can be observed. At 770 nm the 4f and 5g states are equally present in the spectrum. Estimates of the intensity at this wavelength give 6.0×10^{13} W/cm^2. At 770 nm closing of 9- and 10-photon channels is expected at 4.1×10^{13} W/cm^2 and 7×10^{13} W/cm^2, respectively Hence, both (9+1)-photon resonant enhanced ionisation (via g-states) and (8+1)-photon resonant enhanced ionisation (via f-states) may be anticipated. Resonant population of the 4f and 5g states with 8 and, respectively, 9 photons at 770 nm requires intensities equal to 2.8×10^{13} W/cm^2 and 5.1×10^{13} W/cm^2, both easily available in the laser focus volume.

The relative importance of the 4f resonance grows upon the further decrease of the laser wavelength down to 740 nm. At this wavelength the 5g resonance is just on the edge of the appearance threshold: the laser intensity required in order to shift the 5g state into resonance with 9 photons equals the peak laser intensity (6.4×10^{13} W/cm^2). At the same time the resonant population of the 4f state with 8 photons still remains possible in the laser focus volume leading to the dominance of the 4f state in the spectrum. Assignment of this peak is fully confirmed by the presence of 4 minima in the angular distributions for the wavelengths between 770 nm and 740 nm.

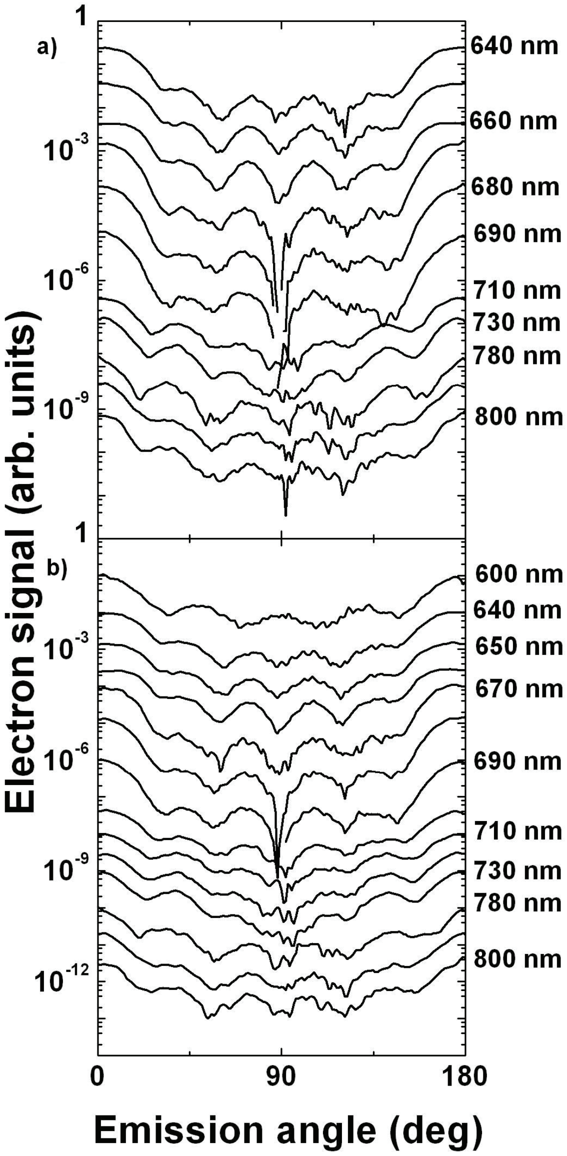
a)
b)
1
10^-3
10^-6
10^-9
1
10^-3
10^-6
10^-9
10^-12
640 nm
660 nm
680 nm
690 nm
710 nm
730 nm
780 nm
800 nm
600 nm
640 nm
650 nm
670 nm
690 nm
710 nm
730 nm
780 nm
800 nm
0
90
180
Electron signal (arb. units)
Emission angle (deg)

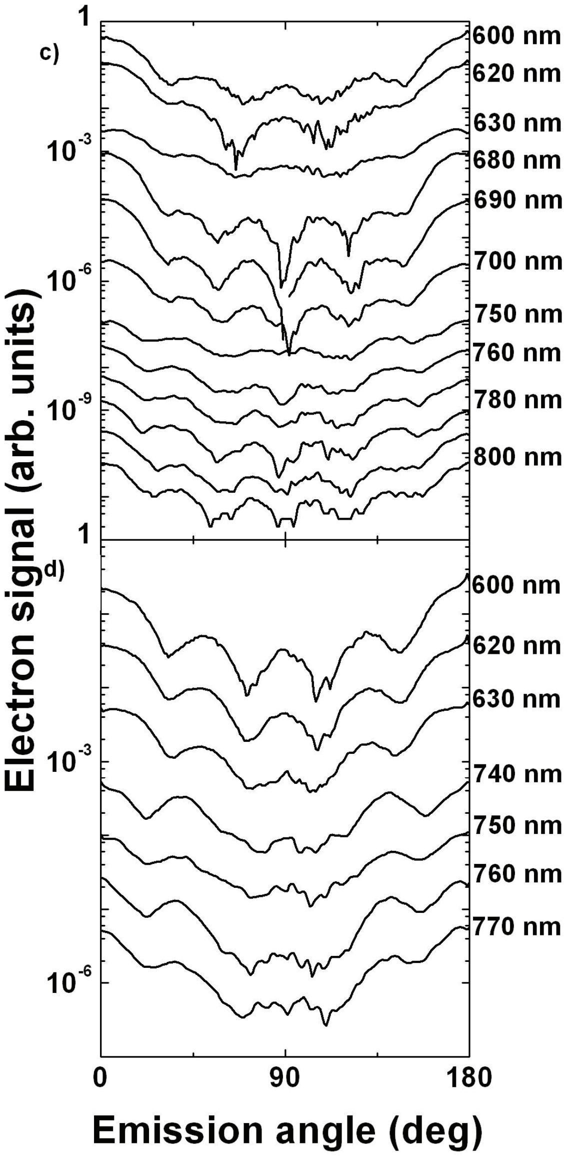

Figure 3-12. Experimental angular distributions calculated at photoelectron kinetic energies resulting from one-photon ionisation resonantly enhanced by resonant states: 7*l* (a), 6*l* (b), 5*l* (c), and 4*l* (d). The angular distributions were acquired by integration of the 3D velocity and angular distribution over a small velocity range corresponding to an energy range of 0.1 eV around the position of a particular resonant peak in the photoelectron spectrum. The angular distributions are shown only for those wavelengths where the corresponding peaks in the photoelectron spectrum were observed. The curves within each panel in Figure 3-12 are plotted with an arbitrary offset for clarity of presentation.

At 730 nm the experimental peak laser intensity drops to 3.9×10^{13} W/cm^2, opening the 9-photon channel. The peak laser intensity turns to be below the appearance threshold for the 4f state in (8+1)-photon ionisation channel (4.4×10^{13} W/cm^2). The dominant peak in the photoelectron spectrum thus can be attributed to (8+1)-photon ionisation via a 6*l* state, where *l* is odd as required by the parity selection rule. Consequently, we expect an even number of minima in the angular distributions of the photoionised electrons. Inspection of the angular distributions evaluated at different wavelengths around the peak corresponding to ionisation via a 6l state, shows predominantly 5 minima between 0 and 180 degrees. A slight broadening of the dip at 90 degrees, which can be observed at 730, 720 and 710 nm hints at the emergence of 6 minima between 0 and 180 degrees, which allows assignment to the h-series (*l*=5). The appearance intensity for the 6h state is 3.4×10^{13} W/cm^2. The broadening observable on the low-energy side of the 6h resonance is due to 9-photon non-resonant ionisation. A broad peak present in the spectra for 730 to 700 nm around the binding energy 1.3 eV is related to the low-energy (below 0.5 eV) pattern in the momentum maps, which is discussed in section 3.7

At 700 nm the estimated peak laser intensity is 4.5×10^{13} W/cm^2 which is the transition intensity between 9 and 8-photon channels at this wavelength. Accordingly we observe the emergence of the resonances from the g-series ionised via (7+1)-photon channel. The 8-photon channel remains responsible for ionisation enhanced by the g-series Rydberg states at wavelengths down to 640 nm as confirmed by the presence of 5 minima in the corresponding angular distributions in the this wavelength range.

At the short-wavelength end of our measurements, the (6+1)-photon channel becomes operative and the spectra are again dominated by the f-series. The angular distributions corresponding to the 5*l* and 6*l* at 600 nm show 4 minima in agreement with one-photon ionisation from the f-states. At 600 nm the estimated laser peak intensity is 5.7×10^{13} W/cm^2. Spectra measured under comparable conditions are known in literature. Kaminski et al [74] observed 6-photon resonant ionisation via the f-series in the wavelength range from 600 to 636 nm. Mevel et al [75] observed f-series in 6-photon resonant ionisation of xenon at 617 nm with 6.2×10^{13} W/cm^2 peak intensity. Agostini et al [51] reported photoelectron spectra taken at 600 nm with the peak intensity around 5×10^{13} W/cm^2, where in addition to 6-photon resonant ionisation from the 4f state, peaks attributed to 7p and 8p were observed. In our experiment the spectrum measured at 600 nm contains a peak at a binding energy of 0.7 eV, which could be attributed to ionisation from 8p. The angular distribution evaluated for this peak contains 4 minima, which does not contradict to the assignment of this peak as 8p. Ionisation from 8p can proceed, for example by the absorption of two and the emission of one photon, leading to the change of the orbital angular momentum from $l=1$ to $l=4$. Alternatively the angular distribution corresponding to the ionisation from this state may be affected by the close presence of the f-series. Helm et al [67] raise a discussion about the origin of the feature at the low-energy side from the 4f resonance, which was also observed by Mevel et al [75] and Agostini et al [51] and traditionally attributed to ionisation via 7p state. In our experiment this feature can be observed from 630 to 600 nm at the binding energy around 1.3 – 1.4 eV and is related to the pattern in the low-energy (below 0.5 eV) region of the momentum map (see section 3.7). The narrow angular distribution of this feature suggests its non-resonant origin.

To summarise this section, we have observed the evolution of the resonant ionisation channel as a function of the laser wavelength in the range from 800 to 600 nm. A number of channel-switching effects have been identified – from 9-photon resonant ionisation at 800 nm to 6-photon resonant ionisation at 600 nm. Inspecting the electron kinetic energy spectra and the angular distributions of the resonantly ionised electrons we have reliably assigned the intermediate Rydberg states involved in the ionisation process. All the experimental results have been carefully reproduced in the TDSE calculations as follows from the comparison of the photoelectron momentum maps.

Resonant ionisation. Calculations with constant U_p.

Unlike in the experiment, control over the laser intensity in the TDSE calculations is a straightforward operation. Control of the intensity gives the possibility of monitoring the non-resonant, strongly intensity-dependent ionisation, its evolution with the laser wavelength and interaction with the resonant contributions in the electron spectra. According to Eqn. (3), the photoelectron kinetic energy in a non-resonant ionisation process depends on the laser intensity through the ponderomotive energy Eqn. (1). Hence we choose to explore the wavelength-dependence of ATI spectra that are calculated at a constant value of the maximum ponderomotive energy in the laser pulse. Requiring a constant laser intensity would lead to a nonlinear frequency dependence, whereas a constant ponderomotive energy provides a linear dependence of the electron kinetic energy on the laser frequency, which facilitates the comparison with the resonant contribution.

In the following calculations we choose U_p = 2.45 eV, which corresponds to a maximum of the vector potential A_{max}=0.6 a.u. At this value of the vector potential both resonant and non-resonant contributions have comparable importance and can be simultaneously observed in the full-angle integrated photoelectron spectra obtained in TDSE calculations (top left panel in Figure 3-13). The photoelectron spectra presented in Figure 3-13 are integrated over the laser focus volume and plotted in a contour plot as a function of the laser frequency. Two sets of branches observable in the contour plot can be fitted according to Eqns. (3) and (4) in section 2.1 with slopes corresponding to high-order (n=11, 12, 13 photons, solid lines) and low-order (n=1, 2, 3 photons, dotted lines) ionisation processes for non-resonant and resonant ionisation, respectively.

Comparing the contour plots for photoelectron spectra integrated along and away from the laser polarisation axis (top right and bottom left panels in Figure 3-13, respectively) one can observe that integration along the polarisation axis leads to a contour plot where narrow resonant features are alternated with broad non-resonant contributions. On the contrary, the presence of the non-resonant features is

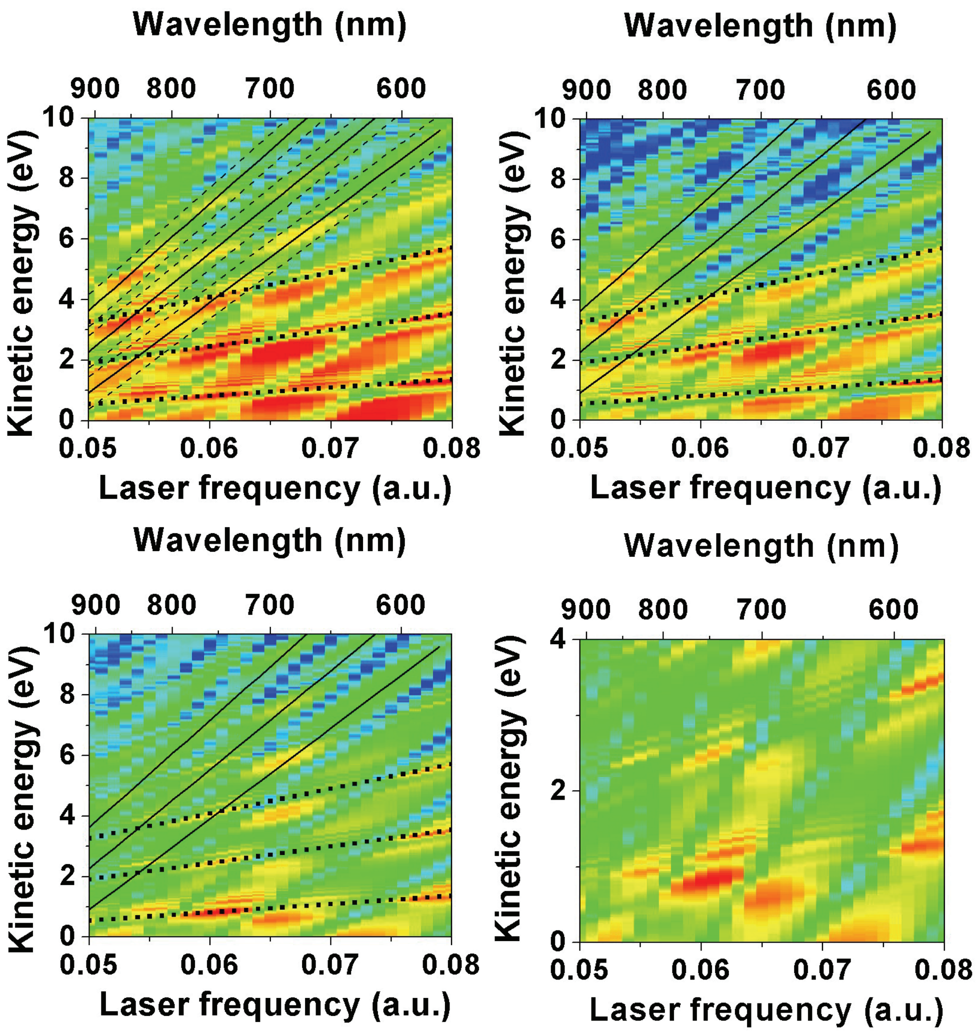

Figure 3-13. Calculations at A_{max}=0.6 a. u.: contour plots showing the frequency dependence of the photoelectron energy spectra integrated over the laser focus volume and over the full angle range (top left); within ±10 degrees along the polarisation axis (top right); beyond ±30 degrees from the polarisation axis (shown for two different energy scales, bottom). The spectra are arbitrarily divided by ω^{10}. The common colour scale covers three orders of magnitude. Two sets of branches observable in the contour plot are fitted according to Eqns. (3) and (4) in section 2.1 with slopes corresponding to high-order (n=11, 12, 13 photons, solid lines) and low-order (n=1, 2, 3 photons, dotted lines) ionisation processes for non-resonant and resonant ionisation, respectively.

strongly suppressed in the PES integrated away from the polarisation axis, where resonant features become the dominant contribution. This is further illustrated in

Figure 3-14 presenting vertical cuts through Figure 3-13 at 800 nm. The curves are plotted with an arbitrary offset and are shown only for the first two ATI orders for clarity of presentation. The photoelectron spectrum integrated away from the laser polarisation axis (dash-dotted curve) entirely consists of narrow sub-structures, whereas an alternation of narrow resonant and broad non-resonant features is observed in the photoelectron spectrum integrated along the polarisation axis.

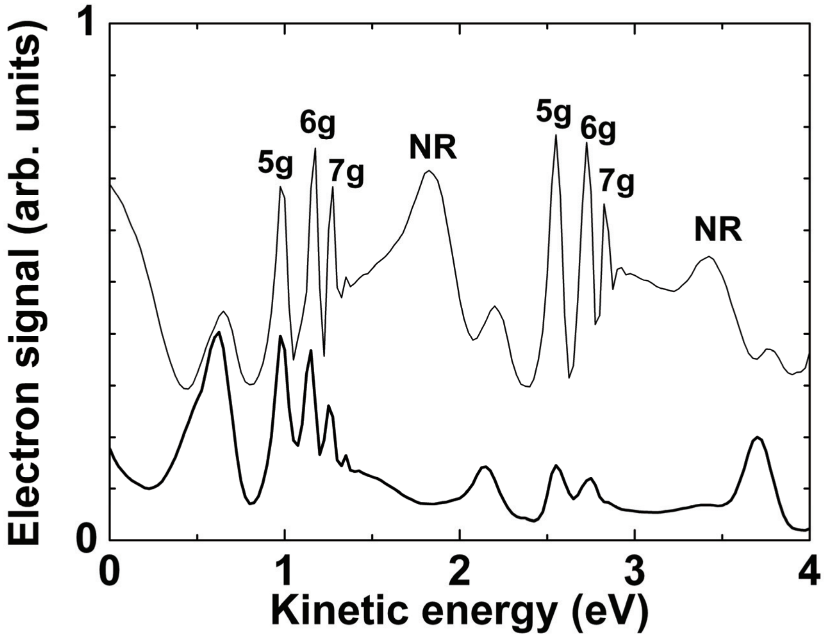

Figure 3-14. Calculated PES integrated beyond ±30 degrees from the polarisation axis (thick line) and within ±10 degrees along the polarisation axis (thin line) at laser frequency 0.057 a.u. (800 nm) and the maximum of the vector potential A=0.6 a.u.

Knowing the laser intensity we can determine the position of the non-resonant ATI peaks in the electron energy spectrum. However, closer inspection of the calculated photoelectron spectra shows that the position of the non-resonant branches cannot be directly related to the value of the maximum of vector potential used in the calculations, since the ponderomotive shift induced by the laser is not exclusively determined by the peak laser intensity, but depends to a large extent on the presence of slightly lower intensities in the laser focal volume. The range of intensities contributing to the ponderomotive shift of the ionisation threshold determines the width of the non-resonant branches. In order to establish the value of the "effective" intensity responsible for the position of the non-resonant branches, we need to evaluate the relative weight of all the intensities that are present in the laser focus, as given by the product of the intensity-dependent energy-integrated ionisation yield $\int_E P_I(E)dE$ and the intensity-dependent laser volume element:

$$P(I) = \int_E P_I(E)dE \frac{\partial V}{\partial I} dI\,, \qquad I \leq I_{max}$$

where I_{max} is the peak intensity in the laser focal volume and $\frac{\partial V}{\partial I} dI$ is the volume element experiencing an intensity between I and $I+dI$. Here it is implicitly assumed that the main effect of a small-intensity shift is the corresponding ponderomotive shift of the photoelectron spectrum. This is an approximation, as the photoelectron spectrum not only shifts but also changes shape when the intensity is changed.

In Figure 3-15 a series of curves are shown, corresponding to the relative weight (as defined above) of the individual intensities in the laser focus, for selected values of the maximum of the vector potential in the laser focus and for ω=0.06 a. u. (760 nm). Interestingly, important differences occur between these curves near the high-energy end. If the peak vector potential is 1 a.u., then the main contribution to the photoionisation comes from the parts of the laser focus, where 0.98<A<1 a.u. On the other hand, if the peak vector potential is 0.8 a.u., the dominant contribution comes from the parts of the laser focus where A≈0.75 a.u. The top left panel in Figure 3-13 shows results of the fits of the calculated full-angle integrated PES at A=0.6 a.u. We can fit non-resonant branches with linear functions of frequency $E_{kin}=n\omega-IP-A^2/4$ using the "effective" value of vector potential A=0.53 a.u. As before the ionisation potential IP =12.13 eV (0.446 a.u.). The width of the branches is determined by intensities in the focal volume corresponding to 0.45<A<0.6 a.u.

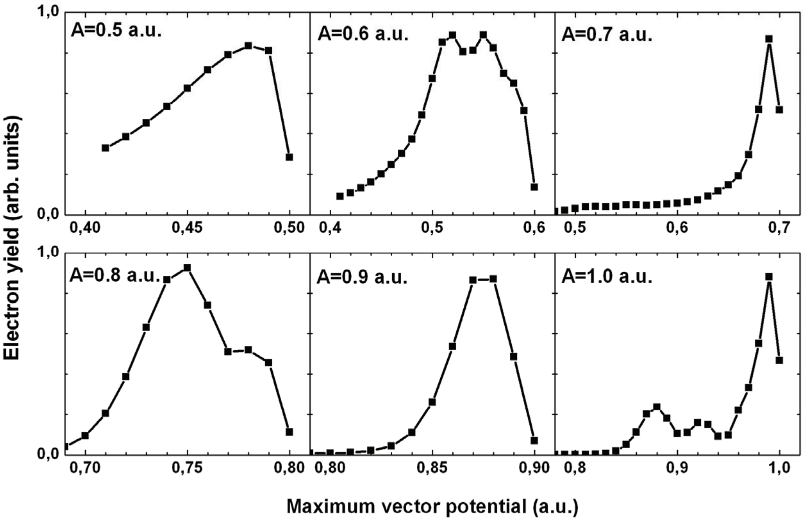

Figure 3-15. Photoelectron yield integrated over all kinetic energies weighted with the intensity-dependent laser volume element as a function of individual intensities in the laser focus for laser frequency ω=0.06 a. u. and for selected values of the maximum of the vector potential A_{max} in the laser focus.

Notably, the non-resonant contribution is competitive with the resonant contribution at this relatively low value of the vector potential (Figure 3-13). Furthermore, it has an effect on the appearance of the resonant sub-structure in the contour plot. The resonant sub-structure is most prominent whenever it overlaps with a non-resonant branch. For example, at the laser frequency 0.061 a.u. resonant sub-structures are very prominent within the first ATI order around kinetic energy equal to 1 eV. Remarkably, the first-order resonant ionisation branch crosses over at this laser frequency and kinetic energy with a 9-photon non-resonant ionisation branch. In contrast, at a laser frequency of 0.066 a.u. the resonant sub-structures are hardly observable within the first order due to the absence of non-resonant ionisation. In other words, at a relatively low intensity we can observe constructive interference between resonant and non-resonant ionisation processes. Nevertheless, resonant sub-structures can be well resolved on top of the non-resonant contributions.

In order to identify the resonant Rydberg states in the calculated spectra we plot angle-integrated photoelectron spectra downshifted by the energy of one photon (Figure 3-16).

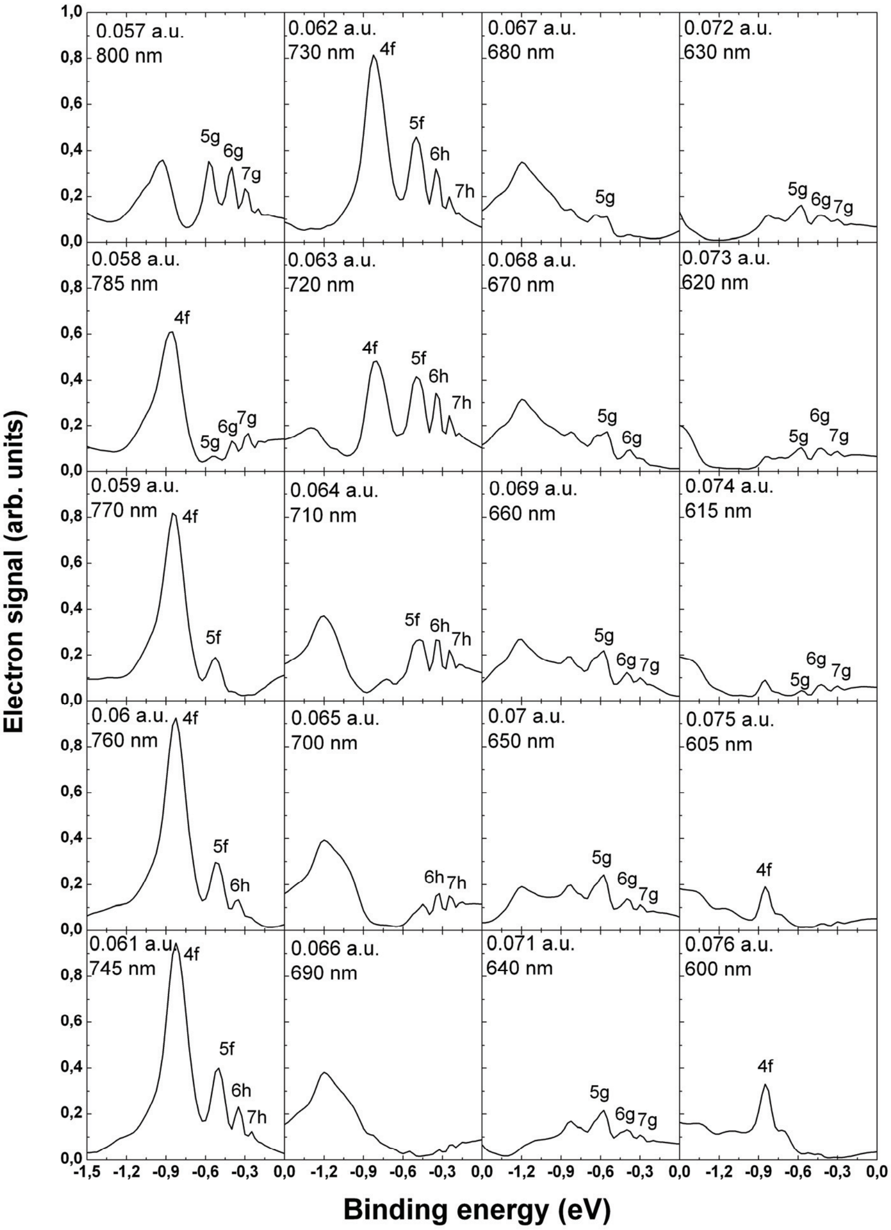

Figure 3-16. Calculated PES at $A_{max}=0.6$ a.u. integrated beyond ±30 degrees from the polarisation axis and downshifted by the energy of one photon.

As in the analysis of the experimental spectra we present photoelectron spectra integrated beyond ±30 degrees from the polarisation axis in order to suppress to some extent the influence of the non-resonant contribution. Assignment of the resonant peaks in the electron energy spectra includes comparison of their binding energies to the NIST database and the inspection of the corresponding electron angular distributions.

The angular distributions are presented in Figure 3-17 as a function of the laser frequency. In order to make these plots calculated angular-resolved photoelectron spectra were integrated within 0.1 eV around the photoelectron kinetic energies given by Eqn. (4). This way we can monitor the evolution of the angular distribution with the laser frequency for photoelectrons ionised via a particular Rydberg state with binding energy E_b. Figure 3-17 shows angular distributions corresponding to one-photon ionisation from $4l$, $5l$, $6l$, and $7l$ Rydberg states. The angular distributions are not normalised. Using Figure 3-17, the observed wavelength dependence of the photoelectron spectra can now be interpreted.

The evolution of the electron energy spectra with the laser frequency shows the following trend. At a laser frequency of 0.057 a. u. (800 nm) the spectrum is dominated by peaks corresponding to (9+1)-photon ionisation via Rydberg states of the g-series. Accordingly the angular distributions in the bottom three panels in Figure 3-17 show 5 minima between 0 and 180 degrees. At ω=0.058 a.u. (785 nm) the 9-photon channel opens and ionisation from the 4f state occurs via the (8+1)-channel, which now becomes the main contribution in the spectrum, whereas the relative contribution of the highest states from the g-series (which still can be ionised via the (9+1)-channel) is strongly decreased.

The (8+1)-photon channel remains operative up to ω=0.065 a.u. The angular distributions in the top panel of Figure 3-17 contain 4 minima at the frequencies ranging between 0.058 and 0.064 a.u., consistent with the presence of the 4f peak in the spectra. At ω=0.065 a.u. the Stark shift required for 8-photon resonant population of the 4f state (U_p=2.86 eV) exceeds the value of the ponderomotive energy at the peak laser intensity (U_p=2.45 eV), leading to the absence of the 4f peak

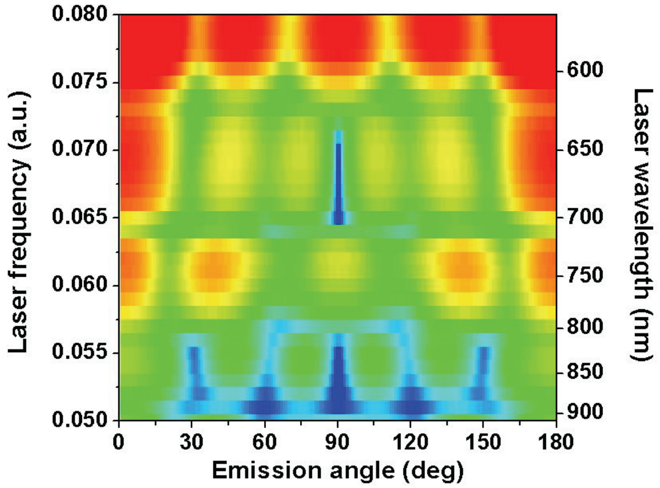
0.080
0.075
0.070
0.065
0.060
0.055
0.050
Laser frequency (a.u.)
600
650
700
750
800
850
900
Laser wavelength (nm)
0
30
60
90
120
150
180
Emission angle (deg)

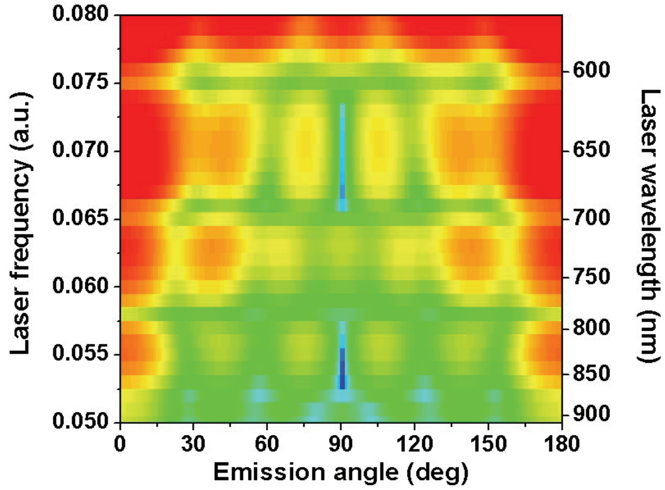
0.080
0.075
0.070
0.065
0.060
0.055
0.050
Laser frequency (a.u.)
600
650
700
750
800
850
900
Laser wavelength (nm)
0
30
60
90
120
150
180
Emission angle (deg)

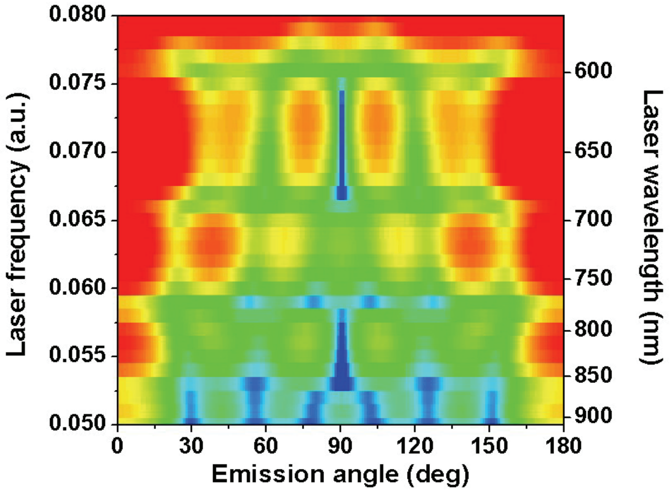
0.080
0.075
0.070
0.065
0.060
0.055
0.050
Laser frequency (a.u.)
600
650
700
750
800
850
900
Laser wavelength (nm)
0
30
60
90
120
150
180
Emission angle (deg)

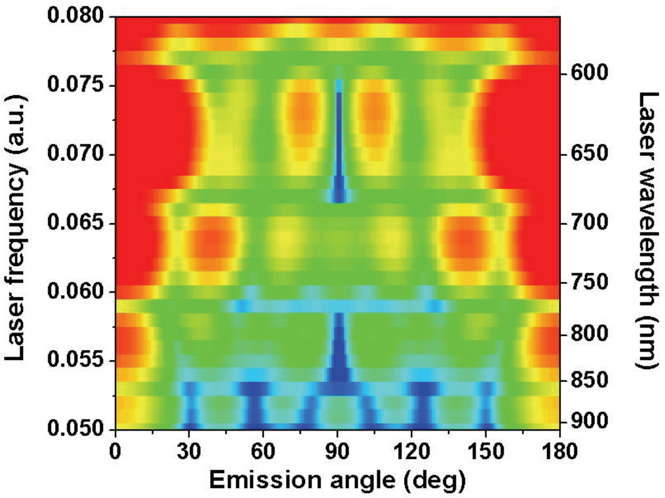

Figure 3-17. Calculations at A=0.6 a. u.: angular distributions calculated at photoelectron kinetic energies resulting from one-photon ionisation resonantly enhanced by resonant states (from top to bottom): 4*l* (E_b = 0.84 eV), 5*l* (E_b = 0.57 eV), 6*l* (E_b = 0.4 eV), 7*l* (E_b = 0.3 eV).

from the spectrum. Unlike the lowest state of the f-series, the angular distributions in the bottom three panels of Figure 3-17 contain an additional peak at 90 degrees in the frequency range from 0.059 to 0.065 a. u., increasing the number of minima up to 6, which implies involvement of the h-series. Both f- and h-series are allowed by the parity selection rule for the 8-photon resonant population.

Opening of the 8-photon channel at ω=0.067 a.u. (680 nm) allows the appearance of the g-series ionised via (7+1)-photon ionisation. The g-series remains in the spectrum until the next channel opening, which occurs at ω=0.074 a. u. (615 nm). Consistent with the g-character the angular distributions in the bottom three panels of Figure 3-17 contain 5 minima at this frequency range. At the high-frequency end (ω>0.074 a.u.) the spectra are again dominated by the contribution from the f-series involved in (6+1)-photon ionisation, followed by the presence of 4 minima in the angular distribution for the 4f peak in the bottom panel of Figure 3-17.

In the calculations we have a possibility to inspect the population distribution over the bound Rydberg states at the end of the laser pulse. Assuming that the states contributing to the ionisation process keep significant residual population we can determine possible candidates responsible for the photoelectron angular distributions containing 6 minima. First, we check the population distribution at the frequencies where the angular distributions contain 5 minima in order to confirm involvement of g-series. At the laser frequency 0.057 a.u. 98% of all the population remains in the ground state, and the rest is distributed predominantly over the bound Rydberg states with even orbital angular momenta (see Table 3-1). The population of the other states is lower by more than two orders of magnitude. At a frequency of 0.07 a.u. the major population remains in l=4.

ω, a.u.	***l*=0**	***l*=1**	***l*=2**	***l*=3**	***l*=4**	***l*=5**
0.057	0.01	---	0.04	---	0.1	---
0.070	0.03	---	0.05	---	0.5	---
0.062	---	---	0.003	0.01	---	0.02

Table 3-1. The population distribution (in percent of the total population) over the bound Rydberg states at the end of the laser pulse for different laser frequencies.

The dominance of l=4 is in agreement with assignment of the g-series being responsible for the observation of 5 minima in the angular distributions. The population of Rydberg states at ω=0.062 a.u., where the angular distributions show 6 minima, remains mainly in l=5 and l=3. The presence of l=3 and l=5 suggests involvement of f- and h-states, therefore we can attribute the series of resonant peaks observable for the frequencies between 0.059 and 0.065 a. u. to the f-series with a possible overlap with the h-series for the states with the principal quantum number higher than 5 (since 6h is the lowest state in the h-series). Involvement of both f- and h-states is consistent with the appearance of 6 minima in the angular distribution. Ionisation via the h-state with the absorption of one photon leads to the angular momentum of the photoelectron l=6. The presence of the 4f resonance in the photoelectron energy spectrum suggests that other states from the f-series may also be expected. Ionisation via an f-state resulting in 6 minima in the photoelectron angular distribution may occur for example via the absorption of two and emission of one photon.

A schematic diagram of channel switching in Xenon with the varying laser frequency is demonstrated in Figure 3-18 at a constant value of the ponderomotive energy. The horizontal dashed line labelled as E_{5l} at 11.58 eV corresponds to the level-energy of the 5f or 5g Rydberg states with respect to the ground state in Xenon in the absence of a laser field. In the presence of the laser field the ionisation threshold and the energy levels of the high-lying Rydberg states (such as 5f and 5g) shift upwards by the value of the ponderomotive energy U_p. In Figure 3-18 the ponderomotively shifted ionisation threshold and the 5l state are shown for U_p=2.45 eV, which we assume to correspond to the peak laser intensity. Solid lines in Figure 3-18 show the energy that can be reached by an integer number of photons from the ground state as a function of the laser frequency. These lines extrapolate to zero energy when $\omega \rightarrow 0$. Resonant excitation of a ponderomotively shifted Rydberg level occurs when it is matched with an integer number of laser photons. Naturally this resonance does not have to occur at the peak laser intensity, but can be reached somewhere in the laser focal volume corresponding to smaller ponderomotive shifts. For example, at ω=0.063 a.u. (720 nm) 8 photons can resonantly populate a 5l Rydberg state ponderomotively shifted by 2.13 eV available at the intensity just below the peak laser intensity. Subsequently, the atom can be ionised from the excited Rydberg state with just one extra photon. The parity selection rules require that (8+1)-photon ionisation in Xenon involve an intermediate Rydberg state with an odd orbital angular momentum. Therefore, at 0.063 a.u. (8+1)-photon resonant ionisation occurs via the 5f state (l=3). The ponderomotive shift required for the resonant population of a certain Rydberg level grows with the laser frequency and at some point reaches the maximum value available in the laser field. Further increase of the laser frequency enforces channel switching – the number of photons involved in the resonant excitation of the Rydberg level decreases by one. For example, resonant population of the 5l state with 7 photons at ω=0.069 a.u. occurs at U_p=1.56 eV. The orbital angular momentum of the intermediate resonant state must have even parity according to the selection rules, thus (7+1)-photon ionisation occurs at 0.069 a.u. via the 5g state (l=4).

At 0.066 a.u. (690 nm) resonant population of the 5l state with 7 photons can occur at U_p=1 eV followed by one-photon ionisation into continuum (note that the intensity at which ionisation from the excited Rydberg state occurs can be higher than the intensity at which the resonant excitation took place). However at this frequency, 9-photon non-resonant ionisation at the peak laser intensity is more favourable than 7-photon excitation of the resonance at a reduced intensity when U_p=1 eV. Therefore the electron energy spectra in Figure 3-16 contain only the non-resonant contribution. At 0.067 a.u. 8-photon channel opening takes place and a probability for non-resonant ionisation with 8 photons becomes comparable to the one for resonant ionisation via the (7+1)-photon channel.

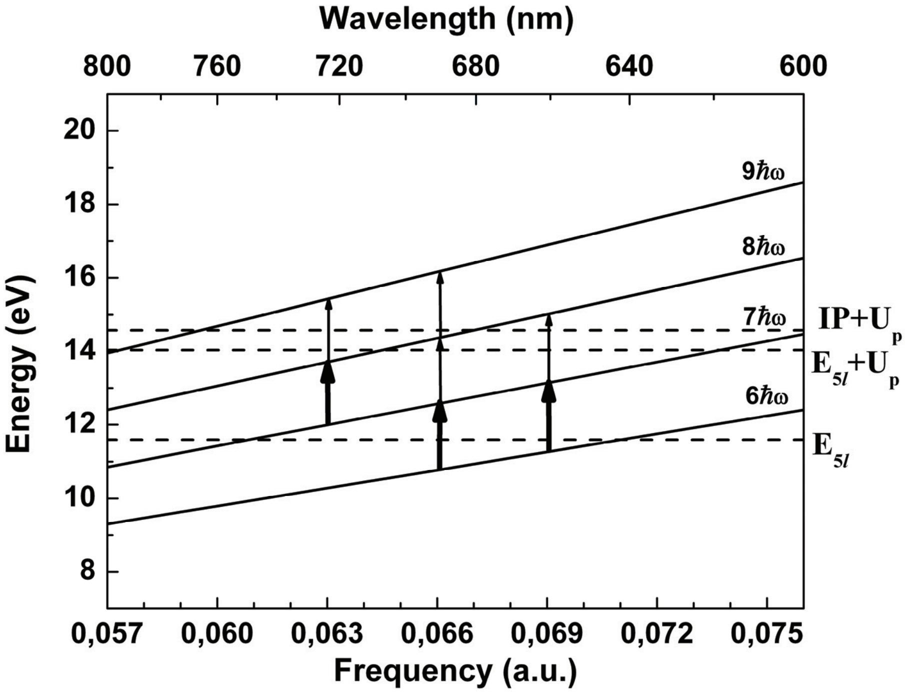

Figure 3-18. Schematic diagram of channel switching in Xenon as a function of laser frequency at a constant value of the ponderomotive energy U_p=2.45 eV. Thick arrows show the order of the resonant excitation of the 5l Rydberg state (channel switching), thin arrows show the order of non-resonant ionisation (channel opening).

To summarise this section, we have observed the evolution of the resonant and non-resonant ionisation channels as a function of the laser wavelength in the range from 800 to 600 nm at a constant ponderomotive energy. We have identified a number of channel-switching effects – from 9-photon resonant ionisation at 800 nm to 6-photon resonant ionisation at 600 nm. Assignment of the involved Rydberg states has been confirmed by the inspection of the residual population in the contributing states. We have shown that the appearance of the resonant sub-structure in the electron energy spectra may be influenced by the presence of the non-resonant contribution. At relatively low laser intensity we have observed constructive interference between resonant and non-resonant ionisation processes.

3.4. Xenon in the infrared frequency range.

The experimental images presented in this section were obtained by summing the electron yield over more than 5 minutes of acquisition time. Electron momentum spectra were measured at 17 wavelengths in the range from 1200 to 1600 nm with a step of 25 nm. In Figure 3-19 a series of experimental momentum maps are compared to the results of the corresponding volume-integrated TDSE calculations. The values of the maximum of the vector potential in the calculations are chosen for the best matching to the experimental results. The same data zoomed in on the electron kinetic energies below 2 eV is shown in Figure 3-20. The comparison shows a good agreement between experimental and theoretical results. All the experimentally observed structures are reproduced in the calculations in high detail.

The momentum maps in the infrared frequency range show a significant qualitative difference in comparison to the momentum maps obtained in the visible frequency range. In the visible frequency range the momentum spectra are dominated by the contributions from resonance-enhanced ionisation, characterised by highly oscillatory angular distributions. In contrast, in the infrared frequency

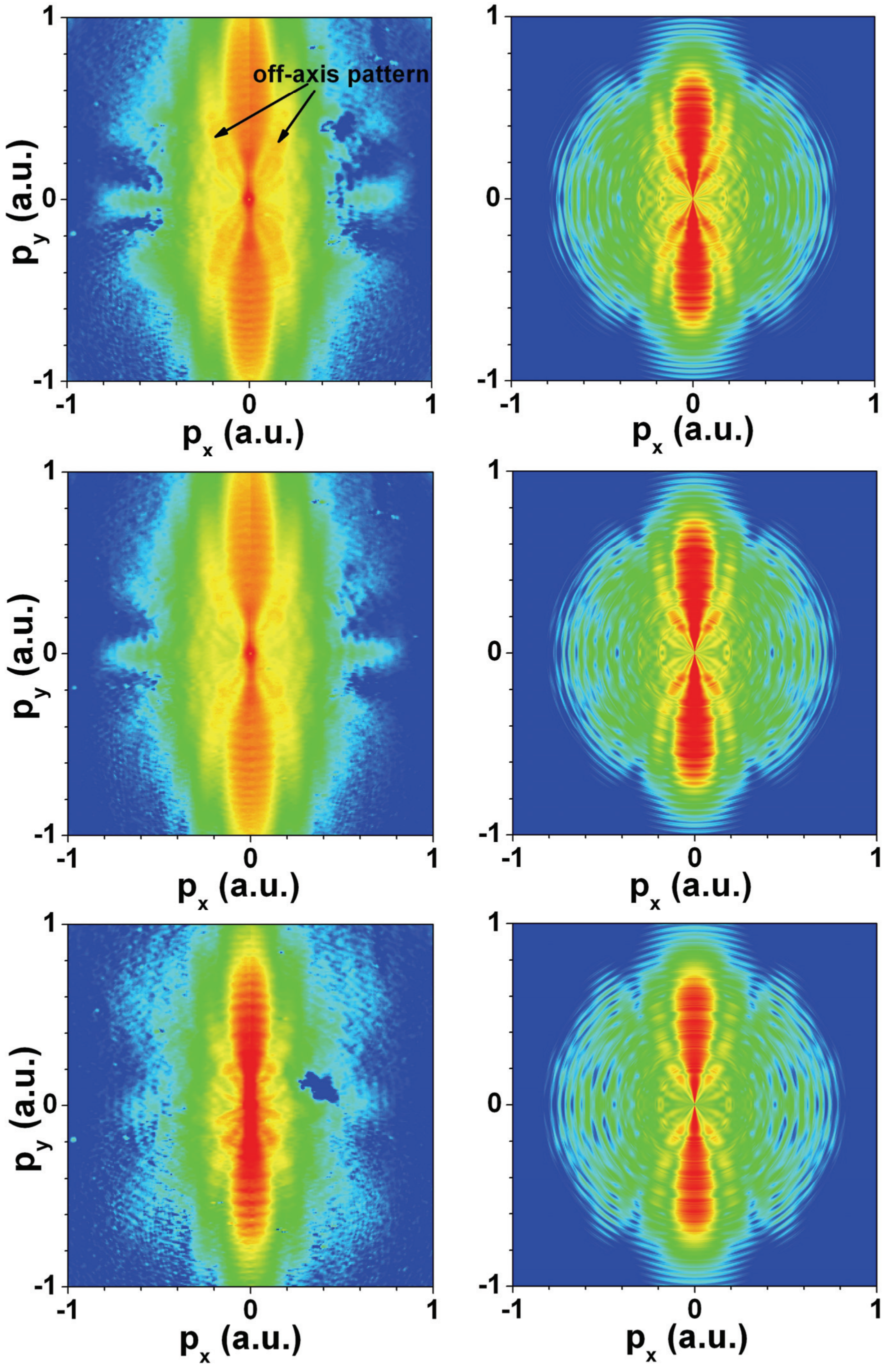
off-axis pattern
p_y (a.u.)
p_x (a.u.)
1
0
-1

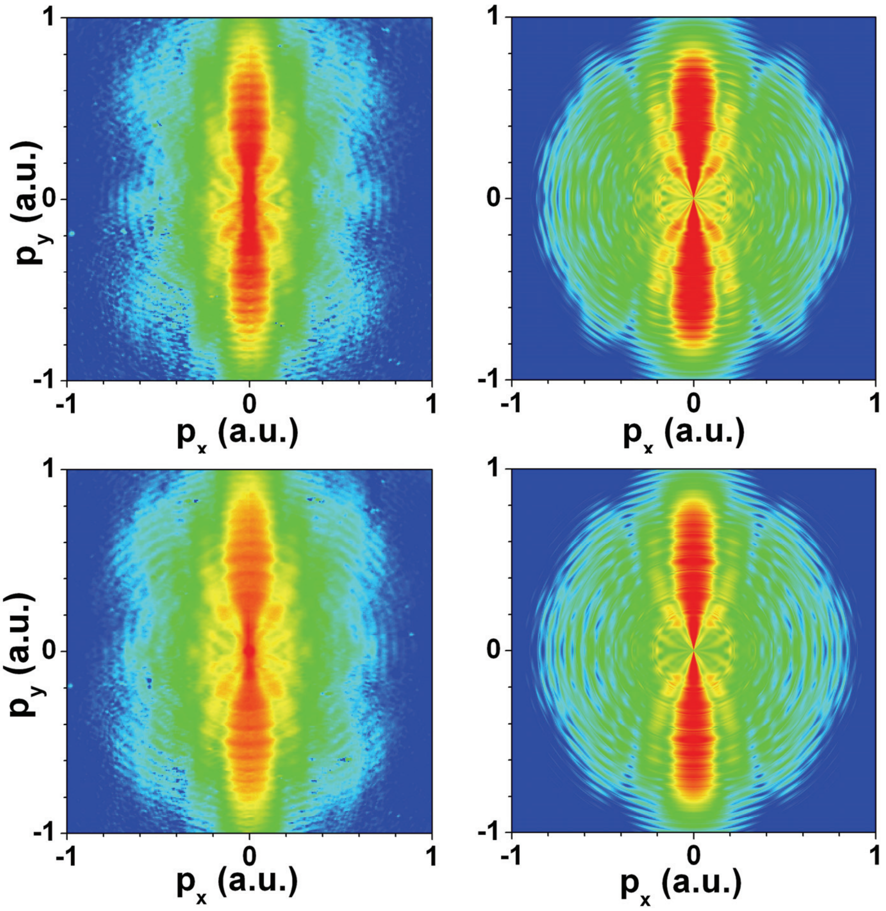

Figure 3-19. Comparison of the experimental (left column) and the calculated (right column) momentum maps of photoelectrons ionised from xenon at 1575 nm, A_{max}=1.0 a.u.; 1475 nm, A_{max}=1.0 a.u.; 1375 nm, A_{max}=0.91 a.u.; 1300 nm, A_{max}=0.96 a.u.; 1200 nm, A_{max}=0.95 a.u. The values of the maximum of the vector potential A_{max} in the calculations were chosen for the best matching to the experimental results. The logarithmic false-colour scale covers 4 orders of magnitude. Note that the calculated spectra are truncated at high energies due to a finite size of the grid used in the TDSE calculations.

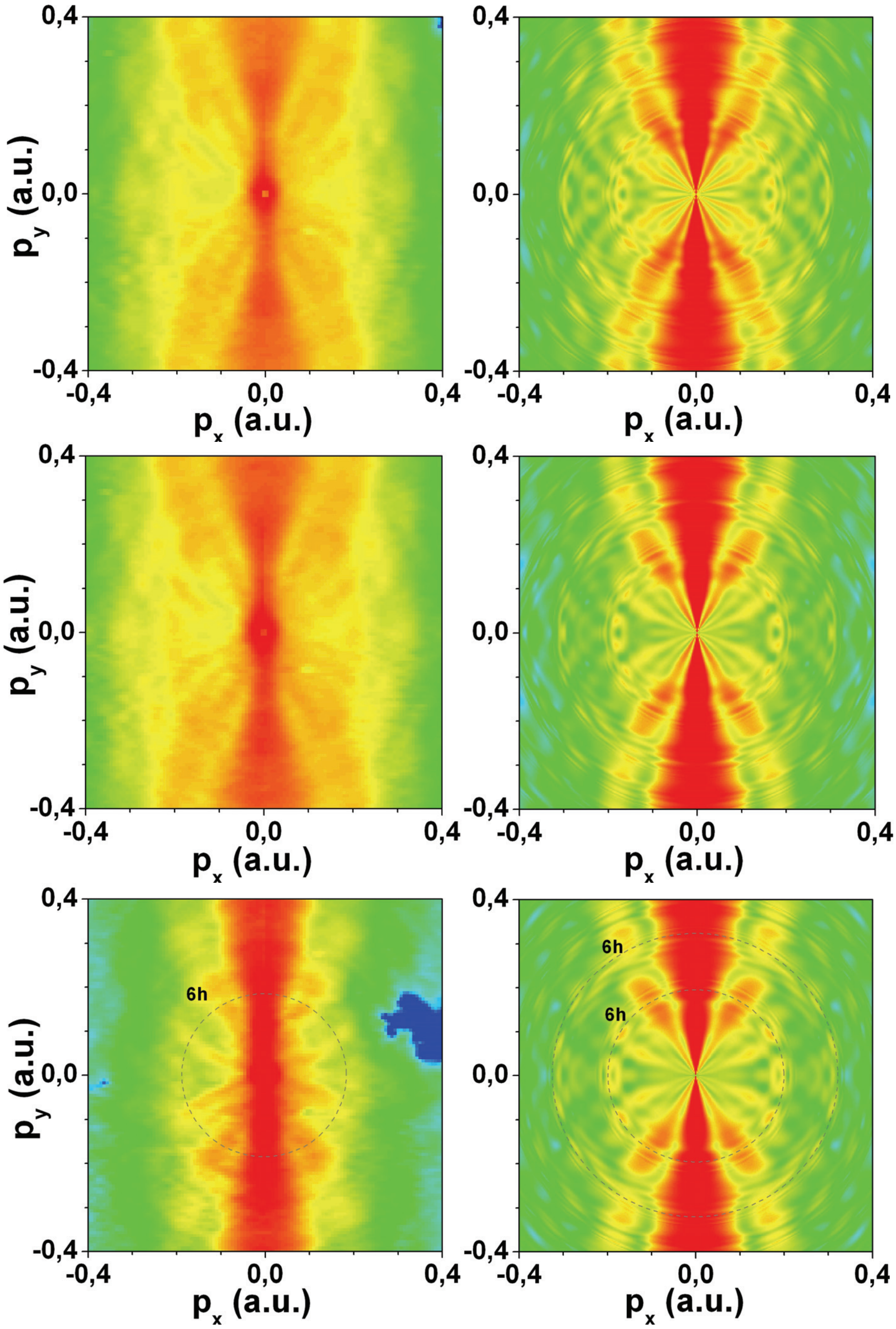
0,4
0,0
-0,4
p_y (a.u.)
p_x (a.u.)
6h
6h
6h

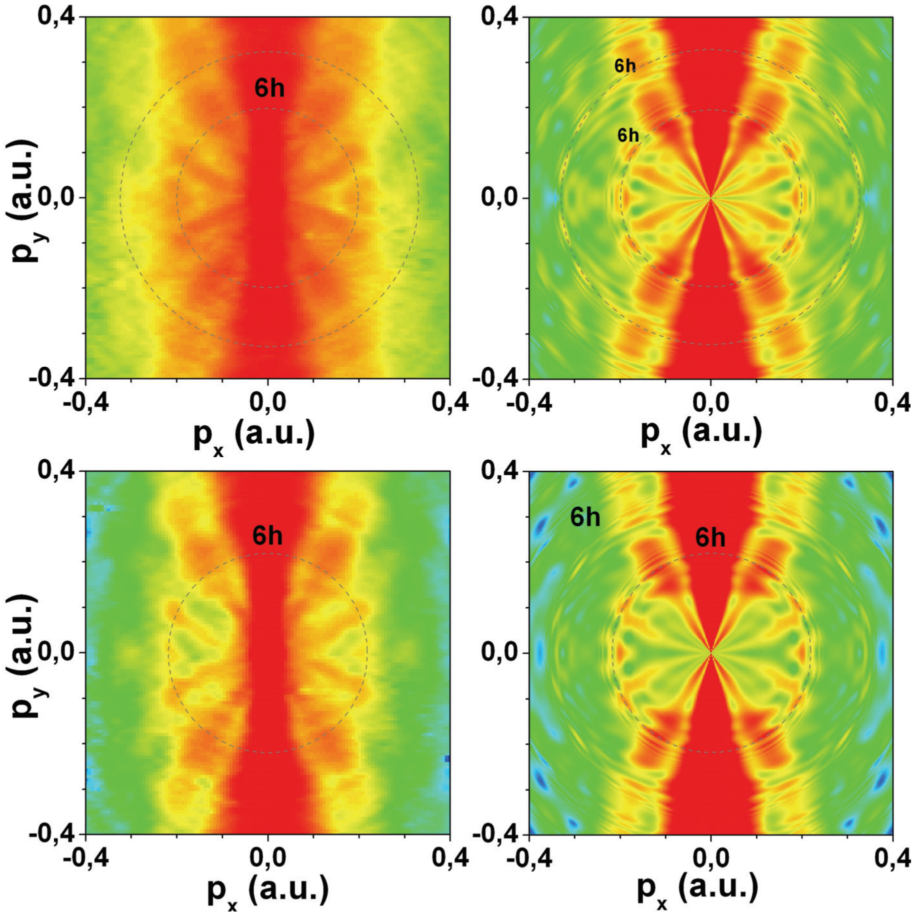

Figure 3-20. The same as in the previous figure zoomed in on the low-energy part. The logarithmic false-colour scale covers 4 orders of magnitude. The black circles show the contribution from electrons, corresponding to one and two-photon ionisation via 6h Rydberg state.

range the momentum maps are completely dominated by an off-axis pattern that extends from the centre of the image into the high-energy region, whereas the contribution from resonance-enhanced ionisation is relatively small. Inspection of the electron kinetic energy spectra and the angular distributions of the resonant contribution observable at the wavelengths between 1375 and 1200 nm (see Figure 3-20) has identified the involvement of the 6*h* state. Furthermore, analysis of resonant features appearing in the TDSE calculations with constant ponderomotive energy, corresponding to a maximum value of the vector potential of 0.95 a.u., provides interpretation consistent with the experimental results.

The qualitative difference between the photoelectron momentum spectra observed upon the transition from the visible to the infrared frequency range may indicate involvement of different ionisation mechanisms. The development of the off-axis pattern with the laser wavelength and intensity as well as a discussion on possible interpretations will be presented in section 3.8.

3.5. Argon in the visible frequency range.

The experimental images presented in this section were obtained by summing the electron yield over 3 minutes of acquisition time. The recorded photoelectron momentum spectra are qualitatively similar to the case of Xenon and are domintated by the resonant-ionisation contributions accompanied by weaker contributions formed by a low-energy radial pattern and an off-axis pattern, which will be discussed in sections 3.7 and 3.8, respectively. In this section we will concentrate on the analysis of the features attributed to the mechanism of resonance-enhanced ionisation.

Electron spectra were measured at 21 wavelengths in the range from 600 to 800 nm with a step of 10 nm. In Figure 3-21 and Figure 3-22 experimental momentum maps at several wavelengths are compared to the results of the corresponding volume-integrated TDSE calculations. The vertical and horizontal axes in Figure 3-21 show the electron momenta in the range between –1 and 1 a.u. parallel and perpendicular to the laser polarisation, respectively. This momentum scale corresponds to the electron kinetic energies up to 13.6 eV. The low-energy part of the momentum spectra is presented in Figure 3-22, where the electron momenta up to 0.4 a.u are shown, corresponding to the kinetic energy up to around 2 eV. The comparison shows a good agreement between the experimental and theoretical results. All the structures observed in the experimental momentum spectra are well reproduced in the TDSE calculations.

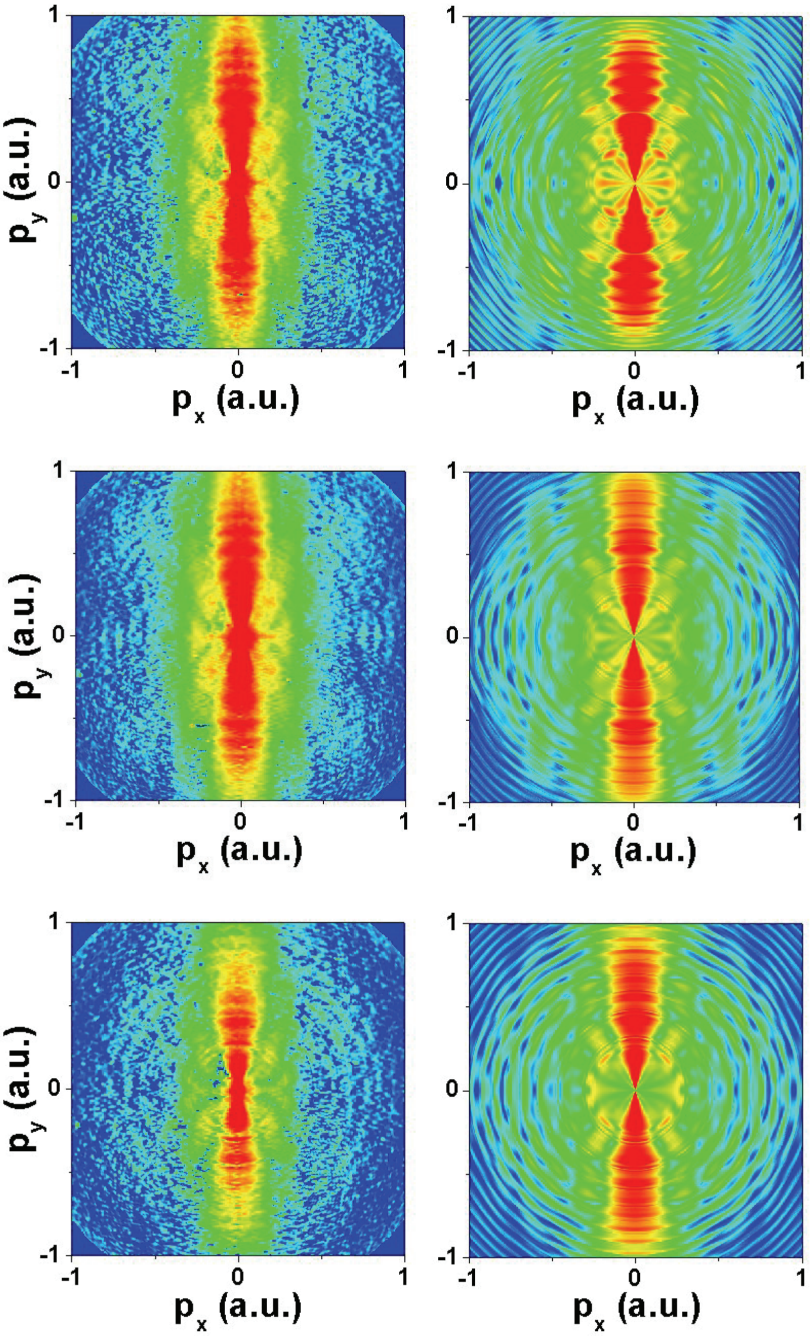

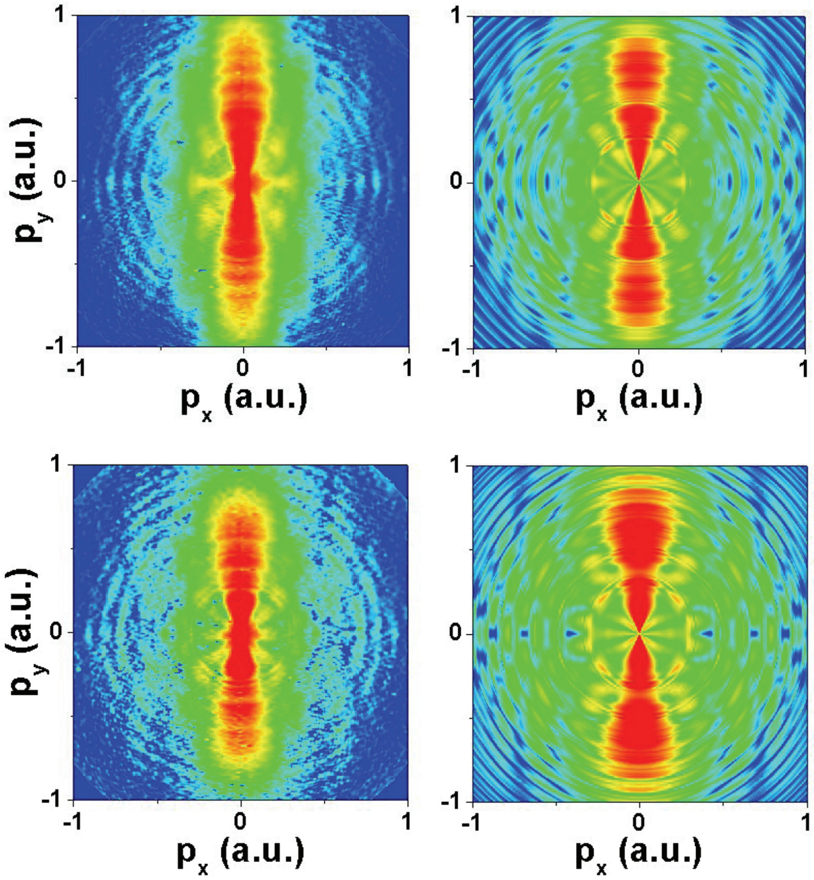

Figure 3-21. Comparison of the experimental (left column) and the calculated (right column) momentum maps of photoelectrons ionised from argon at (from top to bottom) 800 nm, A_{max}=0.85 a. u., 0.82×10^{14} W/cm^2; 750 nm, A_{max}=0.98 a. u., 1.25×10^{14} W/cm^2; 700 nm, A_{max}=0.88 a. u., 1.15×10^{14} W/cm^2; 650 nm, A_{max}=0.93 a. u., 1.48×10^{14} W/cm^2; 600 nm, A_{max}=0.78 a. u., 1.23×10^{14} W/cm^2. The logarithmic colour scales cover three orders of magnitude.

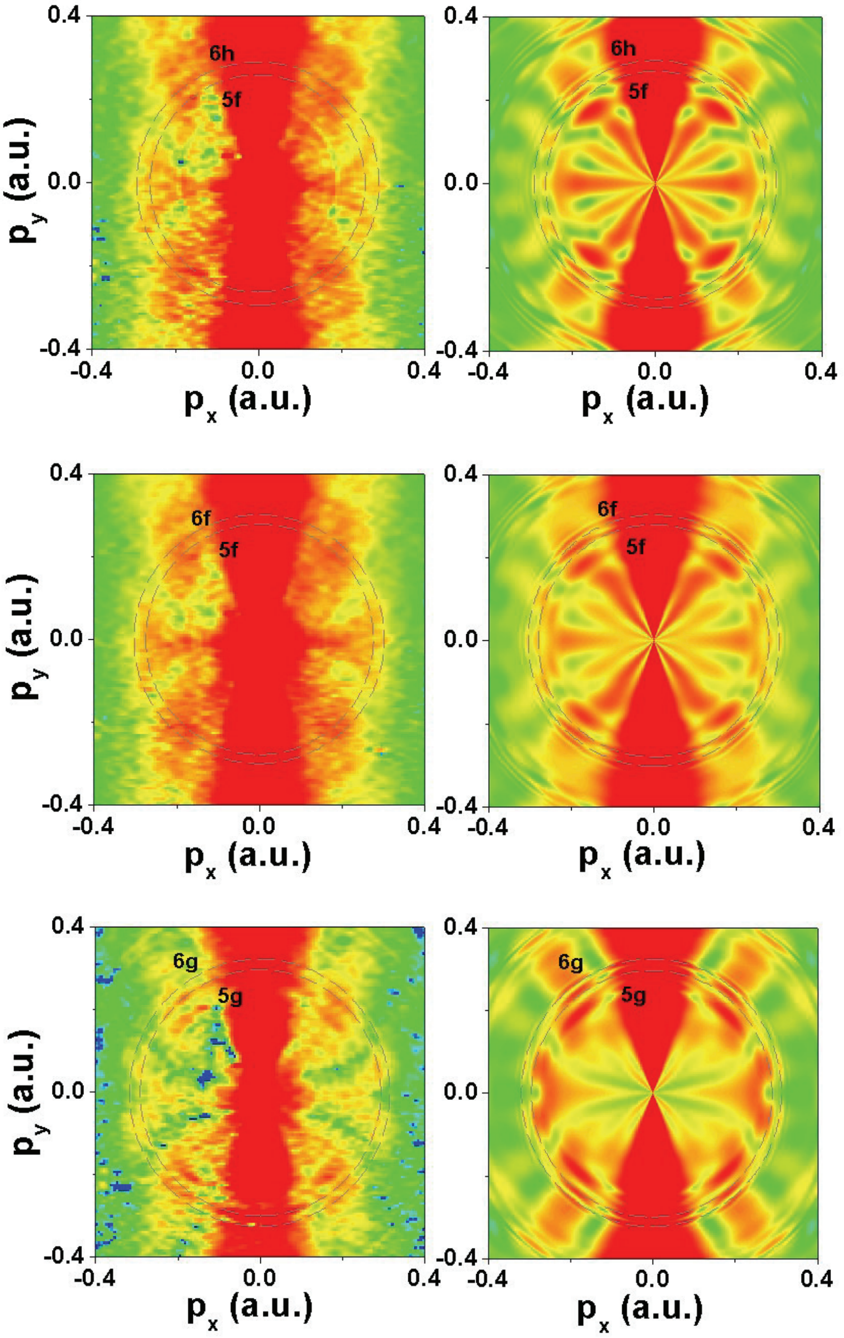
6h
5f
6h
5f
6f
5f
6f
5f
6g
5g
6g
5g
0.4
0.0
-0.4
-0.4
0.0
0.4
p_y (a.u.)
p_x (a.u.)

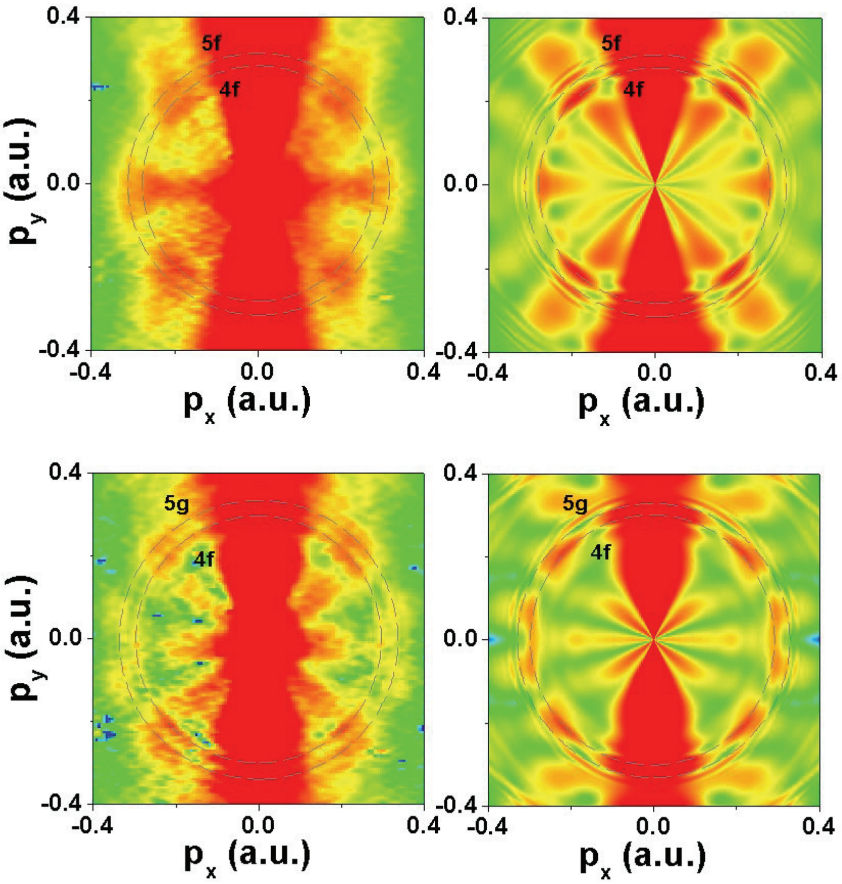

Figure 3-22. The same as in Figure 3-21 zoomed in on the low-energy part (from top to bottom): 800 nm, A_{max}=0.85 a. u., 0.82×10^{14} W/cm^2; 750 nm, A_{max}=0.98 a. u., 1.25×10^{14} W/cm^2; 700 nm, A_{max}=0.88 a. u., 1.15×10^{14} W/cm^2; 650 nm, A_{max}=0.93 a. u., 1.48×10^{14} W/cm^2; 600 nm, A_{max}=0.78 a. u., 1.23×10^{14} W/cm^2. The logarithmic colour scales cover three orders of magnitude and are adapted to emphasize the off-axis structures of the momentum spectrum.

Resonant ionisation. Interpretation of the experimental results.

For an overview of our experimental results it is convenient to present the angle-integrated photoelectron kinetic energy spectra in a contour plot as a function of the laser frequency (Figure 3-23). Individual energy distributions were normalised so that $\int P(E)dE=1$. The probability for a photoelectron to be ionised with a given kinetic energy at a given laser frequency is coded on a logarithmic colour scale, which covers one order of magnitude. A set of continuous branches can be observed in Figure 3-23**.** Black dotted lines were calculated according to Eqn. (4), where E_b=0.85 eV and n varies from 1 to 5, indicating low-order ionisation processes involving the population of intermediate resonant states. The contour plot contains no signature of branches, which could be attributed to high-order non-resonant processes.

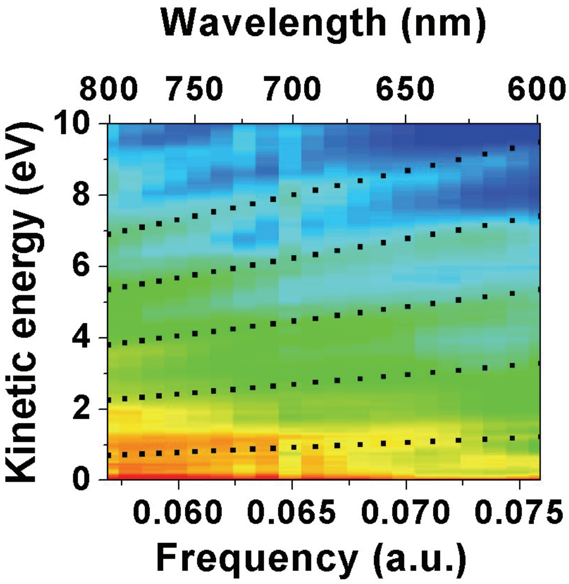

Figure 3-23. Experiment: contour plots showing the frequency dependence of the normalised angle-integrated photoelectron energy spectra. The logarithmic colour scale covers one order of magnitude.

In order to identify the intermediate resonant states involved in the low-order photoionisation processes we plot the experimental photoelectron spectrum integrated beyond ±25 degrees from the polarisation axis and downshifted by the energy of one photon at a number of laser wavelengths (Figure 3-24). The spectra are normalised so that $\int P(E)dE=1$ and are plotted on a common scale.

Assignment of the resonant states was performed based on the binding energy of peaks observed in the spectrum in combination with the photoelectron

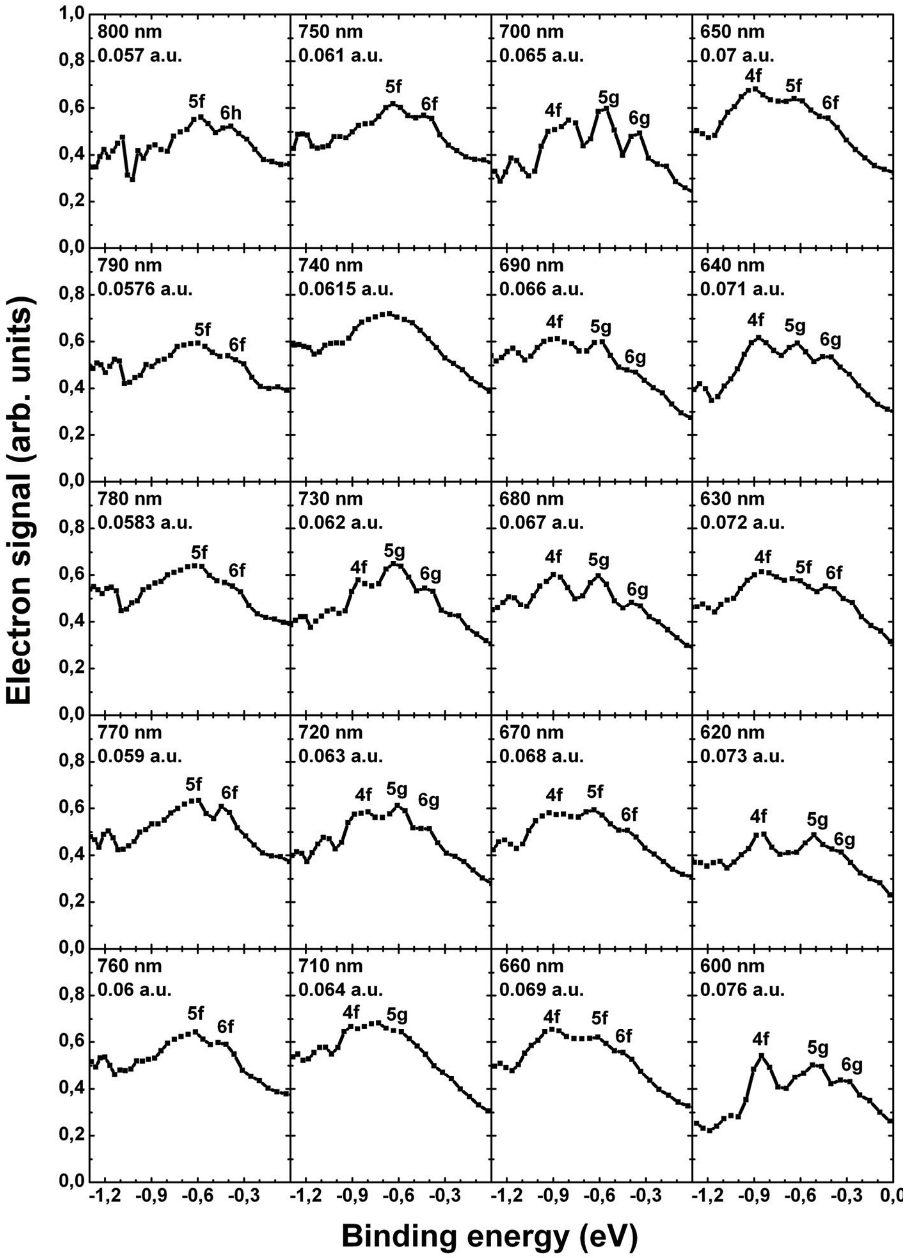

Figure 3-24. Experimental normalised PES integrated over polar angles beyond ±25 degrees from the polarisation axis and downshifted by the energy of one photon.

angular distribution. Figure 3-25 and Figure 3-26 show experimental angular distributions of the photoelectrons appearing in the photoelectron spectra within the first ATI order at the position of the peaks attributed to ionisation via 4*l*, 5*l* and 6*l*

Rydberg states, where *l* is the orbital angular momentum of the particular resonant state.

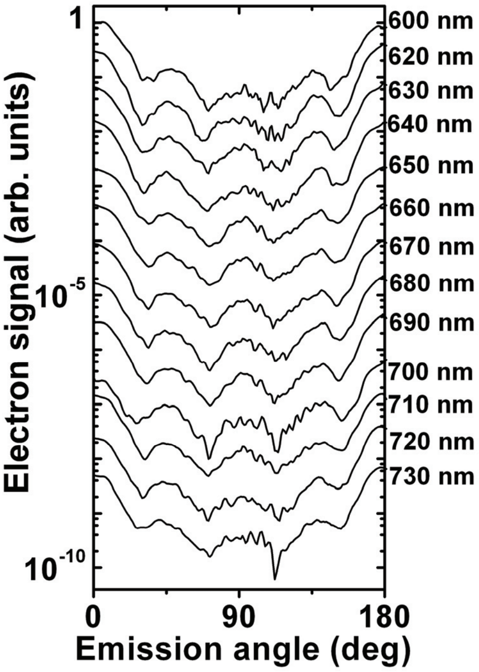

Figure 3-25. Experimental angular distributions evaluated at photoelectron kinetic energies corresponding to one-photon ionisation via the 4*f* state.

At 800 nm peaks in the spectrum are observable at binding energies of 0.6 and 0.4 eV. According to the Rydberg formula this corresponds to 5*l* and 6*l* resonances with high orbital angular momentum *l*, which are expected at 0.55 and 0.38 eV, respectively. The estimated intensity at 800 nm is 0.82×10^{14} W/cm^2. If ionisation were to occur at this intensity it would require at least 14 photons in order to overcome the ponderomotively shifted ionisation threshold. Consequently, resonant population of the Rydberg states should have involved 13 photons. However, resonant population of a 5l state with 13 photons at 800 nm requires an intensity equal to 0.83×10^{14} W/cm^2, which is just above the peak laser intensity in the experiment. Therefore the peaks in the spectrum are expected to be due to 12-photon resonant ionisation. As required by the parity selection rules ionisation should proceed via the states with odd orbital angular momenta. At 800 nm the

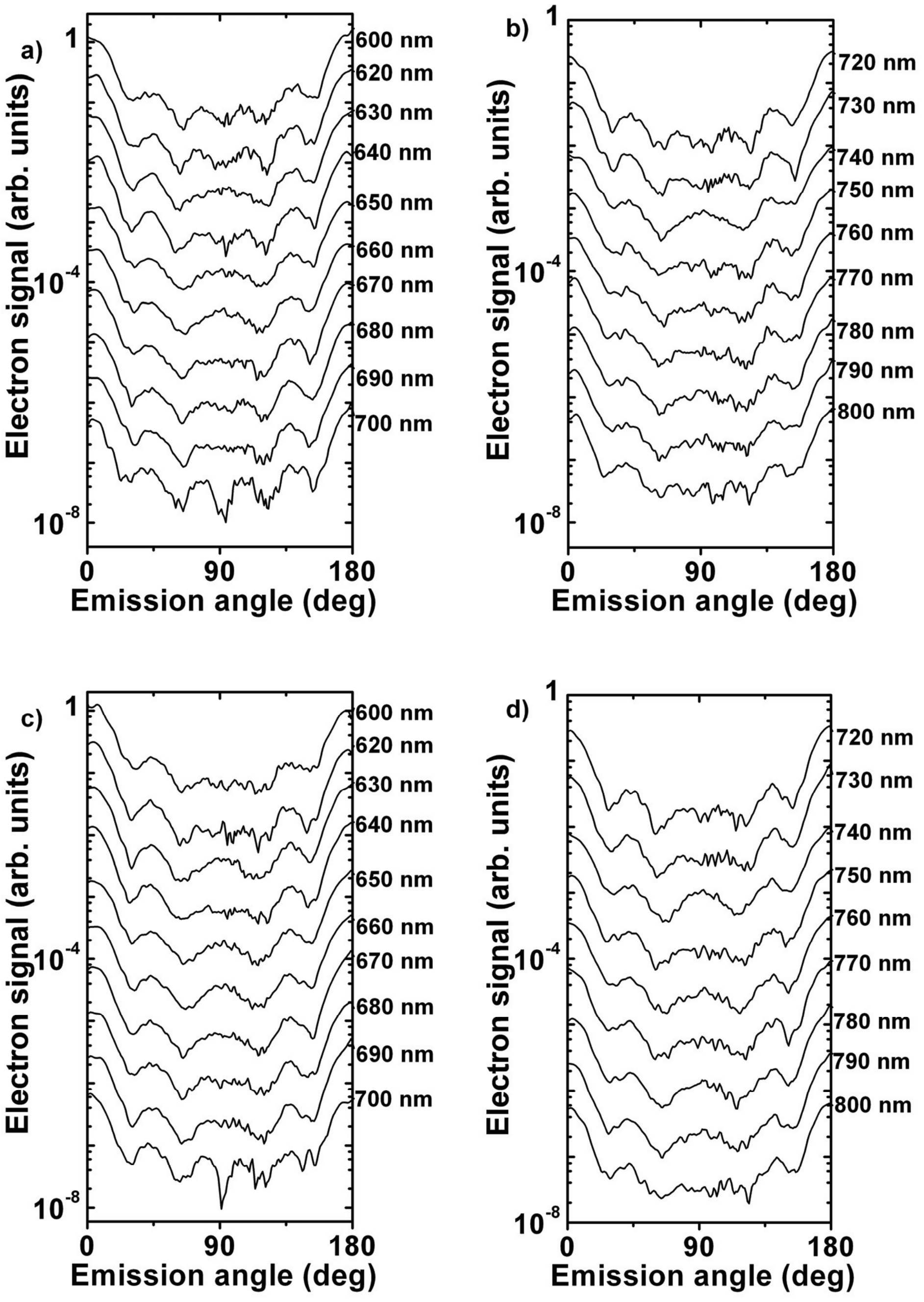

Figure 3-26. Experimental angular distributions evaluated at photoelectron kinetic energies corresponding to one-photon ionisation via 6*l* (a, b) and 5*l* (c, d) resonant states.

angular distributions for the 5*l* and 6*l* resonant states (Figure 3-26) contain 6 minima between 0 and 180 degrees, consistent with the f- (l=3) and h-character (l=5) of the corresponding resonant states.

Our present measurement can be compared to the results of Wiehle et al [71], where a detailed comparison between the experiment and the calculated photoelectron momentum spectra at 800 nm and at various intensities was performed. Wiehle et al attributed the structure observed in the spectrum obtained at 0.7×10^{14} W/cm^2 to 12-photon resonant ionisation via 4f and 5p states. In our case the spectrum acquired at 0.82×10^{14} W/cm^2 contains contributions from 12-photon resonant ionisation via 5f and 6h states, whereas a possible contribution from the 5p state is completely hidden under the non-resonant contribution.

Ionisation via (12+1)-photon resonant ionisation with involvement of the f-series continues to dominate the spectra for the wavelengths down to 750 nm. At the shorter wavelengths 11-photon resonant 12-photon ionisation via the g-series becomes dominant. For example, at 700 nm 11-photon resonant ionisation via the 5g state requires the intensity of 0.93×10^{14} W/cm^2, which is close to the peak laser intensity estimated as 1.15×10^{14} W/cm^2. Channel switching from ionisation via the f-series at 750 nm to ionisation via the g-series at 700 nm is consistently accompanied by the change in the corresponding angular distributions from 4 to 5 minima between 0 and 180 degrees in Figure 3-26. A peak appearing in the spectrum at 700 nm at a binding energy around 0.9 eV can be attributed to 10-photon resonant ionisation via 4f state. Accordingly, the angular distribution in Figure 3-25 contains 4 minima between 0 and 180 degrees.

The relative importance of the 4f resonance grows upon further decrease of the laser wavelength down to 650 nm. At this wavelength the 5g resonance is just on the edge of the appearance threshold. As the laser wavelength decreases, the intensity, where a given state shifts into resonance increases. At 650 nm the laser intensity required in order to shift the 5g state into resonance with 11 photons equals the peak laser intensity (1.5×10^{14} W/cm^2). At the same time the resonant population of the 4f state (and higher f-states) with 10 photons still remains possible in the laser focus volume leading to the dominance of the 4f state in the spectrum. Assignment of the peaks as the f-states is fully confirmed by the presence of 4 minima in the angular distributions.

At the short-wavelength end of our measurements, the (9+1)-photon channel becomes responsible for the appearance of the g-series in the spectra, while the (8+1)-photon channel leads to the peak attributed to the 4f state. The angular distributions corresponding to the 5*l* and 6*l* at 600 nm show 5 minima in agreement with one-photon ionisation from the g-states. At 600 nm the estimated laser peak intensity is 1.23×10^{14} W/cm^2.

To summarise this section, we have observed the evolution of the resonant ionisation channel as a function of the laser wavelength in the range from 800 to 600 nm. A number of channel-switching effects have been identified – from 12-photon resonant ionisation at 800 nm to 9-photon resonant ionisation at 600 nm. Inspecting the electron kinetic energy spectra and the angular distributions of the resonantly ionised electrons we have reliably assigned the intermediate Rydberg states involved in the ionisation process. All the experimental results have been carefully reproduced in the TDSE calculations as follows from the comparison of the photoelectron momentum maps.

Resonant ionisation. Calculations with constant U_p.

In contrast to the experiment, results of the TDSE calculations allow monitoring the evolution of the ATI spectra as a function of the laser wavelength at a constant value of the maximum ponderomotive energy in the laser pulse. In the following calculations we choose $U_p = 5.5$ eV, which corresponds to a maximum of the vector potential A_{max}=0.9 a.u. Under these conditions the ponderomotive shift exceeds the photon energy in our wavelength range more than twice. Therefore any intensity dependent non-resonant features may not appear in the spectra as regular structures but are completely washed out due to the focal volume integration. We note that the results presented in this section cannot be used for quantitative comparison with the experimental results presented above due to the different intensity regimes. However, common qualitative trends can be observed as we show below.

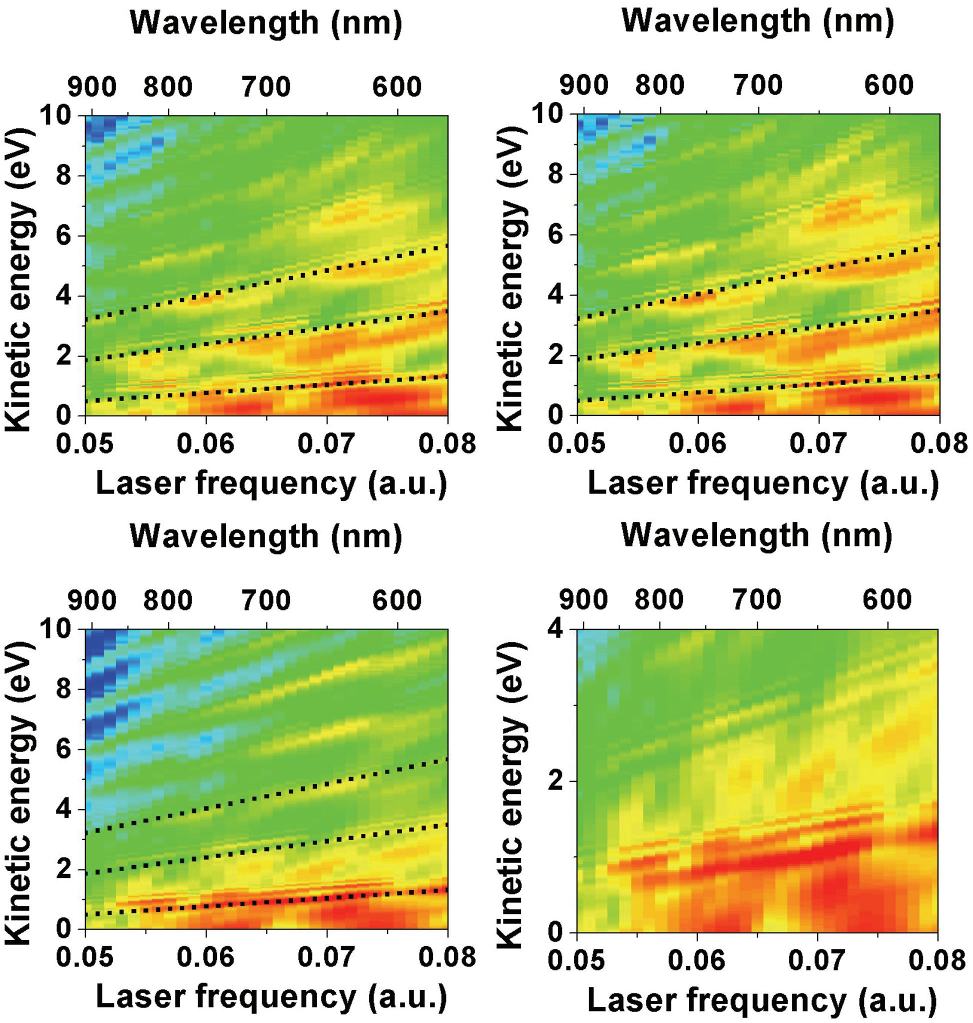

Figure 3-27. Calculations at A_{max}=0.9 a. u.: contour plots showing the frequency dependence of the photoelectron energy spectra integrated over the laser focus volume and over the full angle range (top left); within ±10 degrees along the polarisation axis (top right); beyond ±25 degrees from the polarisation axis (shown for two different energy scales, bottom). In order to enhance visibility of the spectra at the low-frequency edge the spectra are arbitrarily divided by ω^{10}. The colour scales cover two orders of magnitude.

In Figure 3-27 the focal volume averaged photoelectron spectra are presented as a function of the laser frequency. Branches observable in the contour plot can be fitted with slopes corresponding to low-order (n=1, 2, 3 photons) ionisation processes, indicating resonant ionisation. Comparing the contour plots for photoelectron spectra integrated along and away from the laser polarisation axis one can observe qualitative similarity. Both contour plots are dominated by a series of branches with narrow substructures, extrapolating to resonant Rydberg states. For example, the dotted lines in the contour plots extrapolate to a state with the binding energy 0.86 eV. Broad features appearing occasionally between the resonant branches are also present both in the photoelectron spectra integrated along and away from the laser polarisation axis. However, they are much more pronounced along the axis. This is further illustrated in Figure 3-28 presenting vertical cuts through Figure 3-27 at 700 nm.

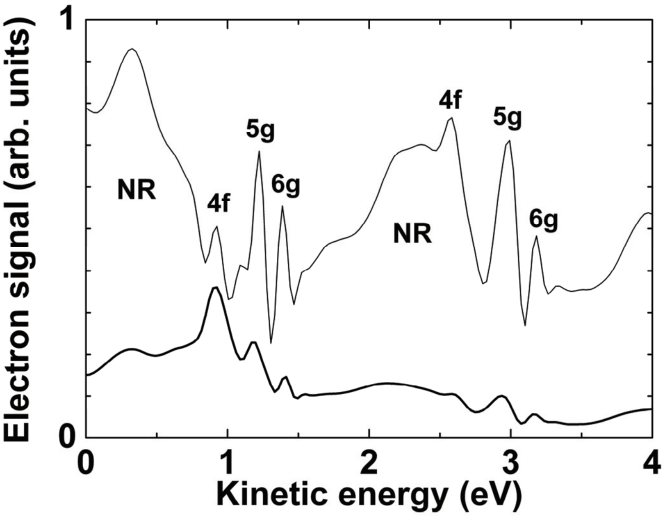

Figure 3-28. Calculated PES integrated beyond ±25 degrees from the polarisation axis (thick line) and within ±10 degrees along the polarisation axis (thin line) at a laser frequency of 0.065 a.u. (700 nm) and for a maximum of the vector potential of A=0.9 a.u.

The curves are plotted with an arbitrary offset and are shown only for the first two ATI orders for clarity of presentation. The photoelectron spectrum integrated away from the laser polarisation axis shows the dominance of narrow sub-structures, whereas in the photoelectron spectrum integrated along the polarisation axis the narrow resonant and broad non-resonant features are of comparable intensity.

In order to identify the resonant Rydberg states in the calculated spectra we plot angle-integrated photoelectron spectra downshifted by the energy of one photon (Figure 3-29). As in the analysis of the experimental spectra we present photoelectron spectra integrated beyond ±25 degrees from the polarisation axis in order to suppress to some extent the influence of the non-resonant contribution. Assignment of the resonant peaks in the electron energy spectra includes comparison of their binding energies to the NIST database and inspection of the corresponding electron angular distributions.

The angular distributions are presented in Figure 3-30 as a function of the laser frequency. In order to make these plots calculated angular-resolved photoelectron spectra were integrated within 0.1 eV around the photoelectron kinetic energies given by Eqn. (4). This way we can monitor the evolution of the angular distribution with the laser frequency for photoelectrons ionised via a particular Rydberg state with binding energy E_b. Figure 3-30 shows angular distributions corresponding to one-photon ionisation from $4l$, $5l$ and $6l$ Rydberg states. The angular distributions are normalised. Using Figure 3-30, the observed wavelength dependence of the photoelectron spectra can now be interpreted.

At a laser frequency of 0.057 a. u. (800 nm) the spectrum contains peaks at $E_b = 0.57$ eV and $E_b = 0.37$ eV corresponding to (13+1)-photon ionisation via Rydberg states of the g-series and a peak at $E_b = 0.84$ eV, which can be attributed to (12+1)-photon ionisation via the 4f state. Accordingly the angular distributions in the middle and the top panels of Figure 3-30 show 5 minima and 4 minima between 0 and 180 degrees at 800 nm. At ω=0.059 a.u. (770 nm) 13-photon resonant population of the g-series requires a ponderomotive shift of 5.6 eV, which is higher than the maximum value in the laser focus. Therefore all the peaks in the spectrum in this case can be attributed to the f-series or h-series ionised in the (12+1)-photon process. Consistent with this assignment the angular distributions in Figure 3-30 contain 4 or 6 minima between 0 and 180 degrees at 770 nm.

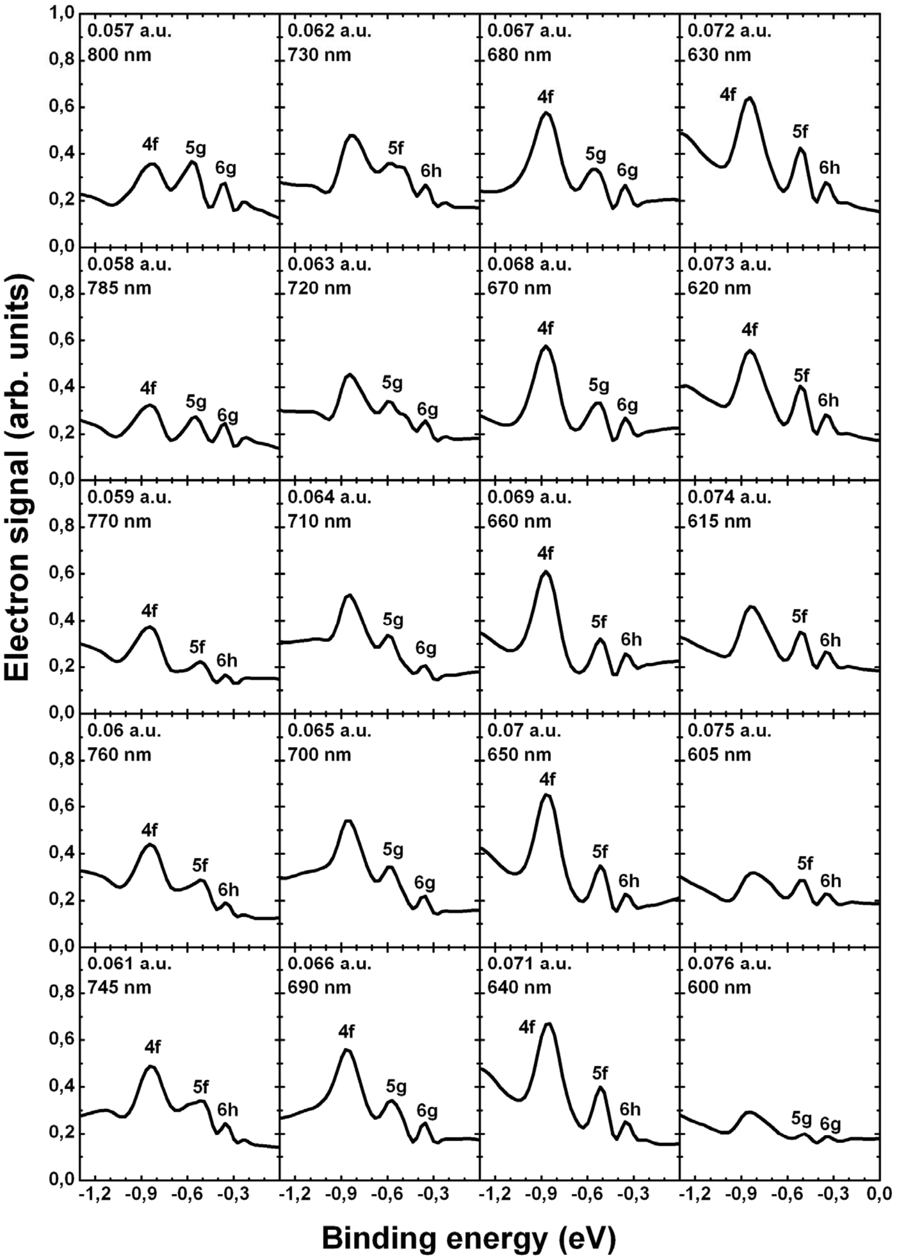

Figure 3-29. Calculated PES at A_{max}=0.9 a.u. integrated beyond ±25 degrees from the polarisation axis and downshifted by the energy of one photon.

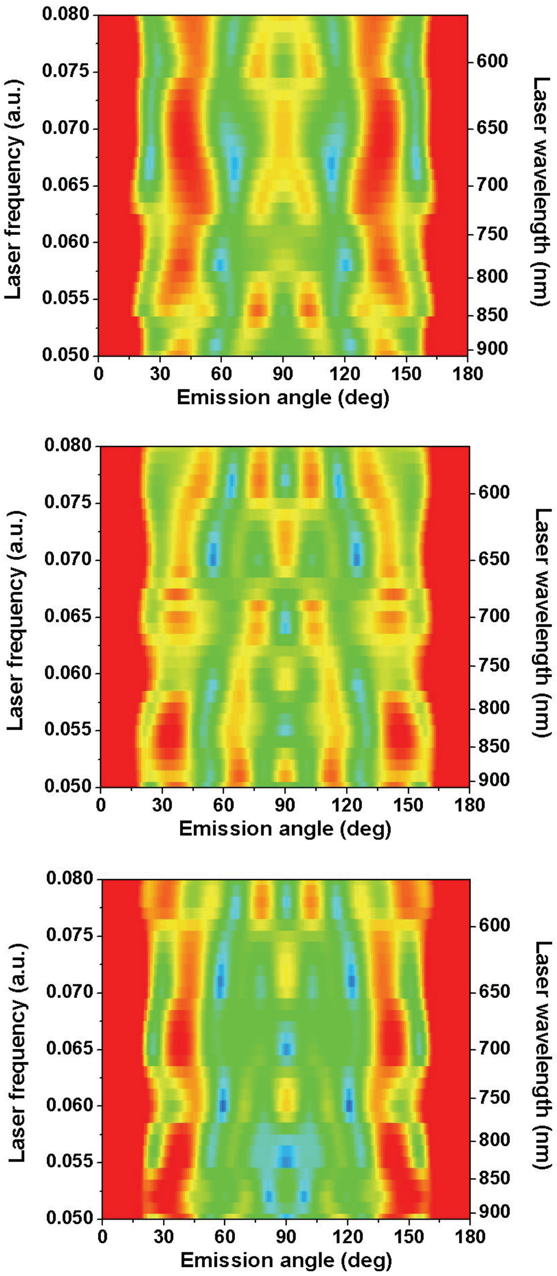

Figure 3-30. Calculations at A=0.9 a. u.: normalised angular distributions calculated at photoelectron kinetic energies resulting from one-photon ionisation via 4*l* (top), 5*l* (middle) and 6*l* (bottom) states. The logarithmic colour scale covers one order of magnitude.

The (12+1)-photon channel remains operative up to ω=0.062 a.u. (730 nm), where the maximum ponderomotive energy falls below the appearance threshold for the 4f resonance via 12-photon resonant ionisation. In this case the peak, which remains visible in the spectrum at E_b = 0.84 eV, could be still attributed to the 4f state involved in 10-photon resonant ionisation. However, the angular distributions calculated at the position of this peak contain 5 minima between 0 and 180 degrees for the frequencies between 0.062 a.u. and 0.065 a.u., which is inconsistent with one-photon ionisation via the f-series. A possible interpretation of this inconsistency will be discussed later in the section.

At 0.063 a.u. (720 nm) the appearance threshold for the 5f resonance via 12-photon ionisation exceeds the maximum ponderomotive energy, leading to the emergence of the g-series ionised in the (11+1)-photon process. Accordingly, the angular distributions corresponding to one-photon ionisation via the 5l and 6l states contain 5 minima (Figure 3-30). This mechanism remains operative for the frequencies up to 0.069 a.u., where a channel switching to the f- and h-series via the 10-photon resonant ionisation occurs. The (10+1)-photon ionisation channel is responsible for the 4f resonance present at the frequencies between 0.066 a.u. and 0.073 a.u. and for the higher states of the f-series present in the photoelectron spectra between 0.069 a.u. and 0.075 a.u. The corresponding angular distributions contain 4 or 6 minima in this frequency range, respectively.

At 0.076 a.u. (600 nm) the spectra are again dominated by the contribution from the g-series involved in (9+1)-photon ionisation, followed by the presence of 5 minima in the angular distributions in Figure 3-30. A broad peak appearing in the spectra between 0.074 a.u. and 0.076 a.u. at E_b = 0.84 eV, which could be possibly assigned to (8+1)-photon ionisation via the 4f state, demonstrates 5 minima in the angular distribution, inconsistent with the f-character of the intermediate resonant state.

In order to explore the probable reasons for this inconsistency we exploit the possibility provided in the TDSE calculations to inspect the population distribution over the bound Rydberg states at the end of the laser pulse. Figure 3-31 shows that for all the frequencies in our range the residual population is mostly preserved in the highest Rydberg states with the binding energy below 1 eV (note the logarithmic vertical scale). Labelling of the peaks has been performed comparing the observed binding energies to the NIST atomic database.

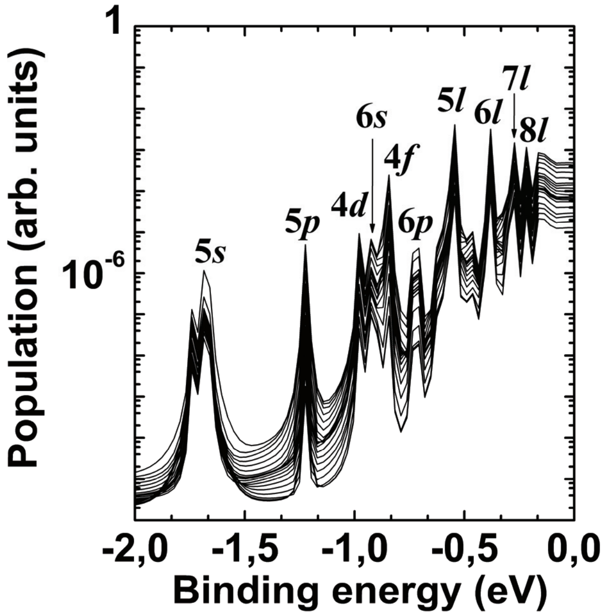

Figure 3-31. Distribution of the residual population in the bound Rydberg states at the end of the laser pulse at various laser frequencies**.**

Assuming that the states contributing to the ionisation process keep significant residual population we can conclude that our assignment of the resonant peaks in Figure 3-29 is consistent with the observation of a significant portion of the residual population in the 4f state and in the states with n≥5 and l≥3. The proximity of the 4f state to the 6s and 4d states on the energy scale in combination with the comparable populations of these states as follows from Figure 3-31 may influence the angular distribution of the 4f resonance observable in the photoelectron spectra. We note that the ambiguity with the assignment of this peak arises when the dominant resonant ionisation channel involves an odd number of photons, which according to the parity selection rules requires involvement of the states with the even orbital angular momentum (s-, d- or g-states). Therefore, one-photon ionisation from the 6s or 4d states leading to the odd number of minima in the photoelectron angular distributions may account for the observation of 5 minima in the angular distribution of the 4f peak in the photoelectron spectra. Note that resonant ionisation via the 4f state involves in this case one less photon compared to the ionisation via 6s or 4d states, therefore ionisation via 4f is relatively suppressed due to the high non-linearity of the multiphoton processes.

To summarise this section, we have observed the evolution of the resonant and non-resonant ionisation channels as a function of the laser wavelength in the range from 800 to 600 nm at constant ponderomotive energy. We have identified a number of channel-switching effects – from 13-photon resonant ionisation at 800 nm to 9-photon resonant ionisation at 600 nm. Assignment of the involved Rydberg states has been confirmed by the inspection of the residual population in the contributing states.

3.6. Argon in the infrared frequency range.

The experimental images presented in this section were obtained by summing the electron yield over more than 5 minutes of acquisition time. Electron momentum spectra were measured at 17 wavelengths in the range from 1200 to 1600 nm with a step of 25 nm. In Figure 3-32 a series of experimental momentum maps are compared to the results of the corresponding volume-integrated TDSE calculations. The values of the maximum of the vector potential in the calculations are chosen for the best matching to the experimental results. Figure 3-32 shows the photoelectron momenta in the range between –1 and 1 a.u., which corresponds to the electron kinetic energies up to 13.6 eV. The low-energy part of the momentum spectra is presented in Figure 3-33, where the electron momenta up to 0.4 a.u are shown, corresponding to the kinetic energy up to around 2 eV. The comparison shows a good agreement between the experimental and theoretical results. All the experimentally observed structures are reproduced in the calculations in high detail.

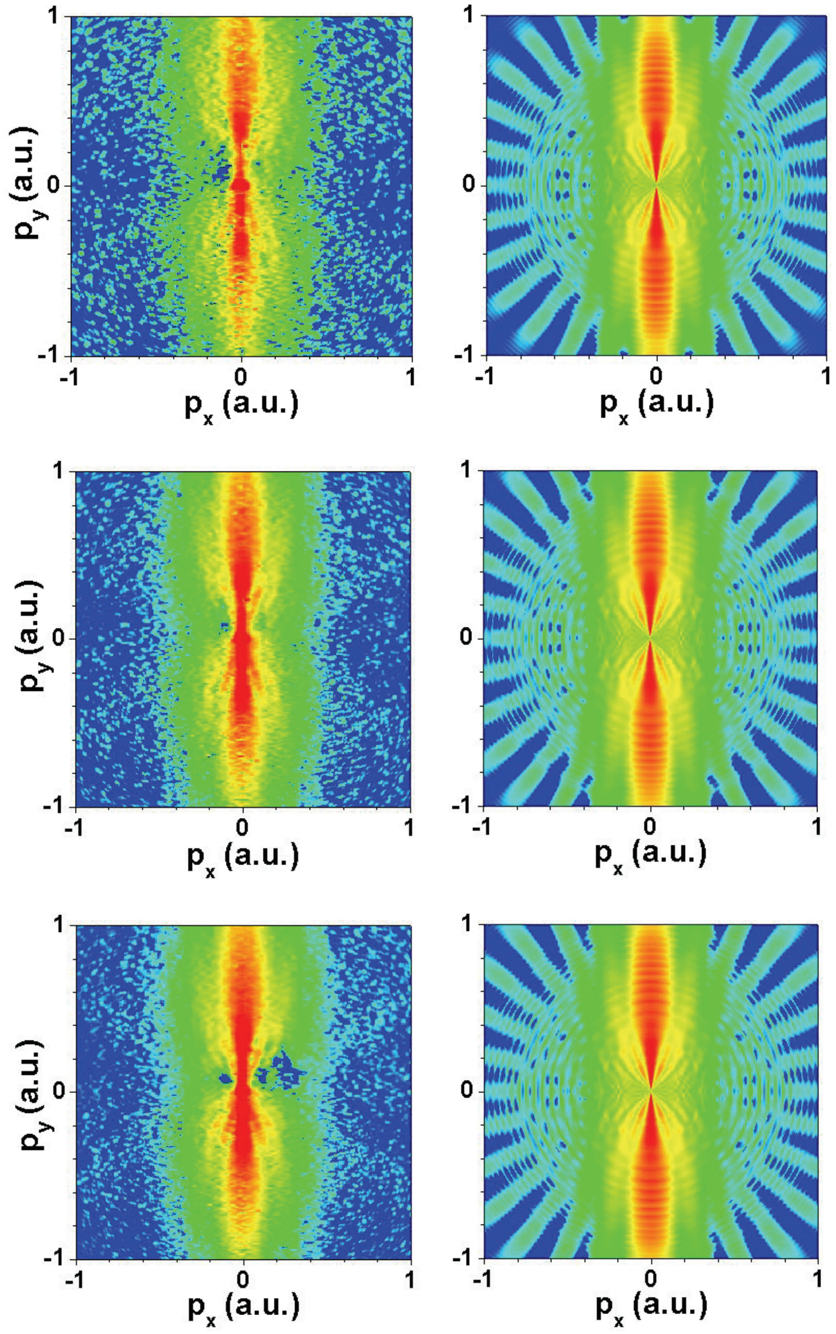
p_y (a.u.)
p_x (a.u.)
-1
0
1

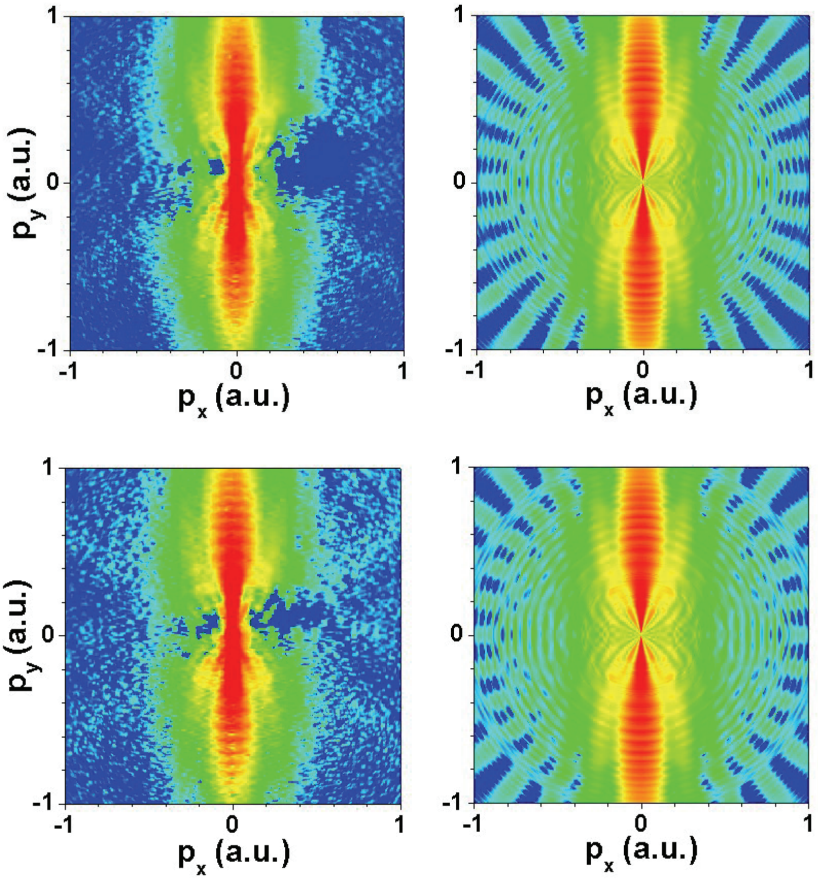

Figure 3-32. Comparison of the experimental (left column) and the calculated (right column) momentum maps of photoelectrons ionised from argon at 1575 nm, A_{max}=1.5 a.u., 6.6×10^{13} W/cm^2; 1475 nm, A_{max}=1.55 a.u., 8.1×10^{13} W/cm^2; 1375 nm, A_{max}=1.5 a.u., 8.6×10^{13} W/cm^2; 1300 nm, A_{max}=1.42 a.u., 8.7×10^{13} W/cm^2; 1200 nm, A_{max}=1.4 a.u., 9.9×10^{13} W/cm^2. The values of the maximum of the vector potential A_{max} in the calculations were chosen for the best matching to the experimental results. The logarithmic colour scales cover four orders of magnitude. Note that the calculated spectra are truncated at high energies due to a finite size of the grid used in the TDSE calculations.

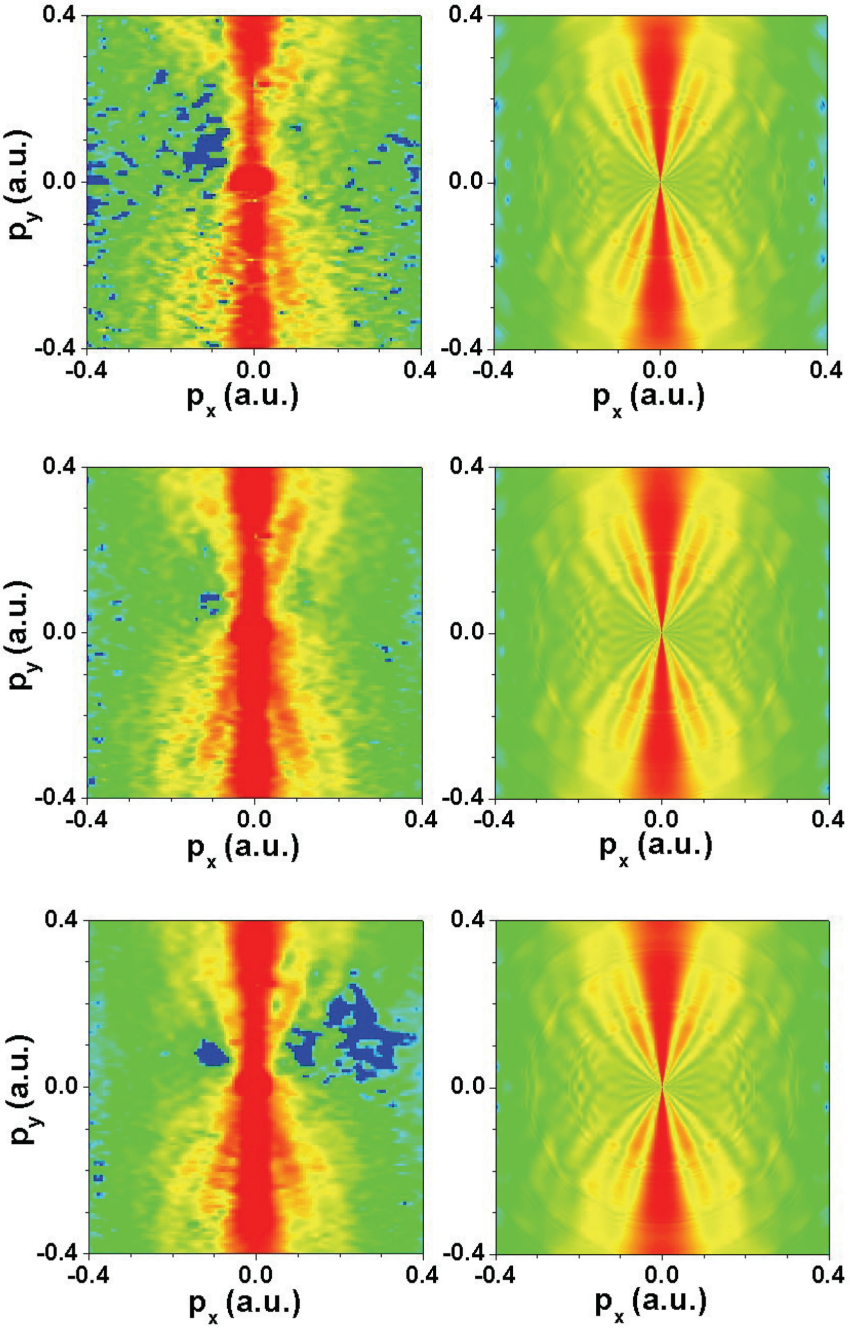
0.4
0.0
-0.4
p_y (a.u.)
-0.4
0.0
0.4
p_x (a.u.)

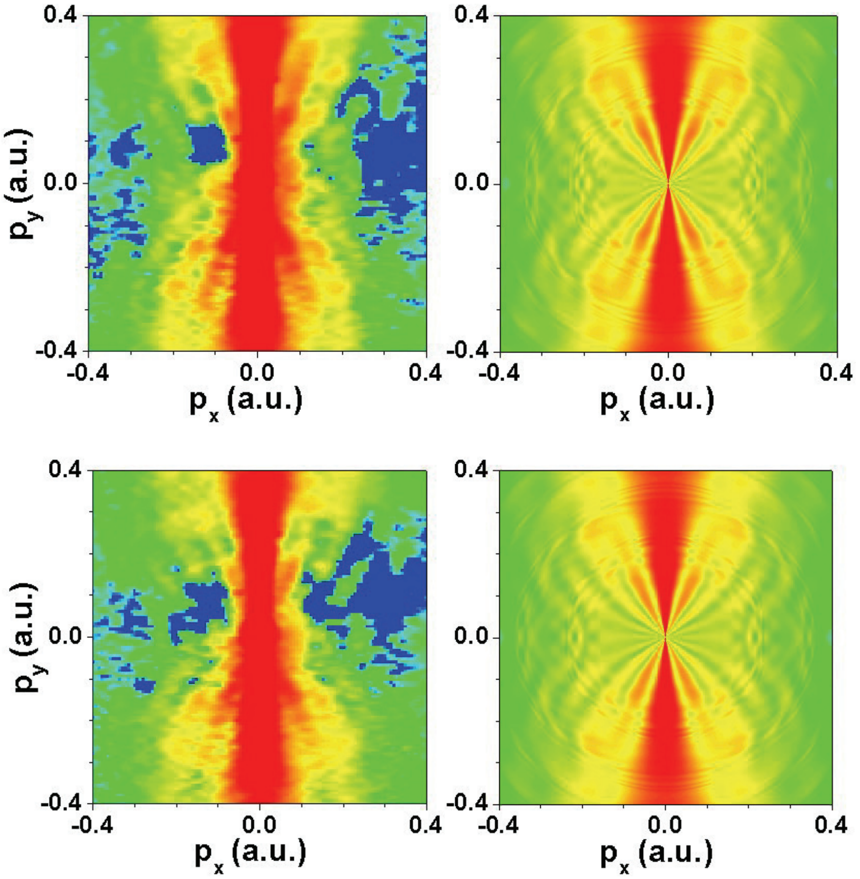

Figure 3-33. The same as in Figure 3-32 zoomed in on the low-energy part (from top to bottom): 1575 nm, A_{max}=1.5 a.u., 6.6×10^{13} W/cm^2; 1475 nm, A_{max}=1.55 a.u., 8.1×10^{13} W/cm^2; 1375 nm, A_{max}=1.5 a.u., 8.6×10^{13} W/cm^2; 1300 nm, A_{max}=1.42 a.u., 8.7×10^{13} W/cm^2; 1200 nm, A_{max}=1.4 a.u., 9.9×10^{13} W/cm^2. The logarithmic colour scales cover four orders of magnitude and are adapted to emphasize the off-axis structures of the momentum spectrum.

Similar to the case of Xenon in the infrared frequency range the contribution of resonance-enhanced ionisation is significantly reduced compared to the visible frequency range and can not be reliably identified in the present data. The photoelectron momentum spectra are dominated by cross-like structures fanning out from the centre of the image, which continue into the high-energy region in the off-axis area of the momentum maps. These contributions will be the subject of the following sections of this chapter.

3.7. Low-energy pattern in Xenon and Argon.

In this section we will concentrate on the pattern observed in our experimental data in the energy region below the first ATI order (typically below 0.5 eV, which corresponds to the part of the electron momentum spectra below 0.2 a.u.). Figure 3-4 shows the evolution of the low-energy pattern with the laser intensity in Xenon at 700 nm. At the lowest intensity one can observe strong contributions at the momentum around 0.18 a.u. (kinetic energy around 0.45 eV) at zero and 45 degrees and weaker features at around 80 degrees away from the laser polarisation axis. Essentially no structure is present at lower energies. Raising the intensity to 4.5×10^{13} W/cm^2 we can see an extension of the observed contributions to lower energies. From here on and up to 8.3×10^{13} W/cm^2 the pattern forming the low-energy region of the momentum maps consists of features fanning out radially from the centre of the image. The angular distribution contains 5 minima between 0 and 180 degrees and remains constant over the intensity range accessible in our experiment.

In order to analyse the evolution of the low-energy pattern with the laser wavelength and intensity, we chose to monitor the number of minima in the angular distributions calculated at a fixed electron kinetic energy of 0.25 eV. Figure 3-34 shows a contour plot where the number of minima between 0 and 180 degrees in the angular distribution (coded in the colour scale) is presented as a function of the laser wavelength and the maximum of the vector potential. The solid black lines are calculated as

$$\omega = (IP+U_p)/n, \qquad (7)$$

where n is the number of photons, required in order to reach the ponderomotively shifted ionisation threshold from the ground state. In Figure 3-34 n=7 for the uppermost curve and n=17 for the lowermost curve. This way the curves highlight the borders for channel closings/openings. The parabolic shape of the curves is related to the quadratic dependence of the ponderomotive shift on the vector potential. A clear correlation between the channel closings/openings and the change in the number of minima in the angular distribution can be concluded from the contour plot.

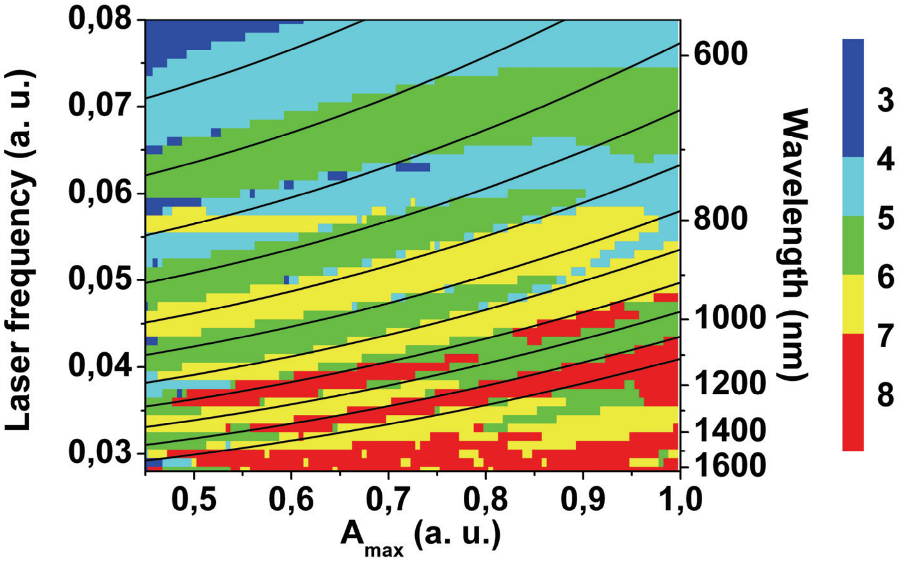

Figure 3-34. Contour plot showing the number of minima between 0 and 180 degrees in the angular distributions in Xenon calculated at the photoelectron kinetic energy 0.25 eV as a function of the laser wavelength and the maximum of the vector potential. The solid black lines show the borders for channel openings/closings.

Comparison of the data in the contour plot to the experimental momentum maps in the visible wavelength range (see Figure 3-9) confirms their quantitative agreement. In the infrared wavelength range the calculated momentum maps contain rich fine structure in the low-energy region, which is not resolvable in the experiment. Therefore comparison for the angular distributions in the low-energy region is not quite reliable here. Thus we will concentrate on the analysis of the low-energy pattern in the visible range.

The available experimental data on the intensity dependence of the low energy pattern (see Figure 3-4) at 700 nm (ω=0.065 a. u.) allows a detailed comparison to the results presented in the contour plot. As observed in the experiment the low-energy pattern demonstrates 5 minima in the photoelectron angular distributions, which remain constant when the maximum of the vector potential is in the range between 0.55 and 0.75 a.u. Accordingly, the contour plot in Figure 3-34 shows 5 minima in this range of parameters. This intensity range is limited by the 8-photon channel closing at A_{max}=0.55 a.u. and 9-photon channel closing at A_{max}=0.75 a.u. Interestingly, both in the experimental and the calculated momentum maps the structure in the low-energy region is very well resolved within the 9-photon channel intensity range and becomes somewhat diffused just beyond that range at A_{max}=0.48 a.u. and A_{max}=0.8 a.u. (see Figure 3-4), where according to the contour plot transitions to the 8-photon and 10-photon channels take place. The appearance of the low-energy photoelectrons at the channel closing was previously observed and described by Schyja et al [54]. In their experiment the observation of the low-energy pattern was related to the 9-photon channel closing at 800 nm as the intensity was increased from 1.2×10^{13} W/cm^2 to 4×10^{13} W/cm^2. The 9-photon channel closing is expected at 3×10^{13} W/cm^2 (A_{max}=0.52 a. u.) at 800 nm. According to the contour plot 6 minima are expected in the angular distribution, which is in full agreement with the angular distribution of the experimental low-energy pattern presented in [54].

As we have observed in our experimental data (Figure 3-4) the low-energy pattern is not sensitive to the channel switching effect. Monitoring the angular distributions of the resonantly ionised photoelectrons we could observe a channel switching from (7+1)-photon resonant ionisation via the g-series to (8+1)-photon resonant ionisation via the f-series at the intensity around 6.4×10^{13} W/cm^2 (A_{max}=0.66 a. u.). However, the low-energy pattern remained unaffected. Therefore, we can conclude that the low-energy pattern is not related to the resonant ionisation mechanism, but rather demonstrates a correlation with channel closing/opening effects related to non-resonant ionisation from the ground state. Remarkably, the correlation between the number of minima in the angular distributions of the low-energy pattern and the conditions for channel closing/opening is much worse at high values of A_{max} for the laser frequencies above 0.06 a.u.

The breakdown of this correlation persists at even higher intensities as can be observed in the TDSE calculations for Argon (Figure 3-35). The solid black lines indicating channel closings/openings in Figure 3-35 are calculated with Eqn.(7), where n=7 for the uppermost curve and n=15 for the lowermost curve. At $A_{max}<1$ a.u. a correlation between the channel closings/openings and the change in the number of minima in the angular distribution can be concluded from the contour plot. At higher intensities however, where $A_{max}>1$ a.u. this correlation breaks down, since the angular distributions become independent of the laser intensity.

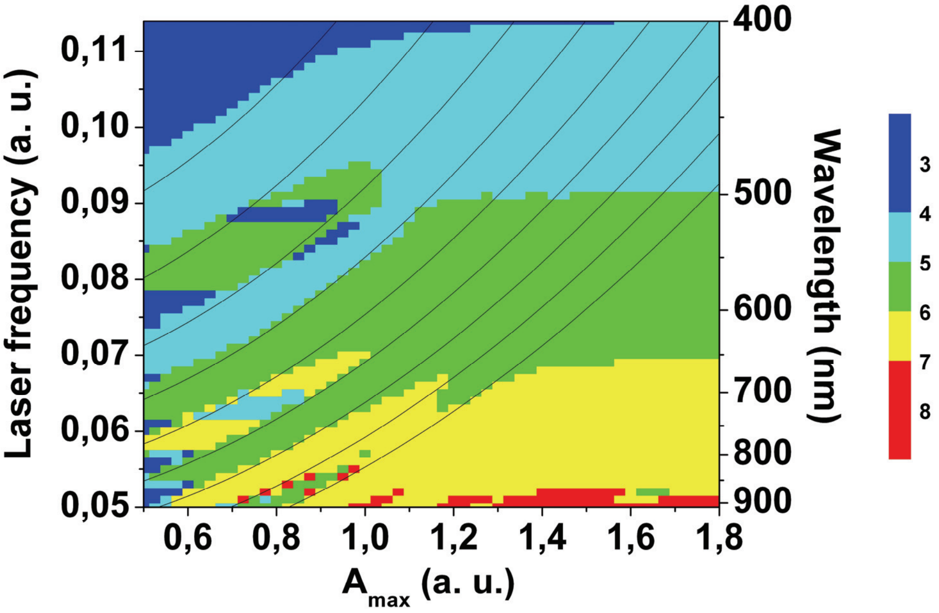

Figure 3-35. Contour plot showing the number of minima between 0 and 180 degrees in the angular distributions in Argon calculated at the photoelectron kinetic energy 0.25 eV as a function of the laser wavelength and the maximum of the vector potential. The solid black lines show the borders for channel openings/closings.

Our results can be compared to the observations made by Maharjan et al [72]. In their experiment the photoelectron momentum spectra measured in Argon at 640 nm at several intensities show almost identical patterns at the intensities of 7.08×10^{14} W/cm^2 and 8.2×10^{14} W/cm^2. The TDSE simulations performed by

Morishita et al [83] explain this observation by taking into account the effect of the ground state population depletion and the laser focus volume effect. They show that an atom can be singly ionised long before the peak intensity is reached in the pulse. Furthermore, inspecting the differential intensity contributions to the low-energy part of the photoelectron spectrum Morishita et al demonstrate that the major contributions to the ionisation yields come from intensities around 2×10^{14} W/cm^2 (A_{max}=1.1 a.u.). Consistent with this explanation, the angular distributions in the low-energy pattern in our calculations remain unchanged at $A_{max}>1$ a.u. (Figure 3-35). We note that the low-energy pattern experimentally observed at 640 nm and at various intensities in [72] and calculated under the same conditions in [83] is also well reproduced in our calculations.

In their theoretical study of the photoelectron momentum spectra in argon, neon, helium and hydrogen Chen et al [82] suggested an empirical rule for the prediction of the dominant angular momentum of the low-energy photoelectrons. According to their model the dominant angular momentum depends only on the number of photons absorbed. Therefore, in agreement with our findings, they conclude that the number of minima in the angular distributions calculated at the low-energy region does not change until the next channel closing. Figure 3-36 shows the dependence of the dominant angular momentum (the number of minima in the angular distribution between 0 and 180 degrees) on the minimum number of photons needed to ionise the atom, where our results for Xenon and Argon are compared to the results of Chen et al for an atom ionised from an initial p state. We can observe a systematic deviation of our results from the results of Chen et al, namely, the dominant angular momentum differs by one unit in the two datasets. A possible reason for the quantitative deviation may be related to the particular value of the kinetic energy of 0.25 eV, where we count the number the minima in the angular distributions of the low-energy pattern, since this number may be different at a slightly higher energy. For example, the angular distribution in the momentum map calculated for Argon at 650 nm, 1.48×10^{14} W/cm^2 in Figure 3-22 shows 5 minima between 0 and 180 degrees at the momentum around 0.1 a.u. and 6 minima at the momentum around 0.2 a.u. In spite of the quantitative disagreement, the general trends are similar. When the number of the absorbed photons increases by one the dominant angular momentum may increase or decrease by one. However, an overall increase of the dominant angular momentum with the raising number of the absorbed photons can be observed.

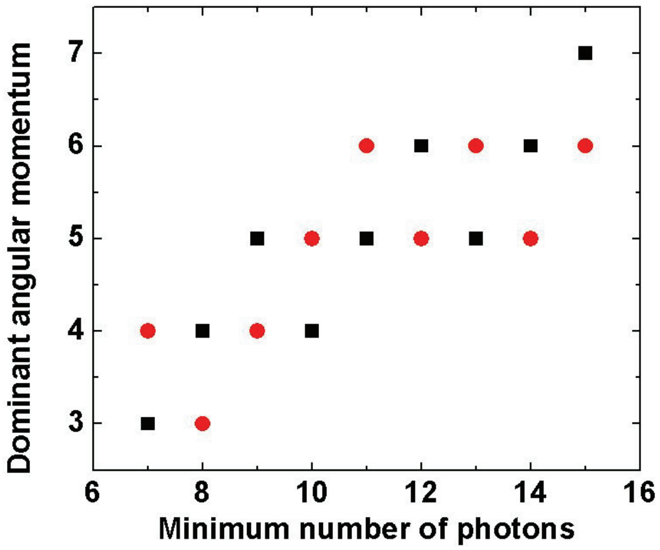

Figure 3-36. Dependence of the dominant angular momentum on the minimum number of photons needed to ionise the atom. Black squares – our calculations, red circles – results of Chen et al [82] for an atom with an initial p orbital.

To summarise our observations: 1) inspection of the low-energy pattern as a function of the laser wavelength and the maximum of the vector potential reveals a correlation between the channel closing/opening effects and the number of minima in the photoelectron angular distributions in the low-energy range; 2) this correlation breaks down at high intensities (A_{max}>0.9 a. u.), where the angular distributions remain unchanged with intensity, which suggests that the pattern originates from the low intensities in the laser focal volume; 3) the low-energy pattern is insensitive to the resonant channel switching effect; 4) when the number of the absorbed photons increases by one the number of minima in the angular distributions may increase or decrease by one; 5) an overall increase of the dominant angular momentum with increasing number of absorbed photons can be observed. In addition, as follows from the TDSE calculations in helium (not presented here), the low-energy pattern does not sensitively depend on the pulse duration and can be observed even with few-cycle pulses. Our observations suggest non-resonant character of the low-energy pattern, however further analysis is required in order to reveal its origin.

3.8. Off-axis pattern in Xenon and Argon.

As we could observe in our experimental data, the resonance-enhanced ionisation is strongly suppressed in the infrared frequency range and the spectra are dominated by intense off-axis patterns (see Figure 3-19 and Figure 3-32). However, the different intensity regimes used in the experiments performed in the visible and in the infrared wavelength ranges prevent us from drawing a conclusion on whether the observed qualitative transition is related to the intensity or the wavelength variation. The excellent agreement between the experimental data and the corresponding results of the TDSE calculations over the whole range of the experimental parameters allows us to exploit the freedom of the parameter choice provided in the TDSE simulations in order to reveal the origin of the experimentally observed effects.

In the following calculations performed for a Xenon atom we vary the laser wavelength between 600 and 1600 nm while keeping a constant value of the maximum of the vector potential, which leads to a constant value of the ponderomotive energy. The evolution of the photoelectron momentum spectra with the laser wavelength is shown in Figure 3-37 for two values of the maximum of the vector potential A_{max}=0.6 a.u. and A_{max}=1 a.u., which correspond to the ponderomotive energy U_p=2.45 eV and U_p=6.8 eV, respectively. Inspection of the momentum spectra corresponding to A_{max}=0.6 a.u. (Figure 3-37 a-f) shows that resonant ionisation forms the dominant contribution in the visible as well as in the infrared wavelength range. A hint of a qualitatively different contribution appears only at λ=1625 nm (Figure 3-37 f), where an off-axis pattern emerges at 25 degrees

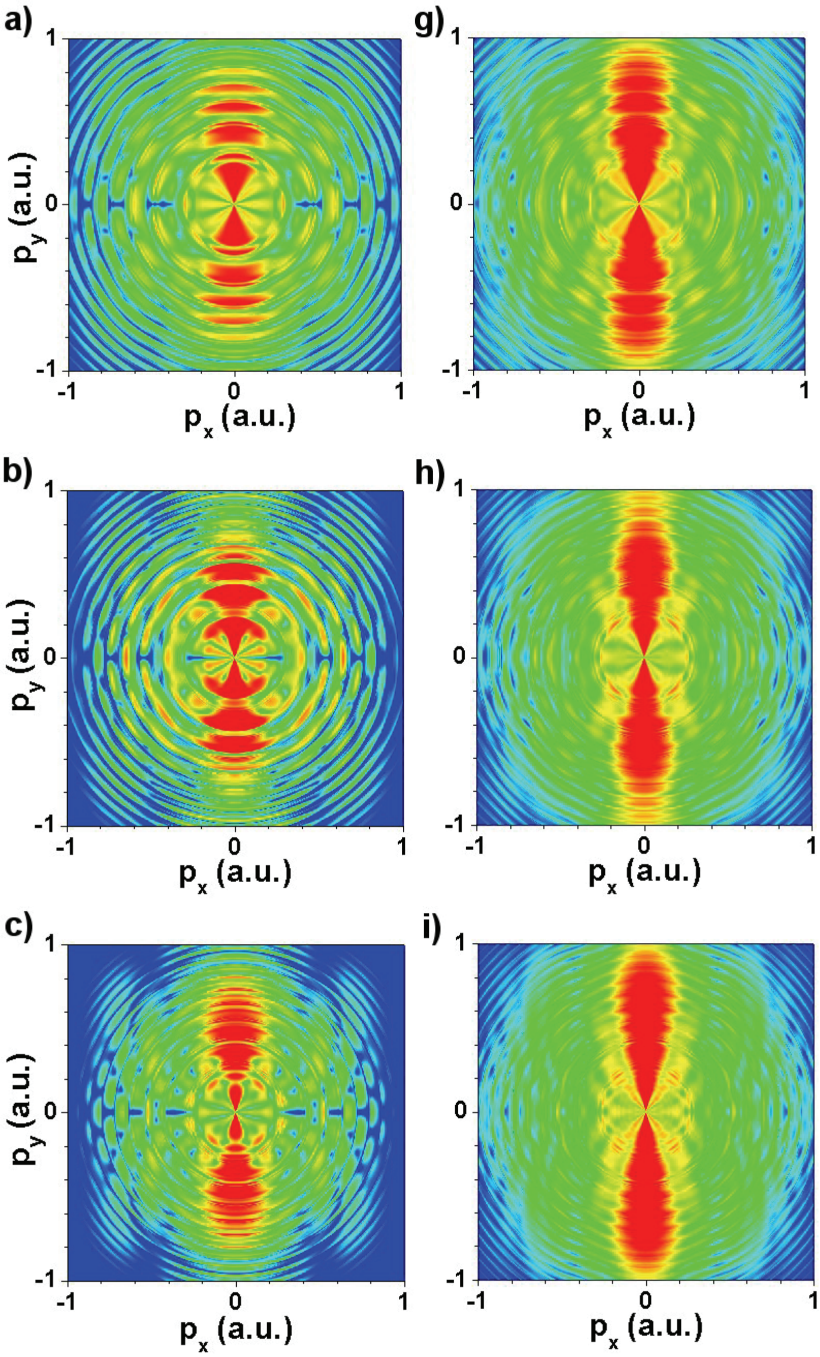
a)
g)
b)
h)
c)
i)
1
0
-1
p_y (a.u.)
-1
0
1
p_x (a.u.)

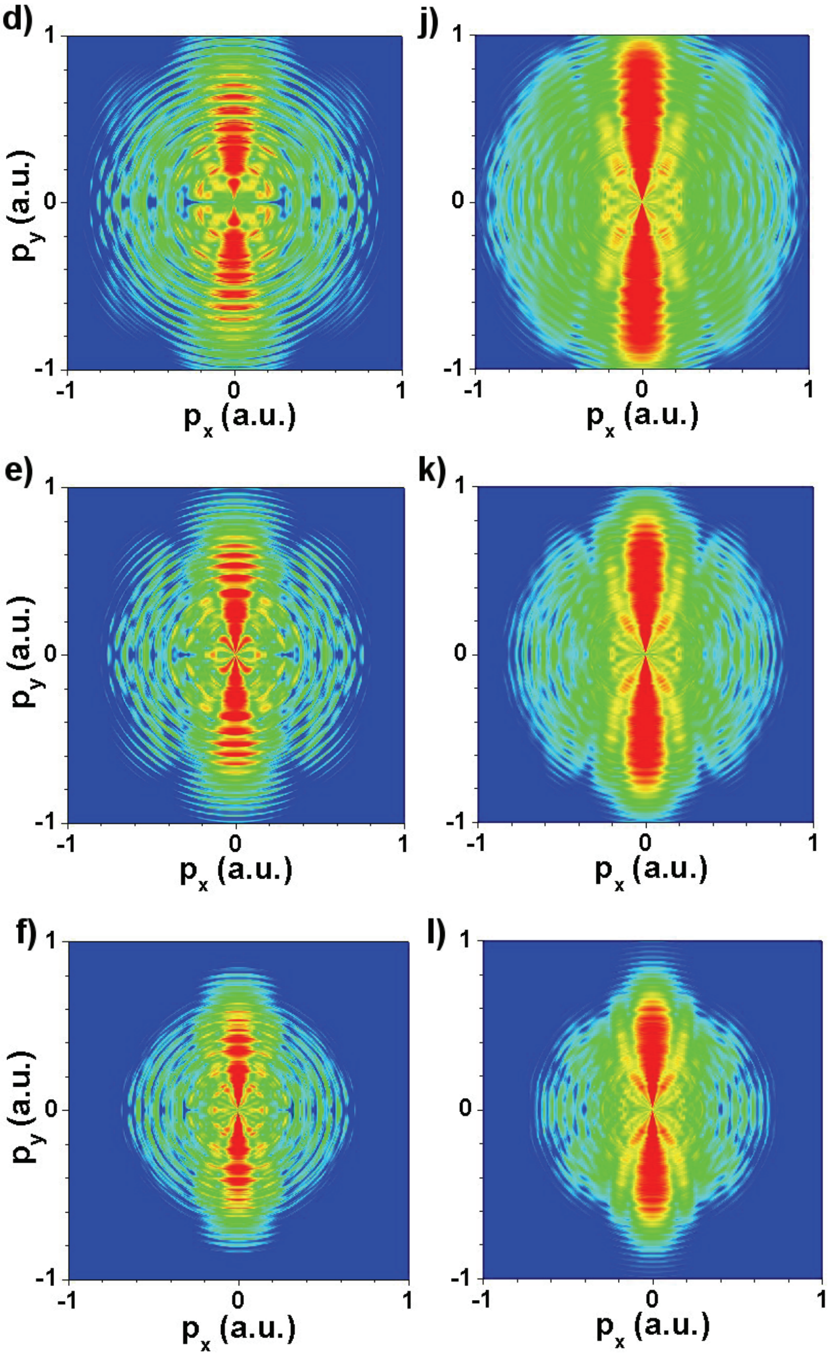

Figure 3-37. Photoelectron momentum spectra for Xenon ionised at A_{max}=0.6 a.u. a) – f) and A_{max}=1 a.u. g) – l) at various wavelengths: a), g) 600 nm, b), h) 700 nm, c), i) 800 nm, d), j) 1010 nm, e), k) 1300 nm, f), l) 1625 nm. The logarithmic colour scales cover three orders of magnitude.

from the polarisation axis in the centre of the momentum map and continues to higher energies approaching the polarisation axis (note the truncation of the momentum spectra at high energy for the long wavelengths due to the use of a finite grid size in the simulation). The evolution of the momentum spectra at higher value of the ponderomotive energy U_p=6.8 eV is presented in Figure 3-37*g-l.* In this case the development of the off-axis pattern begins already at 800 nm and the dominance of the pattern at the expense of the resonant ionisation contribution can be clearly observed at 1300 and 1625 nm (Figure 3-37*k-l*).

Therefore we can conclude that the appearance of the off-axis pattern is not purely determined by the transition from the visible to the infrared wavelength range, but also depends on the intensity regime. The experimental constraints did not allow us to explore the intensity dependence of the photoelectron momentum spectra over a wide range of parameters, keeping our experiment predominantly in the multiphoton regime, where the Keldysh parameter $\gamma>1$. A highly efficient code developed for the TDSE simulations of Argon [87] provides an opportunity to observe the evolution of the photoelectron momentum spectra from the multiphoton to the tunnelling regime.

Figure 3-38 shows a series of momentum maps of electrons ionised from Argon at 640 nm at various laser intensities. The momentum map in Figure 3-38a is calculated for Argon at the intensity of 0.6×10^{14} W/cm^2 (A_{max}=0.6 a.u.). The Keldysh parameter in this case is γ=1.8, corresponding to the multiphoton regime. The spectrum contains a strong contribution from resonant ionisation with a characteristic highly oscillatory angular distribution reflecting the angular momentum of the Rydberg state involved and a radial pattern that can be observed in the low-energy region, where the electron momentum is below 0.2 a.u. As the intensity grows up to 1.8×10^{14} W/cm^2 (Figure 3-38 b) a new contribution develops – a pattern appears at 25 degrees from the polarisation axis in the centre of the momentum maps and continues to the high-energy region. At A_{max}>1 a.u. (Figure 3-38 d-f) the off-axis pattern forms the dominant contribution in the photoelectron

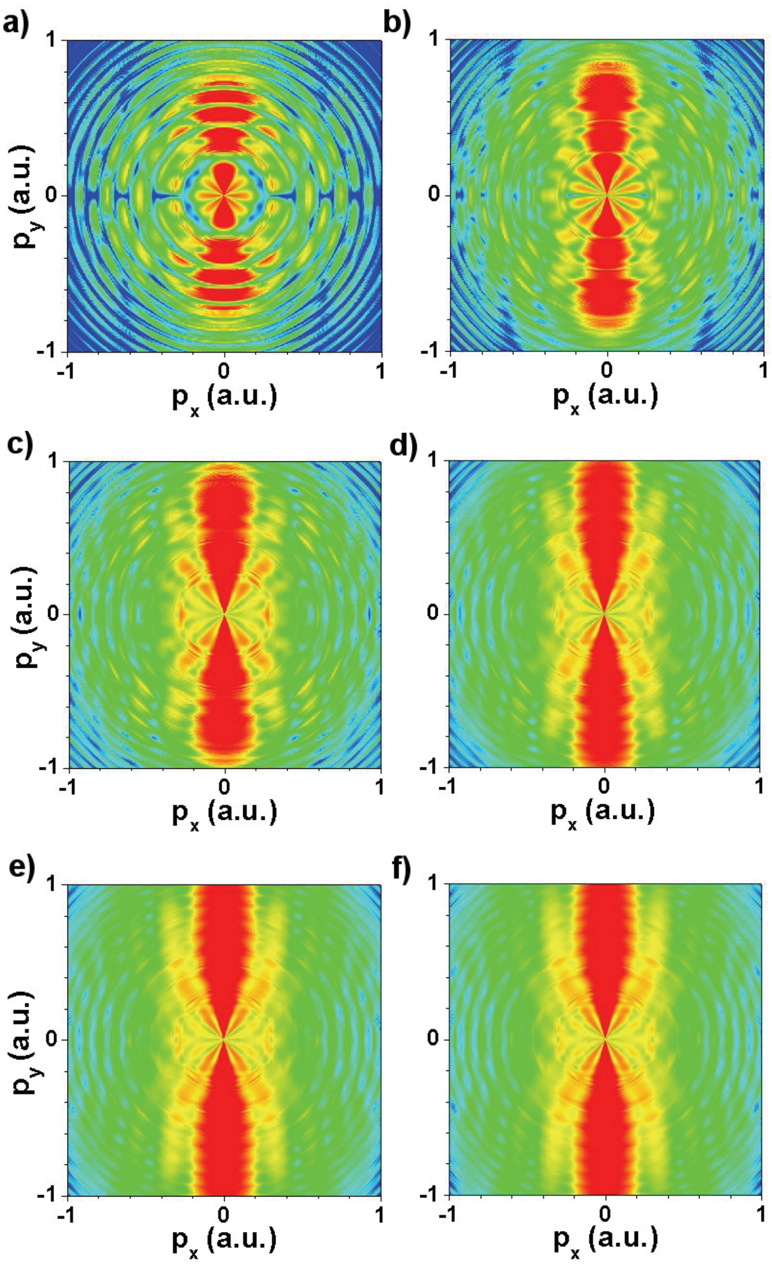

Figure 3-38. Photoelectron momentum spectra in Argon at 640 nm for different intensities: a) A_{max} = 0.6 a.u., I = 0.6×10^{14} W/cm^2, γ=1.8; b) A_{max} = 0.8 a.u., I = 1.1×10^{14} W/cm^2, γ=1.3; c) A_{max} = 1 a.u., I = 1.8×10^{14} W/cm^2, γ=1.1; d) A_{max} = 1.2 a.u., I = 2.5×10^{14} W/cm^2, γ=0.9; e) A_{max} = 1.4 a.u., I = 3.5×10^{14} W/cm^2, γ=0.8; f) A_{max} = 1.6 a.u., I = 4.5×10^{14} W/cm^2, γ=0.7. The logarithmic colour scales cover three orders of magnitude.

momentum spectrum in the high-energy region, where the photoelectron momentum is larger than 0.5 a.u.

The emergence of the off-axis pattern with high laser intensities does not allow us however to attribute the development of this pattern to the transition from the multiphoton to the tunnelling regime, since we have observed qualitatively similar features in Xenon (Figure 3-37) in the infrared wavelength range at γ=0.9 (A_{max}=1 a.u.) and even at γ=1.6 (A_{max}=0.6 a.u.). This way the off-axis pattern can be observed both at the infrared and at the visible wavelengths, in the multiphoton and in the tunnelling regimes. The qualitative transition between the momentum spectra dominated by the contributions from resonant ionisation and the momentum spectra, where the resonant contribution is suppressed in favour of the off-axis pattern, is determined by a combination of the laser parameters, namely the ponderomotive energy and the photon energy. According to our observations this pattern emerges in the photoelectron momentum spectra when the maximum ponderomotive energy exceeds several times the photon energy, an approximate criterion for the appearance of the off-axis pattern can be the following relation: $U_p/\hbar\omega \geq 4$. Requirement of a significant ponderomotive energy relative to the photon energy as well as the apparent independence of the off-axis pattern of the atomic core (qualitatively similar patterns observed in Argon and Xenon) allows to suggest that the origin of the off-axis pattern is related to the interaction of the ionised electrons in the continuum, which may involve interference and re-scattering on the parent core.

This hypothesis is consistent with the recently published results by Chen et al [89], who performed a theoretical analysis of the 2D momentum spectra of high-energy photoelectrons resulting from single ionisation of a Hydrogen atom. In the high-energy region above the classical $2U_p$ cut-off they have established a good agreement between the solutions of TDSE and the results of the second-order strong-field approximation (SFA2), where the re-scattering of the returning electron with the target ion is included. The electron momentum spectra resulting from a few-cycle laser pulse appear to consist of two circular patterns displaced in the opposite directions with respect to each other along the polarisation axis. Using the SFA2 Chen et al conclude that the electrons born and re-scattered on the parent ion in the successive half-cycles are responsible for the appearance of these circular patterns on each side of the origin, and their displacement along the polarisation axis is determined by the value of instantaneous vector potential at the moment of re-scattering.

A series of experimental and theoretical papers followed [90, 91, 92], where photoelectron momentum spectra from various rare gas atoms (Xe, Ar, Kr and Ne) were investigated in the energy region close to the $10U_p$ cut-off. A characteristic high-energy pattern, the so-called back rescattered ridge (BRR), has been identified and interpreted as being due to the electrons rescattering on the parent ion in the backward direction. It has been shown that the electron angular distributions monitored along the BRR provide information on the differential elastic scattering cross-sections of the target atom.

In our experimental data identification of BRR is problematic, since the experimentally accessible energy range typically did not exceed $4U_p$ and even falls below $2U_p$ in the measurements for Argon in the infrared wavelength range. Furthermore, the off-axis pattern can be observed in our experimental data far below the classical $2U_p$ cut-off. This suggests a possibility of contribution from an alternative mechanism, such as interference of the ionised electrons in the continuum without a necessary involvement of rescattering.

A typical structure of an ATI spectrum can be interpreted in the time domain by interference of the electrons generated at several birth times during the laser pulse, separated by one optical cycle. In ATI electrons are launched in the continuum predominantly close to the maxima of the electric field. At this point an analogy can be drawn to the phenomenon of electron interference induced by an attosecond pulse train in the presence of a femtosecond IR pulse [93], where the attosecond pulses coincide with the maxima of the IR field. Constructive interference of electrons, produced by the attosecond pulses separated by one optical cycle, results in a circular pattern in the momentum space displaced along the polarisation axis by the value proportional to the vector potential at the moment of ionisation[2]. The sign of this displacement depends on the whether ionisation occurred close to the maximum or the minimum of the IR field, so that the contributions from electrons produced in consective half-cycles are displaced in the opposite directions along the polarisation axis. The resulting 2D momentum spectrum contains the areas of enhanced electron yield at the intersection points of the two circular interference patterns. A series of such intersection form a pattern qualitatively similar to the off-axis pattern observed in our experimental data. We note that unlike in the experiment on attosecond electron interferometry, where the action of an attosecond pulse can be considered as instantaneous, in the case of ATI there exists a finite time interval around a maximum of the IR electric field, where ionisation rate is non-negligible. This should lead to formation of a more complicated interference pattern in the momentum space. Analysis based on the SFA-type model may help to reveal the origin of the structures observed in our photoelectron momentum spectra.

In conclusion, we have observed the appearance of the off-axis pattern under the conditions when the ponderomotive energy exceeds several times the photon energy. The pattern has been observed both in the infrared and in the visible wavelength range, in the multiphoton and in the tunnelling regimes. Recent attribution of high-energy photoelectron momentum spectra to the electron re-scattering on the parent ion and a qualitative analogy of our results to the effect of electron interference produced by an attosecond pulse train suggest that re-scattering and interference of the ionised electrons in the continuum may be at the origin of the observed pattern.

---

[2] We highlight that displacement of the interference patterns is proportional but not exactly equal to the vector potential at the moment of ionisation. This is in contrast to the BRR pattern, whose displacement along the polarisation axis equals the value of instantaneous vector potential at the moment of re-scattering.

3.9. Conclusion.

In summary, we have presented measurements of 2D photoelectron momentum spectra resulting from ATI of Xenon and Argon in a wide range of wavelengths from 600 to 800 nm and from 1200 to 1600 nm. The collected spectra contain a large amount of information on the ionisation process, where several mechanisms of different origin may be involved. All experimental data have been carefully reproduced in the TDSE calculations.

Analysis of the photoelectron spectra demonstrates the dominance of resonance-enhanced ionisation mechanism in the visible frequency range over a wide range of laser intensities both in the multiphoton and in the tunnelling regimes. The intermediate Rydberg states involved in the ionisation have been assigned based on the information extracted from the energy and angular distributions of the resonantly ionised electrons. A number of consecutive channel-switching effects have been identified as a function of the laser wavelength.

In addition we have observed and investigated two characteristic contributions in the electron momentum spectra, which have attracted a lot of attention within the last two years.

The radial pattern appearing in the momentum maps in the low-energy region within the first ATI ring was earlier observed [72, 79] and attributed to long-range Coulomb interaction of the low-energy electrons with the ionised parent atom [80, 82, 83]. A systematic analysis of our results obtained in TDSE calculations shows that a qualitative variation of this pattern is associated with the occurrence of the channel closing effects. Qualitative invariance of the radial pattern at high intensities suggests that this contribution originates from low intensities present in the focal volume.

The off-axis pattern can be observed in the photoelectron momentum maps practically within the whole detectable energy range above the first ATI order (up to around $4U_p$ in our experiments). Recent analysis of high-energy photoelectron momentum distributions in the energy region around $10U_p$ has attributed the observed features to the scattering of free electrons from the ionic core [89-92]. Preliminary analysis carried out in the frame of the SFA model refers to a significant range of energies, where the off-axis pattern can be observed in our data, and indicates that the origin of the high-energy pattern may be related to the interference of the ionised electrons in the continuum without a necessary involvement of scattering effects [94].

PART III. CLUSTERS IN STRONG LASER FIELDS.

Chapter 4. Bridging atoms and solids.

Strong-field laser interactions with microscopic matter, such as atoms and small molecules, are of fundamental interest. As discussed in Chapter 1 this field has been extensively studied both experimentally and theoretically and continues attracting a lot of attention due to the appearance of new light sources, which provide access to new wavelength regimes. On the other hand, the main interest of applied research lies in the development of optical technology in macroscopic solid-state matter. Clusters are at the interface between microscopic gas phase and the macroscopic condensed matter. This intermediate position makes clusters a unique subject of research, which both offer a wealth of interesting physical phenomena and are invaluable as a model system at the transition from atoms to large and complex structures such as bio-molecules and nanoparticles.

In Chapter 4 we give an overview of the major experimental observations in the physics of clusters interacting with femtosecond infrared (800 nm) lasers, describe briefly the principal theoretical models of laser-cluster interaction for increasing cluster sizes and touch upon the current trends in the research on the interaction of clusters with new light sources in the XUV regime.

4.1. Experimental observations in the infrared regime.

The special transitional nature of clusters determines their highly efficient interaction with intense femtosecond lasers. Having high (near solid) local density, clusters are able to absorb laser energy much more efficiently than isolated atoms. At the same time, in contrast to solids there is practically no dissipation of the deposited energy due to the relatively small (nanometer scale) size of clusters. As a consequence, almost 100% of the laser energy can be coupled into a dense cluster jet [95]. The high efficiency of energy absorption leads to cluster explosion, which can be accompanied by the emission of soft X-ray radiation [39] and the production of highly charged and energetic ions [35], fast electrons [36, 37, 38] and even neutrons [40].

Observation of these remarkable phenomena raised a question of the possible ways to increase the laser-cluster coupling efficiency. In the following studies, a majority of experimental and theoretical work concentrated on the dynamics of laser-cluster interaction under various conditions, since having understood the dynamics of the system one can both ascertain knowledge on the energy absorption mechanism in clusters and obtain a possibility to control the outcome of the laser-cluster interaction through adjustment of laser and cluster parameters.

The efficiency of laser energy deposition into a cluster was commonly probed by varying the laser pulse duration or making use of a pump-probe scheme. Measurements of laser energy absorption in clusters demonstrated that there exists an optimal laser pulse duration (or an optimal pump-probe delay), which depends on the average size of the clusters in the jet [96]. Absorption increased by more than 50% at the optimal conditions as compared to the shortest pulse duration. Note that in this measurement the shortest pulse corresponded to the highest laser peak intensity, since the energy of the laser pulse was kept constant, while the duration increased. Later, Lamour et al [97] observed that the generation of soft X-ray photons from argon and xenon clusters can be maximised at an optimal laser pulse duration. Furthermore, in experiments with a sequence of two laser pulses, kinetic energies of ions produced from cluster explosion were shown to strongly depend on the relative delay between the two pulses [98].

In spite of the valuable insight provided by the pump-probe technique, its applicability is relatively limited, when many parameters play an essential role in the dynamics of a microscopic system. In the case of such a complex system as clusters the full dynamics may turn out to be more complicated than can be revealed in a pump-probe experiment. Rabitz et al [99] discussed a more general case of a stimulus-response experiment, where application of a «learning algorithm» could both perform coherent control over the probed system towards the optimal outcome, as well as reveal the properties of the system itself. In the optimal-control experiment the algorithm iteratively performs thousands of experiments and analyses the results of each of them. Application of a learning algorithm automates and expands the study of the parameter space and may suggest interesting solutions, which were not anticipated in advance of the experiment.

Successful application of learning algorithms in optimal-control experiments was reinforced by the development of femtosecond pulse shaping techniques [100]. A programmable modulation of the complex phase function over the spectrum of a broadband femtosecond laser pulse allows generating diverse complicated time-dependent laser intensity patterns. The produced variety of pulse shapes can be further subjected to a selection procedure under control of a learning algorithm, which drives the evolution of the experiment to the desired outcome.

In Chapter 5 we present an optimal-control experiment on the production of highly charged ions resulting from the interaction of large Xenon clusters with intense femtosecond laser pulses. In the process of optimisation we use adaptive pulse shaping under the control of a genetic algorithm (GA) [101]. We show that the formation of highly charged ions dramatically increases by using a pulse shape consisting of a sequence of two pulses separated by a delay dependent on the average cluster size and the peak laser intensity. Our experimental findings are in line with the results of another optimal-control experiment on optimisation of X-ray emission from argon clusters, where the authors observed the formation of a double-pulse structure as the optimal pulse shape [102].

In summary, a large number of experimental observations indicate that there exists a specific time when the laser field is most efficiently coupled into the cluster. However, interpretation of these observations is not quite straightforward and requires a substantial theoretical effort. The outcome of the multiple laser-cluster interaction modelling attempts indicates that the mechanism of efficient energy coupling is strongly dependent on the parameter regime of the laser-cluster interaction. The following section gives a brief overview of the major models and mechanisms, responsible for the efficient energy coupling from the laser field into a cluster.

4.2. The crucial role of cluster size. Mechanisms of cluster ionisation.

As highlighted in the title of this chapter the key originality of clusters lies in their intermediary role between the microscopic world of atoms and the macroscopic world of solids. The existing techniques allow production of clusters of various sizes in a more or less controllable way. The scalability of clusters makes them an exclusive medium to study the transition from a single-particle to many-particle system, which is equally important for applications as well as for the fundamental research.

In view of possible applications clusters can serve as a model system for bio-molecules and nanoparticles, currently the central subjects of research in natural science. In such systems a size of individual objects in the sample under study is an essential parameter, which determines their interaction with the external laser field. However, the complexity of such many-body multi-electron systems does not yet allow their well-grounded theoretical description. The experimental techniques appropriately addressing the multi-electron response of complex systems to strong external fields also still have to be developed. In the meantime, cluster research, armed with a number of tested experimental methods and theoretical modelling approaches, can provide a valuable insight in the behaviour of a complex gas-phase system subjected to a strong laser field.

In the light of fundamental research clusters offer a unique opportunity to monitor the transition from the behaviour typical for single atoms or molecules to the properties characteristic for condensed matter. For example, a transition from non-crystalline structure to a crystalline lattice was observed at a critical cluster size of several hundred to thousand atoms. Furthermore, the electronic properties of clusters were found to gradually merge into those of macroscopic condensed matter with increasing cluster size. Changes in cluster geometry and electronic structure as a function of cluster size as well as size-dependent changes in inner-shell photoionisation using synchrotron radiation are reviewed in [103]. Recently, photoionisation of medium-sized (up to 10^4 atoms per cluster) xenon clusters with synchrotron radiation has been studied by angle-resolved photoelectron spectroscopy [104]. The photoelectron angular distribution parameter, measured as a function of cluster size, showed distinct differences between the angular distribution of the cluster photoelectrons and those of the isolated atoms. The authors attributed the origin of these differences to elastic photoelectron scattering.

In the interaction of clusters with femtosecond infrared lasers cluster size is the critical parameter, which qualitatively determines the mechanism of laser energy absorption. The existing variety of theoretical models describing femtosecond laser-cluster interaction in the infrared regime can be approximately classified into three groups, corresponding to small (up to the order of N=10 atoms), medium (up to the order of $N=10^4$ atoms) and large clusters [34]. For small clusters maximum energy absorption is governed by the mechanism of enhanced ionisation, which was previously observed in small molecules [105]. It suggests that ionisation is favoured when the average inter-nuclear separation between nearest-neighbour atoms in a cluster reaches a critical value during the cluster expansion [106]. If the average distance between nearest-neighbour atoms in the cluster is defined as

$$r(t) = \frac{1}{N} \sum_{\substack{i=1 \\ i \neq j}}^{N} \min\{|\vec{r}_i - \vec{r}_j|\}, \tag{8}$$

where $\vec{r}_i$ is the position of an ion and N the number of atoms in the cluster, then for small clusters the critical inter-nuclear distance was empirically found to be approximately 1.5 times the equilibrium distance [106].

For medium-sized clusters, numerical simulations [107, 108] revealed that the maximum energy gain is related to collective motion of the quasi-free electrons in a cluster. Electron heating occurs due to dephasing of the motion of the electron cloud with respect to the driving laser field. In the driven and damped harmonic oscillator model of ref. [107] the cycle-averaged energy gain reaches a maximum when the eigenfrequency of the collective electron oscillation becomes equal to the laser frequency or, equivalently, when the phase shift $\Delta\varphi$ between the external driving field and the driven electron cloud becomes equal to $\pi/2$. Note, that for the resonant mechanism to be the reason for the efficient energy absorption in a cluster, the laser pulse must be long enough so that the resonant condition is met before the end of the pulse.

For large clusters several models have been introduced to analyse the cluster explosion. The nanoplasma model for large clusters considers the cluster as a small, spherical and neutral plasma [39]. Early in the interaction, a shielding of the laser field occurs when the electron density rises. A field-enhancement subsequently occurs when – as a result of outer ionisation and cluster expansion - the electron density drops to three times the critical density. Under these conditions the plasma frequency in the cluster becomes equal to the frequency of the laser field. At this point the quasi-free electrons are resonantly heated (the effect known as the Mie plasmon resonance) and a significant enhancement in the outer ionisation is anticipated. The nanoplasma model is qualitatively similar to the model of collective electron oscillations [107]. Specifically, one can show that the predictions of the driven-and-damped oscillator model and the nanoplasma model become equivalent in the limit where the cluster stays charge-neutral (i.e. when outer ionisation is negligible before the resonance occurs).

In addition to the mentioned above *linear* resonant energy absorption mechanisms for medium-sized and large clusters [107, 39], the appearance of *nonlinear* effects in laser-cluster interaction was predicted theoretically [109, 110]. It was shown that nonlinear resonance is responsible for the efficient energy absorption in the cluster if the laser pulse is too short for the linear resonance to occur. The non-linearity of electron motion leads to harmonic generation in laser-irradiated clusters. Enhancement of the third harmonic emission has been demonstrated in simulations [111, 112] and recently observed experimentally [113]. Using a pump-probe scheme Shim et al observed a resonant enhancement of the third harmonic yield from large argon clusters under the condition when the plasma frequency in the cluster becomes equal to three times the laser frequency.

As mentioned earlier, the applicability of the described models strongly depends on the parameter range of the laser-cluster interaction, determined first of all by the cluster size as well as by the laser intensity, pulse duration and pulse shape. Consequently, the mechanism of the efficient energy absorption in clusters varies depending on the interaction regime.

In Chapter 6 we demonstrate that ionisation of medium-sized Xenon clusters can involve two mechanisms in the same cluster expansion. Optimal-control calculations with intense shaped laser pulses show that cluster ionisation can be optimised with a three-pulse sequence, where the optimal pulse shape can be traced back to the mechanisms of enhanced ionisation and resonant driving of collective electron oscillations operative during the second and the third pulses in the sequence, respectively. Our results provide insight into the onset of collective effects with the increasing cluster size and show how the dynamics of clusters in intense laser fields bridges molecular physics and the physics of finite-sized plasmas.

Experimental evidence in favour of one or another model has not been provided so far. Broad cluster size distributions resulting from the process of cluster production and spatial intensity distribution in the laser focus form the major hurdles for the direct quantitative comparison between experiment and theory, since, as we show in Chapter 6, the cluster ionisation dynamics is strongly dependent on the cluster size and the laser pulse intensity. In the final section of Chapter 6 we discuss a possibility for conducting an experiment on size-selected clusters, describe the experimental set-up and the preliminary results leading towards this goal.

4.3. New trends in cluster physics.

A vast majority of experimental studies on interaction of clusters with strong laser fields were performed in the infrared regime. A new parameter regime became available with the advent of the free electron laser at DESY. The first experiments were performed in the vacuum ultra-violet (VUV) regime at laser wavelengths close to 100 nm and intensities of 10^{13} W/cm^2 [114, 115, 116]. Similar to the observations in the infrared regime, complete disintegration of clusters due to Coulomb explosion was observed, followed by the production of highly charged ions [114]. However, the physics of laser-cluster interaction in the VUV regime is completely different. While in the infrared regime the efficient laser energy absorption is predominantly due to collective electron effects, this mechanism is ruled out at short wavelengths, since the resonant frequency is too high to be reached in a cluster within the experimental conditions. Instead, efficient energy extraction from the laser occurs due to multiple scattering events of the quasi-free electrons on the atomic ion cores in the cluster. This mechanism of plasma heating is known as inverse bremsstrahlung. According to theoretical predictions inverse bremsstrahlung is the main energy absorption mechanism in the VUV range for the wavelength down to 62 nm [117, 118, 119, 120, 121].

Recently, the first experiment has been reported [122], where Ar_N clusters (N~100) were irradiated with femtosecond XUV (λ=32.8 nm) pulses from the FLASH free electron laser at intensities up to 5×10^{13} W/cm^2. Comparing the experimental photoelectron spectra to the results of Monte-Carlo simulations the authors have concluded that cluster ionisation in the XUV regime proceeds via a sequence of direct electron emission events (outer ionisation in the conventional terminology) driven by single-photon absorption. Consequently, the formation of plasma in a cluster does not occur until the positive cluster charge is sufficiently high in order trap the quasi-free (inner ionised) electrons. However, no signatures of plasma heating, such as formation of a thermal high-energy tail, could be identified in the photoelectron spectra. This means that the mechanism of inverse bremsstrahlung, efficient in the VUV wavelength range, does not play a significant role at the XUV wavelengths in the experimentally accessible range of intensities. Rather, a multistep ionisation mechanism takes place, where electrons are outer ionised one by one via single-photon absorption leading eventually to the frustration of further cluster ionisation due to the build-up of a large positive space charge.

The development of XFEL at DESY in Germany and at the LCLS in the USA opens a perspective for studies on the dynamics of cluster ionisation and fragmentation in the x-ray range. The first theoretical studies in this regime are reviewed in [34]. Regarded in the light of potential application of XFEL for x-ray diffraction imaging of non-crystalline biological samples, clusters are the most suitable candidates for the initial investigations. In x-ray diffraction imaging experiments a requirement of having a sufficiently intense laser pulse for getting a single-shot diffraction pattern from a sample comes into interplay with its strong ionisation and fragmentation, leading to the loss of structural information of an unperturbed sample [44, 45]. Using clusters as a prototype system of large bio-molecules one can obtain the crucial knowledge about the fragmentation time scale in relation to the intensity and the duration of the x-ray laser pulse employed.

The application of x-ray diffraction imaging technique can be further reinforced by the complementary technology allowing generation of attosecond pulses. Since fragmentation of molecules and clusters typically occurs on a femtosecond time scale, diffraction imaging with attosecond x-ray pulses would allow observation of both the unperturbed structure and dynamics of an excited sample in real time. As an example, a scheme for attosecond resolved probing of the transient cluster charging during its interaction with a strong femtosecond VUV pulse has been recently proposed [43].

Furthermore, attosecond probing of clusters interacting with infrared femtosecond lasers can serve as a critical assessment tool for the present theoretical descriptions. As we discussed earlier in this chapter a mechanism of cluster ionisation and fragmentation is essentially determined by the behaviour of the electrons in the combined Coulomb and laser fields. However, so far our knowledge of the electron dynamics in clusters has to rely on the model assumptions. On the other hand, microscopic simulations of laser-cluster interactions in the infrared regime predict the presence of subcycle electron dynamics within a cluster [41, 42]. Therefore, experimental attosecond probing of clusters would test the applicability of the present theoretical models as well as help revealing time-resolved electron motion in clusters.

Chapter 5. Control of the production of highly charged ions in femtosecond laser-cluster fragmentation.

In Chapter 5 we present the results of optimal-control experiments and calculations on the production of highly charged ions in intense laser field irradiation of large xenon clusters. Experimentally, a spectacular enhancement in the yield of highly charged ions is observed when clusters are subjected to an optimised laser field consisting of a sequence of two pulses, with a time delay that depends on the intensity of the laser and the size of the clusters. Similar results are obtained in optimal-control calculations, which demonstrate that the optimised pulse shape maximises the efficiency of resonant heating.

5.1. Experimental results.

In order to understand the fundamental physical processes that take place during the laser-cluster interaction and to find a way to maximise the yield of products of the cluster explosion in view of possible applications, it is important to ascertain the optimal conditions for energy coupling from the laser field into the cluster. A number of experimental observations have shown possible ways to increase the laser-cluster coupling efficiency through adjustment of laser and cluster parameters such as the laser pulse duration, the average cluster size or the delay between the two pulses in a pump-probe experiment. Making use of optimal-control schemes in combination with laser pulse shaping can provide further insight into the problem of laser-cluster coupling optimisation since in this case the parameter space available for optimisation is significantly broader and the search for the optimum is automated.

Here we present an experimental optimisation of the production of highly charged ions resulting from the interaction of an intense laser field with large xenon clusters using an optimal-control [123] approach. Tailored laser pulses were applied and the production of highly charged ions was used as a diagnostic for the laser-cluster coupling efficiency. We find an optimal pulse shape that reveals resonant heating as predicted by models like the nanoplasma model, and furthermore report optimal-control calculations that lead to optimised pulse shapes similar to those seen in the experiment.

In the experiment the rare gas clusters were produced in a differentially pumped vacuum system. The gas was expanded into the vacuum through a ϕ=500-μm pulsed nozzle (50 Hz repetition rate). Using the Hagena parameter [124] the average number of atoms in the clusters is estimated to be $\langle N \rangle \approx 1.6\times10^4$ with a standard supersonic nozzle and $\langle N \rangle \approx 2\times10^6$ with a conical nozzle, using 6 bars of xenon backing pressure. The high-intensity laser was a chirped-pulse amplification (CPA) system. After compression 100 fs, 230-μJ pulses were produced, at a repetition rate of 1kHz, and with a central wavelength of 800 nm. The laser beam was focused onto the cluster beam with a 150-mm focal-length lens (f/D=7.5). The intensity at the cluster beam was estimated to be 5×10^{15} W/cm^2. Before amplification the pulses were sent through a 4f arrangement with a Spatial Light Modulator (SLM, Jenoptik, SLM-S 640/12) in the Fourier plane (see Figure 5-1). The SLM consists of 640 independent strips, to which voltages were applied (with 12-bit resolution) in order to apply the phase shifts $\phi(\omega)$ to the different spectral components of the pulse. Different phase patterns lead to different temporal pulse shapes, according to the Fourier transform relation $E(t)=\int E(\omega)e^{i\omega t}d\omega$, where $E(\omega)=|E(\omega)|e^{i\varphi(\omega)}$ is the laser field in the frequency domain and $\phi(\omega)$ the phase applied with the SLM. The spectral range covered by the SLM was centred at 800 nm and extended over 100 nm. The parameters describing the laser field were varied in an automated way, in order to find the optimum pulse shape for the production of highly charged ions.

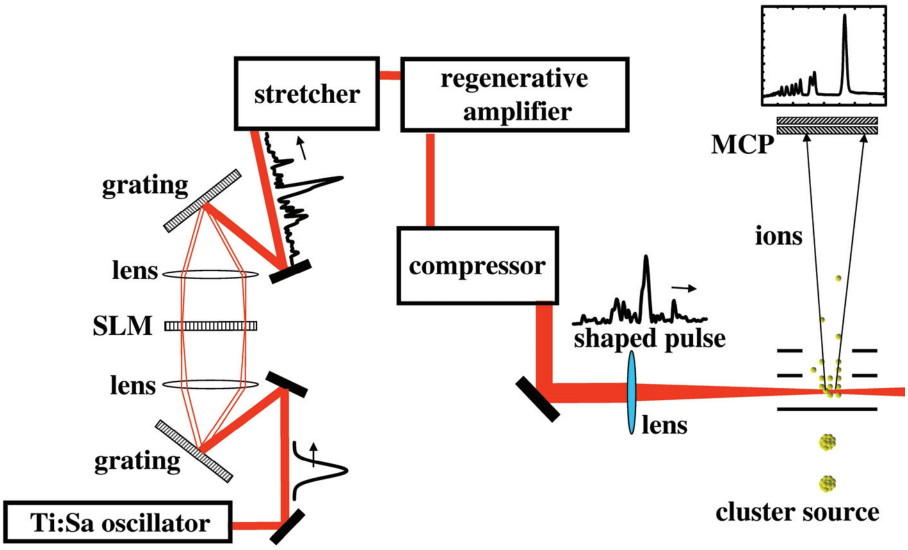

Figure 5-1. Shematic of the experimental set-up. An output pulse of a Ti-Sa oscillator passes through a pulse shaper, which consists of a Spatial Light Modulator placed in the Fourier plane of a 4f arrangement. Upon amplification and compression the shaped laser pulse is focused onto a cluster jet in the velocity-map imaging spectrometer, used as a time-of-flight spectrometer. Ions created in the interaction region are accelerated in a dc electric field towards a dual MCP.

Ions were detected using a velocity-map imaging set-up [125] that was used as a time-of-flight (TOF) spectrometer without making use of its imaging capabilities. The ions were accelerated towards a dual microchannel plate (MCP) and the ratio between the repeller and extractor electrode voltages (5.21 kV and 4.31 kV, respectively) were adjusted in order to have as good a TOF resolution as possible. The TOF traces were recorded with a 0.5 GHz oscilloscope. We note that the experimental arrangement allowed photons and fast electrons to be observed as well.

Figure 5-2 (a) gives a typical TOF trace that was obtained when xenon clusters with an average size of $\langle N \rangle \approx 1.6 \times 10^4$ were irradiated with a nearly Fourier transform limited (FTL) 100 fs, 230 μJ pulse. All the peaks are quite broad due to the kinetic energy release in the laser-cluster interaction. For several charge states, ions emitted towards and away from the detector can be distinguished. No dependence of the shape of these peaks on the laser polarisation axis was observed, which indicates that the ions were emitted isotropically. The forward and backward peaks are seen separately since due to their kinetic energy not all ions were collected on the detector and ions with a very large transverse velocity miss the detector. The maximum charge state observed using the FTL pulse was Xe^{11+}. Extremely efficient coupling of the laser field to the cluster is responsible for these highly charged states. When no clusters were present, the maximum observed charged state was Xe^{4+} under the same experimental laser conditions.

The optimal-control experiment consisted of enhancing the production of Xe^{n+}, with n>11, with the help of a Simple Genetic Algorithm (SGA) [101]. Briefly, the SGA started with a random population of 50 individuals, with each individual representing a string of bits encoding the voltages on the SLM. In the present experiment the voltages applied across the SLM were varied in blocks of 5 pixels over a range of 400 pixels, so the search space consisted of 80 parameters. This way, every individual corresponded to a specific phase pattern applied across the spectrum, with a corresponding different temporal pulse shape. All the individuals were assigned a fitness value by integrating the part of the TOF trace corresponding to the formation of highly charged states (n>11) with a boxcar integrator. These individuals then underwent selection, according to their fitness.

The major concepts used in genetic algorithms can be traced back to the theory of biological evolution. The concept of elitism suggests that the individuals

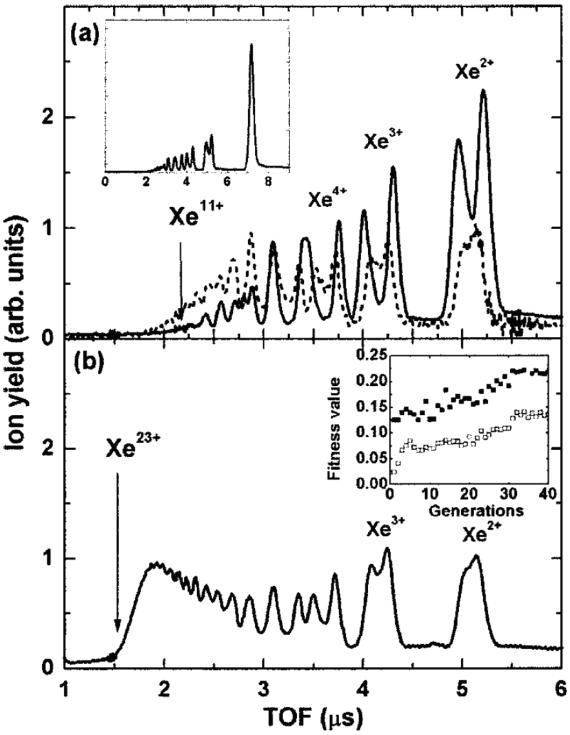

Figure 5-2. TOF traces for the interaction of xenon $<N>\approx 1.6\times10^4$ clusters (a) with a FTL 100 fs, 800 nm, 10^{15} W cm^{-2} laser pulse (N.B. The inset shows the complete TOF trace) (solid line) and the optimal linearly chirped laser pulse (dashed line) for forming highly charged ions derived from the former (500 fs long); (b) with the optimum pulse shape obtained by means of an 80-parameter unrestricted optimisation. As shown in Figure 5-3(a) the optimum pulse consists of a sequence of two 120 fs pulses, separated by 500 fs. The inset in (b) shows the evolution of the fitness value for the 80-parameter optimisation (full squares, maximum fitness; open squares, average fitness).

who have higher ‘fitness’ will have a higher chance of breeding and passing their genetic information to the succeeding generations. The concept of crossover implies that a child’s genetic material is a mixture of his parents. Finally, the concept of mutation means that genetic material is occasionally corrupted which provides to some extent genetic diversity in the population and helps avoiding a convergence of the algorithm to a local optimum. We used elitism for the 4 best individuals, uniform crossover ($P_c = 60\%$) and mutation ($P_m = 1\%$) to create a new generation, again consisting of 50 individuals, which were in turn experimentally tested [101]. As shown in the inset in Figure 5-2 b the average fitness increased until the convergence was achieved. The solid curve in Figure 5-2 b shows the result of the optimisation after 40 generations. A dramatic change in the charge-state distribution is observed, with a strong decrease in the lowest charge-states, and an increase in the highest charge-states up to 23+, compared to 11+ before the optimisation. One should note that Xe^{10+} and Xe^{11+} are of particular importance for the generation of soft x-rays in the 11-13.5 nm range [126], where EUV lithography is developed.

One could argue that the optimised fitness involves not only the yield of highly charged ions but also the detection efficiency of these ions (since by lowering their kinetic energy the detection efficiency of the ions may be increased). We note however, that the current optimisation also led to an increase in the total electron yield, whereas the ion yield for the lower charge-states substantially decreased (even though the kinetic energy for these charge-states decreased). Also based on earlier work using linearly chirped laser pulses, one might suspect that the optimisation simply consisted of applying an appropriate chirp to the pulse [96]. However the results shown in Figure 5-2 b demonstrate substantially higher charge-states than the best (500 fs long) linearly chirped laser pulse that we could apply [the dashed line in Figure 5-2 a].

To interpret the experimental results, the pulse shape leading to the optimal result was determined. The autocorrelation of the optimum pulse shape shown in Figure 5-3(a), suggests that this pulse consists of a sequence of two ~120 fs pulses with a similar amplitude and separated in time by ~500 fs. Evidently there exists a specific time after triggering the cluster explosion when the coupling between the laser field and the cluster is maximal, and the optimisation determines the optimal value of this time delay. We note that the peak intensity in the optimal pulse is only half of the peak intensity of the FTL pulse. Nevertheless, the production of highly charged atoms is strongly enhanced. It should be emphasized that the fact that the optimum pulse shape consists of a sequence of two pulses does not mean that the optimal-control experiment performed here was simply a pump-probe experiment. The experiment was an 80 parameter unbiased optimisation proving that the formation of a sequence of two pulses and the existence of a specific delay between these two pulses are essential features of the optimisation of laser-cluster interactions; very different pulse shapes could have been found if the physics of the problem required this.

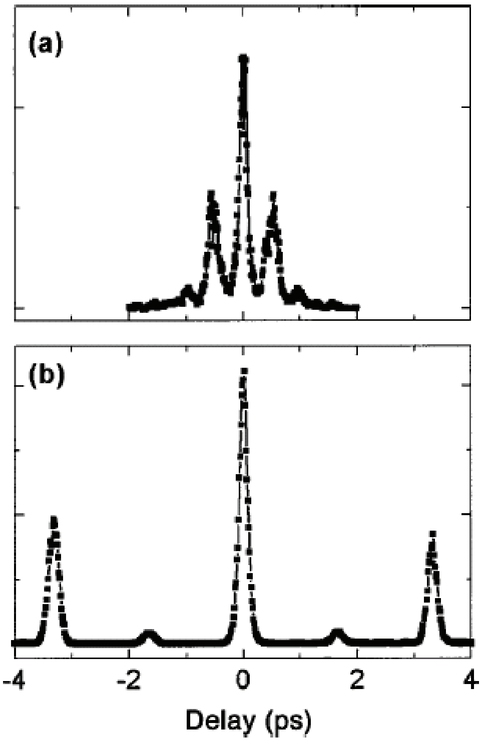

Figure 5-3. Autocorrelation traces for pulses obtained by (a) an unrestricted 80-parameter optimisation for $<N>\approx 1.6\times 10^4$ [as in Figure 5-2 (b)], and (b) a restricted 3-parameter optimisation with larger $<N>\approx 2.0\times 10^6$ clusters. In the latter case the 3 parameters in the optimisation were the amplitude and period of an oscillatory phase pattern applied to the LCD mask (leading to the formation of a pulse train) and the linear chirp of the pulse.

5.2. Interpretation of the experimental results.

In order to elucidate the origin of the optimum pulse shape found in the experiment, a numerical pulse shaping experiment was performed on a computer, using a molecular dynamics simulation on the laser-cluster interaction [127]. Calculations were performed where small Xenon clusters (up to 5056 atoms) interacted with a tailored laser field (derived from a 30 fs 3.5×10^{14}W/cm^2 Fourier-limited pulse). In these calculations atoms in the cluster ionised as a result of both field ionisation and collisional ionisation and trajectories of the ions and electrons were calculated from Newton’s equations. The average ionic charge-state at the end of the laser-cluster interaction was used as fitness parameter for a genetic algorithm optimisation, which in this case employed a population of 30 individuals and used 40 parameters to represent the phase function of the laser pulse. In Figure 5-4(a) the optimised result is shown for Xe clusters consisting of 108 atoms/cluster. Similar to the experimental results, the optimum pulse consists of a pulse sequence where for this combination of cluster size and laser intensity the delay between the first and second pulse is equal to 146 fs. We note that the third pulse in Figure 5-4(a) does not contribute to the ionisation of the cluster.

Having observed that a two-pulse sequence optimises the production of highly charged ions experimentally using clusters of 1.6×10^4 atoms and numerically in calculations for clusters consisting of 108 atoms, the ionisation dynamics of clusters with N=64–5056 were numerically evaluated for two-pulse sequences with a variable time delay between the two pulses. The results of these calculations are shown in Figure 5-4(b). For every cluster size an optimum delay between the two pulses was found that produced a higher average charge-state than the FTL pulse. By monitoring the electron density in the cluster as a function of time delay, we could determine that this optimum corresponds to the time delay where the second pulse interacts with the cluster around the time that the electron density n_e dropped to $3n_{\text{crit}}$. In other words, the simulations provide considerable evidence for the notion that the optimal pulse shape found in our experimental studies using 1.6×10^4

atoms/cluster and in our numerical studies using several hundred atoms/cluster reflects a resonance enhancement as suggested by a nanoplasma description of the

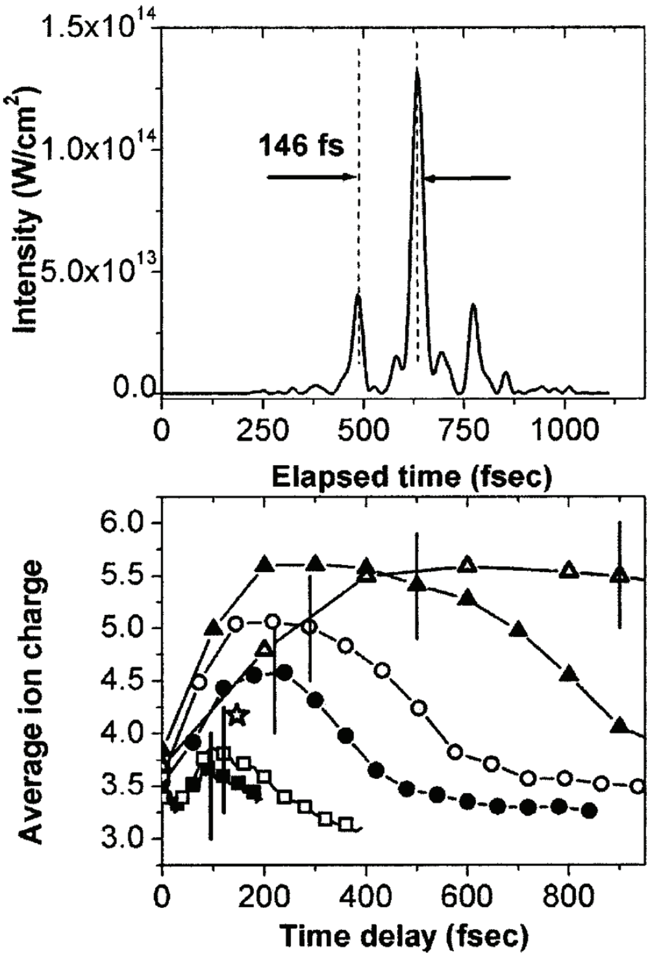

Figure 5-4 (a) Optimal pulse shape found in an optimal-control calculation for the ionisation of Xe_{108} by a tailored laser pulse derived from a 30 fs, 3.5×10^{14} W/cm^2 laser pulse. Efficient ionisation is achieved by a sequence of two pulses separated by 146 fs; (b) average ionic charge-state resulting from the interaction of a sequence of two 30 fs, 1.75×10^{14} W/cm^2 Gaussian pulses with Xe_n clusters, where n=64 (solid squares), 108 (open squares), 302 (solid circles), 588 (open circles), 1524 (solid triangles), and 5056 (open triangles). The result of the optimal-control calculation given in (a) is shown as a star. The vertical lines indicate the times where the electron density n_e of the plasma generated by the first pulse falls to $3n_{crit}$. Very good agreement is observed between this time delay and the optimum delay between the two pulses.

laser-cluster dynamics. In the two-pulse sequence, the first pulse initiates the plasma formation and the expansion of the cluster. However, during the excitation the electron density rapidly rises above $3n_{crit}$, reducing the efficiency of the energy deposition. Maximum energy deposition is achieved when further excitation is delayed until the electron density becomes low enough, which in the experiment occurs after about 500 fs. In further support of this interpretation, we have experimentally observed that the optimum time delay for the formation of highly charged ions depends on the laser intensity and the cluster expansion conditions. Upon increasing the laser intensity a shortening of the optimum time delay was observed, consistent with a more rapid cluster expansion. Conversely, using a conical nozzle, clusters with 100 times more xenon atoms could be produced and – consistent with the slower expansion of these larger clusters – an optimal delay of 3.3 ps was found [see the resulting autocorrelation trace in Figure 5-3b]. Similar cluster-size effects have been observed in experiments where cluster explosions were investigated by means of detection of laser absorption [96], ion energies [128] and transient polarisability [129]. The existence of an optimal time delay for the energy deposition is also consistent with experiments on the production of energetic electrons [37, 38] using a variable-pulse-length laser and pump-probe experiments on the production of multicharged [130] and energetic ions [98].

The experimental results presented in this Chapter received a strong confirmation in later optimal-control pulse-shaping experiments that optimise X-ray emission from Argon clusters. A significant enhancement of the X-ray yield was observed with the double-pulse structure, which was found to be the optimal pulse shape [102]. This result was similarly interpreted in the frame of the nanoplasma model. Shortly upon the completion of our work new models of cluster ionisation were reported [107, 108], which eliminated the inherent assumptions of the nanoplasma model, such as a uniform electron density and the overall plasma neutrality within the cluster, and thus might be more appropriate for interpretation of our numerical simulations of small to medium-sized clusters. However, the predictions of resonant ionisation enhancement remain qualitatively valid and the application of the nanoplasma model is likely justified for the large cluster sizes considered in our experiments.

5.3. Conclusion

In conclusion, we have presented optimal-control experiments and calculations that provide strong support for the resonance enhancement suggested by the nanoplasma model of cluster ionisation. We have shown both experimentally and numerically that there exists a specific time when the laser field is most efficiently coupled to the electrons in the cluster, and have observed in our numerical simulations that the optimum delay of the second laser pulse approximately corresponds to the time where the electron density n_e in the cluster has fallen to $3n_{\text{crit}}$. The fact that we have two well-separated pulses indicates that in the time interval between the two pulses any available laser field interacts poorly with the cluster, since the density of free electrons leads to a screening of the laser field. A detailed analysis of the mechanisms of cluster ionisation and applicability of the models under various conditions is provided in the following chapter.

Chapter 6. Optimal control of femtosecond laser-cluster interactions.

Femtosecond laser-cluster interactions have been analysed in terms of a number of models, each of them predicting a single decisive moment during the laser-cluster interaction when the conditions for laser energy absorption are most favourable. As a result, the search for optimal laser energy deposition is usually limited to variation of a single time variable, which is either the laser pulse duration or the delay between a pair of pulses. While the optimal conditions found in this way provide insight into the laser-cluster interaction, the inherent restrictions in this approach stand in the way of acquiring a more complete physical picture.

In Chapter 6 we report optimal-control calculations of the interaction of xenon clusters with intense shaped laser pulses where a GA controls 40 independent degrees of freedom in the laser pulse shape. The increased flexibility in the available pulse shapes in combination with the strength of evolutionary optimisation leads to the determination of an optimum pulse shape for ionisation of the cluster. To interpret the origin of the optimum pulse shape, calculations are also presented for the interaction of small to medium-size clusters (N=108 – 5056 atoms per cluster) with sequences of pulses with variable time delays and intensities. Our calculations show the influence of *several* mechanisms in the optimal cluster explosion and provide a qualitatively new understanding of the energy deposition for increasing cluster sizes.

Furthermore, we describe our effort towards an experiment on size-selected clusters, which is of crucial importance for quantitative verification of theoretical predictions.

6.1. Microscopic model of the laser-cluster interaction.

The numerical simulations of the laser-cluster interactions were performed for small to medium-size (N = 108 – 5056 atoms per cluster) xenon clusters using a semi-classical molecular dynamics approach [127]. The code used in the simulation initially assumes a cluster that consists of neutral xenon atoms that are arranged within a sphere on a BCC lattice with a lattice constant of 5 Å (providing a local density of the cluster equal to that of liquid xenon). In the absence of the laser field there are no interactions between the neutral cluster atoms. In the calculation bound electrons are not treated explicitly. Free electrons appear in the system as classical particles only after ionisation of a parent atom takes place. Two ionisation mechanisms are taken into account: field ionisation and ionisation by collisions of ions or atoms with fast electrons. In the former case the total electric field at the position of an atom is evaluated as the sum of the laser electric field and the field resulting from all charged particles in the cluster. The ADK formula [3] is used to calculate the rate of field ionisation. Application of the ADK tunnelling formula requires the total electric field at the ionising atom to be sufficiently homogeneous over the distances relevant for tunnelling and therefore imposes a minimum distance to the other charged particles. Consequently, the possibility of field ionisation is disregarded if there is an electron within the proper volume of the atom, where the proper volume is defined as the effective volume occupied by one atom in a neutral cluster. Ionisation by inelastic electron-ion collisions is only allowed to occur if the impacting electron passes through the proper volume of the atom. The collisional ionisation rate is calculated as the product of the Lotz cross-section [131] and the relative velocity of an impacting electron, divided by the proper volume of the atom. The product of the ionisation rate and the time step duration gives the ionisation probability within a small time interval. The trajectories of the ions and the ionised electrons are calculated from Newton's equations.

The efficiency of the laser-cluster coupling was evaluated by monitoring the number of "inner" or "outer" ionisation events. Here "inner" ionisation refers to the total number of quasi-free electrons produced by field ionisation or collisional ionisation, and “outer” ionisation refers to the number of electrons that have been moved to a distance from the centre of the cluster that corresponds to twenty times the cluster radius. At this distance the interaction of the ionised electron with the other particles can be ignored [132] and the electron is considered to be permanently removed from the cluster. The asymptotic properties of the outer ionised electrons (velocity and angular distribution) are evaluated taking into consideration the residual interaction of the electrons with the laser field from the time that they are removed from the calculation.

6.2. Optimal-control calculations.

Optimisation of the laser-cluster coupling efficiency was performed using adaptive laser pulse shaping controlled by a GA [123, 133]. The clusters were exposed to shaped laser pulses that were derived by manipulation of the spectral phase function from a Fourier transform-limited (FTL) laser pulse with a 25 fs full-width-at-half-maximum (FWHM) electric field envelope and a peak intensity of 0.01 a.u. ($3.5*10^{14}$W/cm^2). The spectral phase function was defined by forty parameters distributed across the spectrum of the FTL pulse and spline interpolation at intermediate frequencies. The spectrum was centred at 800 nm, unless otherwise noted. Upon application of different phase functions a wide range of pulse shapes can be obtained.

The GA started with a random population of thirty individuals with each individual representing a specific spectral phase function and, consequently, a specific pulse shape. Each pulse shape was tested in our numerical model and assigned a fitness value, which was defined as the number of “inner” or “outer” ionisation events. The fitness value was used as feedback for the GA in order to determine a new generation of thirty individuals. The genetic algorithm used in these calculations was the micro-GA available online [133]. We used elitism for one best individual, uniform crossover (P_c=50%) and mutation (P_m=2%) to create a new generation. GA optimisations, which were propagated for two hundred generations, were performed for a cluster consisting of 108 Xe atoms. Thus, six thousand numerical experiments were performed in the course of the optimisation, which took approximately 20 days on a 2.8 GHz Pentium processor. Due to the expense of calculating the Coulomb forces between every pair of charged particles, the computational time required for one numerical experiment is proportional to the square of the number of particles in the cluster. For this reason the optimisation s were restricted to cluster sizes up to N=108.

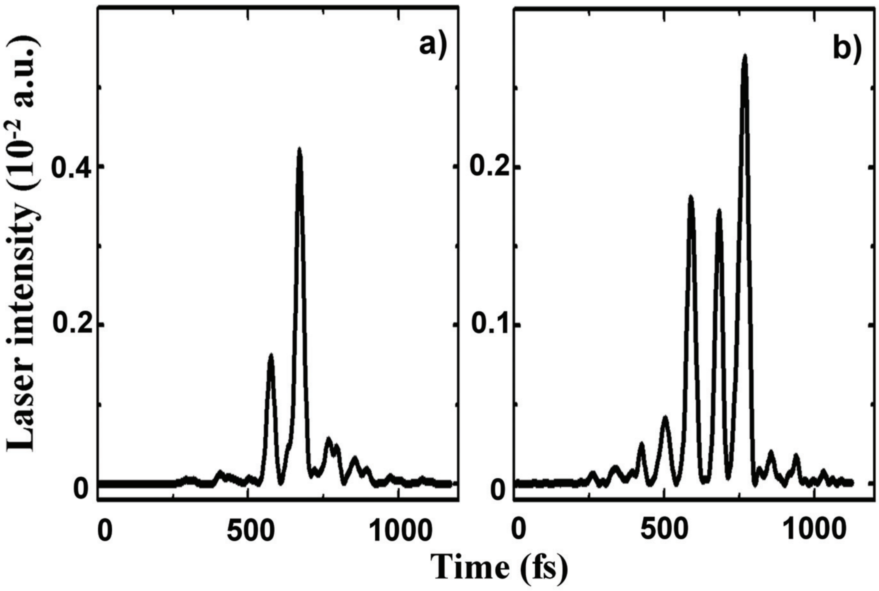

Figure 6-1. Laser pulse shapes optimising inner (a) and outer (b) ionisation for a Xe_{108} cluster. The results were obtained using a genetic algorithm and show that inner and outer ionisation are optimised by a sequence of two, respectively three pulses.

The best pulse shapes that were found for the optimisation of inner and outer ionisation for Xe_{108} are shown in Figure 6-1. Remarkably, the applied optimal phase patterns have broken the laser pulse up into a sequence of two pulses for inner ionisation (Figure 6-1a) and three pulses for outer ionisation (Figure 6-1b), with a separation of approximately 100 fs between the pulses. We note that in a subsequent run with a different set of random numbers controlling the crossover and mutation operators in the GA optimisation procedure, optimised pulse shapes very similar to the ones shown in Figure 6-1 were obtained. The sequence of random numbers involved in the code also influences the ionisation dynamics. Whether or not ionisation takes place is decided by comparison of the ionisation probability with a random number. Therefore, similar to a real-life experiment, the outcome of our numerical experiment may vary if a calculation is repeated, even though the same pulse shape is applied. Finally, we note that we do not claim to have determined the global optimal pulse shapes for cluster ionisation in our present optimal-control calculations. Rather we consider as the main result of the GA calculations the discovery of "interesting" pulse shapes that can help to reveal the dynamics of the laser-cluster interaction. The pulse in Figure 6-1a produces on average 430 electrons by field- and collisional ionisation, which compares favourably to 360 inner ionised electrons in the absence of the phase manipulation, i.e., using an FTL pulse with the same total energy. The pulse in Figure 6-1b produces on average 280 outer ionisation events, which is almost twice as much as an FTL pulse. The difference between Figure 6-1a and b points towards a qualitative difference between the optimal conditions for inner and outer ionisation. In both cases the first pulse in the sequence is the trigger for the ionisation process and the cluster expansion. The second pulse in Figure 6-1a that optimises inner ionisation and that appears at the same delay in Figure 6-1b suggests that there is a specific time during the interaction of a cluster with a laser pulse when inner ionisation can be efficiently enhanced. The third pulse in Figure 6-1b indicates that there are *two* instances when the conditions for outer ionisation are favourably influenced.

To interpret the results of the optimal-control calculations, further simulations were performed using laser pulses consisting of a sequence of three FTL pulses. In a similar manner as in the optimal-control calculations inner and outer ionisation of xenon clusters were monitored as a function of the time delays $\Delta\tau_1$ and $\Delta\tau_2$ between the first and second pair of pulses in a three-pulse sequence. In doing so, we were interested in (a) confirming that a three-pulse sequence is indeed optimal for outer ionisation of Xe_{108}, (b) determining whether a three-pulse sequence also represents an improvement over single pulses ($\Delta\tau_1 = 0$ and $\Delta\tau_2 = 0$) or two-pulse sequences ($\Delta\tau_1$ =0 or $\Delta\tau_2$ =0) for other cluster sizes, laser intensities and laser wavelengths, and (c) being able to interpret the origin of the three-pulse optimum.

6.3. Calculations with a sequence of three pulses.

6.3.1. Cluster size effect.

Simulations with a three-pulse sequence, where inner and outer ionisation of xenon clusters were monitored as a function of the time delays $\Delta\tau_1$ and $\Delta\tau_2$ between the first and second pair of pulses, were performed for Xe_N clusters with N=108-1524. Each FTL laser pulse in the three-pulse sequence had a 25 fs FWHM electric ield envelope and a peak intensity of 0.0033 a.u. ($1.17*10^{14}$W/cm^2). When both delays are zero the overlap of the three pulses results in a single 25 fs FTL pulse with a peak intensity of 0.01 a.u. ($3.5*10^{14}$W/cm^2), i.e. the input pulse that was used – prior to modulation of the spectral phase - in the GA optimisations. Results for Xe_{108} and Xe_{302} are presented in Figure 6-2, followed by results for Xe_{588} and Xe_{1524} in Figure 6-3. A summary of the conditions that lead to maximum inner and outer ionisation is shown in Table 6-1 and Table 6-2. A number of important observations can be made from Figure 6-2. First of all, for both cluster sizes (Xe_{108} and Xe_{302}) and for both inner and outer ionisation, the best results are obtained when at least one of the delays is non-zero. A single FTL pulse ($\Delta\tau_1$ =$\Delta\tau_2$ =0) gives inferior results for both the inner and outer ionisation. Secondly, the optimal pulse shape is qualitatively different depending on whether inner or outer ionisation is monitored. Inner ionisation in Xe_{108} (Figure 6-2a) is maximized with a two-pulse sequence ($\Delta\tau_1$ = 120 fs, $\Delta\tau_2$ = 0), where the intensity of the second pulse is twice the intensity of the first pulse, in qualitative agreement with the GA optimisation in Figure 6-1a. Optimisation of outer ionisation for Xe_{108} requires a laser pulse consisting alternatively of two or three peaks (Figure 6-2b). The latter result (see Table 6-2) is qualitatively similar to the GA optimisation in Figure 6-1b and provides an equivalent fitness value. For slightly larger clusters (Xe_{302}) both inner and outer

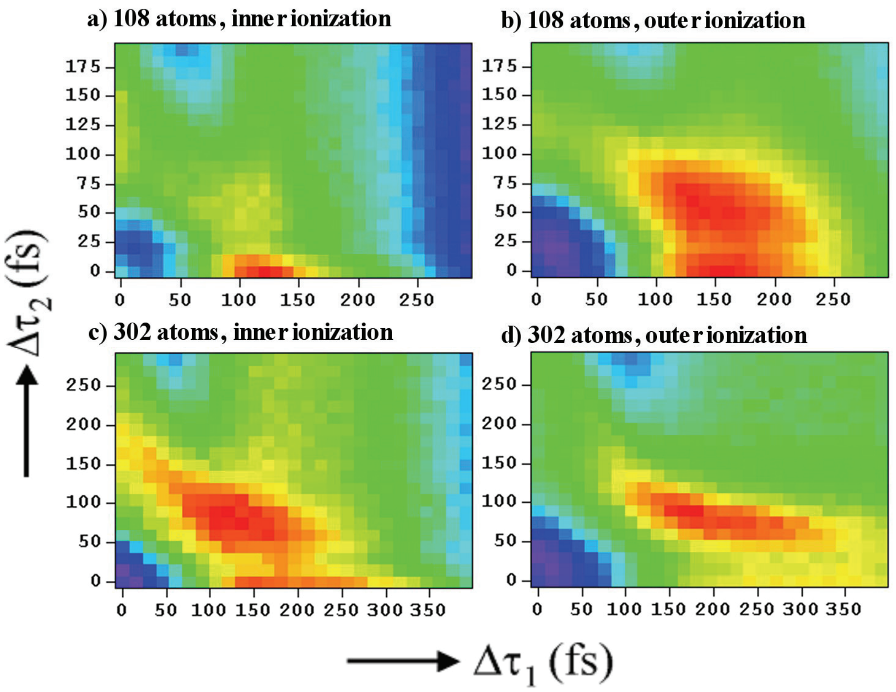

Figure 6-2. Contour plots showing the dependence of inner and outer ionisation yields for Xe_{108} and Xe_{302} on the delays $\Delta\tau_1$ and $\Delta\tau_2$ in a three-pulse sequence consisting of 25 fs FTL pulses with a peak intensity of 0.0033 a.u. each. Red and blue colors (dark gray and black in grayscale version) signify maximum and minimum ionisation levels, respectively; a) inner ionisation for Xe_{108} (max=445, min=340), b) outer ionisation for Xe_{108} (max=280, min=145), c) inner ionisation for Xe_{302} (max=1485, min=1090), d) outer ionisation for Xe_{302} (max=745, min=255).

ionisation are unambiguously optimised by a three-pulse sequence (Figure 6-2c and d). As shown in Figure 6-3, this trend continues for increasing cluster sizes. A distinct maximum for the number of outer ionisation events in Xe_{588} (Figure 6-3b) is obtained by a sequence of three pulses with $\Delta\tau_1 = 225$ fs, $\Delta\tau_2 = 100$ fs. In the case of Xe_{1524} a search for the optimal delays $\Delta\tau_1$ and $\Delta\tau_2$ in a three-pulse sequence allowed us to identify the optimum at $\Delta\tau_1 = 400$ fs, $\Delta\tau_2 = 125$ fs (see Figure 6-3d). We note that the accuracy of determining the optimal pulse shape decreases with increasing cluster size due to the computational expense of the calculations for larger cluster sizes. For example, each point in Figure 6-3c and d required approximately 10 hours of computation, thus requiring about 50 days of computation on a 2.8 GHz Pentium-

4 processor for the two plots shown. We also note that for larger cluster sizes the improvement that the three-pulse sequence represents over an FTL pulse dramatically increases. For example, for Xe_{1524} ionisation by the optimal three-pulse sequence leads to 3538 outer ionised electrons, compared to 450 for an FTL pulse.

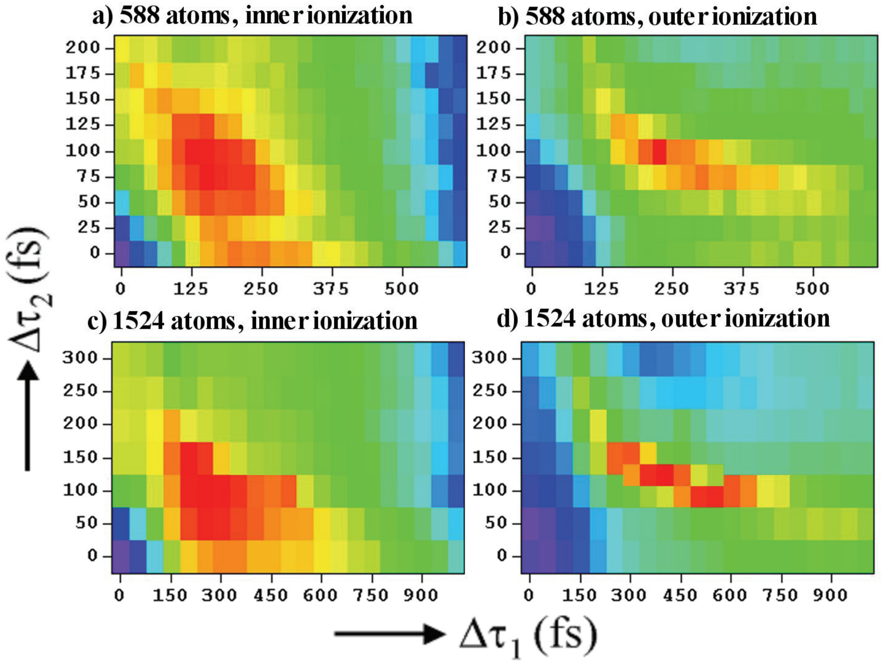

Figure 6-3. Contour plots showing the dependence of inner and outer ionisation yields for Xe_{588} and Xe_{1524} on the delays $\Delta\tau_1$ and $\Delta\tau_2$ in a three-pulse sequence consisting of 25 fs FTL pulses with a peak intensity of 0.0033 a.u. each. Red and blue colors (dark gray and black in grayscale version) signify maximum and minimum ionisation levels, respectively; a) inner ionisation for Xe_{588} (max=3280, min=2250), b) outer ionisation for Xe_{588} (max=1455, min=330), c) inner ionisation for Xe_{1524} (max=9575, min=6290), d) outer ionisation for Xe_{1524} (max=3540, min=450).

Our calculations clearly show an increase of the optimal delays for larger clusters (see Table 6-1 and Table 6-2). For Xe_{108} the optimal delays for outer ionisation are found to be $\Delta\tau_1$ = 140 fs, $\Delta\tau_2$ = 50 fs, which increase respectively to $\Delta\tau_1$ = 400 fs and $\Delta\tau_2$ = 125 fs for Xe_{1524}. Though the range of cluster sizes accessed in our calculations differs from the cluster sizes that have been studied thus far experimentally, these observations are in line with trends found in our experimental observations presented in Chapter 5 and with the results reported in ref. [96].

6.3.2. Laser intensity effects.

The evolution of the optimal pulse shapes with increasing laser intensity is shown in Figure 6-4 for Xe_{108}, Xe_{302} and Xe_{588} clusters. In these simulations the intensity of each pulse in the three-pulse sequence was 0.0066 a.u. ($2.33*10^{14}$W/cm^2), which is twice as much as in the previous calculations. Comparison of the results for Xe_{108} in Figure 6-4 with the relevant results in Figure 6-2 demonstrates qualitative similarity of the optimal pulse shapes obtained in both cases. The inner ionisation is maximized with a two-pulse sequence (Figure 6-4a), whereas outer ionisation is optimised alternatively by a sequence of two or three pulses (Figure 6-4b). In this case the number of outer ionisation events provided by the two-pulse sequence was around 10% higher than the one obtained with three pulses, whereas for lower intensity both sequences provided equivalent outer ionisation. A new feature appears in the cases of Xe_{302} and Xe_{588} at the higher laser intensity, namely, the possibility to maximize outer ionisation by just two laser pulses ($\Delta\tau_1$ = 285 fs, $\Delta\tau_2$ = 0 fs and $\Delta\tau_1$ = 350 fs, $\Delta\tau_2$ = 0 fs for Xe_{302} and Xe_{588} respectively). Thus unlike the lower intensity case in Figure 6-2d and Figure 6-3b where outer ionisation showed a clear maximum for a three-pulse sequence, the results in Figure 6-4d and f display the possibility to obtain similar values for outer ionisation using either two or three laser pulses.

A quantitative comparison of Figure 6-2, Figure 6-3 and Figure 6-4 demonstrates a shortening of the optimal delays for both inner and outer ionisation upon increase of the laser intensity (see Table 6-1 and Table 6-2). For example, the optimal delay between the two pulses for inner ionisation in Xe_{108} decreases from 120 fs to 80 fs when the laser intensity is doubled, whereas for outer ionisation in Xe_{108} the first delay in the optimal three-pulse sequence decreases respectively from $\Delta\tau_1$ = 140 fs to $\Delta\tau_1$ = 100 fs, while the second delay remains constant at $\Delta\tau_2$ = 50 fs.

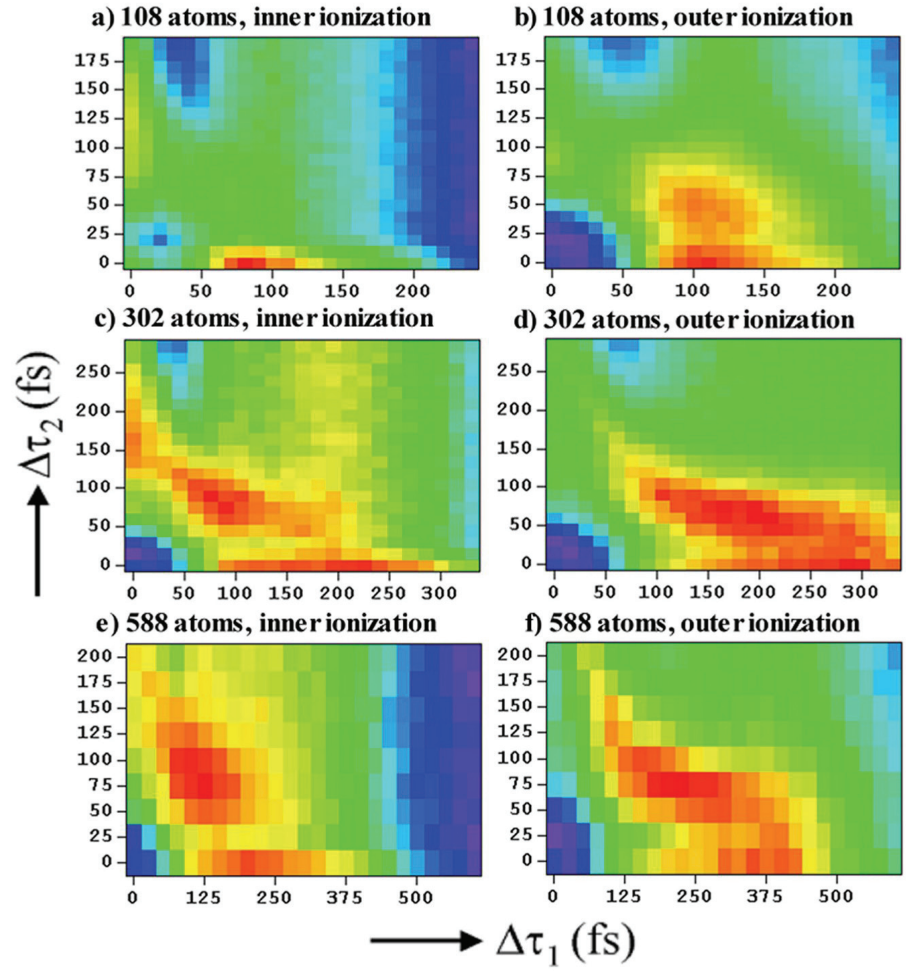

Figure 6-4. Contour plots showing the dependence of inner and outer ionisation yields for Xe_{108}, Xe_{302} and Xe_{588} on the delays $\Delta\tau_1$ and $\Delta\tau_2$ in a three-pulse sequence consisting of 25 fs FTL pulses with a peak intensity of 0.0066 a.u. each. Red and blue colors (dark gray and black in grayscale version) signify maximum and minimum ionisation levels, respectively; a) inner ionisation for Xe_{108} (max=510, min=380), b) outer ionisation for Xe_{108} (max=370, min=210), c) inner ionisation for Xe_{302} (max=1575, min=1180), d) outer ionisation for Xe_{302} (max=900, min=385), e) inner ionisation for Xe_{588} (max=3445, min=2360), f) outer ionisation for Xe_{588} (max=1670, min=535).

The shortening of the optimal delays upon increasing the laser intensity is in line with our experimental observations for large Xe clusters presented in Chapter 5 as well as with the results reported in ref. [96].

Cluster size N, laser intensity I (a.u.), laser wavelength λ (nm)	$\Delta\tau_1$ (fs)	$\Delta\tau_2$ (fs)	Inner ionisation	$(\langle r\rangle/r_0)_{\Delta\tau_1}$	$\Delta\varphi_{\Delta\tau_1}/\pi$	$\Delta\varphi_{\Delta\tau_2}/\pi$
a) Cluster size dependence						
N=108, I=0.0033, λ=800	120 (100; 140)	0	445	1.4 (1.3; 1.5)	0.1 (0; 0.1)	0.1 (0; 0.1)
N=302, I=0.0033, λ=800	120 (75; 195)	90 (45; 120)	1483	1.2 (1.1; 1.6)	0.1 (0; 0.2)	0.54 (0.2; 0.8)
N=588, I=0.0033, λ=800	150 (100; 225)	100 (50; 125)	3278	1.3 (1.1; 1.53)	0.1 (0; 0.2)	0.54 (0.4; 0.7)
N=1524, I=0.0033, λ=800	250 (200; 500)	100 (50; 150)	9575	1.3 (1.2; 2)	0.1 (0; 0.4)	0.3 (0.2; 0.6)
b) Intensity dependence						
N=108, I=0.0066, λ=800	80 (70; 90)	0	509	1.3 (1.2; 1.4)	0.1 (0; 0.2)	0.1 (0; 0.2)
N=302, I=0.0066, λ=800	225 (105; 240)	0	1562	2.3 (1.4; 2.4)	0.45 (0; 0.5)	0.45 (0; 0.5)
	75 (60; 120)	90 (60; 120)	1572	1.2 (1.1; 1.47)	0	0.63 (0.2; 0.7)
N=588, I=0.0066, λ=800	125 (75; 175)	75 (50; 125)	3445	1.4 (1.1; 1.7)	0.1 (0; 0.2)	0.63 (0.3; 0.7)
c) Wavelength dependence						
N=108, I=0.0033, λ=400	50 (30; 60)	0	684	1.2 (1.1; 1.4)	0.2 (0.1; 0.4)	0.2 (0.1; 0.4)
N=108, I=0.0033, λ=600	90 (70; 100)	0	540	1.4 (1.3; 1.47)	0.2 (0; 0.3)	0.2 (0; 0.3)
N=108, I=0.0033, λ=1064	160 (140; 180)	0	373	1.4 (1.3; 1.5)	0.1 (0; 0.2)	0.1 (0; 0.2)

Table 6-1. Summary of the conditions that lead to maximum inner ionisation in a three-pulse sequence The number of inner ionisation events, the average internuclear distance <r> and the phase difference Δφ between the collective electron oscillation and the oscillation of the laser field are given at the optimum time delays $\Delta\tau_1$ and $\Delta\tau_2$ that characterize the three-pulse sequence. Also shown in the table in brackets is the range of values of $\Delta\tau_1$ and $\Delta\tau_2$ where the number of inner ionised electrons remains above 90% of the difference between the maximum and the minimum ionisation levels ($n > n_{\min} + 0.9(n_{\max} - n_{\min})$) as well as the corresponding values of the average internuclear distance <r> and the phase shift Δφ.

Cluster size N, laser intensity I (a.u.), λ (nm)	$\Delta\tau_1$ (fs)	$\Delta\tau_2$ (fs)	Outer ionisation	$(\langle r\rangle/r_0)_{\Delta\tau_1}$	$\Delta\varphi_{\Delta\tau_1}/\pi$	$\Delta\varphi_{\Delta\tau_2}/\pi$
a) Cluster size dependence						
N=108, I=0.0033, λ=800	150 (130; 200)	0	280	1.55 (1.45; 2)	0.1 (0.1; 0.6)	0.1 (0.1; 0. 6)
	140 (110; 200)	50 (20; 80)	278	1.52 (0.3; 0.9)	0.2 (0; 0.6)	0.54 (0.2; 0. 7)
N=302, I=0.0033, λ=800	165 (135; 285)	90 (60; 105)	740	1.46 (1.3; 2.1)	0.2 (0.1; 0.4)	0.7 (0.5; 0. 7)
N=588, I=0.0033, λ=800	225 (200; 250)	100	1455	1.53 (1.46; 1.7)	0.2 (0.2; 0.3)	0.7 (0.7; 0.8)
N=1524, I=0.0033, λ=800	400 (250; 600)	125 (100; 150)	3538	1.7 (1.3; 2.4)	0.3 (0.1; 0.4)	0.6 (0.5; 0.7)
b) Intensity dependence						
N=108, I=0.0066, λ=800	110 (90; 140)	0	366	1.59 (1.4; 1.8)	0.2 (0.2; 0.3)	0.2 (0.2; 0.3)
	100 (90; 110)	50 (40; 60)	353	1.49 (1.4; 1.6)	0.2 (0.1; 0.2)	0.54 (0.4; 0.6)
N=302, I=0.0066, λ=800	285 (195; 330)	0	897	2.8 (2; 3.2)	0.54 (0.4; 0.6)	0.54 (0.4; 0.6)
	165 (105; 240)	75 (45; 90)	896	1.8 (1.4; 2.4)	0.3 (0; 0.5)	0.7 (0.45; 0.8)
N=588, I=0.0066, λ=800	350 (300; 425)	0	1601	3 (2.6; 3.5)	0.63 (0.45; 0.8)	0.6 (0.45; 0.8)
	200 (125; 350)	75 (50; 100)	1667	1.9 (1.4; 2.6)	0.3 (0.1; 0.6)	0.8 (0.6; 0.8)
c) Wavelength dependence						
N=108, I=0.0033, λ=400	70 (50; 70)	0	338	1.48 (1.2; 1.48)	0.6 (0.3; 0.6)	0.6 (0.3; 0.6)
N=108, I=0.0033, λ=600	110 (90; 130)	0	301	1.55 (1.4; 1.7)	0.2 (0.1; 0.4)	0.2 (0.1; 0.4)
	110 (90; 130)	30 (20; 40)	297	1.54 (1.4; 1.7)	0.3 (0.1; 0.5)	0.7 (0.5; 0.8)
N=108, I=0.0033, λ=1064	220 (140; 310)	80 (30; 130)	265	1.7 (1.3; 2.2)	0.2 (0; 0.4)	0.47 (0.2; 0.6)

Table 6-2. Summary of the conditions that lead to maximum outer ionisation in a three-pulse sequence. The number of outer ionisation events, the average internuclear distance <r> and the phase difference Δφ between the collective electron oscillation and the oscillation of the laser field are given at the optimum time delays $\Delta\tau_1$ and $\Delta\tau_2$ that characterize the three-pulse sequence. Also shown in the table in brackets is the range of values of $\Delta\tau_1$ and $\Delta\tau_2$ where the number of outer ionised electrons remains above 90% of the difference between the maximum and the minimum ionisation levels $(n > n_{\min} + 0.9(n_{\max} - n_{\min}))$ as well as the corresponding values of the average internuclear distance <r> and the phase shift Δφ.

6.3.3. Laser wavelength effect.

The dependence of the optimal pulse shapes for inner and outer ionisation in Xe_{108} upon laser wavelength is shown in Figure 6-5. We considered three additional wavelengths, namely 400 nm, 600 nm and 1064 nm. In all calculations the intensity of each pulse in the three-pulse sequence was again 0.0033 a.u. ($1.17*10^{14}$W/cm^2) and hence the results in Figure 6-5 can be directly compared to the results for Xe_{108} in Figure 6-2, where the spectrum was centred at wavelength of 800 nm. For all wavelengths considered, inner ionisation of Xe_{108} is optimised by two pulses. The delay between the two pulses increases from 50 fs at 400 nm to 160 fs at a 1064 nm central wavelength (Figure 6-5a, Figure 6-5c, Figure 6-2a, Figure 6-5e and Table 6-1). The extension of the optimal delays with increasing wavelength is also observed for outer ionisation (Figure 6-5b, Figure 6-5d, Figure 6-2b, Figure 6-5f and Table 6-2). These observations can be explained by the fact that the inner and outer ionisation yields are higher for shorter wavelengths and hence cluster expansion occurs faster. For the shortest wavelength considered here (400 nm) only two laser pulses are required to optimise outer ionisation, whereas for the longest wavelength considered here (1064 nm) the optimal pulse shape consists of three pulses. The calculations at 600 nm and 800 nm represent an intermediate case, exhibiting the transition of the optimal pulse shape from a two- to a three-pulse sequence.

6.4. Analysis and discussion.

In order to interpret the pulse shapes that optimise inner and outer ionisation and to reveal the mechanisms responsible for this optimisation, available numerical observables like the cluster expansion, the electron density and the collective electron motion were monitored as a function of time and examined in relation to the models mentioned in Chapter 4.

Analysis of our numerical results leads us to the conclusion that for all cluster sizes considered here, the enhancement of outer ionisation with a three-pulse

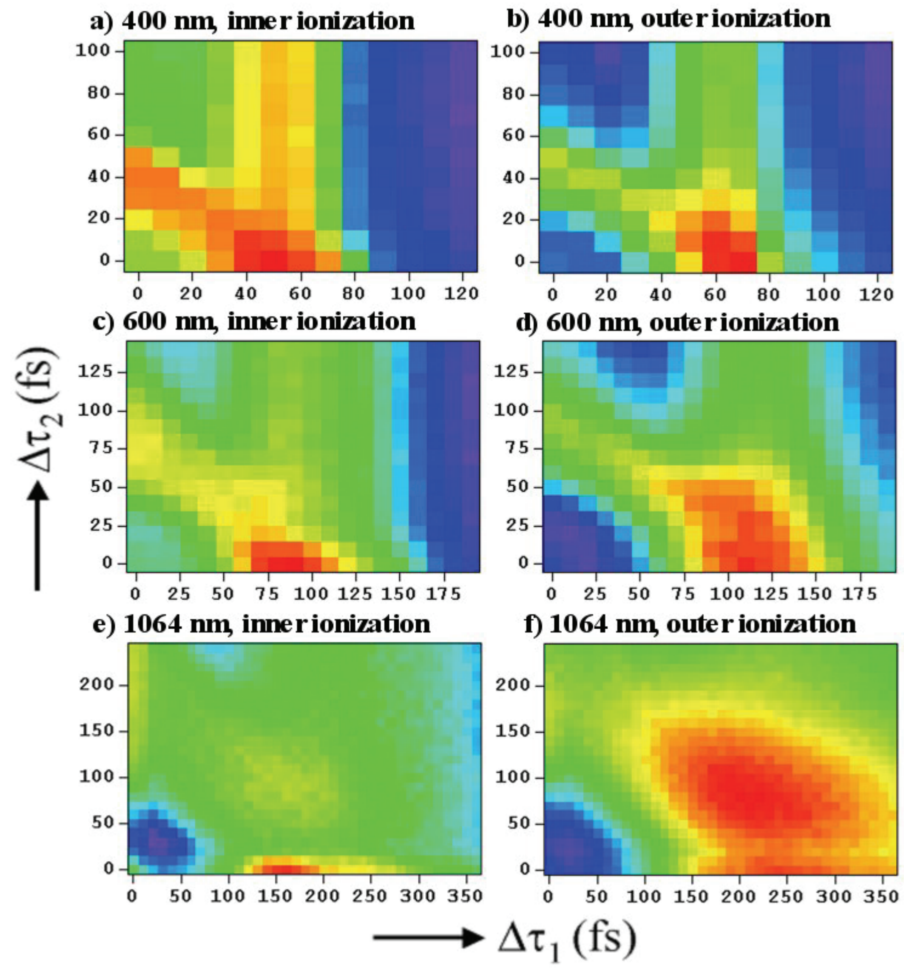

Figure 6-5. Contour plots showing the dependence of inner and outer ionisation yields for Xe_{108} on the delays $\Delta\tau_1$ and $\Delta\tau_2$ in a three-pulse sequence consisting of 25 fs FTL pulses with a peak intensity of 0.0033 a.u. each for different wavelengths. Red and blue colors (dark gray and black in grayscale version) signify maximum and minimum ionisation levels, respectively; a) inner ionisation for 400 nm (max=685, min=475), b) outer ionisation for 400 nm (max=340, min=160), c) inner ionisation for 600 nm (max=540, min=385), d) outer ionisation for 600 nm (max=305, min=160), e) inner ionisation for 1064 nm (max=375, min=290), f) outer ionisation for 1064 nm (max=265, min=120).

sequence can be explained by enhanced ionisation [106] and resonant driving of the collective motion of the electrons [107]. In our case the electron oscillations randomise in the time interval between the pulses when no laser is present, but quickly re-establish themselves when the laser turns back on. This makes it possible to determine the phase delay of the collective electron oscillation with respect to the laser field during the second and – in particular - the third pulse in the sequence by means of a cross-correlation of the instantaneous laser field and the oscillations of the centre of mass of the quasi-free electrons inside the cluster. Importantly, the phase shift depends on the delays that are applied between the laser pulses. We observe that the second pulse in the three-pulse sequence consistently occurs at a time when the optimal condition for enhanced ionisation is satisfied, whereas the third pulse arrives when the collective motion of the quasi-free electrons in the cluster resonantly couples with the laser field (see Table 6-2). Accordingly, inspection of the calculations reveals an increase in the number of field ionisation events at the optimal position of the second pulse, and in the number of electron-impact ionisation events during the third pulse.

Figure 6-6 presents details of the analysis of the optimal pulse for outer ionisation of Xe_{302} (see Figure 6-2d), where - as before - the laser intensity of each peak in the three-pulse sequence was 0.0033 a.u. ($1.17*10^{14}$W/cm^2). Ionisation by the first pulse leads to expansion of the cluster under the influence of Coulomb forces. As shown in Figure 6-6b, the average internuclear distance becomes 1.5 times the equilibrium value at a delay of 170 fs after the maximum of the first pulse, which is almost exactly the value of $\Delta\tau_1$ in the optimum three-pulse sequence. At this point the collective electron oscillations are practically in phase with the laser field ($\Delta\varphi \cong 0$, Figure 6-6c) and play no role in the laser energy absorption. The value of the phase shift $\Delta\varphi$ between the collective electron oscillations and the laser field that occurs during the third pulse increases with the delay of that pulse and goes through $\pi/2$ for $\Delta\tau_2 = 70$ fs, close to the optimum time delay $\Delta\tau_2 = 90$ fs found in Figure 6-2d. A similar analysis applies to all cases where a three-pulse sequence is found to be the optimum for outer ionisation. We note here that in the cases when the optimal values of $\Delta\tau_1$ and $\Delta\tau_2$ for inner or outer ionisation cover a broad range of values (see for example Figure 6-4d and f), assignment of the mechanisms responsible for the optimisation can be only approximate.

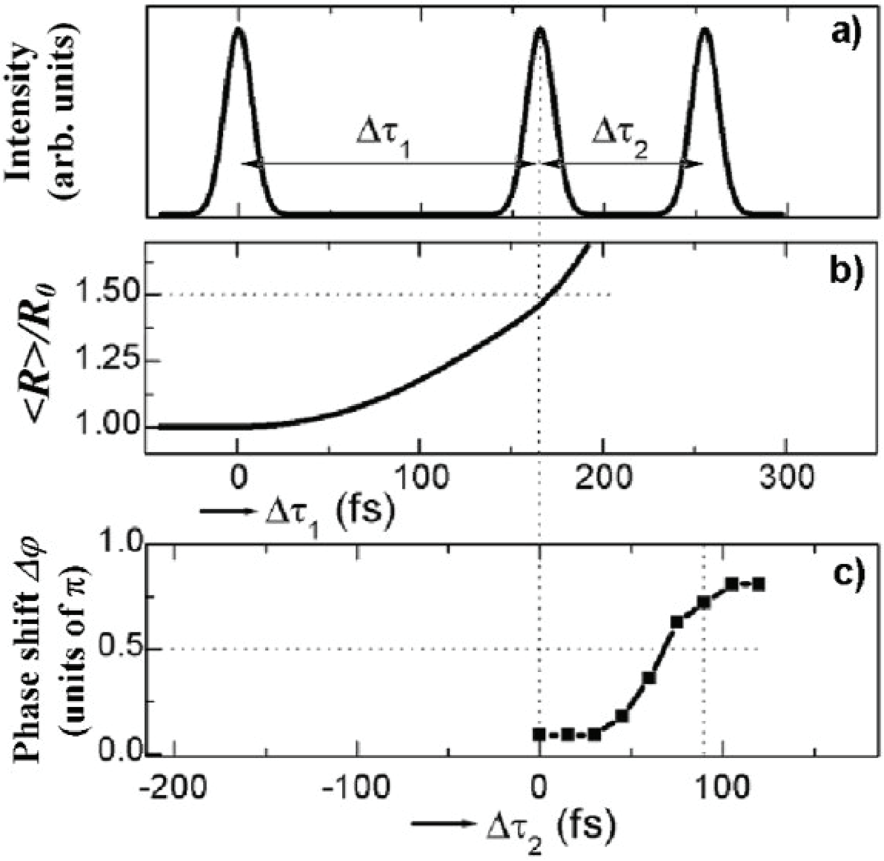

Figure 6-6. Three-pulse sequence that maximizes outer ionisation for Xe_{302} (a), along with the average internuclear distance between the atoms $<R>/R_0$ as a function of $\Delta\tau_1$ (b) and the phase shift between the collective electron oscillation and the laser field oscillation during the third pulse as a function of $\Delta\tau_2$ (c). The occurrence of $<R>/R_0 = 1.5$ and $\Delta\varphi = \pi/2$ at time delays close to $\Delta\tau_1$ and $\Delta\tau_2$ of the pulse in (a), supports the interpretation of the second and third pulse in the sequence in terms of enhanced ionisation and resonant driving of the collective electron oscillation, respectively. We note that the phase shifts plotted in (c) were obtained in a series of calculations where $\Delta\tau_2$ was systematically varied and where $\Delta\varphi$ during the third pulse was determined for each value of $\Delta\tau_2$ using the procedure explained in the text.

In a number of cases it was observed that outer ionisation could also be optimised by a sequence of just two laser pulses. In this case the mechanism that is operative during the second pulse depends on the cluster size, the laser intensity and the laser wavelength. For Xe_{108} and a laser wavelength of 800 nm (Figure 6-2b,

Figure 6-4b) the mechanism is enhanced ionisation. In small clusters the electrons can gain enough energy to leave the cluster through enhanced ionisation during the intense second pulse. This is especially true at higher laser intensities (Figure 6-4b), when a two-pulse sequence gives more extensive outer ionisation than a three-pulse sequence. By contrast, in larger clusters most quasi-free electrons created by enhanced ionisation cannot leave the cluster due to the higher space charge of the cluster and require further heating by the driving laser field, preferably at the collective electron oscillation resonance. This effect is illustrated by our calculations on Xe_{302} and Xe_{588}. At lower intensity (I=0.0033 a.u., Figure 6-2d and Figure 6-3b) a three-pulse sequence involving enhanced ionisation and resonant excitation of the collective electron oscillation is clearly superior to a two-pulse sequence. However, for higher laser intensity (I=0.0066 a.u., Figure 6-4d and f) it is possible to efficiently optimise outer ionisation by just two pulses. Importantly though, the mechanism that is responsible for the efficient outer ionisation is at that point the resonant collective motion of the quasi-free electrons in the cluster (see Table 6-2). Enhanced ionisation on its own is not sufficient for maximizing outer ionisation in larger clusters due to the high space charge in the cluster. Instead, the mechanism of resonant electron oscillations can efficiently heat and outer ionise electrons that were initially inner ionised by the first laser pulse, but remained trapped inside the cluster until the arrival of the second pulse. The two ionisation mechanisms discussed also reveal themselves in the dependence of the optimal pulse shapes for outer ionisation of Xe_{108} on laser wavelength (Figure 6-2b, Figure 6-5b, d, f). For the longest wavelength (1064 nm) the outer ionisation is optimised by a three-pulse sequence with involvement of both ionisation mechanisms. For shorter wavelengths (800 nm and 600 nm) the optimal pulse consists alternatively of two or three peaks, associated respectively with the mechanism of enhanced ionisation or in case of three peaks with both mechanisms of ionisation. The values of the optimal delays in the three-pulse sequence decrease from $\Delta\tau_1 = 220$ fs, $\Delta\tau_2 = 80$ fs for 1064 nm to $\Delta\tau_1 = 110$ fs, $\Delta\tau_2 = 30$ fs for 600 nm. The shift in $\Delta\tau_1$ is due to the higher ionisation efficiency at shorter wavelengths, resulting in a faster cluster expansion. Furthermore, the reduction of $\Delta\tau_2$ with shorter wavelength is consistent with a resonant ionisation mechanism, since for higher resonance frequency the resonance conditions are achieved earlier in time. For the shortest wavelength considered here (400 nm) optimisation of outer ionisation requires only two pulses. The optimal conditions for both ionisation mechanisms are satisfied when the second pulse arrives at $\Delta\tau_1 = 70$ fs. In this case fast cluster expansion and electron heating during the intense second pulse effectively lead to shortening of $\Delta\tau_2$ to zero.

The results for inner ionisation show trends qualitatively similar to outer ionisation (Table 6-1). In Xe_{108} inner ionisation is maximized by a two-pulse sequence for any laser intensity and wavelength considered here (Figure 6-2a, Figure 6-4a, Figure 6-5a, c, e), while for larger clusters a third peak appears in the optimal pulse shapes (Figure 6-2c, Figure 6-3a, c, Figure 6-4c, e). However, interpretation of the optimal pulse shapes for inner ionisation turns out to be less transparent. Inspection of our calculations for Xe_{108} during the second pulse of an optimal two-pulse sequence shows that more than 70% of inner ionised electrons are produced by field ionisation. This observation seems to be consistent with interpretation of the optimal pulse shape in terms of enhanced ionisation, similar to the previously discussed case of outer ionisation. Nevertheless, assigning the optimisation of inner ionisation to enhanced ionisation is problematic. As shown in Table 6-1the second pulse in the optimal two-pulse sequence tends to arrive before the condition for enhanced ionisation is fulfilled. Likewise, for larger clusters, where inner ionisation is optimised by three pulses, the optimal delay for the second pulse does not exactly satisfy the conditions for the enhanced ionisation mechanism.

An inner ionisation event is recorded in our model when a quasi-free electron is created inside the cluster. However electrons with close-to-zero potential energy can stay quasi-bound to their parent atom. Since the interatomic barriers go up with increasing internuclear distance R we would expect inner ionisation to decrease with increasing R. On the other hand, the onset of outer ionisation reduces shielding effects and facilitates inner ionisation. The interplay between these two effects leads to the optimum for inner ionisation at an internuclear distance that is intermediate between the equilibrium internuclear distance and the optimum for outer ionisation.

We note that the arrival of the third pulse in the sequence that optimises inner ionisation (see Table 6-1) matches with resonant coupling of the collective electron oscillations with the driving laser field (with the possible exception of Xe_{1524}, where as mentioned before, the optimal pulse shape was defined with 50 fs uncertainty). Accordingly, most electrons that are inner ionised during the third pulse are produced by electron-impact ionisation.

6.5. Extrapolation to larger clusters (N = 5056).

The calculations with sequences of three pulses discussed above are restricted to relatively small cluster sizes due to the computational expense involved in each calculation. In order to get insight into the evolution of ionisation processes for larger clusters and to make our results relevant to experiments carried out with larger cluster sizes we performed a series of calculations with simple laser pulse shapes for Xe clusters containing 5056 atoms. These calculations and the predictions that they provide for several important and accessible experimental observables are described in this section.

6.5.1. Calculations with a sequence of FTL pulses.

We first considered interaction of Xe_{5056} with a sequence of two FTL laser pulses with a 25 fs FWHM electric field envelope and a peak intensity of 0.005 a.u. ($1.75*10^{14}W/cm^2$). For a zero delay the overlap of the two pulses results in the previously used single FTL pulse with a 25 fs FWHM electric field envelope and a peak intensity of 0.01 a.u. ($3.5*10^{14}W/cm^2$). The efficiency of outer and inner ionisation was examined as a function of the time delay between the two pulses. Results of these calculations are presented in Figure 6-7, where the curves with filled and open symbols correspond to the number of inner and outer ionised electrons respectively. For both inner and outer ionisation a non-zero optimal delay between the two pulses is found. The number of inner ionisation events obtained with an optimal delay of 600 fs between the two pulses is more than 30% higher than with a single FTL pulse with twice the peak intensity. Outer ionisation is optimised with a 1400 fs delay between the two pulses and produces 5 times more outer ionised electrons than with a single FTL pulse with twice the peak intensity. Inspection of the calculations shows that this optimisation of the outer ionisation is accompanied by resonant coupling of the collective electron oscillations with the laser field during the second pulse in the sequence, when the phase shift between the electron collective oscillations inside the cluster and the laser field goes through $\pi/2$. We have seen no indication of enhanced ionisation during the second pulse for both delays that optimise inner or outer ionisation in agreement with the findings for two-pulse sequences reported for Xe_N ($N \geq 302$).

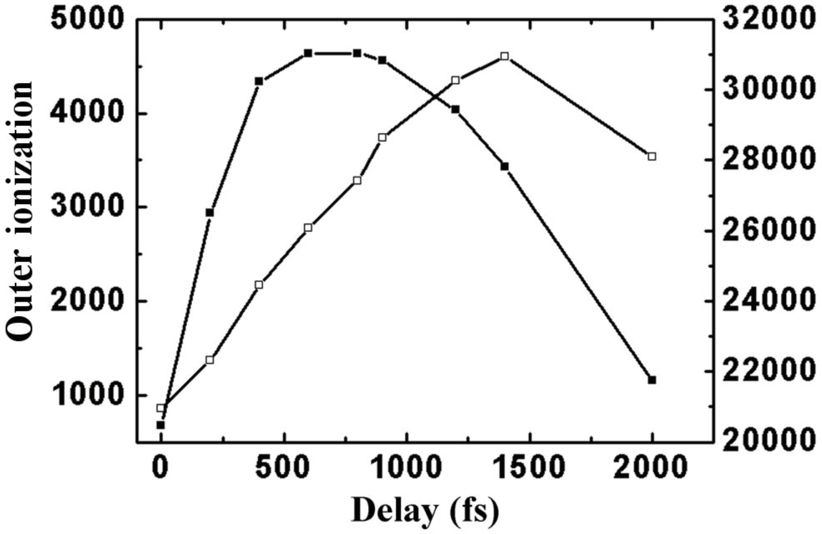

Figure 6-7. Dependence of inner and outer ionisation yields for Xe_{5056} on the delay in a two-pulse sequence consisting of 25 fs FTL pulses with a peak intensity of 0.005 a.u. each. Filled squares – the number of inner ionised electrons (right axis), open squares – the number of outer ionised electrons (left axis).

Extrapolation of the results obtained in our calculations so far allows us to make a prediction for the values of the delays in a three-pulse sequence that would optimise outer ionisation in Xe_{5056}. Applying a sequence of three FTL laser pulses with $\Delta\tau_1$ = 1060 fs and $\Delta\tau_2$ = 150 fs between the first and second pair of pulses, where each pulse has a 25 fs FWHM electric field envelope and a peak intensity of 0.0033 a.u. ($1.17*10^{14}$W/cm^2), we obtained more than 11500 outer ionisation events. This is a considerable improvement over a single FTL pulse with three times higher peak intensity, which leads to 860 outer ionisation events, and compares favourably to 4600 outer ionised electrons obtained in the previous optimal case of two pulses (Figure 6-7). We note that this significant enhancement of the outer ionisation yield was achieved even though our prediction for the optimal values of delays $\Delta\tau_1$ and $\Delta\tau_2$ does not provide exact matching of the second and the third peaks in the sequence to the optimal conditions for the two mechanisms of ionisation. Thus, further improvement of outer ionisation efficiency may be possible with more accurate estimates of the optimal delays in a three-pulse sequence.

6.5.2. Electron energy and angular distributions.

In order to explore the relation between the optimal conditions for inner or outer ionisation and the optimal conditions for energy coupling from the laser field into the cluster, the electron kinetic energy and angular distribution at the end of the laser-cluster interaction were examined. This also gives us a possibility to qualitatively compare the results of our simulations to earlier experiments [36, 37, 38], where the occurrence of features in the electron kinetic energy distributions due to resonant heating of the clusters has been discussed.

Figure 6-8a shows asymptotic electron kinetic energy distributions of outer ionised electrons from Xe_{5056} for four different laser pulse shapes, namely a single FTL pulse with a 25 fs FWHM electric field envelope and a peak intensity of 0.01 a.u. ($3.5*10^{14}$W/cm^2) (filled squares), two sequences of two FTL pulses with a 25 fs FWHM electric field envelope and a peak intensity of 0.005 a.u. ($1.75*10^{14}$W/cm^2) with a delay of 600 fs (open squares) and 1400 fs (filled triangles) between them, respectively, and finally a sequence of three FTL pulses with a 25 fs FWHM electric field envelope and a peak intensity of 0.0033 a.u. ($1.17*10^{14}$W/cm^2) with delays $\Delta\tau_1$

= 1060 fs and $\Delta\tau_2$ = 150 fs between the first and second pair of pulses (open triangles).

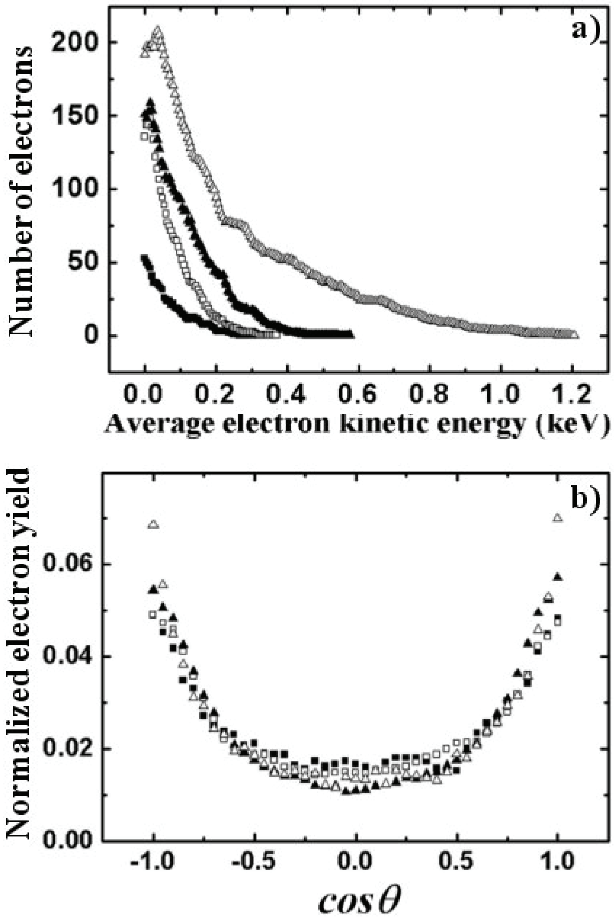

Figure 6-8 a) Asymptotic electron kinetic energy distributions b) and electron angular distributions of outer ionised electrons from Xe_{5056} for four different laser pulse shapes, namely, a single 25 fs FTL pulse with a peak intensity of 0.01 a.u. (filled squares), a sequence of two 25 fs FTL pulses with a peak intensity of 0.005 a.u. each with a delay of 600 fs (open squares) and 1400 fs (filled triangles), and a sequence of three 25 fs FTL pulses with a peak intensity of 0.0033 a.u. each with delays $\Delta\tau_1$ = 1060 fs and $\Delta\tau_2$ = 150 fs (open triangles).

All electron kinetic energy distributions are qualitatively similar and display a single-peaked structure. Furthermore, an increase in the yield of outer ionisation through the application of a better laser pulse shape is accompanied by an enhancement of the average kinetic energy of outer ionised electrons. For a single FTL pulse the average temperature of the electrons leaving the cluster is approximately 85 eV. Electrons that are ejected from the cluster after the first pulse in a two-pulse sequence are characterized by an electron temperature of about 80 eV. The average temperature of the electrons that are emitted after the second laser peak depends on the value of delay between the laser peaks and grows from 90 eV for a delay of 600 fs to a maximum of 140 eV with a delay of 1400 fs between the two pulses. The average electron temperature goes down when the delay is further increased. So the 1400 fs delay that optimises the number of outer ionised electrons (see Figure 6-7) also provides the most efficient laser energy transfer to the electrons emitted from a Xe_{5056} cluster.

The sequence of three pulses with delays $\Delta\tau_1$ = 1060 fs and $\Delta\tau_2$ = 150 fs between the first and second pair of pulses provides electrons that are characterized by an average electron temperature of 270 eV, which compares favourably to the optimal two-pulse sequence. We note also that for any considered laser pulse shape the single-peaked structure of electron kinetic energy distributions remains unaffected. Qualitatively similar results were observed experimentally in [37] for slightly larger clusters.

Asymptotic electron angular distributions are given in Figure 6-8b. The distributions are normalized to the number of electrons emitted from the cluster and are shown for the same conditions as in Figure 6-8a. For all pulse shapes quantitatively similar electron angular distributions are observed with the majority of electrons being ejected along the laser polarization axis. We have also observed that electrons that leave the cluster after the first peak in a two-pulse sequence have angular distributions equivalent to the ones acquired after the second laser peak. Our observation that the electron angular distribution is peaked along the laser polarization axis is consistent with earlier experimental results for larger Xe clusters [37].

Our simulations predict that for selected combinations of the cluster size, the laser intensity and the laser wavelength the ionisation may be optimised by a three-pulse sequence involving both enhanced ionisation and resonant driving of the collective electron oscillations. We have observed that altering the conditions of the laser-cluster interaction (for example, an increase of the laser intensity) can simplify the dynamics, so that only one mechanism remains involved. This may be the reason why the optimal-control experiments presented in Chapter 5 and in ref. [102] observed a two-pulse sequence as the optimal pulse shape for the production of highly charged ions and X-ray photons: both experiments were performed with larger clusters and at higher intensities, and moreover made use of samples containing a broad cluster size distribution. Quantitative verification of our results requires an experiment on size-selected clusters, where the efficiency of laser energy coupling into a cluster of a given size can be measured as a function of applied pulse shapes and the mechanisms of laser-cluster energy transfer can be determined experimentally.

6.6. Towards an experiment on size-selected clusters.

Generation of rare-gas cluster beams is based on the expansion of a dense gas through a nozzle into a vacuum or a region of small pressure. As a result, the random thermal energy is converted into the directed kinetic energy, the temperature of an expanding gas drops strongly and the gas becomes supersaturated leading to formation of liquid or solid density droplets, or clusters, bonded by van der Waals forces. This method of cluster formation can be realised in a pulsed regime, which leads to formation of a dense target as well as allows synchronisation with the laser.

The mean cluster size produced via gas expansion in vacuum depends on the gas backing pressure, the initial gas temperature, the gas species and the geometry of the nozzle. In order to estimate the average cluster size N as a function of experimental conditions, Hagena introduced an empirical parameter Γ [124], which also characterises the onset of clustering in a gas jet:

$$\Gamma = k\frac{(d/\tan\alpha)^{0.85}p_0}{T_0^{2.29}} \qquad N = 33\left(\frac{\Gamma}{1000}\right)^{2.35}, \tag{9}$$

where d is the jet throat diameter in μm; α is the jet expansion half angle (α=45° for a sonic expansion, but it can be much smaller for a supersonic expansion), p_0 is the backing pressure in mbar, T_0 is the initial gas temperature, and k is an empirical constant that depends on the atomic species (k = 5500 for Xe, 2890 for Kr, 1650 for Ar, 185 for Ne and 3.85 for He [134]). Most studies show that clustering begins when the Hagena parameter $\Gamma > 1000$. Large clusters ($>10^4$ atoms per cluster) predominate when $\Gamma > 5\times10^4$. For example, in the experiment described in Chapter 5 for the values of parameters used (d = 500 μm, α = 45°, T_0 = 300 K and p_0 = 6 bars) we estimated that $\Gamma = 1.4\times10^4$ and $N = 1.6\times10^4$ for Xe gas.

The Hagena scaling suggests that clustering is more significant for heavier noble gases such as Xe and Kr (large values of the constant k). The scaling also indicates that larger clusters can be produced with more narrow nozzle (smaller opening angle) and higher backing pressure. Using these parameters we can to some extent control the average size of the clusters produced. Experimentally the average cluster size in the jet can be determined by performing Rayleigh scattering measurements [39, 135]. However both the Hagena formula and the scattering technique only provide information on the average size of the clusters, whereas cluster size distribution remains unknown. In the meantime the width of this distribution can be as large as 100% [136].

Wide cluster-size distribution commonly used in practice is the major problem for the direct quantitative comparison between experiment and theory. First of all, since theoretical models and numerical simulations consider a single cluster size, an adequate comparison requires averaging over the cluster-size distribution. Such averaging is computationally too demanding and moreover the exact shape of the distribution is unknown. Furthermore, as we have seen in our simulations, variation of the cluster size by a relatively small amount can have a significant effect on the dynamics of the cluster expansion and consequently on the resonant effects of laser energy coupling into a cluster. Therefore, a size effect observed in the simulations can be significantly reduced in the experiment. Finally, experiments on rare-gas clusters dealing with wide cluster-size distributions are limited to large average sizes, while the range of tens to hundreds atoms per cluster remains inaccessible. At the same time the results of experiments on small clusters could be directly compared to the predictions of the enhanced ionisation model for clusters [106], which so far has not been tested experimentally. The above-mentioned considerations demonstrate the need for experimental results on selected cluster sizes.

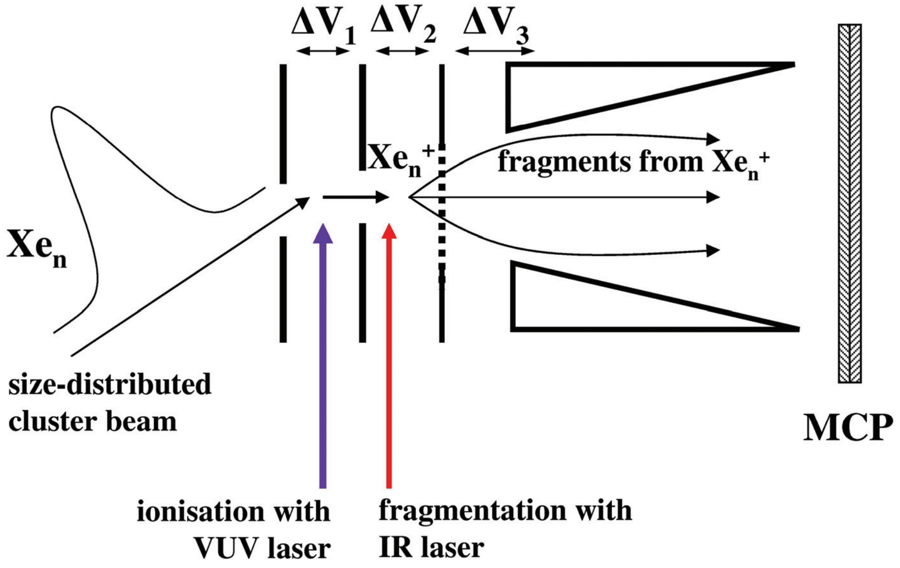

Figure 6-9. A schematic of a VMIS assembly modified for detection of high-energy ions and electrons resulting from the interaction of size-selected clusters with intense laser fields.

Figure 6-9 shows a schematic of our experimental set-up for performing experiments on size-selected clusters. The set-up consists of a VMIS assembly modified for detection of high-energy electrons expected from interaction of clusters with intense laser fields and involves two synchronised lasers for size-selection and for cluster fragmentation, respectively. A cluster jet was formed by expansion of

Xenon under a backing pressure of 3 bars into vacuum through the supersonic nozzle used in the experiments described in Chapter 5 According to Hagena scaling the estimated average cluster size was N = 3×10^3. The cluster beam was pulsed at a repetition rate of 12.5 Hz with a pulse duration of 250 μs, which kept the pressure in the interaction chamber around 10^{-7} mbar during experiments, while the background pressure remained on the order of 10^{-8} mbar.

A cluster beam containing a broad size distribution entered the VMIS between the first and the second electrodes in the direction perpendicular to the spectrometer axis, where it was crossed at a right angle with the first laser beam. This beam delivered vacuum-ultraviolet (VUV) radiation at 118 nm, which was obtained by generating the third harmonic of a YAG laser operating at 355 nm (typically 5-10 ns pulse duration, 30 mJ/pulse) in a cell filled with xenon. The resulting photon energy of 10.5 eV allows single-photon ionisation of all neutral xenon clusters containing more than 12 atoms per cluster [137]. The singly charged clusters were accelerated towards the detector in a strong electrostatic field created between the first two electrodes, and consequently were spatially and temporally separated.

Interaction of singly charged clusters with a femtosecond infrared (IR) laser occurs between the second and the third electrodes of the VMIS. We note that any clusters, which remained neutral after the interaction of the cluster jet with the VUV radiation, cannot reach the interaction region with the IR laser, since the electrostatic field applied between the first and the second electrodes does not affect them. By changing the delay between the VUV and the IR lasers we can selectively choose a single cluster size which would experience the interaction with the IR laser. The cluster fragments resulting from the interaction with the IR laser are projected onto the MCP and their properties are monitored with time-of-flight (TOF) or VMI techniques. The voltages on the second and the third electrodes can be adjusted in order to obtain the optimal conditions for imaging, whereas the fourth, shaped electrode is designed in order to confine the trajectories of high-energy electrons on the detector.

In the imaging regime of VMIS significant kinetic energies of cluster fragments expected from intense laser-cluster interaction should allow us to distinguish the contribution of fragments from the close-to-zero-energy contributions of the parent clusters and the background created by the IR laser. In the TOF regime, however, detection of the ionic fragments from a selected cluster size can be obscured by the signal from the parent singly charged clusters of different sizes and by background ions resulting from the IR laser. For this reason, in order to observe the ionic fragments of a selected cluster size in the TOF regime we set equal voltages on the second and the third electrodes, so that the ions created by the IR laser from background atoms with zero initial kinetic energy cannot reach the detector, and second, we perform a subtraction of the TOF traces recorded with the single VUV laser from the traces recorded when both the VUV and the IR lasers are present.

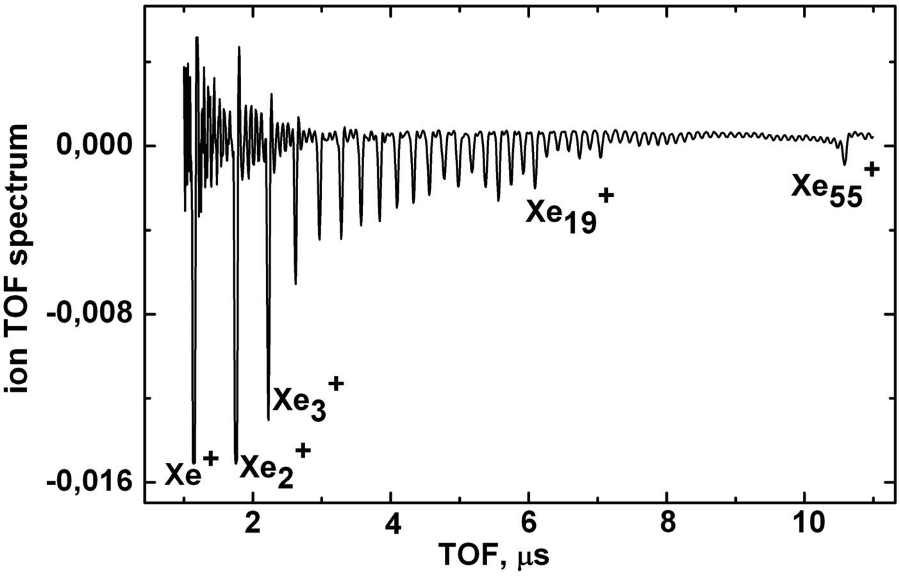

Figure 6-10. A TOF trace recorded with a single VUV laser interacting with a neutral cluster jet. The TOF spectrum shows presence of singly charged ions Xe_N^+ with N = 1 – 58.

Figure 6-10 shows an ion TOF trace recorded with a single VUV laser interacting with a neutral cluster jet. The following voltages were applied to the electrodes: V_1 = 12.5 kV, V_2 = 5 kV, V_3 = 5 kV, V_4 = 5.05 kV. The TOF spectrum shows the presence of singly charged ions Xe_N^+ with N = 1 – 58. Higher masses at longer TOF cannot be detected due to limited detection efficiency of the detector. The pronounced peak at N=55 corresponds to the magic number of atoms required for complete-shell icosahedra [138]. As mentioned earlier one-photon absorption at 118 nm can only ionise clusters containing more than 12 atoms. Therefore the appearance of lighter ions in the TOF regime must be due to dissociation of larger clusters, whose absorption cross-section might be sufficiently large for absorption of an additional photon.

Interaction with a selected cluster size can be directly monitored in the TOF spectrum by choosing an appropriate delay between the VUV and the IR lasers. The left panel in Figure 6-11 shows depletion of the signal from Xe_{19}^+ due to fragmentation of this particular cluster size with the IR laser when the delay between the lasers is set for 1.65 μs. The signal of the neighbouring cluster sizes remains unaffected. Visualisation of small ionic fragments resulting from the interaction of Xe_{19}^+ with the IR laser is achieved via subtraction of the signal obtained with the single VUV laser from the signal obtained with both the VUV and the IR lasers. Depletion of the Xe_{19}^+ peak in the right panel in Figure 6-11 appears as a positive signal, whereas the negative signal in this representation corresponds to the new fragments resulting from the interaction of Xe_{19}^+ with the IR laser. According to the calibration of the TOF spectrum the observed fragments are singly charged ions containing up to three xenon atoms. No ions with higher charge-states could be observed. This indicates that the experiment was performed at low IR laser intensity leading to fission of the parent clusters into smaller neutral and singly charged fragments. Our results are consistent with a recent observation of singly charged fragments resulting from interaction of medium-sized clusters with an IR laser at the intensity of 3.6×10^{13} W/cm^2 [139]. Analysing the velocity distributions of the observed fragments the authors concluded that the fragmentation mechanism involves a process of indirect double ionisation with the formation of an excited singly charged ion, followed by relaxation and charge transfer by auto-ionising collision, which leads to a Coulomb explosion and fission of the cluster into two singly charged fragments.

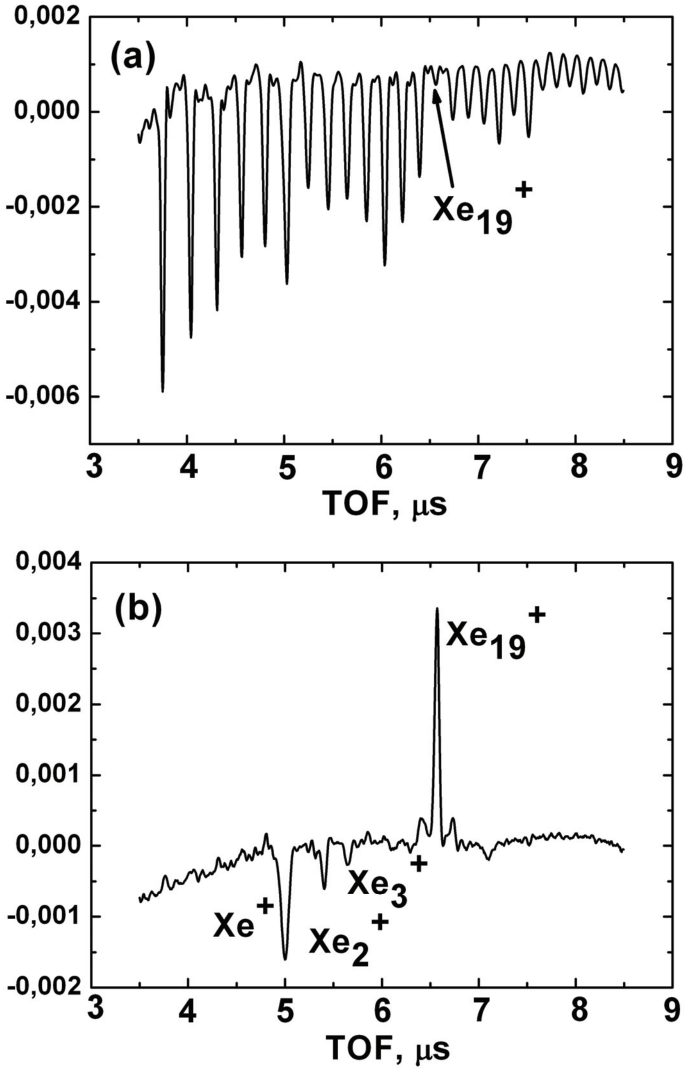

Figure 6-11. A TOF spectrum recorded with the IR laser coming 1.65 μs after the VUV laser: (a) depletion of the signal from Xe_{19}^{+} due to fragmentation of this particular cluster size with the IR laser; (b) subtraction of the signal obtained with the single VUV laser from the signal obtained with both the VUV and the IR lasers. Depletion of the Xe_{19}^{+} peak appears as a positive signal, the negative signal corresponds to small singly charged fragments resulting from the interaction of Xe_{19}^{+} with the IR laser.

The experiment developed and initiated in our present work has a high potential for further progress. First of all, observation of high-intensity laser-cluster interaction with production of highly charged ions must be possible under our experimental conditions. This requires a fine adjustment of a spatial overlap between the focus of the IR laser and the singly ionised cluster jet. In its turn, the singly ionised cluster jet has to form a dense target for the the interaction with the IR laser.

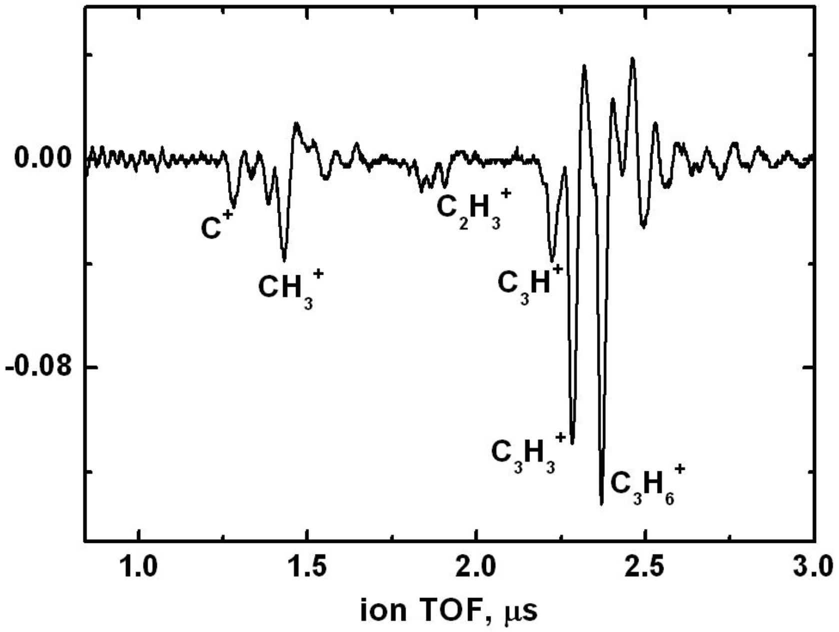

Figure 6-12. A TOF spectrum of a propylene molecule C_3H_6 ionised with the VUV laser. The light fragments containing a single Carbon atom result from 2-photon ionisation.

In other words, the singly charged clusters must originate from the focus of the VUV laser, which is not trivial, since single-photon ionisation of clusters may occur anywhere within the focal volume. We have made an important step towards the solution of this problem. Replacing the jet of Xenon clusters with a jet of propylene molecules $\mathbf{C_3H_6}$ (IP=9.73 eV) we have managed to observe 2-photon ionisation and fragmentation of the molecule with the VUV laser (Figure 6-12). Non-linearity of the process allows us to accurately determine the overlap of the VUV focus with the gas jet and ensure formation of a dense target for the interaction with the IR laser at the next step.

Implementation of the VMI technique will allow observation of ion charge-state distributions as well as ion and electron momentum distributions. Measuring the properties of fragments resulting from the high-intensity fragmentation of a selected cluster size as a function of the laser pulse shape one can directly compare the experimental observations to the results of numerical modelling and therefore determine the mechanism of laser-cluster interaction.

6.7. Conclusion.

In conclusion, we have presented numerical simulations of cluster ionisation by intense shaped laser pulses. We have shown that the interaction of Xe_N (N = 108-1524) clusters with an intense laser pulse is governed by two special instants of time when the conditions for laser energy absorption in the cluster are most favourable. The mechanisms that are operative at these moments are enhanced ionisation and resonant driving of collective electron oscillations, the former having its origin in intense field interactions of small molecules, and the latter in plasma physics. Our results thus show how the physics of clusters in intense laser fields evolves from dynamics of small molecules and provide insight into the onset of collective effects when increasingly large clusters are studied.

Furthermore, we have demonstrated a possibility of performing an experiment on size-selected clusters. An original experimental set-up has been developed and the first results demonstrate a high potential for studies of strong laser interactions with a single cluster size, which will allow verification of the proposed mechanisms of the efficient laser-cluster energy coupling.

SUMMARY

This thesis describes experimental and theoretical studies on the interaction of strong infrared laser fields with atoms and atomic clusters. The thesis is divided into three parts.

Part I contains a single Chapter 1, which gives an introduction to the physics of strong-field and multiphoton phenomena and provides an overview of the main strong-field phenomena observed in atoms, molecules and clusters. Furthermore, Chapter 1 describes the state-of-the-art in strong-field science and sets the scene for the future progress towards the fundamental control of matter in space and time.

Part II, consisting of Chapter 2 and 3, is devoted to the phenomenon of above-threshold ionisation (ATI) in rare-gas atoms, which since its discovery in 1979 became the first experimental manifestation of strong-field light-matter interactions and has remained an active subject of research ever since.

Chapter 2 gives an overview of the major aspects of atomic ATI, crucial for shaping of the modern understanding of this phenomenon, and highlights the open questions in the field, which are addressed in Chapter 3 of this thesis.

Chapter 3 describes the experimental results on ATI in Xenon and Argon in a wide range of laser wavelengths from 600 to 800 nm and from 1200 to 1600 nm. Photoelectron momentum spectra recorded with an imaging spectrometer are carefully reproduced in TDSE calculations. We have established the dominance of resonance-enhanced ionisation mechanism in the visible frequency range over a wide range of laser intensities both in the multiphoton and in the tunnelling regimes. In addition we have observed and investigated two characteristic contributions in the electron momentum spectra, which have attracted a lot of attention within the last two years and whose origin so far remained an open question. Preliminary analysis of these patterns has been carried out and general trends on their evolution with the laser wavelength and laser intensity observed in our experimental data as well as in the TDSE calculations over a broad range of parameters are investigated and described in detail.

Summary

Part III of this thesis, consisting of Chapter 4, 5, and 6, is devoted to the interactions of strong laser fields with rare-gas clusters, which both offer a wealth of interesting physical phenomena and are invaluable as a model system at the transition from atoms to large and complex structures such as bio-molecules and nanoparticles.

Chapter 4 gives an overview of the major experimental observations in the physics of clusters interacting with femtosecond infrared (800 nm) lasers, describes briefly the principal theoretical models of laser-cluster interaction for increasing cluster sizes and touches upon the current trends in the research on the interaction of clusters with new light sources in the XUV regime.

Chapter 5 describes the results of optimal-control experiments and calculations on the production of highly charged ions in intense laser field irradiation of large xenon clusters. We have observed both experimentally and numerically that there exists a specific time when the laser field is most efficiently coupled to the electrons in the cluster, and have observed in our numerical simulations that the optimised pulse shape maximises the efficiency of resonant cluster heating.

Chapter 6 describes the results of numerical simulations of medium-sized xenon clusters interacting with intense shaped laser pulses under control of a genetic algorithm and provides a detailed analysis of the mechanisms of cluster ionisation under various conditions. We have identified the influence of several mechanisms in the optimal cluster explosion having their origin in molecular and plasma physics. Our results thus show how the physics of clusters in intense laser fields evolves from dynamics of small molecules and provide insight into the onset of collective effects when increasingly large clusters are studied. Furthermore, we have demonstrated a possibility of performing an experiment on size-selected clusters, which will allow verification of the proposed mechanisms of the efficient laser-cluster energy coupling.

SAMENVATTING

Dit proefschrift beschrijft een experimentele en theoretische studie naar de invloed van sterke laservelden in het infrarode gebied op atomen en atoomclusters. Het is onderverdeeld in drie delen.

Deel I (hoofdstuk 1) geeft een inleiding tot de fysica van sterke-velden en multifoton verschijnselen die optreden wanneer atomen, moleculen of clusters zich in intense laser-velden bevinden. Tevens wordt in hoofdstuk 1 de huidige stand van de sterke-velden wetenschap samengevat en blikt het vooruit naar een toekomstige fundamentele controle van materie in ruimte en tijd.

Deel II (hoofdstuk 2 en 3) is gewijd aan de zogenaamde *above-threshold-ionisation (ATI)* in edelgassen. Sinds de eerste observatie van interacties tussen licht en materie in sterke velden in 1979, heeft deze tak van wetenschap veel belangstelling gekregen.

In hoofdstuk 2 worden de belangrijkste aspecten van ATI in atomen beschreven, die cruciaal zijn voor het hedendaagse begrip van dit fenomeen. Daarnaast worden de huidige open vragen in dit gebied omschreven, die verder in hoofdstuk 3 worden behandeld.

Hoofdstuk 3 beschrijft experimentele resultaten van ATI in Xenon en Argon die behaald zijn met lasergolflengtes tussen de 600 en 800 nm en tussen the 1200 en 1600 nm. Foto-electron spectra die opgenomen zijn met een *imaging spectrometer* zijn zorgvuldig gereproduceerd met *time-dependent Schrödinger equation (TDSE)* berekeningen. We hebben de dominantie van het *resonance-enhanced ionisation* mechanisme in het zichtbare frequentie gebied vastgesteld bij tal van laser intensiteiten, zowel in het multifoton en in het tunneling regime. Daarnaast hebben we 2 karakteristieke bijdragen in de electron momentum spectra waargenomen en nader onderzocht. Deze waarnemingen hebben in de afgelopen 2 jaar veel aandacht gekregen van de wetenschappelijke gemeenschap en de oorsprong van deze bijdragen is tot heden een open vraag. We hebben een voorlopige analyse van deze patronen uitgevoerd en de algemene tendens hoe deze evolueren met lasergolflengte en intensiteit in de data en in de TDSE berekeningen, zijn onderzocht en in detail beschreven.

Deel III van dit proefschrift, bestaande uit hoofdstuk 4,5,6 is gewijd aan de interactie van intense laser velden met clusters van edelgasatomen. Deze systemen vertonen een varieteit aan interessante fysische verschijnselen en zijn daarnaast zeer waardevol als model systeem tussen de transitie van atomen naar grote en complexe structuren, zoals biomoleculen en nanodeeltjes.

Hoofstuk 4 geeft een overzicht van de belangrijkste experimentele observaties wanneer clusters blootgesteld worden aan femtoseconde laserpulsen in het infrarode gebied (800 nm) en beschrijft kort de voornaamste theoretische modellen voor laser-cluster interacties voor toenemende cluster-groottes. De huidige trends in het onderzoek naar interactie van clusters met nieuwe lichtbronnen in het extreem-ultraviolet (XUV) gebied, worden kort besproken.

Hoofdstuk 5 beschrijft de resultaten van *optimal-control* experimenten. Daarnaast worden berekeningen aan de vorming van meervoudig geladen ionen, wanneer grote xenon clusters blootgesteld worden aan intense laser-velden, besproken. We hebben gezien, zowel experimenteel als numeriek, dat er een specifieke tijd bestaat waar het laserveld het meest efficient koppelt aan de electronen in het cluster. Numerieke simulaties hebben daarnaast laten zien dat een geoptimaliseerde puls-vorm de efficientie van resonante *cluster heating* maximaliseert.

Hoofdstuk 6 beschrijft de resultaten van numerieke similaties, wanneer gemiddeld grote xenon clusters interacteren met intense laser pulsen, waarvan de pulsvorm gecontroleerd wordt door een genetisch algoritme. Daarnaast wordt er een gedetailleerde analyse gegeven van de mechanismes waarmee clusters ionizeren onder verschillende omstandigheden. We hebben de invloed van verschillende mechanismes, die hun oorsprong hebben in de moleculaire en plasma fysica, op de optimale cluster explosie bepaald. Onze resultaten laten zien hoe de fysica van clusters in intense laser velden vanuit de dynamica van kleine moleculen evolueert en geeft inzicht in het begin van collectieve effecten wanneer steeds grotere clusters worden bestudeerd. Verder demonstreren we de mogelijkheid voor het uivoeren van een experiment waarin de grootte van clusters geselecteerd kan worden, wat de verificatie van de voorgestelde mechanismes van de efficiente laser-cluster energiekoppeling, toelaat.

BIBLIOGRAPHY

[1] L V Keldysh 1964 *Ionisation in the field of a strong electromagnetic wave* Zh. Eksp. Teor. Fiz. **47** 1945
L V Keldysh 1965 Sov. Phys. – JETP **20** 1307 (Engl. transl.)

[2] M Yu Ivanov, O Smirnova and M Spanner 2005 *Anatomy of strong-field ionisation* J. Mod. Opt. **52** 165-84

[3] M V Ammosov, N B Delone and V P Krainov 1986 *Tunnel ionisation of complex atoms and of atomic ions in an alternating electromagnetic field* Sov. Phys. – JETP **64** 1191 (Engl. transl.)
M V Ammosov, N B Delone and V P Krainov 1986 Zh. Eksp. Teor. Fiz. **91** 2008

[4] B Walker, B Sheehy, K C Kulander and L F DiMauro 1996 *Elastic rescattering in the strong field tunneling limit* Phys. Rev. Lett. **77** 5031

[5] B Walker, B Sheehy, L F DiMauro, P Agostini, K J Schafer, and K C Kulander 1994 *Precision measurement of strong field double ionization of helium* Phys. Rev. Lett. **73** 1227

[6] R Lafon, J L Chaloupka, B Sheehy, P M Paul, P Agostini, K C Kulander, and L F DiMauro 2001 *Electron energy spectra from intense laser double ionization of helium* Phys. Rev. Lett. **86** 2762

[7] K D Schultz, C I Blaga, R Chirla, P Colosimo, J Cryan, A M March, C Roedig, E Sistrunk, J Tate, J Wheeler, **P** Agostini, L F Dimauro 2007 *Strong field physics with long wavelength lasers* J. Mod. Opt. **54** 1075

[8] Y Ni, S Zamith, F Lépine, T Martchenko, M Kling, O Ghafur, H G Muller, G Berden, F Robicheaux and M J J Vrakking 2008 *Above-threshold ionization in a strong dc electric field* Phys. Rev. A **78**, 013413

[9] H B Van Linden van den Heuvell and H G Muller 1988 in *Multi-photon Processes*, edited by S. J. Smith and P. L. Knight, Cambridge University Press.

[10] K C Kulander, K J Schafer, and J L Krause 1993 in *Super-intense laser-atom physics(SILAP III)*, edited by B. Piraux, volume 316, page 95, NATO, Plenum Press, New York.

[11] K J Schafer, B Yang, L F DiMauro and K C Kulander 1993 *Above threshold ionization beyond the high harmonic cutoff* Phys. Rev. Lett. **70** 1599

[12] P Corkum 1993 *Plasma perspective on strong field multiphoton ionization* Phys. Rev. Lett. **71** 1994

[13] D Fittinghoff, P Bolton, B Chang, and K Kulander 1992 *Observation of nonsequential double ionization of helium with optical tunnelling* Phys. Rev. Lett. **69** 2642

[14] P Agostini and L F DiMauro 2004 *The physics of attosecond light pulses* Rep. Prog. Phys. **67** 813
[15] M Lewenstein, P Balcou, M Ivanov, A L'Huillier, and P Corkum 1994 *Theory of high-harmonic generation by low-frequency laser fields* Phys. Rev. A **49** 2117

[16] M Drescher, M Hentschel, R Kienberger, G Tempea, Ch Spielmann, G A Reider, P B Corkum, F Krausz 2001 *X-ray Pulses Approaching the Attosecond Frontier* Science **291** 1923

[17] M Hentschel, R Kienberger, Ch Spielmann, G A Reider, N Milosevic, T Brabec, P Corkum, U Heinzmann, M Drescher and F Krausz 2001 *Attosecond metrology* Nature **414** 509

[18] P B Corkum, N H Burnet and M Y Ivanov 1994 *Subfemtosecond pulses* Opt. Lett. **19** 1870

[19] I J Sola, E Mevel, L Elouga, E Constant, V Strelkov, L Poletto, P Villoresi, E Benedetti, J-P Caumes, S Stagira, C Vozzi, G Sansone, M Nisoli *Controlling attosecond electron dynamics by phase-stabilized polarization gating* 2006 Nature Phys. **2** 319

[20] P B Corkum and F Krausz 2007 *Attosecond science* Nature Phys. **3** 381

[21] J H Posthumus 2004 *The dynamics of small molecules in intense laser fields* Rep. Prog. Phys. **67** 623

[22] C B Madsen, A S Mouritzen, T K Kjeldsen, and L B Madsen 2007 *Effects of orientation and alignment in high-order harmonic generation and above-threshold ionization* Phys. Rev. A **76** 035401

[23] A S Alnaser**,** X M Tong**,** T Osipov, S Voss, C M Maharjan, P Ranitovic, B Ulrich, B Shan, Z Chang, C D Lin, C L Cocke 2004 *Routes to control of* H_2 *coulomb explosion in few-cycle laser pulses* Phys. Rev. Lett. **93** 183202

[24] Th Ergler, A Rudenko, B Feuerstein, K Zrost, C D Schröter, R Moshammer, and J Ullrich 2005 *Time-Resolved Imaging and Manipulation of* H_2 *Fragmentation in Intense Laser Fields* Phys. Rev. Lett. **95** 093001

[25] M F Kling, Ch Siedschlag, A J Verhoef, J I Khan, M Schultze, Th Uphues, Y Ni, M Uiberacker, M Drescher, F Krausz, M J J Vrakking 2006 *Control of Electron Localization in Molecular Dissociation* Science **312** 246

[26] T Zuo, A D Bandrauk and P B Corkum 1996 *Laser Induced Electron Diffraction: A New Tool for Probing Ultrafast Molecular Dynamics* Chem. Phys. Lett. **259** 313

[27] M Lein, J P Marangos and P L Knight 2002 *Electron diffraction in above-threshold ionization of molecules* Phys. Rev. A **66** 051404

[28] M Spanner, O Smirnova, P Corkum and M Ivanov 2004 *Reading diffraction images in strong field ionisation of diatomic molecules* J. Phys. B **37** L243

[29] J Itatani, J Levesque, D Zeidler, H Niikura, H Pepin, J C Kieffer, P B Corkum and D M Villeneuve 2004 *Tomographic imaging of molecular orbitals* Nature **432** 867

[30] T Kanai, S Minemoto and H Sakai 2005 *Quantum interference during high-order harmonic generation from aligned molecules* Nature **435** 470

[31] S Baker, J S Robinson, C A Haworth, H Teng, R A Smith, C C Chirilă, M Lein, J W G Tisch, J P Marangos 2006 *Probing Proton Dynamics in Molecules on an Attosecond Time Scale* Science **312** 424

[32] M Lein 2007 *Molecular imaging using recolliding electrons* J. Phys. B **40** R135

[33] K C Kulander, K J Schafer, and J L Krause 1992 in *Atoms in Intense Laser Fields,* edited by M. Gavrila (Academic Press, New York)

[34] U Saalmann, Ch Siedschlag, and J M Rost 2006 *Mechanisms of cluster ionization in strong laser pulses* J. Phys. B **39** R39

[35] T Ditmire, J W G Tisch, E Springate, M B Mason, N Hay, R A Smith, J Marangos, M H R Hutchinson 1997 *High-energy ions produced in explosions of superheated atomic clusters* Nature (London) **386** 54

[36] Y L Shao, T Ditmire, J W G Tisch, E Springate, J P Marangos, and M H R Hutchinson 1996 *Multi-keV Electron Generation in the Interaction of Intense Laser Pulses with Xe Clusters* Phys Rev Lett **77** 3343

[37] E Springate, S A Aseyev, S Zamith, and M J J Vrakking 2003 *Electron kinetic energy measurements from laser irradiation of clusters* Phys. Rev. A **68** 053201

---

[38] V Kumarappan, M Krishnamurthy, and D Mathur 2002 *Two-dimensional effects in the hydrodynamic expansion of xenon clusters under intense laser irradiation* Phys. Rev. A **66** 033203

[39] T Ditmire, T Donnelly, A M Rubenchik, R W Falcone, and M D Perry 1996 *The Interaction of Intense Laser Pulses with Atomic Clusters* Phys. Rev. A **53** 3379

[40] T Ditmire, J Zweiback, V P Yanovsky, T E Cowan, G Hays, and K B Wharton 1999 *Nuclear Fusion from Explosions of Femtosecond-Laser Heated Deuterium Clusters* Nature (London) **398** 489

[41] U Saalmann and J M Rost 2005 *Electron dynamics in strong laser pulse illumination of large rare gas clusters* Eur. Phys. J. D **36** 159

[42] Th Fennel, T Doppner, J Passig, C Schaal, J Tiggesbaumker, and K-H Meiwes-Broer 2007 *Plasmon-Enhanced Electron Acceleration in Intense Laser Metal-Cluster Interactions* Phys. Rev. Lett. **98** 143401

[43] I Georgescu, U Saalmann, and J M Rost 2007 *Attosecond Resolved Charging of Ions in a Rare-Gas Cluster* Phys. Rev. Lett. **99** 183002

[44] R Neutze, R Wouts, D van der Spoel, E Weckert and J Hajdu 2000 *Potential for biomolecular imaging with femtosecond X-ray pulses* Nature **406** 752

[45] H N Chapman, A Barty, M J Bogan, S Boutet, M Frank, S P Hau-Riege, S Marchesini, B W Woods, S Bajt, W H Benner, R A London, E Plönjes, M Kuhlmann, R Treusch, S Düsterer, Th Tschentscher, J R Schneider, E Spiller, Th Möller, Ch Bostedt, M Hoener, D A Shapiro, K O Hodgson, D van der Spoel, F Burmeister, M Bergh, C Caleman, G Huldt, M M Seibert, F R N C Maia, R W Lee, A Szöke, N Timneanu and J Hajdu 2006 *Femtosecond diffractive imaging with a soft-X-ray free-electron laser* Nature Phys. **2** 839

[46] A Scrinzi, M Yu Ivanov, R Kienberger and D M Villeneuve 2006 *Attosecond Physics* J. Phys. B **39** R1

[47] T Pfeifer, C Spielmann and G Gerber 2006 *Femtosecond X-ray science* Rep. Prog. Phys. **69** 443

[48] P Agostini, F Fabre, G Mainfray, G Petite, and N Rahman 1979 *Free-Free Transitions Following Six-Photon Ionization of Xenon Atoms* Phys. Rev. Lett. **42** 1127

[49] P H Bucksbaum, R R Freeman, M Bashkansky, and T J McIlrath 1987 *Role of the ponderomotive potential in above-threshold ionization* J. Opt. Soc. Am. B **4** 760

[50] R R Freeman, P H Bucksbaum, H Milchberg, S Darack, D Schumacher, and M Geusic 1987 *Above-Threshold Ionization with Subpicosecond Laser Pulses* Phys. Rev. Lett. **59** 1092

[51] P Agostini, P Breger, A L' Huillier, H G Muller, G Petite, A Antonetti and A Migus 1989 *Giant Stark shifts in multiphoton ionization* Phys. Rev. Lett. **63** 2208

[52] M P de Boer and H G Muller 1992 *Observation of large populations in excited states after short-pulse multiphoton ionization* Phys. Rev. Lett. **68** 2747

[53] G N Gibson, R R Freeman and T J McIlrath 1992 *Verification of the dominant role of resonant enhancement in short-pulse multiphoton ionization* Phys. Rev. Lett. **69** 1904

[54] V Schyja, T Lang and H Helm 1998 *Channel switching in above-threshold ionization of xenon* Phys. Rev. A **57** 3692

[55] G G Paulus, W Nicklich, Huale Xu, P Lambropoulos, and H Walther 1994 *Plateau in above threshold ionization spectra* Phys. Rev. Lett. **72** 2851

[56] T F Gallagher 1988 *Above-Threshold Ionization in Low-Frequency Limit* Phys. Rev. Lett. **61** 2304

[57] P B Corkum, N H Burnett, and F Brunel 1989 *Above-threshold ionization in the long-wavelength limit* Phys. Rev. Lett. **62** 1259

[58] G G Paulus, W Becker, W Nicklich, and H Walther 1994 *Rescattering effects in above threshold ionization: a classical model* J. Phys. B **27** L703

[59] P Hansch, M A Walker, and L D Van Woerkom 1997 *Resonant hot-electron production in above-threshold ionization* Phys. Rev. A **55** R2535

[60] M P Hertlein, P H Bucksbaum, and H G Muller 1997 *Evidence for resonant effects in high-order ATI spectra* J. Phys. B **30** L197

[61] H G Muller and F C Kooiman 1998 *Bunching and Focusing of Tunneling Wave Packets in Enhancement of High-Order ATI* Phys. Rev. Lett. **81** 1207

[62] H G Muller 1999 *Numerical simulation of high-order above-threshold-ionization enhancement in argon* Phys. Rev. A **60** 1341

[63] M J Nandor, M A Walker, L D Van Woerkom, and H G Muller 1999 *Detailed comparison of above-threshold-ionization spectra from accurate numerical integrationsand high-resolution measurements* Phys. Rev. A **60** R1771

[64] F Grasbon, G G Paulus, H Walther, P Villoresi, G Sansone, S Stagira, M Nisoli, and S DeSilvestri 2003 *Above-Threshold Ionization at the Few-Cycle Limit* Phys. Rev. Lett. **91** 173003

[65] B Yang, K J Schafer, B Walker, K C Kulander, P Agostini, and L F DiMauro 1993 *Intensity-dependent scattering rings in high order above-threshold ionization* Phys. Rev. Lett. **71** 3770

[66] M Nandor, M Walker, and L Van Woerkom 1998 *Angular distributions of high-intensity ATI and the onset of the plateau* J. Phys. B **31** 4617

[67] H Helm, N Bjerre, M J Dyer, D L Huestis, and M Saeed 1993 *Images of photoelectrons formed in intense laser fields* Phys. Rev. Lett. **70** 3221

[68] H Helm and M J Dyer 1994 *Resonant and nonresonant multiphoton ionization of helium*
Phys. Rev. A **49** 2726

[69] P Hansch, M A Walker, L D Van Woerkom 1998 *Eight- and nine-photon resonances in multiphoton ionization of xenon* Phys. Rev. A **57** R709

[70] V Schyja, T Lang, and H Helm 1996 in *Ultrafast Processes in Spectroscopy*, edited by Swelto et al. (Plenum Press, New York), p. 311

[71] R Wiehle, B Witzel, H Helm, E Cormier 2003 *Dynamics of strong-field above-threshold ionization of argon: Comparison between experiment and theory* Phys. Rev. A **67** 063405

[72] C M Maharjan, A S Alnaser, I Litvinyuk, P Ranitovic, C L Cocke 2006 *Wavelength dependence of momentum-space images of low-energy electrons generated by short intense laser pulses at high intensities* J. Phys. B **39** 1955

[73] H Rottke, B Wolff, M Tapernon, K H Welge, and D Feldmann 1990 *Resonant multiphoton ionization of xenon in intense sub-ps-laser pulses* Z. Phys. D **15** 133

[74] P Kaminski**,** R Wiehle**,** V Renard, A Kazmierczak, B Lavorel, O Faucher, and B Witzel 2004 *Wavelength dependence of multiphoton ionization of xenon* Phys. Rev. A **70** 053413

[75] E Mevel, P Breger, R Trainham, G Petite, P Agostini, A Migus, J-P Chambaret, and A Antonetti *1993 Atoms in Strong Optical Fields: Evolution from Multiphoton to Tunnel Ionization* Phys. Rev. Lett. **70** 406

[76] M Wickenhauser, X M Tong and C D Lin 2006 *Laser-induced substructures in above-threshold-ionization spectra from intense few-cycle laser pulses* Phys. Rev. A **73** 011401

[77] C P J Martiny and L B Madsen 2007 *Finite bandwidth and carrier envelope phase difference effects in strong-field ionization of atoms by few-cycle circularly polarized laser pulses* Phys. Rev. A **76** 043416

[78] A S Alnaser, C M Maharjan, P Wang, and I V Litvinyuk 2006 *Multi-photon resonant effects in strong-field ionization: origin of the dip in experimental longitudinal momentum distributions* J. Phys. B **39** L323

[79] A Rudenko, K Zrost, C D Schröter, V L B de Jesus, B Feuerstein, R Moshammer and J Ullrich 2004 *Resonant structures in the low-energy electron continuum for single ionization of atoms in the tunnelling regime* J. Phys. B **37** L407

[80] D G Arbó, S Yoshida, E Persson, K I Dimitriou, and J Burgdörfer 2006 *Interference Oscillations in the Angular Distribution of Laser-Ionized Electrons near Ionization Threshold* Phys. Rev. Lett. **96** 143003

[81] M Wickenhauser, X M Tong, D G Arbó, J Burgdörfer, and C D Lin 2006 *Signatures of tunneling and multiphoton ionization in the electron-momentum distributions of atoms by intense few-cycle laser pulses* Phys. Rev. A **74** 041402

[82] Z Chen, T Morishita, A T Le, M Wickenhauser, X M Tong, and C D Lin 2006 *Analysis of two-dimensional photoelectron momentum spectra and the effect of the long-range Coulomb potential in single ionization of atoms by intense lasers* Phys. Rev. A **74** 053405

[83] T Morishita, Z Chen, S Watanabe, C D Lin 2007 *Two-dimensional electron momentum spectra of argon ionized by short intense lasers: Comparison of theory with experiment* Phys. Rev. A **75** 023407

[84] M J J Vrakking 2001 *An iterative procedure for the inversion of two-dimensional ion/photoelectron imaging experiments* Rev. Sci. Instrum. **72** 4084

[85] K J Schafer and K C Kulander 1990 *Energy analysis of time-dependent wave functions: application to above-threshold ionization* Phys. Rev. A **42** 5794

[86] K C Kulander and T N Rescigno 1991 *Effective potentials for time-dependent calculations of multiphoton processes in atoms* Comput. Phys. Commun. **63** 523

[87] H G Muller 1999 *An efficient propagation scheme for the time-dependent Schrödinger equation in the velocity gauge* Laser Phys. **9** 138

[88] S Augst, D D Meyerhofer, D Strickland, S L Chin 1991 *Laser ionization of noble gases by Coulomb-barrier suppression* J. Opt. Soc. Am. B **8** 858
[89] Z Chen, T Morishita, A T Le, and C D Lin 2007 *Analysis of two-dimensional high-energy photoelectron momentum distributions in the single ionization of atoms by intense laser pulses* Phys. Rev. A **76** 043402

[90] D Ray, B Ulrich, I Bocharova, C Maharajan, P Ranitovic, B Gramkow, M Magrakvelidze, S De, I V Litvinyuk, A T Le, T Morishita, C D Lin, G G Paulus and C L Cocke 2008 *Large-Angle Electron Diffraction Structure in Laser-Induced Rescattering from Rare Gases* Phys. Rev. Lett. **100** 143002

[91] M Okunishi, T Morishita, G Prumper, K Shimada, C D Lin, S Watanabe and K Ueda 2008 *Experimental Retrieval of Target Structure Information from Laser-Induced Rescattered Photoelectron Momentum Distributions* Phys. Rev. Lett. **100** 143001

[92] T Morishita, A T Le, Z Chen, and C D Lin 2008 *Accurate Retrieval of Structural Information from Laser-Induced Photoelectron and High-Order Harmonic Spectra by Few-Cycle Laser Pulses* Phys. Rev. Lett. **100** 013903

[93] T Remetter, P Johnsson, J Mauritsson, K Varjú, Y Ni, F Lépine, E Gustafsson, M Kling, J Khan, R López-Martens, K J Schafer, M J J Vrakking and A L'Huillier 2006 *Attosecond electron wave packet interferometry* Nature Phys. **2** 323

[94] M J J Vrakking et al In preparation.

[95] T Ditmire, R A Smith, J W G Tisch and M H R Hutchinson 1997 *High Intensity Laser Absorption in Gases of Atomic Clusters* Phys. Rev. Lett. **78** 3121

[96] J Zweiback, T Ditmire, and M D Perry 1999 *Femtosecond Time-Resolved Studies of Noble Gas Cluster Explosion Dynamics* Phys. Rev. A **59** R3166

[97] E Lamour, C Prigent, J P Rozet and D Vernhet 2005 *Physical parameter dependence of the X-ray generation in intense laser–cluster interaction* Nucl. Instrum. Methods B **235** 408

[98] E Springate, N Hay, J W G Tisch, M B Mason, T Ditmire, J P Marangos, and M H R Hutchinson 2000 *Enhanced Explosion of Atomic Clusters Irradiated by a Sequence of Two High-Intensity Laser Pulses* Phys. Rev. A **61**, 044101

[99] H Rabitz, R de Vivie-Riedle, M Motzkus, K Kompa 2000 *Whither the Future of Controlling Quantum Phenomena?* Science **288** 824

[100] A M Weiner 2000 *Femtosecond pulse shaping using spatial light modulators* Rev. Sci. Instrum. **71** 1929

[101] D E Goldberg 1999 Genetic Algorithms in Search Optimisation and Machine Learning 20th ed (Addison-Wesley Longman, Reading, MA)

[102] A S Moore, K J Mendham, D R Symes, J S Robinson, E Springate, M B Mason, R A Smith, J W G Tisch, and J P Marangos 2005 *Control parameters for ion heating and X-ray emission from laser induced cluster explosion* Appl. Phys. B: Lasers Opt. **80** 101

[103] E Rühl 2003 *Core level excitation, relaxation, and fragmentation of free clusters* Int. J. Mass Spectrom. **229** 117

[104] D Rolles, H Zhang, Z D Pesic, R C Bilodeau, A Wills, E Kukk, B S Rude, G D Ackerman, J D Bozek, R Díez Muiño, F J García de Abajo, and N Berrah 2007 *Size effects in angle-resolved photoelectron spectroscopy of free rare-gas clusters* Phys. Rev. A **75** 031201(R)

[105] T Seideman, M Yu Ivanov, and P Corkum 1995 *Role of Electron Localization in Intense-Field Molecular Ionization* Phys. Rev. Lett. **75** 2819

[106] C Siedschlag and J M Rost 2002 *Electron Release of Rare-Gas Atomic Clusters under an Intense Laser Pulse* Phys. Rev. Lett. **89** 173401

[107] U Saalmann and J M Rost 2003 *Ionization of Clusters in Intense Laser Pulses through Collective Electron Dynamics* Phys. Rev. Lett. **91** 223401

[108] C Jungreuthmayer, M Geissler, J Zanghellini, and T Brabec 2004 *Microscopic Analysis of Large-Cluster Explosion in Intense Laser Fields* Phys. Rev. Lett. **92** 133401

[109] P Mulser, M Kanapathipillai, and D H H Hoffmann 2005 *Two Very Efficient Nonlinear Laser Absorption Mechanisms in Clusters* Phys. Rev. Lett. **95** 103401

[110] M Kundu and D Bauer 2006 *Nonlinear Resonance Absorption in the Laser-Cluster Interaction* Phys. Rev. Lett. **96** 123401

[111] S V Fomichev, D F Zaretsky, D Bauer, W Becker 2005 *Classical molecular-dynamics simulations of laser-irradiated clusters: Nonlinear electron dynamics and resonance-enhanced low-order harmonic generation* Phys. Rev. A **71** 013201

[112] M Kundu, S V Popruzhenko, and D Bauer 2007 *Harmonic generation from laser-irradiated clusters* Phys. Rev. A **76** 033201

---

[113] B Shim, G Hays, R Zgadzaj, T Ditmire, and M C Downer 2007 *Enhanced Harmonic Generation from Expanding Clusters* Phys. Rev. Lett. **98** 123902

[114] H Wabnitz, L Bittner, A R B de Castro, R Döhrmann, P Gürtler, T Laarmann, W Laasch, J Schulz, A Swiderski, K von Haeften, T Möller, B Faatz, A Fateev, J Feldhaus, C Gerth, U Hahn, E Saldin, E Schneidmiller, K Sytchev, K Tiedtke, R Treusch, M Yurkov 2002 *Multiple ionization of atom clusters by intense soft X-rays from a free-electron laser* Nature **420** 482

[115] T Laarmann, A R B de Castro, P Gürtler, W Laasch, J Schulz, H Wabnitz, and T Möller 2004 *Interaction of Argon Clusters with Intense VUV-Laser Radiation: The Role of Electronic Structure in the Energy-Deposition Process* Phys. Rev. Lett. **92** 143401

[116] T Laarmann, A R B de Castro, P Gürtler, W Laasch, J Schulz, H Wabnitz, and T Möller 2005 *Photoionization of helium atoms irradiated with intense vacuum ultraviolet free-electron laser light. Part I. Experimental study of multiphoton and single-photon processes* Phys. Rev. A **72** 023409

[117] R Santra and C H Greene 2003 *Xenon Clusters in Intense VUV Laser Fields* Phys. Rev. Lett. **91** 233401

[118] Z B Walters, R Santra, and C H Greene 2006 *Interaction of intense vuv radiation with large xenon clusters* Phys. Rev. A **74** 043204

[119] C Siedschlag and J M Rost 2004 *Small Rare-Gas Clusters in Soft X-Ray Pulses* Phys. Rev. Lett. **93** 043402

[120] C Jungreuthmayer, L Ramunno, J Zhanghellini, and T Brabec 2005 *Intense VUV laser cluster interaction in the strong coupling regime* J. Phys. B: At. Mol. Opt. Phys. **38** 3029

[121] I Georgescu, U Saalmann, and J M Rost 2007 *Clusters under strong vuv pulses: A quantum-classical hybrid description incorporating plasma effects* Phys. Rev. A **76** 043203

[122] C Bostedt, H Thomas, M Hoener, E Eremina, T Fennel, K-H Meiwes-Broer, H Wabnitz, M Kuhlmann, E Plönjes, K Tiedtke, R Treusch, J Feldhaus, A R de Castro, and T Möller 2008 *Multistep Ionization of Argon Clusters in Intense Femtosecond Extreme Ultraviolet Pulses* Phys. Rev. Lett. **100** 133401

[123] R S Judson and H Rabitz 1992 *Teaching lasers to control molecules* Phys. Rev. Lett. **68** 1500

[124] O F Hagena 1992 *Cluster ion sources* Rev. Sci. Instrum. **63** 2374

[125] A T J Eppink and D H Parker 1997 *Velocity map imaging of ions and electrons using electrostatic lenses: Application in photoelectron and photofragment ion imaging of molecular oxygen* Rev. Sci. Instrum. **68** 3477

[126] M A Klosner and W T Silfvast 1998 *Intense xenon capillary discharge extreme-ultraviolet source in the 10–16-nm-wavelength region* Opt. Lett. **23** 1609

[127] E S Toma and H G Muller 2002 *Laser disintegration of Van der Waals clusters of carbon-containing molecules* Phys. Rev. A **66** 013204

[128] E Springate, N Hay, J W G Tisch, M B Mason, T Ditmire, M H R Hutchinson, and J P Marangos 2000 *Explosion of atomic clusters irradiated by high-intensity laser pulses: Scaling of ion energies with cluster and laser parameters* Phys. Rev. A **61** 063201

[129] K Y Kim, I Alexeev, E Parra, and H M Milchberg 2003 *Time-Resolved Explosion of Intense-Laser-Heated Clusters* Phys. Rev. Lett. **90** 023401

[130] E M Snyder, S A Buzza, and A W Castleman, Jr *Intense Field-Matter Interactions: Multiple Ionization of Clusters* Phys. Rev. Lett. **77** 3347

[131] W Lotz 1968 *Electron-Impact Ionization Cross Sections and Ionization Rate Coefficients for Atoms and Ions from Hydrogen to Calcium* Z. Phys. **216** 241

[132] I Last and J Jortner 2000 *Dynamics of the Coulomb explosion of large clusters in a strong laser field* Phys. Rev. A **62** 013201

[133] D L Carroll at http://cuaerospace.com/carroll/ga.html

[134] R A Smith, T Ditmire, J W G Tisch 1998 *Characterization of a Cryogenically Cooled High Pressure Gas Jet for Laser/Cluster Interaction Experiments* Rev. Sci. Instrum. **69** 3798

[135] A M Bush, A J Bell, J G Frey, and J M Mestdagh 1998 *Rayleigh Scattering of Laser and Synchrotron Radiation from Pulsed Free Jets of* Ar_n *and* $(N_2O)_n$ *Clusters* J. Phys. Chem. A **102** 6457

[136] V P Krainov M B Smirnov 2002 *Cluster beams in the super-intense femtosecond laser pulse* Phys. Rep. **370** 237

[137] G Ganteför, G Bröker, E Holub-Krappe, and A Ding 1989 *Photoionization thresholds of rare gas clusters* J. Chem. Phys. **91** 7972

[138] O Echt, K Sattler, and E Recknagel 1981 *Magic Numbers for Sphere Packings: Experimental Verification in Free Xenon Clusters* Phys. Rev. Lett. **47** 1121

[139] L Poisson, K D Raffael, M-A Gaveau, B Soep, J-M Mestdagh, J Caillat, R Taïeb and A Maquet 2007 *Low Field Laser Ionization of Argon Clusters: The Remarkable Fragmentation Dynamics of Doubly Ionized Clusters* Phys Rev Lett **99** 103401